SURPRISING CHEMISTRY IN LI-ION CELLS

By

Deijun Xiong

Submitted in partial fulfilment of the requirements

for the degree of Doctor of Philosophy

at

Dalhousie University

Halifax, Nova Scotia

August 2017

To my wife and my daughter

Table of contents

LIST OF TABLES

LIST OF FIGURES

ABSTRACT

High voltage LiNi$_x$Mn$_y$Co$_{(1-x-y)}$O$_2$ (NMC) cells with conventional ethylene carbonate-based electrolytes do not have good charge-discharge capacity retention above 4.3 V. It is therefore important to investigate the failure of the NMC cells at high voltage. In this thesis, lithiated graphite and delithiated NMC electrode materials taken from high voltage NMC/graphite full cells were studied individually using the pouch bag method and thermogravimetric analysis coupled with mass spectrometry (TGA-MS). The results obtained from the pouch bag method show that charged NMC positive electrodes stored at elevated temperature in pouch bags create more gas than the same electrodes stored in pouch full cells at the same temperature. Surprisingly, the charged NMC electrodes removed from pouch bags after storage at elevated temperature had larger impedance than those removed from pouch full cells. These results suggest that electrolyte oxidation at the positive electrode mainly contributes to gas generation and impedance growth in Li-ion cells. The results also show that the use of an Al$_2$O$_3$ surface coating and fluorinated electrolyte can hinder impedance growth at the positive electrode. The results obtained from the TGA-MS experiments show that oxygen can be released from charged NMC electrodes at high voltage at mild temperature. The results show that the amount of oxygen released can be greatly limited by utilizing larger NMC particles. These results provide new support that the released oxygen from charged NMC electrodes causes electrolyte oxidation resulting in cell failure.

In this thesis, the effects of different salt concentrations in ethylene carbonate (EC)-free electrolytes on cell performance and on their physical properties were also studied. The results show that 1.5 M salt concentration should be used to improve overall cell performance. Unexpectedly, at low salt concentrations below 0.4 M, the impedance of cells increased greatly. It was found that this result was due to the formation of contact ion pairs in the electrolyte. The results obtained from studies of the physical properties of EC-free electrolytes suggest that limited amount of dimethyl carbonate (a widely used linear carbonate) should be used in conventional electrolytes to improve low temperature cell performance.

LIST OF ABBREVIATIONS USED

AC – alternating current

A_c – peak area of a component of the calibration gas mixture

A_s – peak area of a component of the gas sample

ATR – attenuated total reflectance

C – capacitance of a capacitor

CI – chemical ionization

CMC-SBR – carboxymethyl cellulose-styrene butadiene

C_N – double layer capacitance of the negative electrode

C_P – double layer capacitance of the positive electrode

C-Si – graphite and silicon composite

DEC – diethyl carbonate

DMC – dimethyl carbonate

DMMP – dimethylmethylphosphonate

DTA – differential thermal analysis

DTD – 1,3,2-dioxathiolane-2,2-dioxide

e – electron

EC – ethylene carbonate

EI – electron ionization

EIS –electrochemical impedance spectroscopy

EMC – ethyl methyl carbonate

ES – ethylene sulfite

F – Faraday constant

f- frequency

$F_{buoyant}$ – buoyant force

FEC – fluoroethylene carbonate

$F_{tension}$ – force of the tension

FT-IR – Fourier transform infrared spectroscopy

GC – gas chromatography

GC-MS – gas chromatography coupled with mass spectrometry

GC-TCD – gas chromatography coupled with thermal conductivity detection

HFiP – tris(hexafluoro-iso-propyl)phosphate

IMFP – inelastic mean free path

IRC – irreversible specific capacity

KT – kilotons

L – inductance of an inductor

LCO – $LiCoO_2$

LEDC – lithium ethylene decarbonate

LFP – $LiFePO_4$

Li – lithium

Li^+ – lithium cation

$LiBF_4$ – Lithium tetrafluoroborate

LiBOB – Lithium bis(oxalato)borate

LIBs – lithium ion batteries

LiFSI – Lithium bis(fluorosulfonyl)imide

$LiPF_6$ – Lithium hexafluorophosphate

LiTFSi – Lithium bis(trifluoromethanesulfonyl)imide

LMO – $LiMn_2O_4$

LTO – $Li_4Ti_5O_{12}$

m – mass

MA – methyl acetate

$m_{balance}$ – change of weight measured by balance

MMDS – methylene methanedisulfonate

MP – methyl propionate

MS – mass spectrometry

M_w – molecular weight

n – number of moles of charge

NCA – $LiNi_{0.8}Co_{0.15}Al_{0.05}O_2$

NMC – $LiNi_xMn_yCo_{(1-x-y-z)}O_2$

NMC111 – $LiNi_{1/3}Mn_{1/3}Co_{1/3}O_2$

NMC442 – $LiNi_{0.4}Mn_{0.4}Co_{0.2}O_2$

NMC532 – $LiNi_{0.5}Mn_{0.3}Co_{0.2}O_2$

NMC622 – $LiNi_{0.6}Mn_{0.2}Co_{0.2}O_2$

NMC811 – $LiNi_{0.8}Mn_{0.1}Co_{0.1}O_2$

PBF – pyridine trifluoroborate

PC – propylene carbonate

PES – prop-1-ene-1,3-sultone

PES211 – 1M $LiPF6$ in EC/EMC (3:7 w/w) with 2% PES + 1% DTD + 1% TTSPi

PES222 – 1M $LiPF6$ in EC/EMC (3:7 w/w) with 2% PES + 2% DTD + 2% TTSPi

PVDF – polyvinylidene fluoride

Q – usable capacity of a Li-ion cell

Q_C – charge specific capacity

Q_D – discharge specific capacity

Q_{sc} – specific capacity

R – resistance of a resistor

R_N – resistance to the motion of Li^+ ions and electrons through the SEI for the negative electrode

R_P - resistance to the motion of Li^+ ions and electrons through the SEI for the positive electrode

SEI – solid electrolyte interphase

R_{ct} – charge transfer impedance

R_e – electrolyte resistance

TAP – triallyl phosphate

TCD – thermal conductivity detection

TFEC – bis (2,2,2 – trifluoroethyl) carbonate

TGA – thermogravimetric analysis

TGA-MS – thermogravimetric analysis coupled with mass spectrometry

TTSP – tri(trimethylsilyl)phosphate

TTSPi – tri(trimethylsilyl)phosphite

V – voltage or potential

V_a – volume of a component of the gas sample

VC – vinylene carbonate

V_c – volume of a component of the calibration gas mixture

V_{cell} – cell voltage

VEC – vinyl ethylene carbonate

V_{neg} – potential of the negative electrode vs Li/Li$^+$

V_{pos} - potential of the positive electrode vs Li/Li$^+$

XPS – X-ray photoelectron spectroscopy

Z' – real component of the impedance

-Z" – imaginary component of the impedance

$Z_{+/+}$ – impedance of a positive/positive symmetric cell

$Z_{+/-}$ – impedance of a full cell

$Z_{-/-}$ – impedance of a negative/negative symmetric cell

ΣF – sum of forces

$\Delta F_{tension}$ – change of the force of the tension

$\Delta F_{buoyant}$ – change of the force of the buoyant

ΔV – volume change

Δm – weight change

ρ – density

ω – angular frequency

ACKNOWLEDGEMENTS

CHAPTER 1:   INTRODUCTION

1.1   Motivation

Lithium-ion batteries (LIBs) are widely used in portable consumer electronics such as cell phones, laptops and camcorders. Other applications for LIBs include electric vehicles and electricity storage which require improved energy density, extended lifetime and decreased cost of LIBs.[1,2]

Lithium cobalt oxide, $LiCoO_2$, (LCO) is the most common positive electrode material used in portable electronic devices (45000 tons/year).[2] The major disadvantages of this material are its high cost (the use of cobalt) and poor thermal stability in the charged state (Li_xCoO_2, x<0.5).[3-5] Throughout this thesis, thermal stability will specifically refer to the ability of positive electrode materials to resist releasing oxygen at elevated temperature. $LiNi_xMn_yCo_{(1-x-y)}O_2$ (NMC) materials with low cobalt content are popular alternatives to LCO because these provide a good combination of cost, cycle life, energy density and thermal stability.[5-7] Furthermore, NMC grades such as $LiNi_{0.4}Mn_{0.4}Co_{0.2}O_2$(NMC442) can be operated up to 4.7 V vs Li/Li^+ without structural change providing opportunities to improve the energy density of LIBs.[8]

It is a great challenge to cycle NMC/graphite cells well at high voltage (above 4.3 V).[9-11] One approach to improve the existing NMC technology is the development of new electrolyte solution chemistries. The use of new solvent blends and the introduction of electrolyte additives are two practical ways to improve the lifetime of high voltage NMC cells.[12-15] Another approach to improve cell performance is the application of a surface

coating onto the NMC particles.[16–19] Even though both of these approaches have proven to be quite valuable, the lifetime of these high voltage NMC cells is not still good enough.

Great efforts have been expended to investigate why high voltage NMC cells show poor cycling retention during charge-discharge cycling. Analytical approaches have included monitoring the volume and composition of gas produced,[20–24] impedance growth,[15,25,26] and the heat flow due to undesirable parasitic reactions[9,10,27,28]. However, the origin of gas production and impedance growth, and negative/positive electrode interactions in the cells are not well understood. Throughout this thesis, positive/negative electrode interactions refer to a phenomenon where species generated at one electrode move to the other electrode and cause further parasitic reactions. Recently, linear carbonate electrolytes were successfully used to improve high voltage NMC cell performance.[29–31] However, the use of different salt concentrations in linear carbonate electrolyte systems has not been explored.

Chapter 1 gives an overview of Li-ion cells especially focusing on the electrode/electrolyte interfaces, where impedance growth and gas generation occur. Chapter 2 introduces the current understanding of interactions which occur in Li-ion cells and cell failure mechanisms. Chapter 3 describes the experimental tools and theory used throughout this work. Chapter 4 presents the "pouch bag" method, a simple way to explore negative/positive interactions as well as the origins of gas production and impedance growth in Li-ion cells with conventional carbonate electrolyte. Chapter 5 explores the impact of fluorinated electrolytes on gas production and impedance growth using the pouch bag method. Chapter 6 presents the impact of surface coatings on gas production and impedance growth using the pouch bag method. Chapter 7 proposes a

chemical origin (oxygen release) to high voltage NMC cell degradation. Chapter 8 describes the impact of different salt concentrations in linear carbonate electrolytes on cell performance. Chapter 9 presents the impact of different salt concentration on the physical properties of linear carbonate electrolytes. Chapter 10 gives a summary of the work and describes future work.

1.2   Li-ion Cells

A lithium-ion battery includes several identical Li-ion cells connected in series and/or parallel. Each Li-ion cell is a rechargeable electrochemical cell made of a lithium-containing positive electrode, a negative electrode, an electrolyte and a microporous separator placed between the positive and negative electrodes. The positive electrode material is coated on aluminum foil while the graphite negative electrode is coated on copper foil. An electrolyte consists of a lithium salt such as $LiPF_6$ dissolved in a mixture of carbonate solvents serving as the medium for the transfer of lithium ions.[32] A separator is comprised of porous polyethylene and/or polypropylene which allow lithium ions to travel from one electrode to the other during cell use but prevent electrical contact between the two electrodes.[33]   Since NMC442 and graphite are the main materials reported in the thesis, Figure 1.1 shows a schematic of a Li-ion cell with NMC442 as the positive electrode and graphite as the negative electrode.
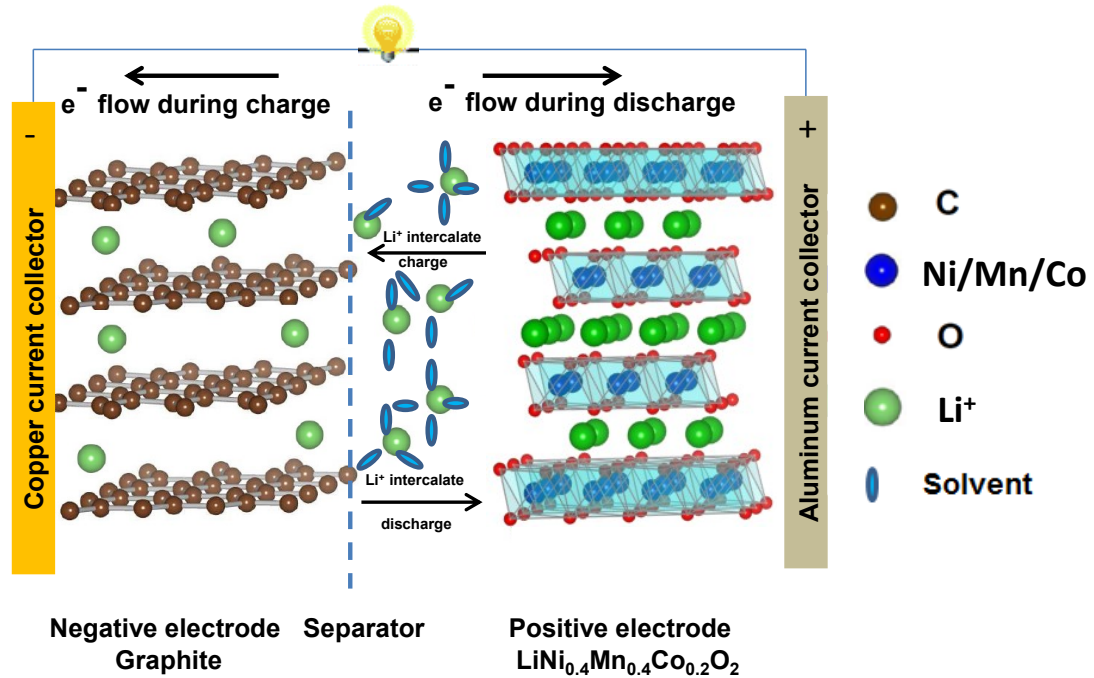
Figure 1.1 Schematic of a Li-ion cellwith a $\text{Li(Ni}_{0.4}\text{Mn}_{0.4}\text{Co}_{0.2})\text{O}_2$ (NMC442) positive electrode (right) and a graphite negative electrode (left). Taken with permission from Deijun Xiong, STUDIES OF THE EFFECTS OF ELECTROLYTE ADDITIVES ON LITHIUM-ION CELL PERFORMANCE, Preliminary Report, Dalhousie University, Halifax, NS (2014).During charge,

lithium ions are extracted from the positive electrode and electrons are transferred to the

negative electrode through the external circuit. After the released lithium ions pass

through the electrolyte and separator, they intercalate into the negative electrode and

combine with the transferred electrons. During charge, the two half reactions in the Li-

ion cell are given by

$$\text{Li(Ni}_{0.4}\text{Mn}_{0.4}\text{Co}_{0.2})\text{O}_2 \rightarrow \text{Li}_{1-x}(\text{Ni}_{0.4}\text{Mn}_{0.4}\text{Co}_{0.2})\text{O}_2 + x\ \text{Li}^+ + x\ \text{e}^- \quad (1.1)$$

$$y\ \text{C}_6 + x\ \text{Li}^+ + x\ \text{e}^- \rightarrow y\ \text{Li}_{x/y}\text{C}_6 \quad (1.2)$$
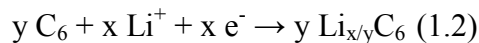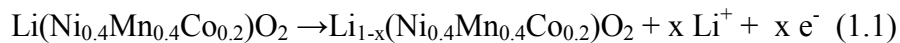
The overall reaction is given by

$$\text{Li(Ni}_{0.4}\text{Mn}_{0.4}\text{Co}_{0.2})\text{O}_2 + y\ \text{C}_6 \rightarrow \text{Li}_{1-x}(\text{Ni}_{0.4}\text{Mn}_{0.4}\text{Co}_{0.2})\text{O}_2 + y\ \text{Li}_{x/y}\text{C}_6 \quad (1.3)$$
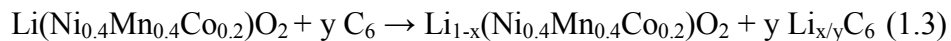
During discharge, the reverse reactions occur. Therefore, the basic electrochemistry of a Li-ion cell is the transfer of lithium ions between the positive and negative electrodes during charge/discharge.

During cell operation, the cell voltage changes according to the change of chemical potential of Li in the negative and positive electrodes. The cell voltage is the potential difference between the positive electrode and the negative electrode, given by

$$V_{cell} = V_{pos} - V_{neg} \qquad (1.4)$$

where V_{cell} is the cell voltage, V_{pos} is the potential of the positive electrode vs Li/Li^+ and V_{neg} is the potential of the negative electrode vs Li/Li^+. Figure 1.2 shows the voltage vs capacity of a NMC442/graphite cell and the potential vs capacity of NMC442 and graphite during charge. During this process, Li moves from NMC442 to graphite, and the potential of NMC442 vs Li/Li^+ increases while the potential of graphite vs Li/Li^+ decreases. Since the cell voltage is the potential difference between the positive electrode and the negative electrode, the cell voltage increases accordingly.
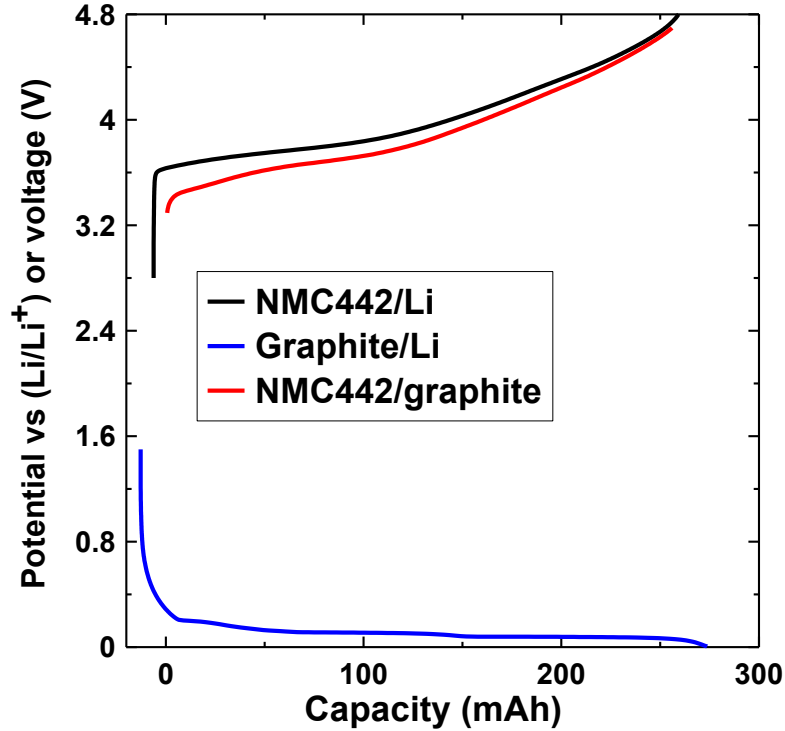
Figure 1.2 The voltage versus capacity curve of a NMC442/graphite cell and the potential vs capacity curves for the corresponding positive and negative electrodes during charging

This thesis uses units that the LIB community normally uses since this provides a good comparison with literature. The capacity unit used in Figure 1.2 is mAh rather than the IUPAC unit, Coulomb (1 mAh = 3.6 C).

Today, LIBs dominate the small rechargeable battery market due to high gravimetric and volumetric energy density compared to other rechargeable technologies. The gravimetric and volumetric energy density of a Li-ion cell (Wh/L and Wh/kg) are given by

$$W_g = \frac{\int Q\, dV}{Volume} \quad (1.5) \quad W_v = \frac{\int Q\, dV}{Mass} \quad (1.6)$$

where W_g and W_v are the gravimetric and volumetric energy density, respectively, Q is the usable capacity of a Li-ion cell in amp-hours (Ah), V is the cell voltage in volts,

6

Volume is the cell volume in liters and Mass is the cell mass in kg. The usable capacity of the cell is based on the choice of positive and negative electrode materials and the selected operating voltage window. High specific capacity electrode materials are desired to increase the usable capacity of the cell.

The specific capacity of a negative or positive electrode material in milliamp-hours per gram (mAh/g) is given by

$$Q_{sc} = \frac{F \times n}{M_w} \times \frac{1}{3.6 \text{ coulombs/mAh}} \quad (1.7)$$

where Q_{sc} is the specific capacity (mAh/g), F is the Faraday constant (96485.33 coulombs/mol), n is the number of moles of charge during charging or discharging for one mole of active material and M_w is the molecular weight of the active material (g/mol). For example, the theoretical specific capacity of NMC442 is given by

$$\frac{96485.33 \times 1}{96.18} \times \frac{1}{3.6} \text{ mAh/g} = 278.60 \text{ mAh/g} \quad (1.8)$$

However, the practical specific capacity is typically much lower than the theoretical specific capacity since only part of the lithium can be reversibly removed from the active material. For NMC442, only about seventy-four percent of the lithium (charged to 4.7 V vs Li/Li$^+$) can be reversibly removed, so the practical specific capacity of NMC442 is only about 206 mAh/g.[8]

1.3 Positive Electrode Materials

The positive electrode materials commonly used in commercial Li-ion cells are LiFePO$_4$ (LFP), LiCoO$_2$ (LCO), LiNi$_x$Mn$_y$Co$_{(1-x-y)}$O$_2$ (NMC), LiNi$_{0.8}$Co$_{0.15}$Al$_{0.05}$O$_2$ (NCA), and LiMn$_2$O$_4$ (LMO). These materials can be classified into three types: LFP

(olivine, 1 D lithium diffusion channels), LCO, NMC and NCA (layered, 2D lithium diffusion channels) and LMO (spinel structure, 3D lithium diffusion channels). The worldwide market share in kilotons (KT) of each positive electrode material in 2014 is listed in Figure 1.3. [34] The volume of these materials used in 2014 is 104 KT and their predicted use in 2025 will be 350 KT.[34]
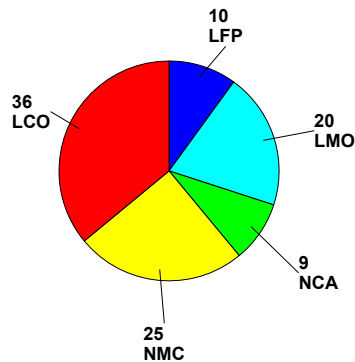
Figure 1.3. the worldwide market share (%) of each positive material in 2014.

Each electrode material has its own advantages and disadvantages. LFP has excellent thermal stability, long cycle life and good power capability.[35–37] However, pure LFP has low electronic and ionic conductivity.[35,38] Through carbon coating and reduced size, these problems have been overcome and the power capability of LFP cells is excellent.[39–42] However, its low energy density due to low crystalline density and low average working potential hampers its future application in electric vehicles. LCO is widely used due to its good cycle life and high energy density.[43,44] The disadvantages of LCO are its poor thermal stability, high cost and toxicity due to the use of cobalt.[3,4,37] Even though LCO currently occupies the largest share of the market, its growth is leveling off. The use of NMC is growing due to a good combination of cost, thermal stability and energy density.[5,6] NMC materials are usually distinguished by their transition metal atomic ratio

8

as NMC442, NMC532, NMC622 and NMC811 (except for x=y=1/3, which is called NMC111). [11,45] When the content of nickel in NMC increases, the specific capacity and energy density increase but cell lifetime and thermal stability normally become worse.[46,47] NCA is also widely used due to its high energy density and its moderate thermal stability which is similar to that of some NMC grades. However, its cost is high due to a stringent synthesis process[48,49]. LMO is also widely used in Li-ion cells because of its good thermal stability and low cost.[50,51] However, its low energy density and poor cycling performance especially at elevated temperatures restrict its application.[52–55] Table1.1 shows electrode materials used in LIBs in present electric vehicles sold in the US and their impact on energy and vehicle range.

Table 1.1 LIBs for present electric vehicles sold in the US where C and C - Si represent graphite and graphite- silicon composite, respectively.[2]

Manufacturer	Model	Battery size (kWh)	Battery chemistry	Vehicle range (mile)	Vehicle range (km)
Tesla	S	60–100	C-Si/NCA	208–315	334–508
Tesla	X	60–100	C-Si/NCA	208–315	334–508
BMW	i3	22-33	C/NMC	80-114	129-183
Nissan	Leaf	24-30	C/LMO	80-107	135-172
Volkswagen	e-Golf	24-35.8	C/NMC	83-124	135-200
Chevrolet	Spark	19	C/LFP	82	132
Kia	Soul EV	27	C/NMC	90	145
Ford	Focus EV	35.5	C/NMC	100	160
Mercedes	B-Class Electric	28	C/NCA,	85	137
Mitsubishi	I	16	LTO/NMC	62	100

1.4 Negative Electrode Materials

Graphite is widely used as the negative electrode material in LIBs due to its high specific capacity (372 mAh/g, theoretical), low irreversible capacity loss in the first cycle (<10 %), low average working potential (below 0.2 V vs Li/Li$^+$), improved safety

compared to lithium metal and low volume expansion during lithiation (approximately 10%). [56] Figure 1.4 shows a representative potential (V) vs specific capacity (mAh/g) curve of a Li/graphite half cell during the first cycle. The discharge specific capacity (Q_D) is the total charge measured during cell discharge. More than 90 % of the charge is used to intercalate Li^+ ions into the graphite electrode. This intercalation reaction is highly reversible. Therefore, this charge can be recovered which is equal to the charge measured during cell charge, the specific charge capacity (Q_c). However, the rest of the charge during discharge is used to form the graphite/electrolyte interface and cannot be recovered during the subsequent charge. Therefore, the irreversible specific capacity (IRC) of the cell is equal to the difference between the discharge specific capacity and the charge specific capacity shown in Figure 1.4. Figure 1.4 shows that IRC for the Li/graphite cell during the first cycle is approximately 26.3 mAh/g, which represents 7.6% of the first cycle discharge specific capacity.
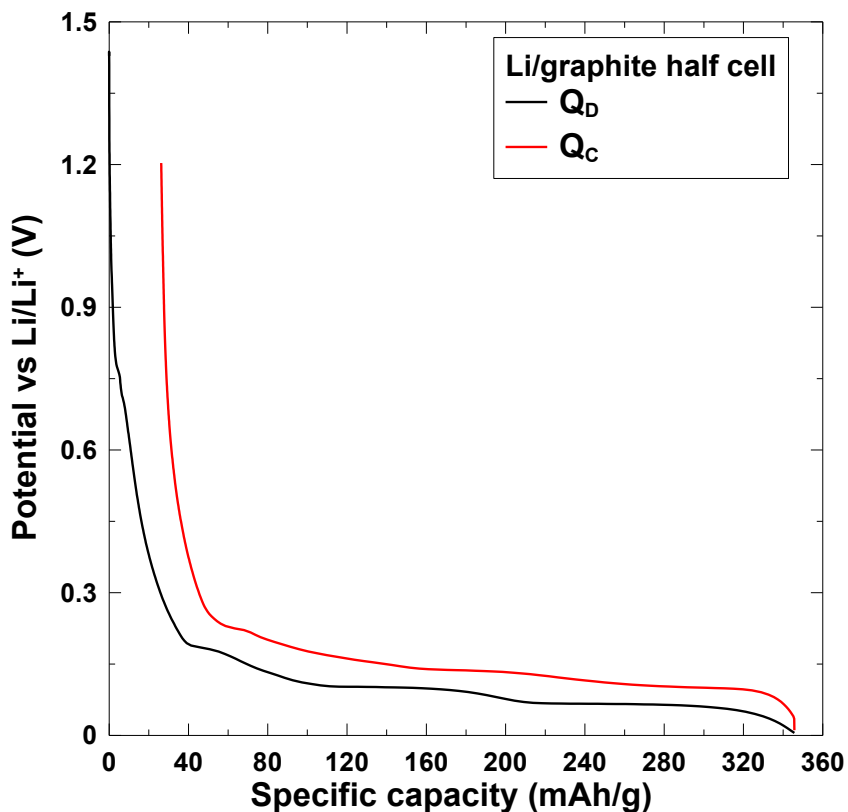
Figure 1.4 The potential vs the discharge specific capacity (Q_D) and the charge specific capacity (Q_C) for a Li/graphite half cell during the first cycle at 30°C.

Lithium titanium oxide, $Li_{4/3}Ti_{5/4}O_4$ (LTO) is not as widely used as graphite in commercial LIBs but is a promising negative electrode for some niche applications that require high rate capability and long cycle life.[57–60] LTO has a higher average working potential (1.5 V vs Li/Li$^+$) and lower specific capacity (175 mAh/g, theoretical) compared to graphite. This leads to lower energy density Li-ion cells compared to those using graphite. However, due to its zero-expansion during lithiation and less reductive working potential, a Li-ion cell using LTO renders longer cycle life than those using a graphite electrode[57]

Silicon is being introduced in commercial Li-ion cells due to its high specific capacity (3579 mAh/g, theoretical), an acceptable low working potential (around 0.2 V vs Li/Li$^+$)

and good safety.[61,62] However, silicon-based materials cause large volume expansion during lithiation and subsequent volume contraction during delithiation resulting in particle pulverization upon cycling when micron-sized crystalline silicon is used. In addition, large IRC loss during the first cycle and the loss of electronic contact between particles during repeated cycling also occur.[63,64] Therefore, silicon-based electrode materials are added to the graphite electrode in small amounts to increase cell energy density and to limit their impact on cell capacity fade.[56,65]

1.5   Electrolyte

The most common electrolyte for a Li-ion cell is comprised of a mixture of carbonate solvents containing a lithium salt, $LiPF_6$. So far, there has been no single solvent meeting the requirements of high dielectric constant (the ability to dissolve salt), low viscosity (the ability to facilitate ion transport) and high interfacial stability on both negative and positive electrodes. In order to achieve these well-balanced properties, solvents either having high dielectric constant or low viscosity are mixed. The former is normally a cyclic carbonate, ethylene carbonate (EC). The latter are linear carbonate solvents such as diethyl carbonate (DEC), dimethyl carbonate (DMC) and ethyl methyl carbonate (EMC). Another cyclic carbonate, propylene carbonate (PC) is used as a co-solvent in some applications as it has high dielectric constant, wide liquid range and high interfacial stability on the positive electrode.[32] Ester solvents such as methyl acetate (MA) and methyl propionate (MP) have much lower melting point than carbonate solvents (except DEC), so they are added to an electrolyte to improve low temperature performance and rate capability.[66,67] The chemical stuctures of common solvents are listed in Figure 1.5.
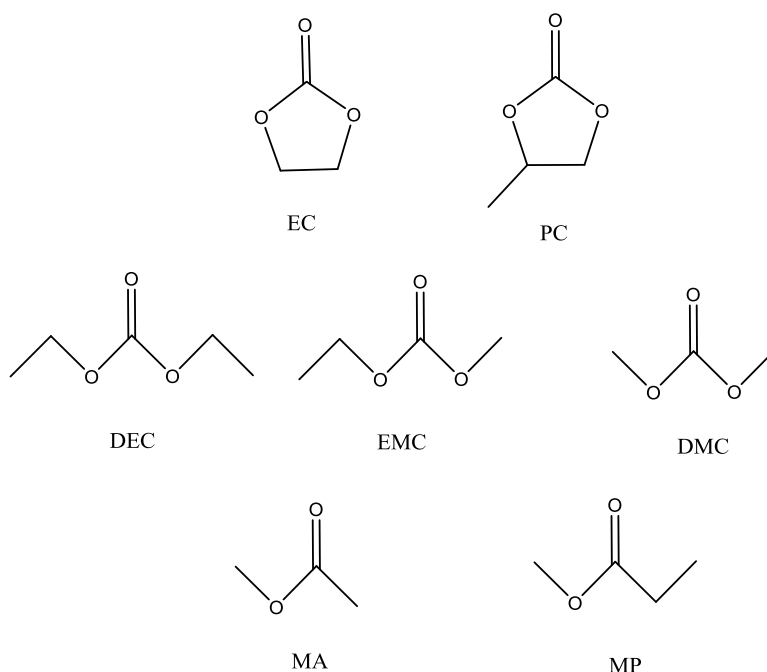
Figure 1.5 Chemical structures of common solvents

Common lithium salts are lithium hexafluorophosphate (LiPF$_6$), lithium tetrafluoroborate (LiBF$_4$),[68] lithium bis(fluorosulfonyl)imide (LiFSI),[69,70,71] lithium bis(oxalato)borate (LiBOB),[72,73,74,75] and lithium bis(trifluoromethanesulfonyl)imide (LiTFSI).[76,77] Figure 1.6 shows the chemical structure of these common salts. LiPF$_6$ is the overall winner due to a combination of well-balanced properties in carbonate solvents such as good ion conductivity, good solubility, high anodic stability up to 5.1 V (vs Li$^+$/Li) and minimal corrosion of the aluminum substrate used as the current collector for the positive electrode. However, there is an equilibrium for LiPF$_6$ decomposition which exists even at ambient temperature:

$$LiPF_6 \leftrightarrow LiF + PF_5 \quad (1.9)$$
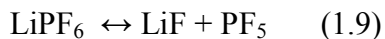
This reaction leads to two main drawbacks of LiPF$_6$. One is the low thermal stability.[78,79] The other is highly reactive hydrofluoric acid from PF$_5$ reacting with water. The

13

generated hydrofluoric acid can attack passivation films and positive electrode materials as well.[80] The latter is the main reason why LIB electrolyte producers try to reduce water content as low as possible. Some salts such as LiTFSI[81,82,83] and LiBOB[84,85] can be used as additives to improve cell performance.
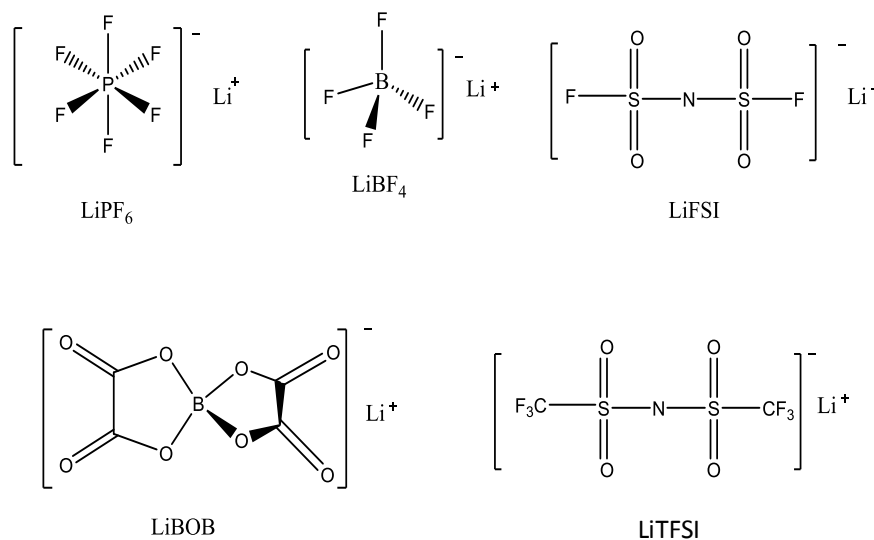
Figure 1.6 Chemical structure of common salts

1.6 Solid Electrolyte Interphase (SEI) and Ways to Modify its Properties

The nonaqueous electrolytes in a Li-ion cell, especially where graphite is utilized as the negative electrode, are highly thermodynamically unstable because their reduction potentials (vs Li/Li$^+$) are much higher than the potential of the graphite electrode (vs Li/Li$^+$) during cycling. A surface layer forms due to the electrolyte reduction on the surfaces of the Li$_x$C$_6$ particles in the negative electrode. This surface layer acts as an interphase between the electrode and electrolyte, has the properties of a solid electrolyte and can significantly slow down electrolyte reduction. For this reason, the surface layer is called a solid electrolyte interphase (SEI). A SEI can also be formed at the positive electrode due to electrolyte oxidation. Since the SEI is a key to good cell performance, it

has been intensively studied for two decades. Effective ways to modify the SEI are the use of surface coatings and electrolyte additives.

1.6.1 Solid Electrolyte Interphase (SEI) on the Negative Electrode

Even though the SEI is essentially responsible for the reversibility of the lithium ion intercalation process and influences the kinetics of overall cell reactions, it is difficult to characterize the SEI due to a lack of reliable *in situ* tools, its sensitive chemical nature and its complicated composition.[32] There is a consensus that the main species in the SEI on graphite are decomposed electrolyte solvents and salts. These species include lithium alkyl carbonates, LiF and Li_2O in the EC-based electrolytes where $LiPF_6$ is used. A mechanism has been proposed for the main reduction product of carbonate-based electrolytes to form the SEI on graphite. It is suggested that EC reacts with Li^+ and e^- and generates a gaseous product, ethylene, and creates an organic compound, lithium ethylene dicarbonate (LEDC) at the surface of graphite electrode, which is the main component of SEI. Figure 1.7 shows the formation of LEDC through EC reacting with Li^+ and e^- residing in Li_xC..[86]
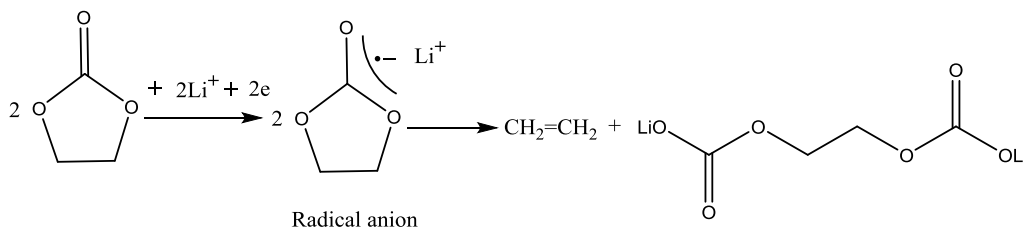
Figure 1.7 The formation of LEDC through EC reacting with Li^+ and e^- at Li_xC_6 according to Reference 51.

1.6.2 SEI on the Positive Electrode

Compared to extensive studies of the SEI on the negative electrode, there have been fewer effort to understand the interphase on the positive electrode. Few reports have been published about its chemical composition and formation mechanism.[87,88] A native film consisting of Li_2CO_3 on lithium transition metal oxides, usually forms during synthesis, processing and storage in the atmosphere, where CO_2 can react at the surface.[89,90,91,92,93] The SEI on the positive electrode normally includes LiF, alkoxides and polycarbonates.[94,95,96,97] There is a belief that the formation of the SEI on the surface of the positive electrode may occur in three steps:

(1) the formation of the native surface film ;

(2) spontaneous chemical reactions of the native film upon exposure to electrolytes;

(3) electrochemical reactions between the positive electrode and electrolytes during the initial and subsequent cycles.

1.6.3 Electrolyte Additives for the Graphite Negative Electrode

Since the introduction of LIBs, enormous efforts have been made to explore electrolyte additives which can form an unique SEI on the graphite negative electrode which can allow the reversible intercalation/de-intercalation of lithium in graphite. Examples of additives believed to act in this manner include vinylene carbonate (VC),[98,99,100] vinyl ethylene carbonate (VEC),[101] fluoroethylene carbonate (FEC),[102,103] ethylene sulfite (ES)[103,104] and 1,3,2-dioxathiolane-2,2-dioxide (DTD).[105] Among them, VC is the most successful additive which is being used in many commercial Li--ion cells.

Aurbach *et al.* found that VC reacts with Li^+ and e^- on the surface of Li_xC particles prior to EC.[106] This prior reaction from VC forms a flexible and cohesive polymeric species acting as a better SEI. The authors also believed that similar polymeric species may form on the surface of the positive electrode and may be beneficial to the positive electrode. Ota *et al.* found that the addition of VC has a significant effect on the negative electrode but could benefit the positive electrode as well.[107,108] The Dahn group confirmed that the addition of VC is beneficial to the positive electrode using various techniques such as automated storage, high precision couloumetry and electrochemical impedance spectroscopy.[109,110,111,112,113] In addition, the Dahn group found that the addition of VC eliminates the formation of lithium alkoxides which not only cause EMC transesterification, but also migrate to the positive electrode and cause further side reactions.[114,115] Recently, prop-1-ene-1,3-sultone (PES) has gained importance, since it suppresses gassing especially for cells cycled at elevated temperature, and improves coulombicic efficiency dramatically. Results suggest that PES has impacts on both the negative electrode and the positive electrode.[116,117] Figure 1.8 shows the chemical structure of these common additives.
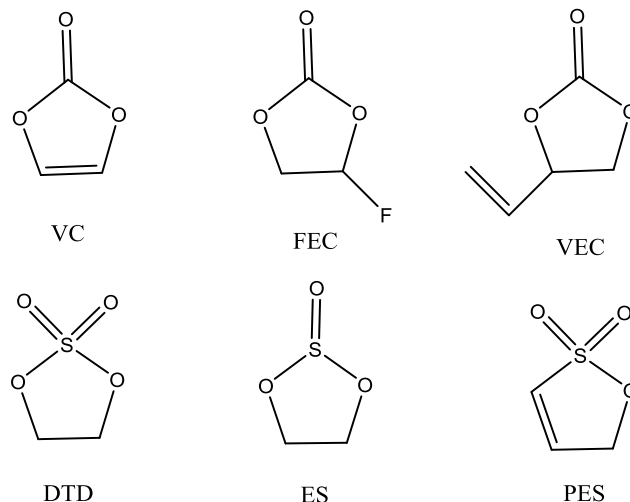
Figure 1.8 Chemical structure of common additives.

1.6.4 Electrolyte Additives for the Positive Electrode

There have been fewer efforts to develop additives for improving the interphase on the positive electrode compared to those made for graphite. Before 2007, Li-ion cells were normally operated below 4.2 V (vs Li/Li$^+$), where cell performance is dominated by negative electrode issues.[118] Now there is a great interest in higher voltage NMC positive electrode materials. Examples of additives for high voltage cells include tri(trimethylsilyl)phosphate (TTSP),[119] tri(trimethylsilyl)phosphite (TTSPi),[120] tris(hexafluoro-iso-propyl)phosphate (HFiP),[121] methylene methanedisulfonate (MMDS),[122,123] and dimethylmethylphosphonate (DMMP).[124] These additives are believed to be oxidized at the surface of positive electrodes before the oxidation of carbonate solvents used in a Li-ion cell.[125] Additive blends such as PES, DTD or MMDS and TTSPi or TTSP are also used together to improve cell performance.[11,15,25] Even though these additives and additive blends can improve cell performance to some degree, it is still a great challenge to find or invent additives which can allow cells to operate at or

above 4.5 V (vs Li$^+$/Li) for many years. The mechanisms of how these additives and others function at the surface of the positive electrode are not well understood. Figure 1.9 shows the chemical structure of some additives believed to be useful for positive electrodes.
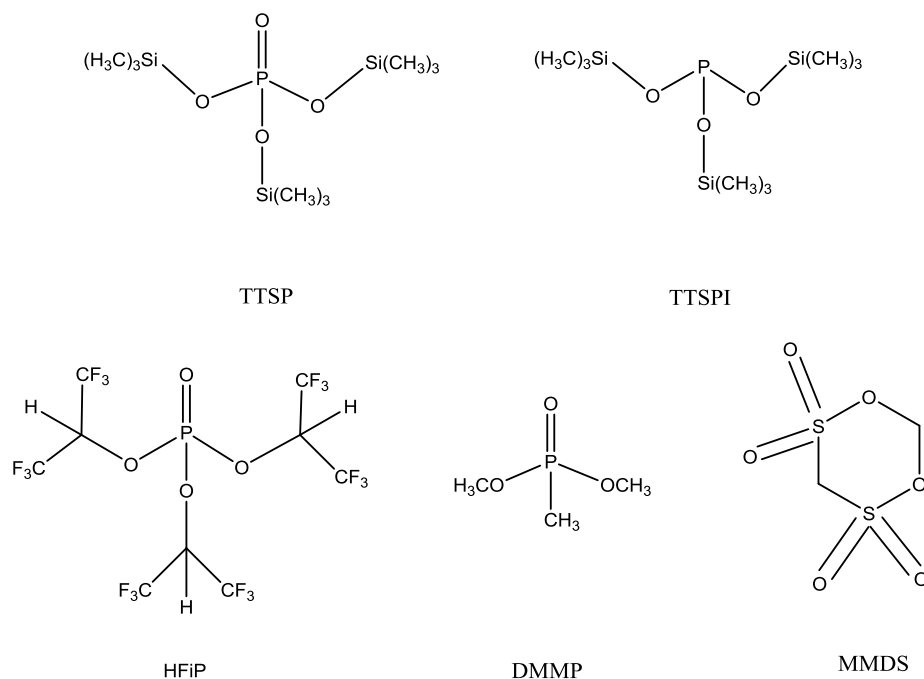
Figure 1.9 Chemical structure of some electrolyte additives believed to be useful for positive electrodes.

1.6.5   Surface Coatings on Positive Electrode Materials

Surface coating has proven to improve the performance of Li-ion cells. Many materials such as Al$_2$O$_3$[126–129], AlF$_3$[130–132] and ZrO$_2$,[128,129] were investigated as surface coatings for LCO. Currently, the same strategy is also applied to NMC electrode materials.[16,19,133–135] Among all the surface coating materials, Al$_2$O$_3$ seems to be a good candidate and has been commercially used on NMC532 and NMC622 by Umicore (a well-reputed positive electrode manufacturer).[16]

Surface coatings and electrolyte additives are also used together to further improve NMC high voltage cell performance. Arumugam et $al.$ reported that Al_2O_3 surface coatings had special synergies with an additive blend of 2% PES, 1% MMDS and 1% TTSPi by weight percentage to a conventional EC-based electrolyte in NMC622/graphite pouch cells. These synergies greatly suppressed cell impedance growth and improved coulombic efficiency and cycle life of the cells.[16] However, the use of both surface coatings and electrolyte additives is not always beneficial. Nelson et $al.$ found that $LaPO_4$-coated NMC442/graphite pouch cells with an additive blend of 2% PES, 2% DTD and 2% TTSPi had worse cell performance than uncoated NMC442/graphite pouch cells with the same electrolyte.[25]

CHAPTER 2: MAIN AGING MECHANISMS AND INTERACTIONS BETWEEN POSITIVE/NEGATIVE ELECTRODES IN LI-ION CELLS

2.1 Main Aging Mechanisms in Li-ion Cells

Aging mechanisms that occur at the negative electrode and at the positive electrode differ significantly in a Li-ion cell.[53] In this thesis, electrolyte reduction, electrolyte oxidation, interactions between positive/negative electrodes and material degradation were mainly investigated. Therefore, this chapter overviews main aging mechanisms related to electrolyte reduction at the graphite electrode, electrolyte oxidation at the positive electrode, active material degradation and interactions between positive/negative electrodes.

2.1.1 Electrolyte Reduction at the Graphite Electrode

The reduction potential of the electrolyte used in Li-ion cells is much higher than the working potential of graphite vs Li/Li^+, thus unwanted electrolyte reduction can occur. It is observed that the reduction of electrolyte components like EC and EMC during the first charge occurs around $0.8 - 1.3$ V vs Li/Li^+ and the average working potential of graphite is below 0.2 V vs Li/Li^+.[32,136] Electrolyte reduction leads to the SEI formation, which mainly occurs during the first few cycles.[137–139] Although the SEI can differ dramatically depending on the cell components (the type of graphite, electrolyte, electrolyte additives and temperature etc.), the Li atoms used in forming the SEI are always consumed irreversibly. The SEI is Li^+ ion conducting but electronically insulating film.[137,140,141] This implies that an electrolyte molecule needs to diffuse through the SEI layer to a

distance where an e⁻ can tunnel in order to react with a Li^+ and an e⁻ that originate from Li_xC_6. Therefore, as the SEI grows, the SEI growth rate slows significantly and so does the rate of electrolyte reduction.[142] SEI growth increases with cell temperature due to increased reaction rate. It was found that SEI growth depends predominately on time rather than on cycle count and is approximately proportional to time^{½}.[118,138,143]
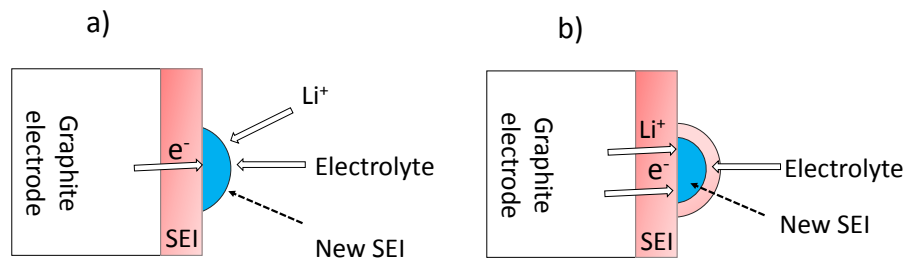
Figure 2.1 Simplified possible SEI growth mechanisms. The new SEI and the old SEI are represented in red and blue, respectively.

Figure 2.1 shows two simplified possible mechanisms of the SEI growth. Figure 2.1a shows that a new SEI layer is formed on the surface of the old SEI when a Li^+ from the electrolyte meets an e⁻ which tunnels through the old SEI and then reacts with the electrolyte. Figure 2.1b shows a new SEI layer formed close to the surface of graphite electrode where the Li^+ and e⁻ meet the electrolyte diffusing through the old SEI layer. The new SEI layer then pushes out the old SEI layer.[142]

Apart from the SEI growth, the SEI repair can also take place since the volume expansion and contraction of the graphite electrode (approximately 10% of its total volume) during cycling can break the SEI layer.[144,145] The SEI growth and repair which consume lithium irreversibly is a primary cause for cell failure when Li-ion cells are

operated below 4.2 V and above 30 °C. [53,118,143,146,147] The SEI growth can also lead to impedance rise in the cell, so power capability decreases with cycling.[95,118,148–150]

2.1.2 Electrolyte Oxidation at the Positive Electrode and Positive/Negative Electrode Interactions

The conventional carbonate electrolyte can be oxidized above 3.9 V vs Li/Li$^+$ at the positive electrode due to its intrinsic instability at high potential.[32,151] Figure 2.2 shows a schematic of a typical electrolyte oxidation process occurring at a positive electrode connected to a charger or under open circuit conditions. Figure 2.2 shows that the electrolyte is oxidized at the surface of the positive electrode and loses an equivalent number of electrons. The released electrons can transfer to the negative electrode and combine with Li$^+$ ions and intercalate as Li atoms into the negative electrode if the cell is connected to a charger (Figure 2.2a). The released electrons can also combine Li$^+$ ions and intercalate into the positive electrode if the cell is under open circuit condition (Figure 2.2b). Therefore, electrolyte oxidation does not normally cause a loss of cyclable lithium but can cause irreversible loss of electrolyte components.[142]
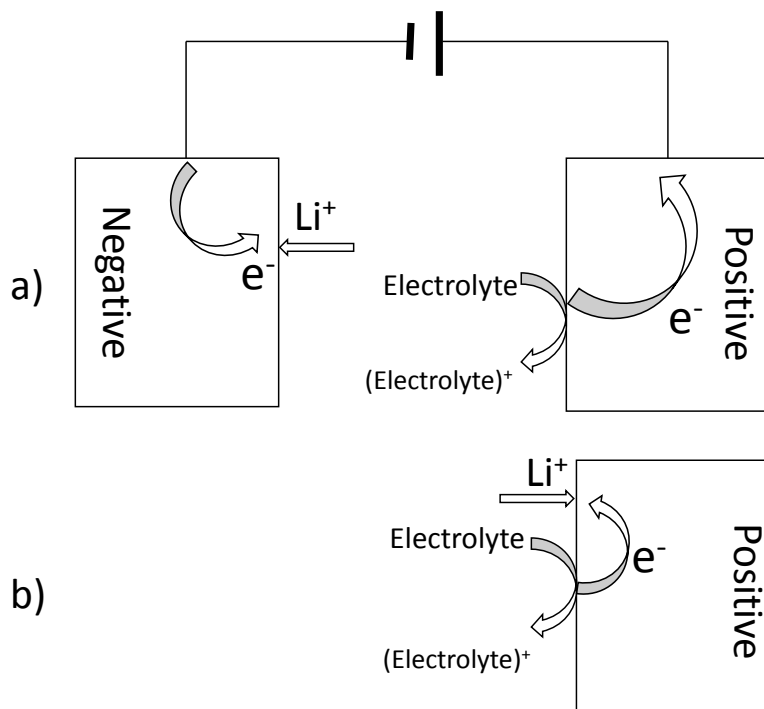
Figure 2.2 A schematic of possible electrolyte oxidation process at the positive electrode

Figure 2.3 shows possible oxidation pathways of EC [152–154] which is a major solvent used in this thesis. Figure 2.3 shows that some oxidation products are gaseous products like CO_2 and CO. It has been suggested that CO_2 can migrate to the graphite electrode can be reduced there. The possible reduction pathways of CO_2 described by Sloop et al. [155] are given by

$$2Li^+ + 2e^- + 2CO_2 \rightarrow Li_2C_2O_4 \quad (2.1)$$

$$2Li^+ + 2e^- + 2CO_2 \rightarrow Li_2CO_3 + CO \quad (2.2)$$
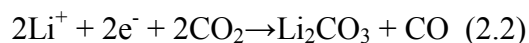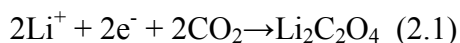
Figure 2.3 shows possible soluble and insoluble products from EC oxidation as well. The soluble species might migrate to the negative electrode and could be reduced there. This interaction between the positive and negative electrodes might lead to impedance rise at the negative electrode and hydrogen generation in the cells. [24,156–159] The insoluble

oxidized species might deposit at the surface of the positive electrode and might cause impedance growth at the positive electrode.
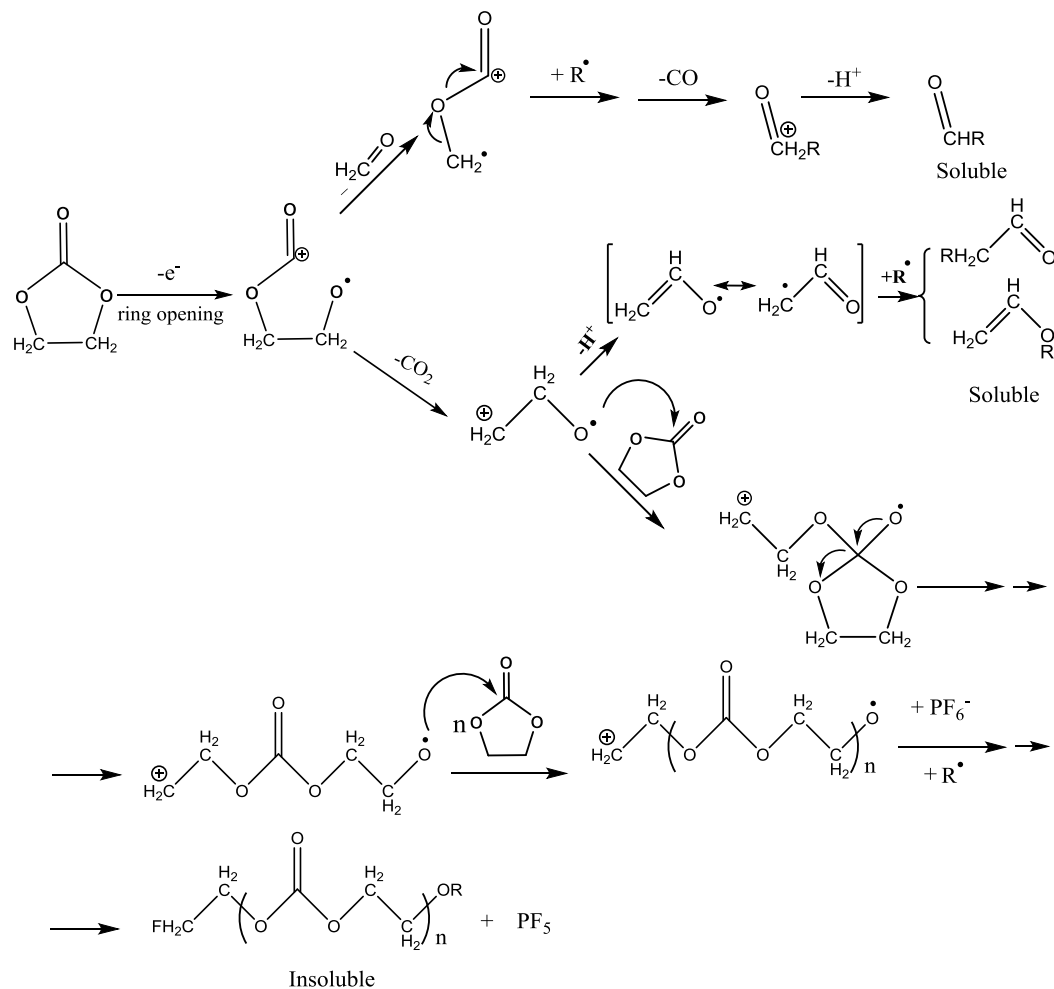
Figure 2.3 Possible oxidation pathways for EC.[152–154] R$^{\bullet}$ and R$^+$ represent an alkyl radical and an alkyl cation, respectively.

2.1.3 Active Material Degradation and Positive/Negative Electrode Interactions

The parasitic reactions between the electrolyte and the surface of the positive electrode were suggested to be a primary cause of the cell failure when the cells are cycled above 4.2 V.[10,14,15,25] These parasitic reactions were proposed to induce surface degradation of

the positive electrode. Lin *et al.* found that the surface of NMC442 experienced a structural reconstruction from ($R\bar{3}m$) to rock salt (Fm3m).[160] During the phase change, transition metal ions migrate and occupy some lithium sites in lithium layers with a possible loss of Li and O from the surface of the structure. This surface reconstruction was ascribed to the cause of a significant impedance rise in the cell during high voltage cycling. The released oxygen is highly reactive. The oxidation of solvent via reaction with the O atoms of the NMC electrode [161] could be

$$Solvent + MO_2 \rightarrow Solvent\text{-}O + MO$$
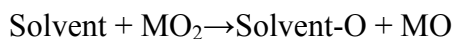
where Solvent represents a solvent molecule, MO_2 represents the charged surface of a layered positive electrode at high potential, Solvent-O represents the oxidized products between oxygen released from the charged positive electrode surface and a solvent molecule and MO represents a rock salt structure resulting from the loss of oxygen from the surface of a charged positive electrode.

This phase transformation phenomenon was also observed in many published papers about NCA and different NMC grade materials where surface reconstruction was described as a main cause of cell failure.[160,162–164] However, the argument is debatable. Some studies show that the rock salt layer, the degraded surface, can be beneficial to cell performance. [165–167] Furthermore, Makimura et al. claimed the rock salt layer could hinder the bulk material from further structural degradation and hinder electrolyte oxidation at the surface of the positive electrode. [167]

Apart from the surface phase transformation of the positive electrode, the positive electrode also could lose active material. This is really true when $LiMn_2O_4$ is used as the

26

positive electrode in a Li-ion cell operated at elevated tempeature.[168–176] It was found that the manganese can dissolve into the electrolyte and move to the graphite electrode and be trapped in the SEI. Although the manganese dissolution causes active material loss resulting in a contribution to capacity fade, the main effect of manganese dissolution in a Li-ion cell is impedance growth at the negative electrode due to hindered mobility of Li^+ ions through the SEI.[168,177,178] When $LiFePO_4$ cells are operated at high temperature, Fe dissolution is also pronounced.[179,180] However, transition metal dissolution is not an issue for NMC positive electrode materials.[181]

CHAPTER 3: EXPERIMENTAL TECHNIQUES

3.1 Cell Chemistry and Preparation

3.1.1 NMC442/Graphite Pouch Cells

Commercially made NMC442/graphite pouch cells were primarily used in this thesis. Figure 3.1a shows a NMC442/graphite pouch cell (402035 size, 40 mm long, 20 mm wide and 3.5 mm thick) as received from LiFUN, (China). Figure 3.1b shows the jelly roll of the pouch cell after unwinding. The cells were balanced to 4.7 V. The positive electrode formulation was 96:2:2 NMC442:carbon black:polyvinylidene fluoride (PVDF). The negative electrode formulation was 96:2:2 graphite:carbon black:carboxymethyl cellulose-styrene butadiene (CMC-SBR). Carbon black was used as a conductive additive in both the positive electrode and the negative electrode while PVDF and CMC-SBR were used as a binder for the positive electrode and the negative electrode, respectively. The positive electrode coating was 35 μm thick on both sides of the Al current collector (13 μm thick) to give a total electrode thickness of 83 μm. The mean particle size of the NMC442 was 10 μm. The negative electrode coating was 67 μm thick on both sides of the Cu current collector (10 μm thick) to give a total electrode thickness of 144 μm. The mean particle size was 20 μm. The total active area and the total mass of the positive electrode were 71 cm^2 and 0.79 g, respectively while the total active area and the total mass of the negative electrode were 81 cm^2 and 0.82 g, respectively. Thus, the areal loadings of the positive and negative electrodes were approximately 11 and 10 mg/cm^2, respectively. The separator used in the cells was microporous polypropylene with an

Al_2O_3 ceramic coating (particle size about 1–2 µm) on the side in contact with the positive electrode.
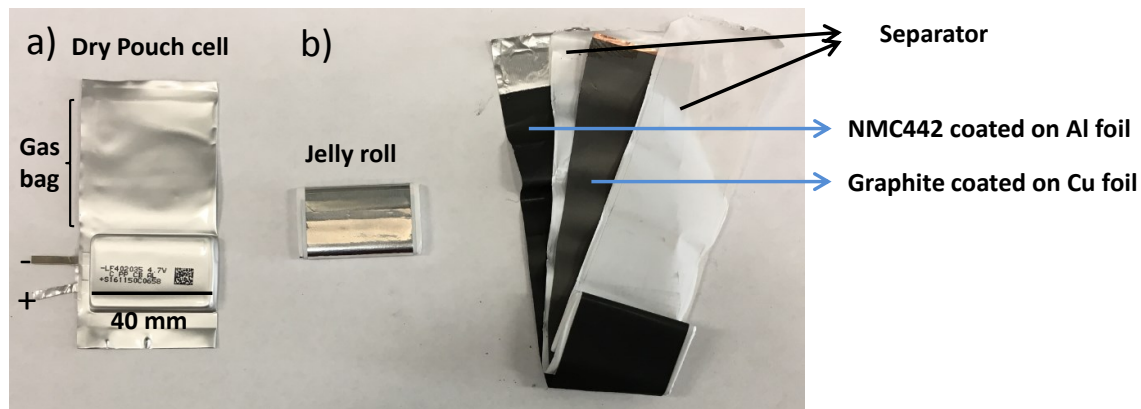
Figure 3.1 A NMC442/graphite pouch cell before (a) and after opening (b).

3.1.2 A Summary of Other Pouch Cells Used in This Work

In addition to the NMC442/graphite pouch cells, eight other different pouch cell types were also used in this work. These pouch cells had the same or similar size as the NMC442/graphite pouch cells. The electrode formulations of these cells are also similar to the electrode formulations of the NMC442/graphite pouch cells. Table 3.1 gives a summary of the electrode formulation, cell balance (maximum upper cut-off voltage), nominal capacity, and manufacturer for all the pouch cells used in this thesis. A proprietary material was used as surface coating for NMC532 and NMC622 for high voltage application. These coated NMC532 and NMC622 positive materials with this proprietary material were called HV-coated NMC532 and HV-coated NMC622, respecitively.

Table 3.1 A summary of all pouch cells used in this thesis

Pouch cell	Ratio among the active material, carbon black and PVDF of the NMC positive electrode (by weight)	Ratio of the active material, carbon black and CMC/SBR of the graphite electrode (by weight)	Cell balance (V)	Capacity (mAh)	Manufacturer
NMC442/graphite	96:2:2	96:2:2	4.7	200 or 240	LIFUN
LaPO$_4$-coated NMC442/graphite	96:2:2	96:2:2	4.7	200	LIFUN
NMC532/graphite	96:2:2	96:2:2	4.7	200	LIFUN
Al$_2$O$_3$-coated NMC532/graphite	96:2:2	96:2:2	4.5	200	Umicore
HV-coated NMC532/graphite	96:2:2	96:2:2	4.5	200	Umicore
Single crystal NMC532/graphite	96:2:2	96:2:2	4.5	200	NA
NMC622/graphite	96:2:2	96:2:2	4.5	200	Umicore
Al$_2$O$_3$-coated NMC622/graphite	96:2:2	96:2:2	4.5	220	Umicore
HV-coated NMC622/graphite	96:2:2	96:2:2	4.5	220	Umicore

3.1.3 Coin Cells and Pouch Bags

In addition to pouch cells, coin cells including full coin cells, symmetric cells and half cells were used. Coin cells were mainly used for the analysis of electrodes after a variety of tests. Figure 3.2 shows the components of a NMC442/graphite full coin cell. The gasket provides an air tight seal and prevents cells from shorting. In a symmetric cell, the counter electrode and the working electrode are identical electrodes. In a half cell, Li metal is used as the reference/counter electrode and the working electrode is either a NMC positive electrode or a graphite negative electrode.

In order to study electrodes separately, pouch bags containing either the negative electrode or positive electrode plus electrolyte were made. Figure 3.3 shows the steps in

the construction of pouch bags where the electrodes were taken from a charged NMC442/graphite pouch cell. The color of the graphite electrode depends on the Li content in the graphite.[182] An unlithiated graphite electrode is black. When the graphite electrode is fully lithiated, it is gold. Therefore, the graphite electrode from the NMC442/graphite pouch cell at 4.4 V shown in Figure 3.3 is golden while the graphite electrode from the dry pouch cell shown in Figure 3.1 is black. More details about the construction of pouch bags will be presented in Chapter 4.
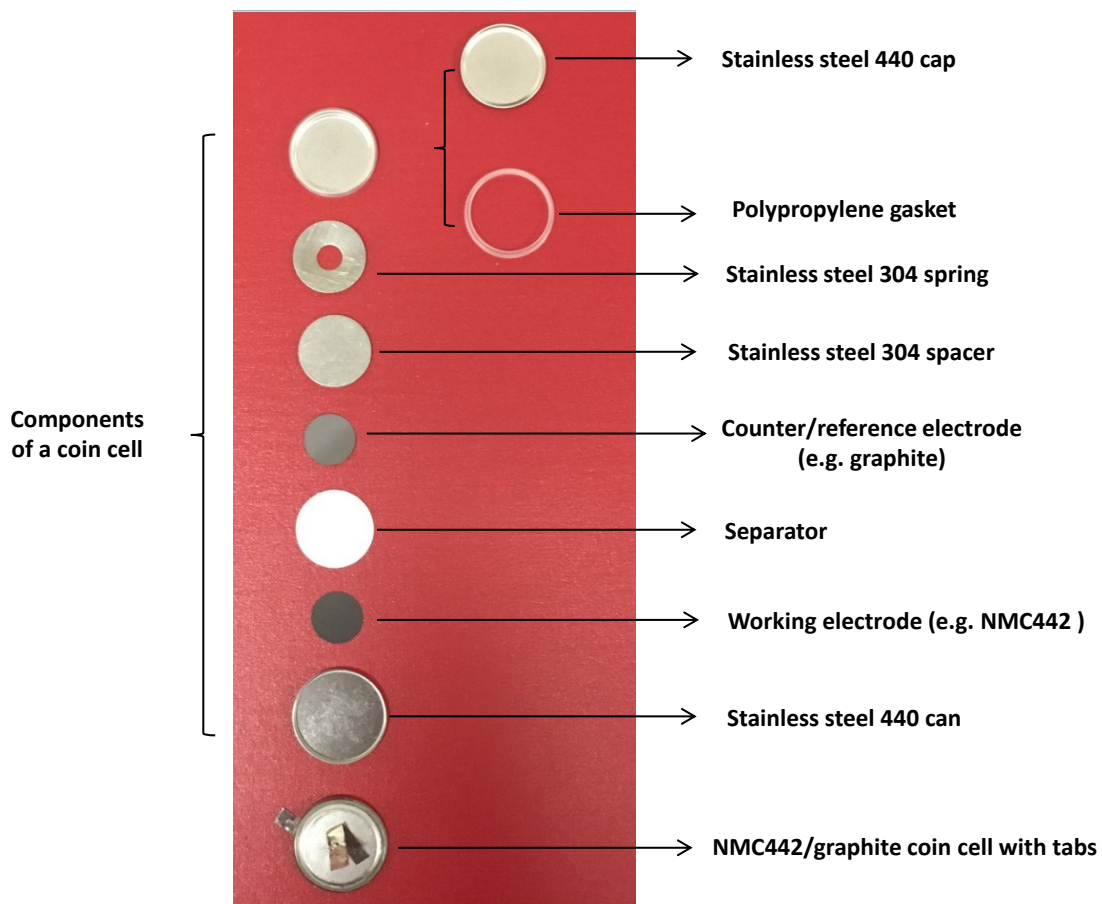
Figure 3.2 The components of a coin cell (2325 size, 23 mm diameter and 2.5 mm high)
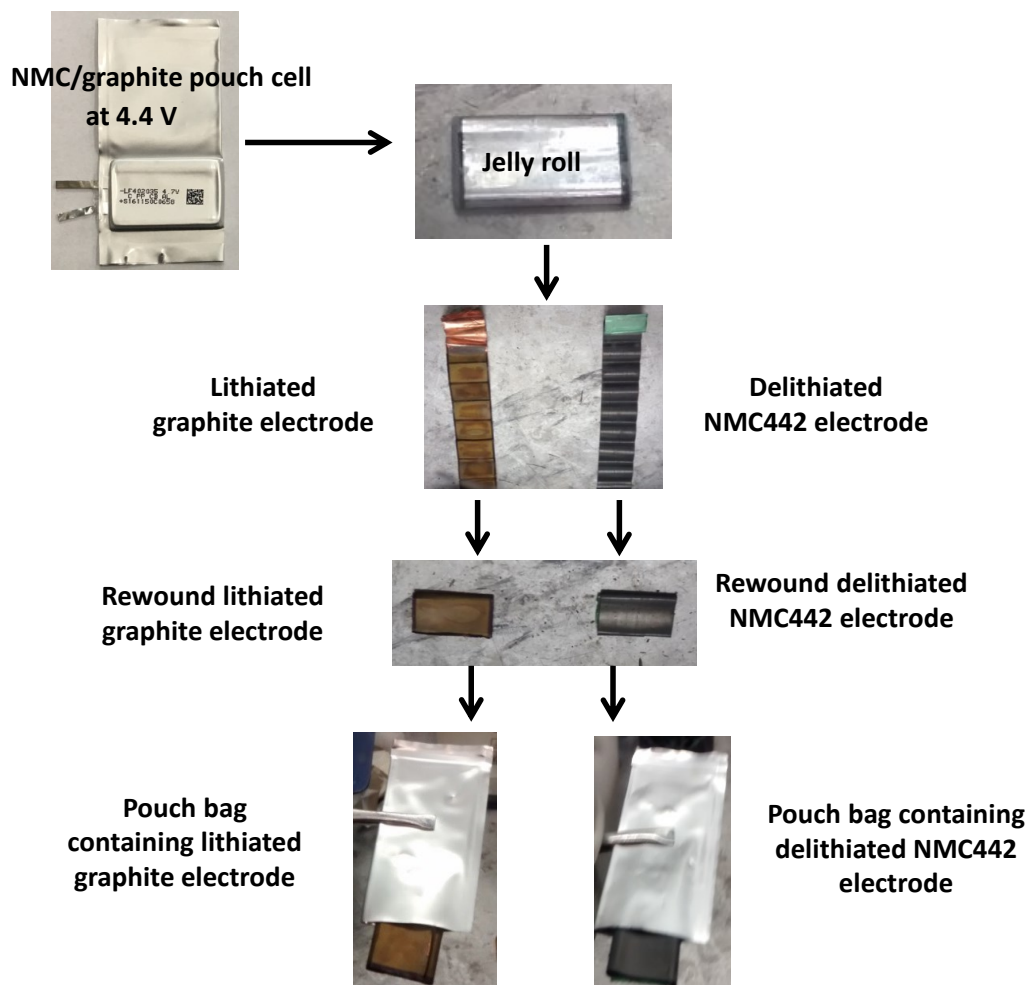
Figure 3.3 The steps in the construction of pouch bags containing either a lithiated graphite electrode or a delithiated NMC442 electrode taken from a NMC442/graphite pouch cell at 4.4 V. Electrolyte is normally added before the pouch bags are sealed.

3.1.4 Importance of the Formation Procedure for Pouch Cells

During the first charge cycle (called formation in this thesis), electrolyte is reduced on the surface of the graphite electrode and the initial SEI is formed there. As discussed in Chapter 1, gas can be generated from electrolyte reduction. The formed gas can cause pouch cell to swell. Therefore, it is important to remove the initial formed gas before further tests. The formation procedure used in this thesis was based on *in situ* gas

measurements of pouch cells [20,183] and experience gained from tests on about 20,000 pouch cells in the Dahn lab.

3.1.5   Formation Procedure for Pouch Cells

Dry pouch cells (without electrolyte) were vacuum sealed in China and shipped to Dalhousie University. The pouch cells were cut just below the seal and dried at 80 or 100°C under vacuum for 14 hours to remove residual water prior to electrolyte filling. The pouch cells were filled with a certain amount of electrolyte (depending on the cell and electrolyte type) and then sealed under vacuum at a gauge pressure of -90 kPa. After adding the electrolyte, the cells were placed in a 40.0 ± 0.1°C temperature controlled box, and held at 1.5 V for 12-24 h. They were then charged to 3.5 V at C/20. (A C/20 rate means that the current used will discharge the entire capacity of a cell in 20 h. For example, for a NMC442/graphite cell at a cutoff voltage of 4.4 V, its capacity is around 180 mA. A C/20 rate means a 0.009 A current is applied.) In order to remove the gas formed, the cells were transferred to a glove box for degassing (the first degassing step) (cut open below the seal and re-sealed under vacuum). After degassing, cells were normally charged to 4.4 V and held for 1 h and then degassed again (the second degassing step). These degassing voltages were selected based on the *in situ* gas measurements, which indicated that most of the gas was produced during the first cycle at voltages below 3.5 V and 4.3 V.[20] After the two degassing steps, cells were used for different purposes.

3.1.6 Electrolyte Chemicals

Electrolyte chemicals were obtained from a variety of manufacturers and used as received without additional purification. Table 3.2 shows the supplier, purity and water content (when available) of each chemical used.

Table 3.2 Supplier, purity and water content of electrolyte chemicals used

Electrolyte Chemical	Common name	Company	Purity (%)	Water content (ppm)
EC	ethylene carbonate	BASF	99.95	< 10
EMC	ethyl methyl carbonate	BASF	99.92	< 20
DMC	dimethyl carbonate	BASF	99.95	< 20
		ALFA AESAR	99	NA
DEC	diethyl carbonate	BASF	99.95	< 20
FEC	fluoroethylene carbonate	BASF	99.94	< 20
TFEC	bis(2,2,2-trifluoroethyl) carbonate	HSC Corporation	99.80%	NA
VC	vinylene carbonate	BASF	99.5	< 100
TAP	triallyl phosphate	TCI America	> 94	NA
DTD	1,3,2-dioxathiolane-2,2-dioxide or ethylene sulfate	Suzhou Yacoo Chemical Reagent Corporation	98	NA
PES	prop-1-ene-1,3-sultone	Lianchuang Medicinal Chemistry Co., Ltd.	98.2	NA
TTSPi	tris(trimethylsilyl) phosphite	TCI America	> 95	NA
PBF	pyridine trifluoroborate	3M	> 97	NA
$LiPF_6$	lithium hexafluorophosphate	BASF	99.94	< 20

3.2   Open Circuit Voltage Storage

A Li-ion cell can undergo self-discharge (a drop in open circuit voltage) due to parasitic reactions.[53,155] These parasitic reactions include electrolyte reduction on the surface of the negative electrode, electrolyte oxidation on the surface of the positive electrode and transition metal dissolution from the positive electrode.[110,184] The potential of an intercalation electrode material (vs Li/Li^+) depends on the amount of lithium residing in the material. When the intercalation electrode material experiences a two-phase region during lithium intercalation or deintercalation, the electrode potential (vs. Li/Li^+) versus the lithium content or state of charge in the two-phase region is constant. For a Li-ion cell in the charged state, if the negative electrode is in a two-phase region and the positive electrode is not in a two-phase region, the change in cell potential during storage must be due to a change in state of charge of the positive electrode. Since the cell voltage decreases, the lithium content residing in the positive electrode must increase. The lithium ions and the corresponding electrons need to be inserted into the positive electrode. These lithium ions must come from the salt and/or the negative electrode. The corresponding electrons must come from the electrolyte via electrolyte oxidation rather than the negative electrode because electrons from the negative electrode are blocked by the separator.

Figure 3.4 shows potential-capacity curves of a Li/graphite half cell, a Li/LCO half cell and a graphite/LCO full cell whose voltage-capacity curve is constructed from the difference between the potential-capacity curves for the Li/graphite and Li/LCO half cells. Figure 3.4 shows that the voltage of the Li-ion cell decreases due to the potential drop from the LCO while the graphite is in a two-phase region. Two arrows representing the

voltage drop of the Li/LCO cell and the graphite/LCO cell were added in the figure to guide readers. If an electrolyte additive or a surface coating slows down the rate of electrolyte oxidation on the surface of the positive electrode, a full cell with this additive or surface coating should show less voltage drop than a control cell over time. Therefore, a storage system is an excellent tool to gain insight how electrolyte additives and surface coatings work in a Li-ion full cell.
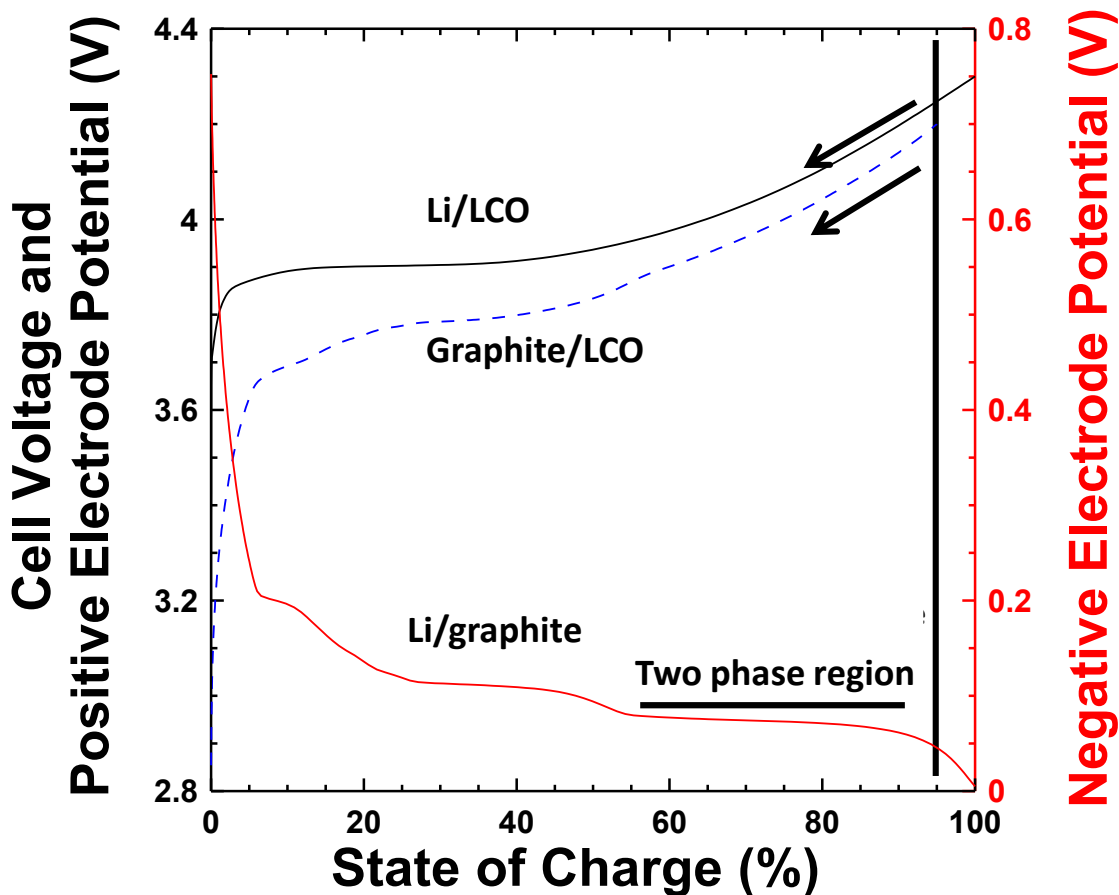
Figure 3.4 The potential vs state of charge curve of a Li/graphite half cell (red solid curve), the potential vs state of charge of a Li/LCO half cell (black solid curve) and the voltage vs state of charge of a graphite/LCO full cell (dashed blue curve).

A storage system was built in the Dahn lab in 2012.[184] The storage system can track self-discharge by measuring the open-circuit voltage of a cell as a function of time at

36

various temperatures.[184] Since this system can only measure voltage as a function of time, a cell must be charged or discharged to the desired state of charge before it is transferred to this storage system. In order to reach equilibrium, cells were normally held at the desired state of charge for some time. In this thesis, the holding time was normally 30 hours and the storage period was 500 hours..

3.3   Electrochemical Impedance Spectroscopy

Electrochemical impedance spectroscopy (EIS) is a powerful technique to guide electrolyte choice and monitor the state of health of a Li-ion cell.[11,12,14,185–194] EIS measurements are quick and non-destructive. Therefore, EIS is widely used in the LIB field.

EIS measurements apply a small AC voltage to Li-ion cells to invoke a current response over a range of frequencies from mHz to MHz. In order to achieve a linear current response, the applied amplitude of AC voltage is normally ± 5-10 mV. The impedance (ohms) is calculated at each frequency as the ratio of the applied voltage (volts) to the measured current (amps). Equivalent circuit models are normally used to interpret the impedance spectra. Table 3.3 shows a schematic of simple circuit elements, simplified circuit models of electrodes and a full Li-ion cell, and their corresponding impedance. The capacitance of a capacitor (farads) is designated as C, the resistance of a resistor (Ohms) is designated as R and the inductance of an inductor (Henrys) is designated as L. The angular frequency ω is equal to $2\pi f$ where f is the frequency (Hertz).

Table 3.3 Equivalent circuit model and the calculated impedance
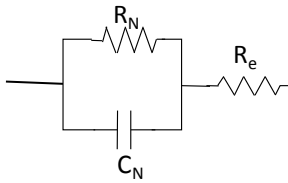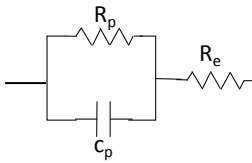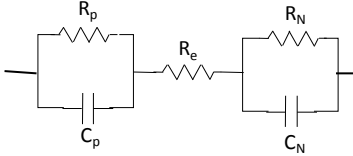
Component	Circuit Symbol	Impedance
Resistor		R
Capacitor		$\dfrac{1}{i\omega C}$
Inductor		$i\omega L$
Simplified model of a negative electrode in electrolyte		$R_e + \dfrac{R_N}{1 + \omega^2 C_N^2 R_N^2} - \dfrac{i\omega C_N R_N^2}{1 + \omega^2 C_N^2 R_N^2}$
Simplified model of a positive electrode in electrolyte		$R_e + \dfrac{R_p}{1 + \omega^2 C_P^2 R_P^2} - \dfrac{i\omega C_P R_P^2}{1 + \omega^2 C_P^2 R_P^2}$
Simplified model of a full Li-ion cell		$R_e + \dfrac{R_P}{1 + \omega^2 C_P^2 R_P^2} - \dfrac{i\omega C_P R_P^2}{1 + \omega^2 C_P^2 R_P^2}$ $+ \dfrac{R_N}{1 + \omega^2 C_N^2 R_N^2} - \dfrac{i\omega C_N R_N^2}{1 + \omega^2 C_N^2 R_N^2}$

Figure 3.5 shows the motions of Li^+ ions and electrons through the SEI on a negative electrode during charge/discharge and the electrical double layer on the electrode surface. For example, during charging, Li^+ ions pass through the electrolyte and then pass through the SEI layer in addition to some Li^+ ions charging the double layer surface. Therefore, the equivalent circuit for the negative electrode in electrolyte can be modelled as a circuit containing a resistor (R_N) and a capacitor (C_N) in parallel and then in series with a resistor (R_e). R_N represents the resistance to the motion of Li^+ ions and electrons through the SEI, C_N represents the capacitance of the electrical double layer and R_e represents the electrolyte resistance. The positive electrode in electrolyte can be described similarly with a resistor (R_P, representing the motion of Li^+ ions and electrons through the SEI) and a capacitor (C_P, representing the capacitance of the electrical double layer) in parallel and in series with a resistor (R_e, representing the electrolyte resistance). Thus, a full Li-ion cell can be described as the equivalent circuit of the positive electrode in series with the equivalent circuit of the negative electrode. As the negative electrode and positive electrodes are in the same electrolyte, only one resistor representing the electrolyte resistance is needed in the circuit.
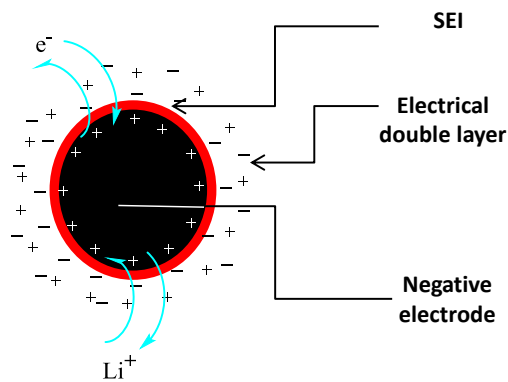
Figure 3.5 Schematic of a negative electrode particle in the electrolyte

EIS spectra can be represented as a Nyquist plot or a plotted Bode plot. A Nyquist plot is the imaginary component of the impedance ($-Z''$) on the y-axis versus the real component of the impedance (Z') on the x-axis. A Nyquist plot of a full Li-ion cell typically shows a semi-circular feature and the real component of the impedance typically increases as frequency decreases. A Bode plot is either the real component of impedance or the imaginary component of impedance in the y-axis as a function of frequency on a logarithmic scale in the x-axis. This is valuable since the impedance is shown at each measured frequency. Figure 3.6 shows Nyquist and Bode plots from circuit model calculations. Figure 3.6a shows a Nyquist plot for a negative electrode in electrolyte. The shift of the start of the semi-circle from zero is the electrolyte resistance, R_e. Figure 3.6b shows a Nyquist plot for a full Li-ion cell where the impedance of the two electrodes is close. If the two electrode impedances differ from one another, the Nyquist plot will not show a smooth semi-circular shape. Figure 3.6c shows a Bode plot of the real component of impedance of the full Li-ion cell and Figure 3.6d shows the imaginary component of impedance of the Li-ion cell.
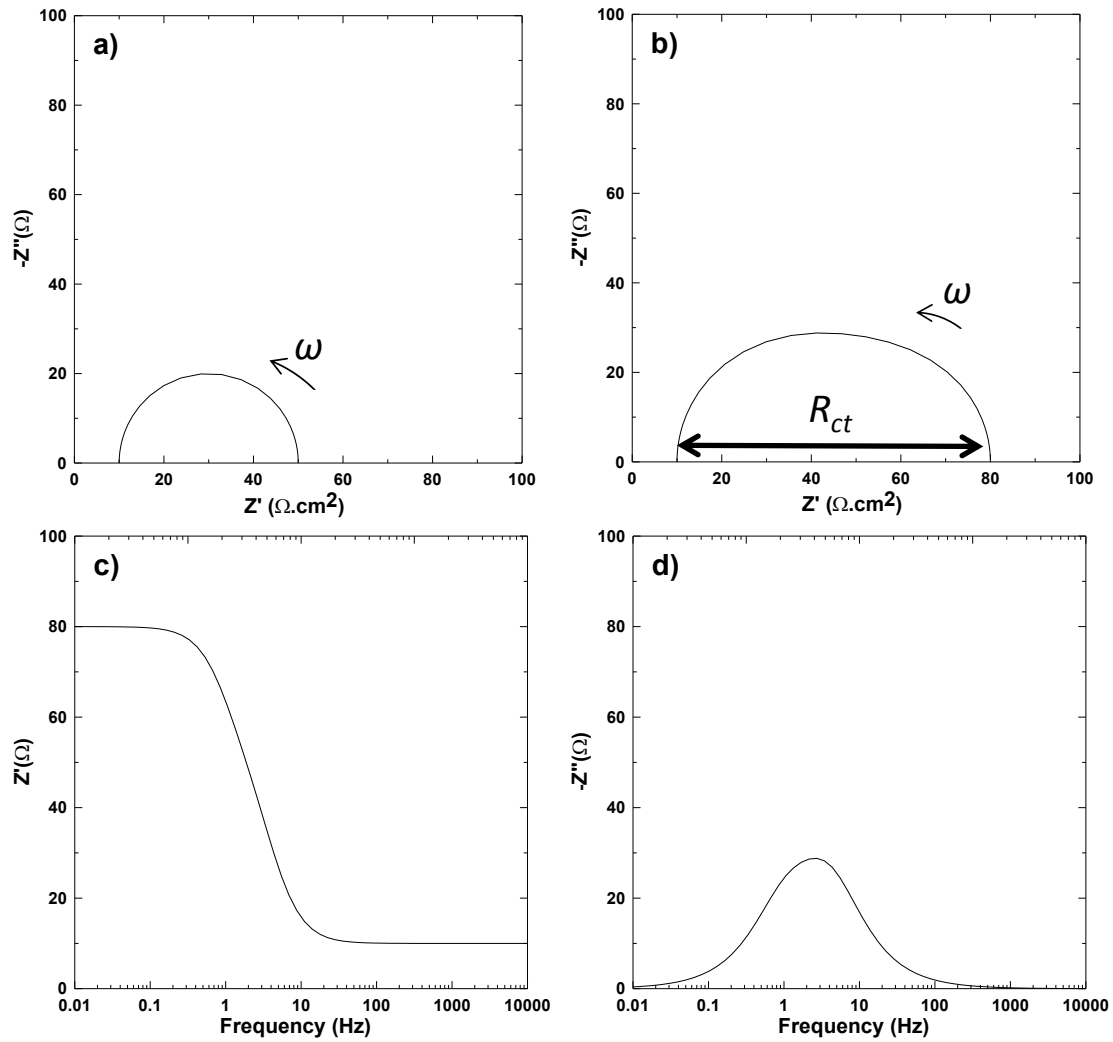
Figure 3.6 A Nyquist plot of a negative electrode in electrolyte (a) and a full Li-ion cell (b). A Bode plot of the real component of impedance (c) and the imaginary component of impedance (d) of a full Li-ion cell. The numbers used in the circuits are: R_e = 10 Ω, C_N = 0.001 F, R_N = 40 Ω, C_p = 0.005 F, and R_p = 30 Ω. Adapted from K. Nelson, *Studies of the effects of electrolyte additives on the performance of lithium-ion batteries*, M.Sc. thesis, Dalhousie University, Halifax, NS, Canada (2014). R_{ct} represents charge transfer impedance which is resistance due to the motion of Li$^+$ ions and electrons through the SEI (both negative and positive electrodes)..
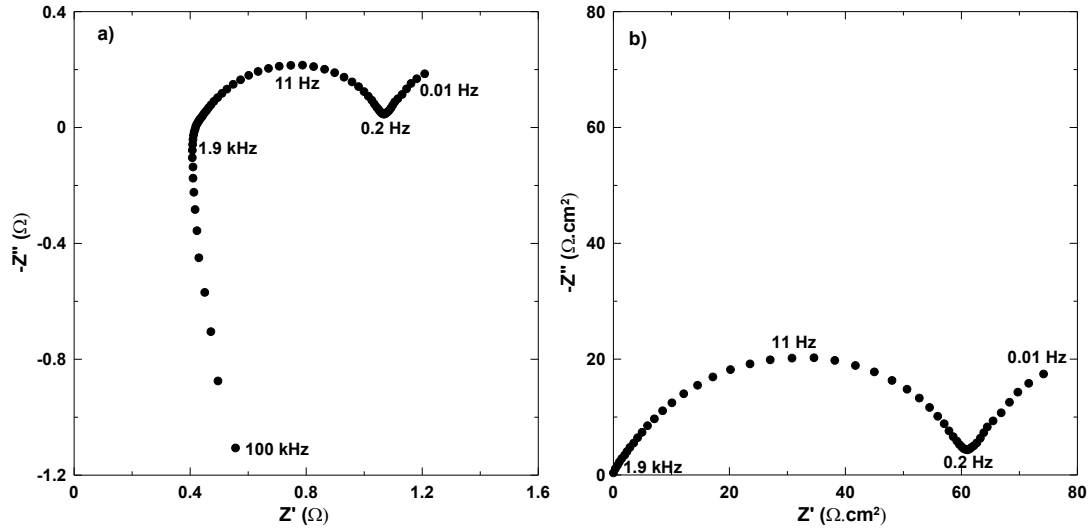
Figure 3.7 A Nyquist plot for a cell without subtracting and normalization (a) and with subtracting and normalization (b)

In this thesis, most impedance spectra are presented as Nyquist plots. Figure 3.7a shows a Nyquist plot of a pouch cell using measured data. The EIS equipment most used in this thesis has two wire connections to the pouch cells. The lead resistance contributes to the intercept at high frequency which otherwise could originate from the electrolyte resistance. In many cases, the electrolyte resistance is not of interest of this thesis. Therefore, Nyquist plots obtained from these two wire EIS measurements were shifted back to zero along the x-axis. Cell impedance depends on the surface area of the electrodes used in the cell. In order to allow the impedance to be independent of the electrode surface area, cell impedance was normalized by multiplying the impedance values by the electrode surface area. Figure 3.7b shows a Nyquist plot of the same cell where the impedance has been normalized and shifted back to zero. The normalized impedance is commonly called the area specific impedance.

In this thesis, the resistance due to the motion of Li$^+$ ions and electrons through the SEI is called the charge transfer impedance (R_{ct}). R_{ct} can be extracted from the Nyquist

plot as the "diameter" of the "semicircle", as indicated in Figure 3.6b. Measurements of R_{ct} will be used to compare how electrolyte additives, storage conditions and cycling conditions *etc.* affect the SEI layer.

3.3.1 Electrochemical Impedance Spectroscopy of Symmetric Cells

The impedance spectra of the negative and positive electrodes in a full Li-ion cell often overlap over the range of measured frequencies so it is difficult to distinguish the contributions to the cell impedance from each electrode. However, it is of great importance to separate their contributions since doing so can lead to an understanding of the role of additives and cell failure mechanisms. A good method is to use symmetric cells. The symmetric cell method is more reliable than the reference electrode method. In the reference electrode method, a reference electrode is incorporated within a Li-ion cell. A reference electrode of choice is usually Li metal.[195–197] However, it is hard to insert a Li metal reference electrode into a cell in the right place, especially in commercial cells.[198] Furthermore, the introduction of Li metal can alter the behavior of the cell during long time testing since Li metal is more reactive with electrolyte than lithiated graphite.

Figure 3.2 shows the construction of coin full cells, positive/positive and negative/negative symmetric cells. The impedance of a coin full cell, positive/positive symmetric cell and negative/negative symmetric cell is given by

$$Z_{+/-} = Z_+ + Z_- + Z_e \qquad\qquad\qquad\qquad 3.1$$

$$Z_{+/+} = 2Z_+ + Z_e \qquad\qquad\qquad\qquad 3.2$$

$$Z_{-/-} = 2Z_- + Z_e \qquad\qquad\qquad\qquad 3.3$$

where $Z_{+/-}$ represents the impedance of a coin full cell, $Z_{+/+}$ represents the impedance of a positive/positive symmetric cell, $Z_{-/-}$ represents the impedance of a negative/negative cell, Z_+ represents the impedance of a positive electrode, $Z-$ represents the impedance of a negative electrode and Z_e represents the resistance of the electrolyte.

If the electrodes used in these symmetric cells and coin full cells are taken from the same cell and the electrolyte used in these cells is the same, then the sum of the impedance of the positive/positive symmetric cell and negative/negative symmetric cell is twice that of the coin full cell,

$$Z_{+/+} + Z_{-/-} = 2Z_+ + Z_e + 2Z_- + Z_e = 2(Z_+ + Z_- + Z_e) = 2Z_{+/-} \qquad\qquad 3.4$$

Chen *et al.* proved the validity of Equations 3.1 to 3.4 using symmetric cells reconstructed from a 18650 cylindrical cell with a $LiNi_{0.8}Co_{0.2}O_2$ positive electrode and a graphite negative electrode. [199] Petibon *et al.* further explored the effects of various electrolyte additives on both electrodes for Li-ion cells of various chemistry using this method.[111,200,201] Figure 3.8 shows Nyquist plots and Bode plots of a coin full cell, negative/negative symmetric cell and positive/positive symmetric cell. The impedance spectra of the symmetric cells have been divided by 2 for ease of comparison to the prediction of equation 3.4. The sum of half of the negative/negative symmetric cell impedance and half of the positive/positive symmetric cell impedance is shown in the Bode plot. The electrodes used in these cells were taken from the same pouch cell. The electrolyte used was also the same. Figures 3.8e and f demonstrate that the sum of half the negative/negative symmetric cell impedance and half the positive/positive symmetric cell impedance is equal to that of the reassembled full cell. Figures 3.8a, b, c and d show

that the main contribution to the full cell impedance is from the negative electrode for this example. Figure 3.6c shows that there are two semicircles for the positive/positive symmetric cell. The high frequency semicircle is the contact impedance due to the contact between the positive electrode and cell hardware since a double sided positive electrode was used in the symmetric cell.[111]

This section should acknowledge that the simple circuit models used here are too simple. They cannot explain Fiugre 3.8c, for example. It may be worth directing readers the paper described by Abarbanel *et al.* [192] as well as other papers about interpreting impedance spectra of Li-ion cells. [189,202–208]
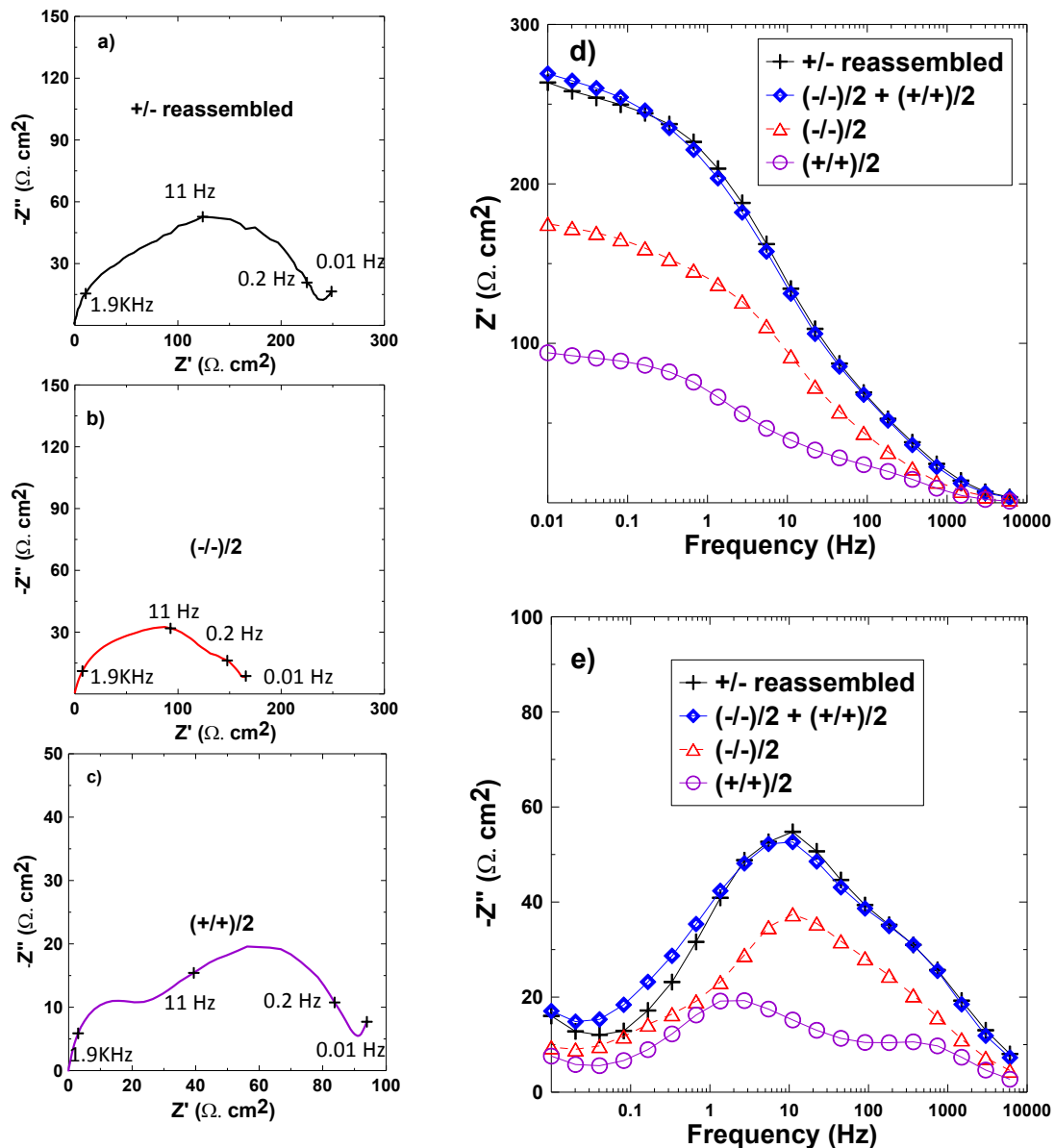
Figure 3.8 A Nyquist plot of a reassembled full cell (a), a negative/negative symmetric cell (spectrum has been divided by two) (b) and a positive/positive symmetric cell (spectrum has been divided by two) (c) where the electrodes were taken from the same pouch cell. A Bode plot of the real component (d) and the imaginary component (e) of the reassembled full cell, a negative/negative cell (spectrum has been divided by two), the positive/positive symmetric cell (spectrum has been divided by two). Panels d and e show that calculated full cell impedance is the sum of half the negative/negative cell and half the positive/positive symmetric cell impedance.

3.4 Pouch Cell and Pouch Bag Volume Change Measurements

The electrodes and electrolytes reacting in pouch cells and pouch bags can produce gas during storage. It is important to track how these products are evolved (for example gas production vs time and temperature). Figure 3.9 shows a setup for *ex situ* gas volume measurements of pouch cells and pouch bags. Archimedes' Principle is used to relate the buoyant force on a pouch cell or bag to the volume of the cell or bag. Figure 3.9 shows a pouch cell suspended in water by a hook under a balance. The hook is attached to the weighing arm of the balance. The sum of forces acting on the cell is given by

$$\Sigma F = F_{tension} - mg + F_{buoyant} = 0 \qquad\qquad 3.5$$

where $F_{tension}$ is the force of the tension due to the hook, m is the cell mass, g is the magnitude of gravitational acceleration and $F_{buoyant}$ is the buoyant force As the volume of the cell changes, the buoyant force changes, while the cell weight stays constant. Therefore, the change of the tension force due to the hook is opposite to the change of buoyant force on the cell,

$$\Delta F_{tenstion} = - \Delta F_{buoyant} \qquad\qquad 3.6$$

The change of buoyant force on the cell is given by

$$\Delta F_{buoyant} = \Delta V \rho g, \qquad\qquad 3.7$$

where ΔV is the volume change of the cell, ρ is the density of water and g is the magnitude of gravitational acceleration.

As the hook supporting the cell is attached to a balance, the tension force on the hook can be determined by the balance. Therefore, the change of the tension force is given by

$$\Delta F_{tenstion} = \Delta m_{balance} g \qquad\qquad 3.8$$

where $\Delta m_{balance} g$ is the change of weight measured by the balance. Laboratory balances report "mass" even though they measure weight. Balances assume that g is constant..

Combining equations 3.6, 3.7 and 3.8, one obtains

$$\Delta V = - \Delta m_{balance}/\rho \, , \qquad\qquad 3.9$$

The density of water is very close to 1.000 g/mL at room temperature. The measurements were made at room temperature. Therefore, the change of the volume of the cell is virtually equal to the change of the mass reading from the balance.

$$\Delta V = - \Delta m_{balance} \qquad\qquad 3.10$$

This implies that the volume of gas produced in a pouch cell or pouch bag can be easily obtained by weighing the cell or pouch bag under water before and after testing.
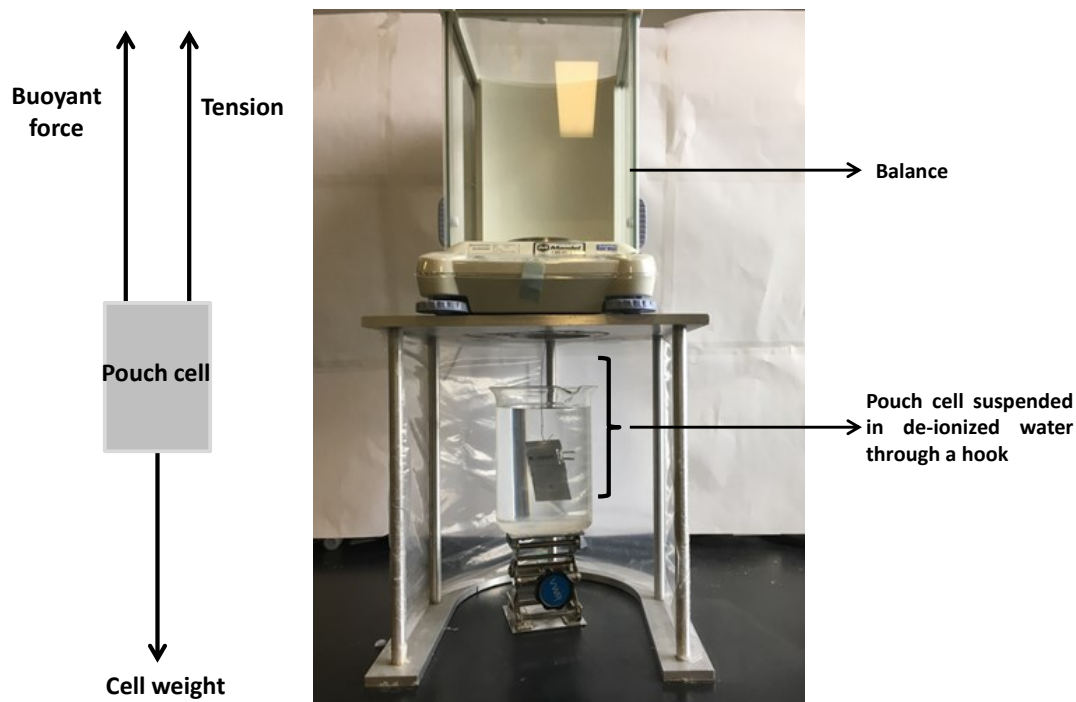
Figure 3.9 Photograph of the set-up for *ex situ* gas measurements where a pouch cell is weighed while submerged in water. The diagram at the left shows a free body diagram of the forces acting on the cell.

3.5 Gas Chromatography coupled with Mass Spectrometry and Thermal Conductivity Detection

In this thesis, gas chromatography (GC) coupled with mass spectrometry (MS) and GC coupled with thermal conductivity detection (TCD) were used to analyze gas compositions produced in pouch cells and pouch bags.

3.5.1 Gas Chromatography

A GC can separate volatile and gaseous compounds. Figure 3.10 shows a schematic of a GC. A typical GC includes a carrier gas supply, an injector, the separation column located in a temperature controlled oven and a detector.
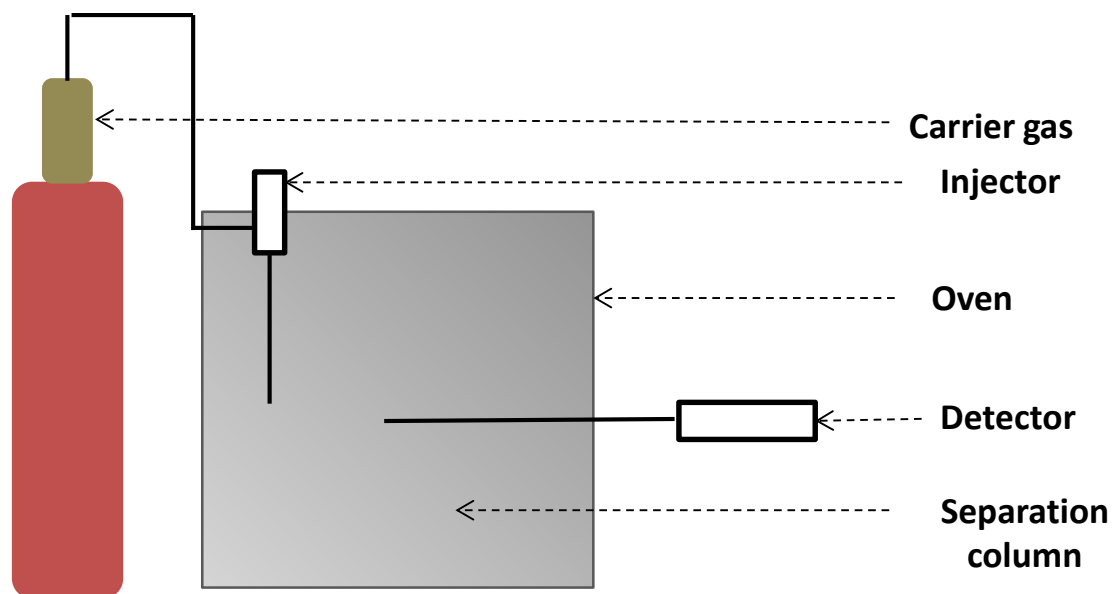
Figure 3.10 A schematic of a typical GC

The carrier gas is called the mobile phase (moving through the column) which carries the sample through the separation column. Common carrier gases are H_2, N_2 and He. The majority of separation columns are long and narrow capillary tube made of fused silica (SiO_2) and coated with polyimide outside (capable of withstanding 350 °C) for support and protection from atmospheric moisture. [209] Column inner diameters are typically 0.1 to 0.53 mm and lengths are 15 to 100 m. The inner wall of the column is commonly coated with functionalized polysiloxanes which are chemically bonded to the inside of the column or onto the surface of solid particles packed in the column. The coated functionalized polysiloxanes in the column are called the "stationary phase" (staying in place inside the column).

When a volatile liquid or gaseous sample is introduced through the heated injection port, it rapidly evaporates because of the high temperature (up to 300 °C) there. As the components of the sample travel through the column, they interact with the stationary

phase to different degrees depending on their affinity to the stationary phase. As a result, components travel with different speeds through the column and exit from the column after a distinct retention time (the time required for a component to exit from the column after it is injected). The temperature of the oven containing the column can be controlled to optimize the separation. A multiple heating step is normally used. When the separation conditions are optimized, sample components exit one by one and each peak represents a specific compound. When each component reaches the detector, a signal is produced related to its concentration.

3.5.2 Mass Spectrometry

MS is normally used coupled with GC. Figure 3.11 shows a schematic of a MS. A MS comprises a sample inlet, an ionization chamber, a mass analyzer and an ion detector. The sample is first introduced into the sample inlet and then transferred to the ionization chamber where an ion source is formed. After the ions are separated based on the mass to charge ratio (m/z) by the mass analyzer, they exit and hit the detector and generate a signal. These major components of a MS are all in high vacuum (10^{-5} pa) during operation so that the produced ions are not affected by the gas molecules in the air. [209]
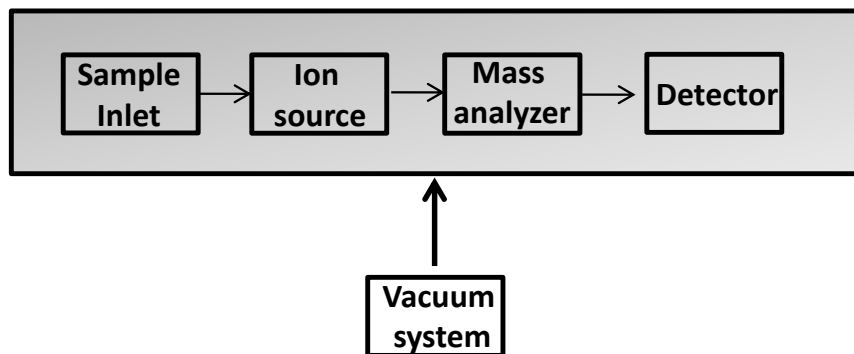
Figure 3.11 A simplified schematic of a MS

51

Several ionization methods can be used in mass spectrometer. Electron ionization (EI) is a basic one. In the EI method, sample components are hit by fast electrons (70 eV) produced from a hot filament and thereby ionized. Molecules can be broken down. The breaking of molecules is called fragmentation. Therefore, in the EI method, molecular ions (the intact molecule with missing electrons) and fragment ions are produced. The molecular weight can be identified from the molecular ions and the molecular structure can usually be determined from the fragment ions. However, in some cases, the molecular ions cannot be observed in the EI method. For this reason, other ionization methods such as chemical ionization (CI) are used. In the CI method, a reagent gas is produced from the collision with fast electrons. The ionized gas reagent then collides with sample molecules. Most of the ions generated are the molecular ions and very few fragment ions are created. Therefore, in the CI method, the molecular weight of sample molecules are easily identified but structural information is not obtained. In the work in this thesis, the EI method was used.

Each molecule has its own ion fragmentation pattern in EI mode. Therefore, its ion fragmentation pattern can be used as a fingerprint to identify its molecular structure by searching the mass spectral library. In this thesis, the NIST/EPA/NIH Mass Spectral Library Demo Version 2.0 f was used as the mass spectral library.

3.5.3   Thermal Conductivity Detection

The MS used in this thesis cannot detect H_2 produced in pouch cells and pouch bags. A TCD is normally used to detect H_2. Therefore, GC-TCD was also used to analyze gases produced in these pouch cells and pouch bags in this thesis.
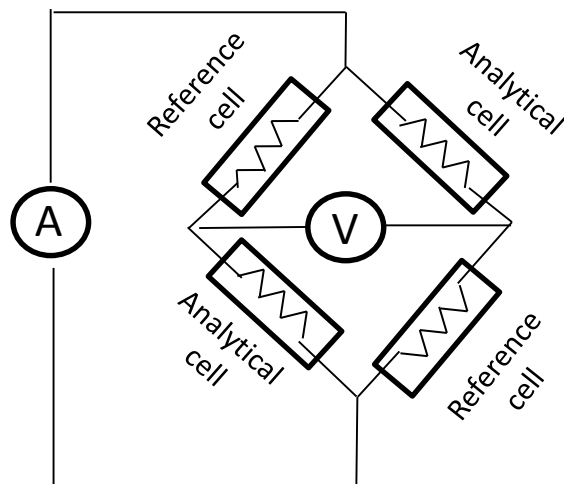
Figure 3.12 A schematic of a TCD with a bridge electronic circuit design

Figure 3.12 shows a simplified TCD with a bridge electronic circuit design.[210] Figure 3.12 shows that the TCD comprises four cells. Two are called analytical cells and the other two called reference cells. Each cell comprises a heated chamber containing a resistor whose resistance depends on its temperature. Pure carrier gas flows through the reference cells while gas eluted from the GC column flows through the analytical cells. During operation, the resistor is heated to a certain temperature and the flow rate of gas into the reference cells is adjusted to be equal to the flow rate of gas into the analytical cells. A current is applied for the bridge electrical circuit and a voltage across the bridge is monitored.

When no compound is eluted from the GC column, the pure carrier gas flows through both reference cells and analytical cells. Thus, all the resistors have the same resistance and the voltage across the bridge is zero. When a compound with different thermal conductivity is eluted from the GC column, the different gas compositions cause heat to be conducted away at different rates in the reference cells and the analytical cells. The

resistance of a resistor depends on its temperature. Therefore, the resistors in the analytical cells have different resistance from those in the reference cells. As a consequence, a voltage across the bridge is created. The sensitivity of a TCD strongly depends on the thermal conductivity differences between the gases analyzed and the carrier gas chosen. In this thesis, argon is chosen as the carrier gas.

3.5.4 A Home-made Device for Extracting Gas

In order to investigate the gaseous products in a pouch cell or bag, a home-made device was designed to extract gas. Figure 3.13 shows this home-made device designed by Remi Petibon. It consists of a brass cylindrical chamber where a pouch cell or bag was placed. The screw top is equipped with a punch which can be pressed into the chamber and pierce the cell or bag. One gas line was connected to the chamber for vacuum pumping and argon filling. The other gas line contained a silicone septum allowing a syringe to pierce and extract gas from the chamber. To extract the gas, a pouch cell was placed in the chamber properly. In order to avoid safety risks related to a short circuit, the cell was discharged to around 2.0 V volts before it was inserted into the chamber. Once the cell or bag was positioned in the chamber, the chamber was connected to a vacuum pump. In order to make sure that the punch did not pierce the cell or bag, the punch was held by hand during pumping. After the pressure of the vacuum pump reached 100 millitorr, the chamber was disconnected from the pump. The punch was then pressed to pierce the cell or bag. Once gas was released from the cell or bag, the chamber was connected to an argon cylinder which allowed argon to dilute the gas from the cell or bag. After a few seconds, normally 30 seconds, the chamber was disconnected from the

cylinder. A syringe was then used to extract gas using the septum. Typically 50 µL was taken to inject into GC-MS for analysis.
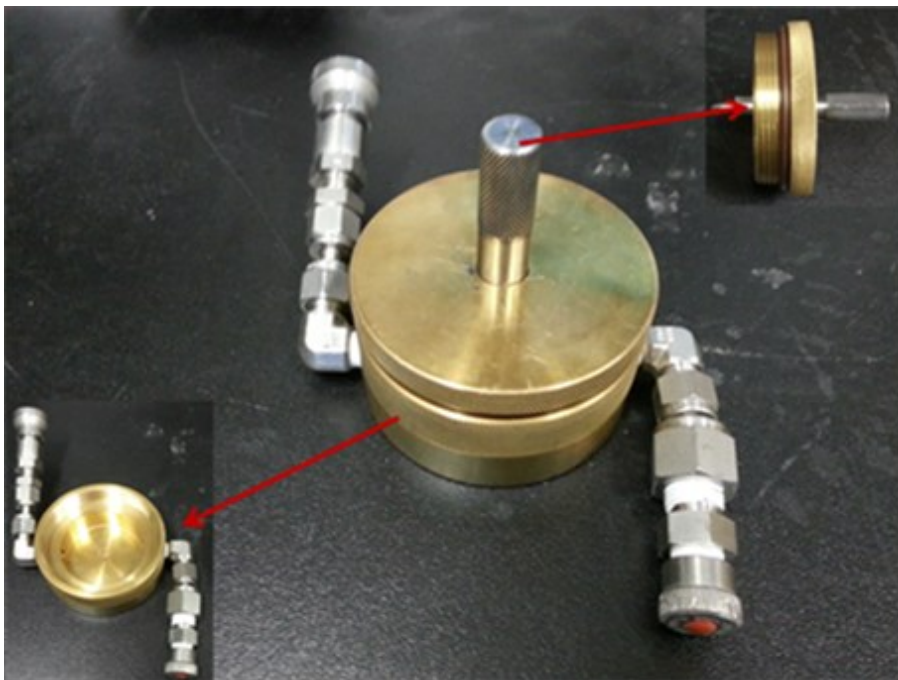
Figure 3.13 Photograph of the device used to extract gas from pouch cells. The inset at the top right corner is the screw top of the device with a punch. The inset at the bottom left corner is the base of the chamber.

3.5.5 Quantitative Analysis of Gas Compositions in Pouch Bags and Pouch Cells

It is important to carry out quantitative analysis of gaseous products generated in pouch bags and pouch cells to learn about cell degradation mechanisms. Quantitative analysis of gas compositions is based on the area of a chromatographic peak. In the linear response concentration range, the area of a peak is proportional to the quantity of that component.

In this thesis, a gas mixture is used as external standard for calibration. The gas mixture contained butane, carbon dioxide, carbon monoxide, ethane, hydrogen, methane,

propane, propylene and argon. Each gas was 10 ± 0.1 mol % in the mixture. Since the calibration gas mixture and the gas sample generated in pouch bags and pouch cells were analyzed with the same procedure in this thesis, the total volume used for the gas sample can be considered as the same as that for the gas mixture. Futhermore, the number of gas molecules is proportional to the volume of gas at atmosphere pressure. Therefore, the volume of a component of the gas sample generated in pouch cell and pouch bags can be simply calculated using equation 3.11

$$\frac{A_c}{V_c} = \frac{A_s}{V_s}$$ 3.11

where A_c is the peak area of a component of the calibration gas mixture, V_c is its corresponding volume in the calibration gas mixture, A_s is the peak area of the corresponding component of the gas sample generated in pouch cells and pouch bags and V_s is its corresponding volume in the gas sample. In this thesis, since the extracted gas device has a volume of 4 mL and each gas was 10 ± 0.1 mol% in the gas mixture, 0.4 mL is used for V_c.

3.5.6   Experimental Procedure for GC-MS

The GC-MS equipment consists of two main components which are a Bruker 436-GC and a Bruker Scion single-quadrupole mass spectrometer. The Bruker 436-GC is equipped with a split/split-less injector and a BR-Q-PLOT 30 m column with an inner diameter of 0.25 mm. The Bruker Scion single-quadrupole MS connected to the GC is equipped with an electron impact ionization module. Helium was used as carrier gas at a constant flow rate of 1 mL/min. The injector temperature was set to 250°C. The

temperature program was set for a 3 min 35°C hold followed by a 9 min 200°C hold after a rise to 200°C at 20°C/min and finally followed by a 5 min 250°C hold after a rise to 250°C at 100°C/min. The transfer line and ion source were set to 250°C and 200°C, respectively. 70 eV was used for the electron energy. The MS was set to a full scan mode with 10-250 amu range.

3.5.7   Experimental Procedure for GC-TCD

The GC-TCD consisted of a Bruker 436-GC equipped with a split/splitless injector (270°C) and a TCD (Bruker) equipped with a custom-made capillary column.   The column consisted of a 5A molecular sieve column (Bruker, 10 m, 0.32 mm ID, 30 μm coating), in parallel with a Q-PLOT column (Bruker, 50 m, 0.53 mm ID, 20 μm coating). This custom column allows for permanent gases (H_2, O_2, N_2, CO) and light hydrocarbons (CH_4, C_2H_6, C_2H_4, etc.) as well as CO_2 to be well-separated in a single injection. Argon was used as the carrier gas at a flow rate of 9 mL min^{-1}. In order to maximize the sensitivity of the detector, the reference cell flow rate of the TCD was set to 30 mL min^{-1} and the make-up flow rate of the analytical cell was set to 5 mL min^{-1}. The TCD temperature was set to 230°C while the filament temperature was set to 370°C.

To quantitatively analyze the gas compositions, a calibration gas mixture was purchased from Praxair for retention time determination and signal calibration. The gas mixture contained butane, carbon dioxide, carbon monoxide, ethane, ethylene, hydrogen, methane, propane, propylene and argon.   Each gas was 10 ± 0.1 mol% in the mixture. The pressure in the tank was supplied at only 13 bar (gauge pressure) to ensure that each species was entirely in the gas phase.

3.6   Thermal Gravimetric Analysis coupled with Mass Spectrometry.

Thermogravimetric analysis (TGA) is a thermal technique to characterize the thermal properties of materials. TGA continuously monitors the weight of a sample while the sample is heated under a programmed heating process in a specific atmosphere such as air, argon and helium. During this process, the weight loss of the sample due to its decomposition can be measured and is usually plotted with temperature.

Even though TGA gives a quantitative measure of weight loss of the sample, it does not provide information on the nature of the products that are lost from the sample. When TGA is coupled with MS, the released gases can be analyzed and identified giving additional valuable information. In this thesis, TGA-MS was used to monitor the weight loss of charged positive electrodes and analyze gas compositions released from these charged positive electrodes.

3.7   Error Calculation

All results presented in this thesis are the average of the measurements of two samples. The error bars shown in the various figures were calculated as the range of the two samples. This provides a good idea of the repeatability of the measurements.

CHAPTER 4: A SIMPLE AND NOVEL WAY (THE POUCH BAG METHOD) TO EXPLORE NEGATIVE/POSITIVE ELECTRODE INTERACTIONS, THE ORIGIN OF GAS PRODUCTION AND IMPEDANCE GROWTH IN A LI-ION CELL WITH CARBONATE ELECTROLYTE

In this chapter, pouch bags containing a delithiated NMC442 or a lithiated graphite electrode, taken from pouch cells with 1M LiPF$_6$ in EC/EMC (3:7 w/w) (control electrolyte), control + 2% VC, control + 2% PES, control + 2% PBF, control + 2% TAP electrolytes, were used to investigate gas production, impedance growth and gas consumption at high temperature and high voltage. The results from the pouch bag studies were compared to results from the corresponding pouch cells which contained both electrodes. The majority of this work was adapted from the following peer-reviewed articles:

D.J. Xiong, R. Petibon, M. Nie, L. Ma, J. Xia, J.R. Dahn, Interactions between Positive and Negative Electrodes in Li-Ion Cells Operated at High Temperature and High Voltage, J. Electrochem. Soc. 163 (2016) A546–A551. doi:10.1149/2.0951603jes.

D.J. Xiong, L.D. Ellis, K.J. Nelson, T. Hynes, R. Petibon, J.R. Dahn, Rapid Impedance Growth and Gas Production at the Li-Ion Cell Positive Electrode in the Absence of a Negative Electrode, J. Electrochem. Soc. 163 (2016) A3069–A3077. doi:10.1149/2.1031614jes.

Deijun Xiong developed the pouch bag method. Deijun Xiong prepared the pouch cells and pouch bags and also prepared the materials for the XPS studies. Deijun Xiong performed the gas measurements, the impedance measurements and the electrode potential measurements. Deijun Xiong performed the GC-MS studies of gas compositions together with Remi Petibon. Deijun Xiong performed the gas consumption measurements using the method originally developed by Leah Ellis. The XPS measurements and the analysis of XPS spectra were performed by Leah Ellis. Deijun Xiong prepared all the figures except for Figure 4.2 and Figure 4.13 (prepared by Leah Ellis). Jeff Dahn provided guidance and participated in experimental design and the interpretation of all the data. Deijun Xiong prepared the manuscripts of both articles mentioned above except for the XPS section and received revisions from Leah Ellis, Remi Petibon and Jeff Dahn.

4.1 Experimental

4.1.1 Pouch Cells and Pouch Bags

The NMC442/graphite pouch cells were prepared according to the method described in Section 3.1.5 and filled with 0.9 g of 1M $LiPF_6$ in EC:EMC (3:7 by weight) (control electrolyte) in an argon-filled glove box and vacuum sealed in the same glove box. To some electrolytes, 2 % VC, 2% PES, 2% PBF, or 2% TAP were added. After electrolyte filling, cells were placed in a 40. ± 0.1°C temperature controlled box, and held at 1.5 V for 24 h. They were then charged to 3.5 V at C/20 and transferred to a glove box for degassing (cut open below the seal and re-sealed under vacuum). After degassing, they were charged to either 4.2 or 4.4 V, discharged to 2.8 V and charged back to the same upper charge cut-off voltage and held at that voltage for 30 hours. Figure 4.1 shows

photographs to illustrate how the pouch cells were disassembled, the pouch bags were created and how the pouch cells and pouch bags were then used.
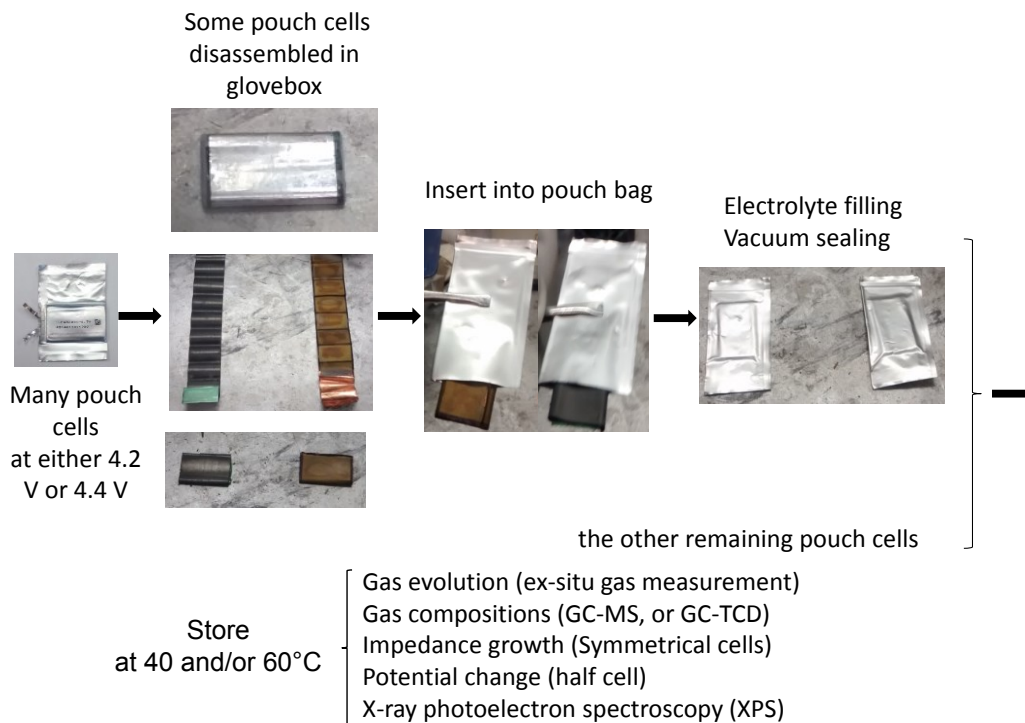
Figure 4.1 Photographs of steps and a flow path of the process used to make and test pouch cells and pouch bags.

Six cells either at 4.2 V or 4.4 V were used for head-to-head comparison in the gas evolution experiments. Two pouch cells were moved to a 60°C temperature box for storage. The other identical pouch cells were transferred to an Ar-filled glovebox and disassembled there. Two delithiated NMC442 electrodes collected from the pouch cells were inserted into pouch bags with 0.3 g of EMC. The addition of 0.3 g of EMC to the pouch bags created a similar electrolyte environment as in the original pouch cells since EC and $LiPF_6$ remained in the electrode and some EMC evaporated during the time (less than 5 minutes) it took to assemble the pouch bags. The other two delithiated NMC442 electrodes harvested from the pouch cells were rinsed with DMC three times, to remove

LiPF$_6$, dried, and then inserted into pouch bags with 0.4 g of EC/EMC (3:7 w/w). These pouch bags were also moved to a 60°C temperature box for storage. The volume of the pouch bags and pouch cells during the 500 h storage period were measured from time to time, using the *ex situ* gas volume equipment described in Chapter 3.4.

Eight pouch cells at 4.4 V were used for the impedance studies. Two pouch cells were moved a 40°C temperature box. Another two pouch cells were moved to a 60°C temperature box. The other four identical pouch cells were transferred to the glovebox and dissected there. The four delithiated NMC442 electrodes were inserted into pouch bags with 0.3 g of EMC. Two pouch bags were moved to a 40°C temperature box. The other two pouch bags were moved to a 60°C temperature box. All these pouch cells and pouch bags were stored for 500 h storage period.

4.1.2   Analysis of the Gas Composition in NMC442/Graphite Pouch Cells and NMC442-containing Pouch Bags

GC-MS was used to analyze the gases evolved in the pouch cells and pouch bags. The GC-MS procedure enabled detection of all gases other than H$_2$ and CO. The gas extraction procedure followed that described in Section 3.5.5. In this procedure, gas from the cell or pouch bag is mixed with a fixed amount of argon before injecting into the GC-MS. In order to keep signals in the linear range of the GC-MS, it was necessary to adjust the amount of gas injected when the amount of gas in the pouch cells or pouch bags was large. For most of pouch cells and pouch bags, 100 µL of the gas was injected into the GC-MS for analysis. 50 µL of the gas was injected from pouch bags containing delithiated NMC442 electrodes rinsed with DMC. The GC-MS used was a Bruker 436-

GC coupled to a Bruker Scion single-quadrupole mass spectrometer. The operating parameters are described in Section 3.5.6. The procedures for quantitative analysis of gas compositions produced in pouch bags and pouch cells can be found in Section 3.5.5.

4.1.3 Investigation of CO_2 Consumption in Pouch Bags containing Lithiated Graphite Electrodes and Intentionally Added CO_2

It is first important to describe how gas was intentionally added to the pouch bags. First, one side of a rubber septum was roughened with a hand file. The roughened septum was glued to a pouch bag using Gorilla^{TM} glue (a polyurethane-based waterproof glue, available at many hardware stores – see www.gorillatough.com). A heat gun, coupled with light pressure, was used to dry the glue rapidly. Rubber septa, attached to pouch bags by this method, provided a gas-tight seal, as evidenced by immersion of inflated pouch bags under water for several minutes.
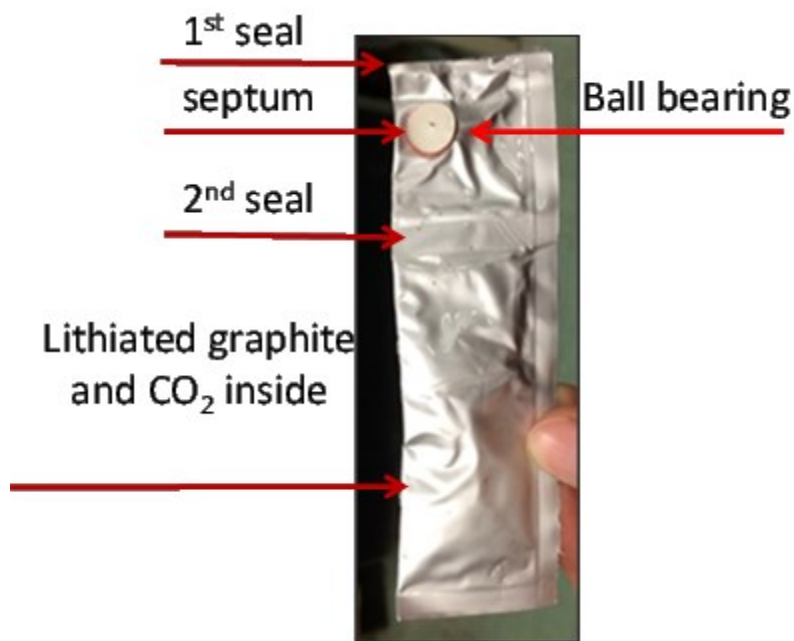
Figure 4.2. A photograph of the pouch bag, showing where the rubber septum is attached and

63

where the first seal, the second seal and the steel ball are located

Lithiated graphite electrodes, taken from pouch cells with control, control + 2% VC, control + 2% PES and control + 2% PBF, were inserted into the pouch bags along with 0.3 g of EMC in a glovebox. A 6 mm diameter hardened steel ball was placed in the pouch bag, near the septum, to assist in injecting CO_2. The purpose of the ball was to make space so the gas syringe needle could be inserted into the pouch bag, through the septum, without puncturing the back side of the pouch bag. The bulge due to the steel ball can be seen in Figure 4.2. After the pouch bags were vacuum sealed (the first seal shown in Figure 4.2), CO_2 (more than 5 mL) was injected using a syringe through the septum. The pouch bags were then heat sealed at a position below the septum and ball (the second seal shown in Figure 4.2), without the application of vacuum. Then the portion of the pouch bag containing the septum and the hardened steel ball was cut away, above the second seal. Then the pouch bags containing electrode and electrolyte were stored at elevated temperature. Pouch bags with 1 mL of EC/EMC (3:7) + intentionally added CO_2 (no electrodes) were also made for comparison.

The volumes of the pouch bags with injected CO_2 were measured, from time to time, using the *ex situ* gas volume measurement in Chapter 3. Normally, the pouch bags floated on water so the same "bulldog" paper clamp was clamped to the edge of the pouch bag (at the heat seal) to cause submersion. The weight of the bulldog clamp (measured under water) was subtracted from all the weights measured where the bulldog clamp was employed. The absolute amounts of CO_2 in the initial and final inflated pouch bags cannot be determined unless all details of the pouch bags and electrodes are known, but the amount of gas consumed can be accurately measured, and this is what was desired

to be measured.

4.1.4 Symmetric Cell and Half Cell Construction

Some NMC442/graphite pouch cells and NMC442-containing pouch bags were disassembled in an Ar-filled glove box after the 500 h storage period. Li/graphite and Li/NMC442 half cells and NMC442/NMC442 symmetric cells were constructed from electrodes harvested from both pouch cells and pouch bags. The importance of using symmetric cells to determine the charge transfer impedance (R_{ct}) (resistance to the motion of Li^+ ions and electron through the SEI) of electrodes was detailed in Section 3.3. Coin cells were made using one polypropylene (Celgard 2320) separator for half cells and one additional polypropylene blown microfiber separator (available from 3M Co., 0.275 mm thickness, 3.2 mg/cm^2) for symmetric cells. A voltmeter was used to measure the open-circuit voltage of the half cells, once their voltage stabilized after a few minutes. EIS measurements were conducted using a Biologic VMP-3 potentiostat, with ten points per decade from 100 kHz to 10 mHz and a 10 mV input signal amplitude. All EIS spectra were collected at 10°C. This temperature was chosen to magnify the difference between the impedances of the cells.

4.1.5 X-ray Photoelectron Spectroscopy (XPS) Analysis

Pouch cells and pouch bags containing positive electrodes were dissected inside an Ar-filled glovebox. The electrodes were rinsed with EMC, to remove dried electrolyte. The samples were transferred to ultra-high vacuum, without exposure to air, using a specially designed air-tight apparatus.[211] The samples were left under ultra-high vacuum for one night prior to their introduction to the analysis chamber, which was maintained at

a pressure below 2 x 10^{-9} mbar at all times. Analysis was performed with a SPECS spectrometer, equipped with a Phoibos hemispherical analyzer, using unmonochromatized Mg Kα radiation and a pass energy of 20 eV. Preliminary and final survey scans were compared to ensure that no photochemical degradation was induced during analysis. Calibration of the binding energy scale was deemed unnecessary, as all peak positions remained constant while the x-ray flux was varied, indicating the absence of charging effects. XPS spectra were fit with a non-linear Shirley-type background. This background was subtracted from the signal, to allow for qualitative comparison of atomic concentrations between samples, using relative peak height.

4.2   Results and Discussion

Figure 4.3 shows the gas evolution in pouch bags containing lithiated graphite electrodes which were taken from pouch cells with control electrolyte, control + 2% PES, control + 2% VC or control + 2% PBF. No volume changes were detected for these pouch bags during approximately 500 h of storage at 60°C. This suggests that parasitic reactions between the lithiated graphite and electrolyte do not contribute to gas generation when a cell is stored at 60°C or lower temperature. This is consistent with the results found by Kim et al [212].
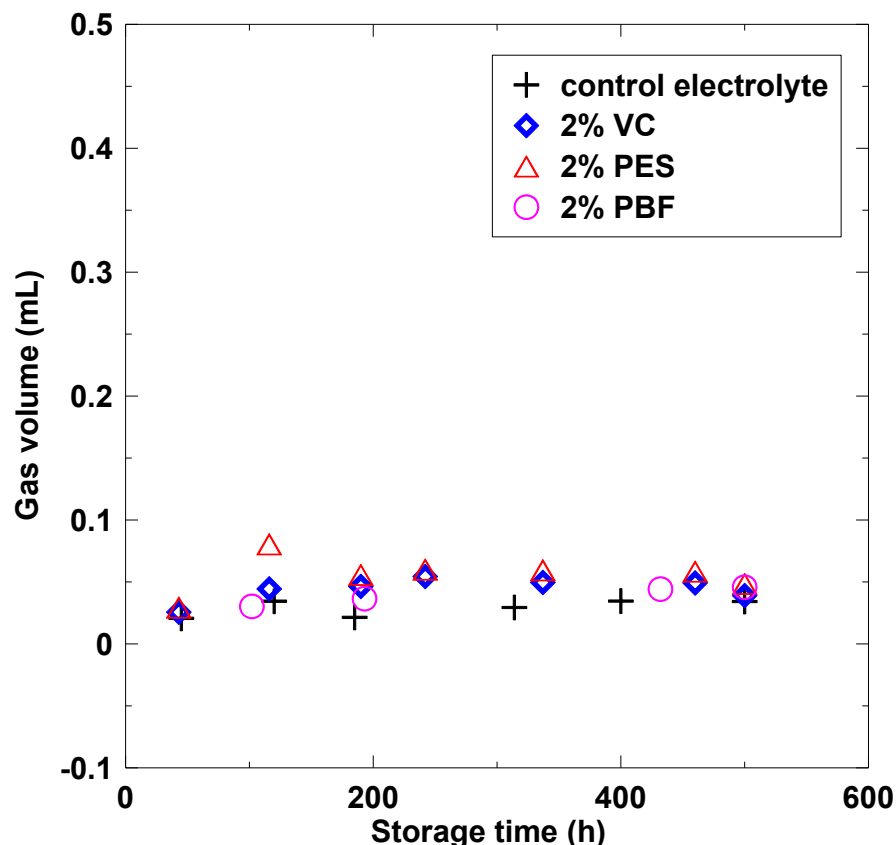
Figure 4.3 Gas volume versus time for pouch bags containing lithiated graphite electrodes taken from pouch cells with control electrolyte, control + 2% VC, control + 2% PES and control + 2% PBF. The storage was done at 60°C

Figure 4.4 shows the volume change versus time for pouch cells with control electrolyte, control + 2% VC, control + 2% PES or control + 2% PBF during the 500 h storage period at 60°C. Figure 4.4 also shows the volume change for pouch bags containing delithiated NMC442 positive electrodes taken from the brother pouch cells during the same storage period. Figure 4.4 shows that the gas volume of all the pouch cells and bags increased with time during storage, except for pouch cells with 2% PES or 2% PBF having an initial voltage of 4.2 V. Much more gas was generated in pouch bags with charged NMC442 than in charged pouch cells. Pouch bags containing the washed delithiated NMC442 electrode (DMC washing) + EC:EMC 3:7 produced a larger amount

of gas than those containing the delithiated NMC442 electrode without washing. This implies that the presence of $LiPF_6$ can slow gas generating reactions at the positive electrode. This may be due to the increased oxidative stability of the electrolyte when $LiPF_6$ is present.[213]

There was concern about the size of the error bars in Figure 4.4 for the pouch bags with control + 2% PES electrolyte. These error bars originate from measurements on at least three different pouch bags. EMC can be lost during pouch bag loading and sealing, due to its high vapor pressure. In order to understand the origin of the large error bars, different amounts of EMC were added to delithiated NMC442-containing pouch bags, to examine how the amount of added EMC affected gas evolution. Figure 4.5 shows the gas volume (mL) versus time for pouch bags with delithiated NMC442, taken from pouch cells with control electrolyte, having an initial voltage of 4.4 V. Prior to the pouch bag sealing, 0.0, 0.15 or 0.3 g EMC was added to the pouch bags. Figure 4.5 demonstrates that the rate of gas production has a strong inverse correlation to the added amount of EMC. When more EMC was added, less gas was produced. It appears that electrolytes with higher EC concentration generate more gas. In any event, the dependence of gassing on EMC content suggests a source for the error bars in Figure 4.5. For example, the large error bars for pouch bags containing 2% PES may be due to small differences in the actual amount of EMC added to the pouch bags.
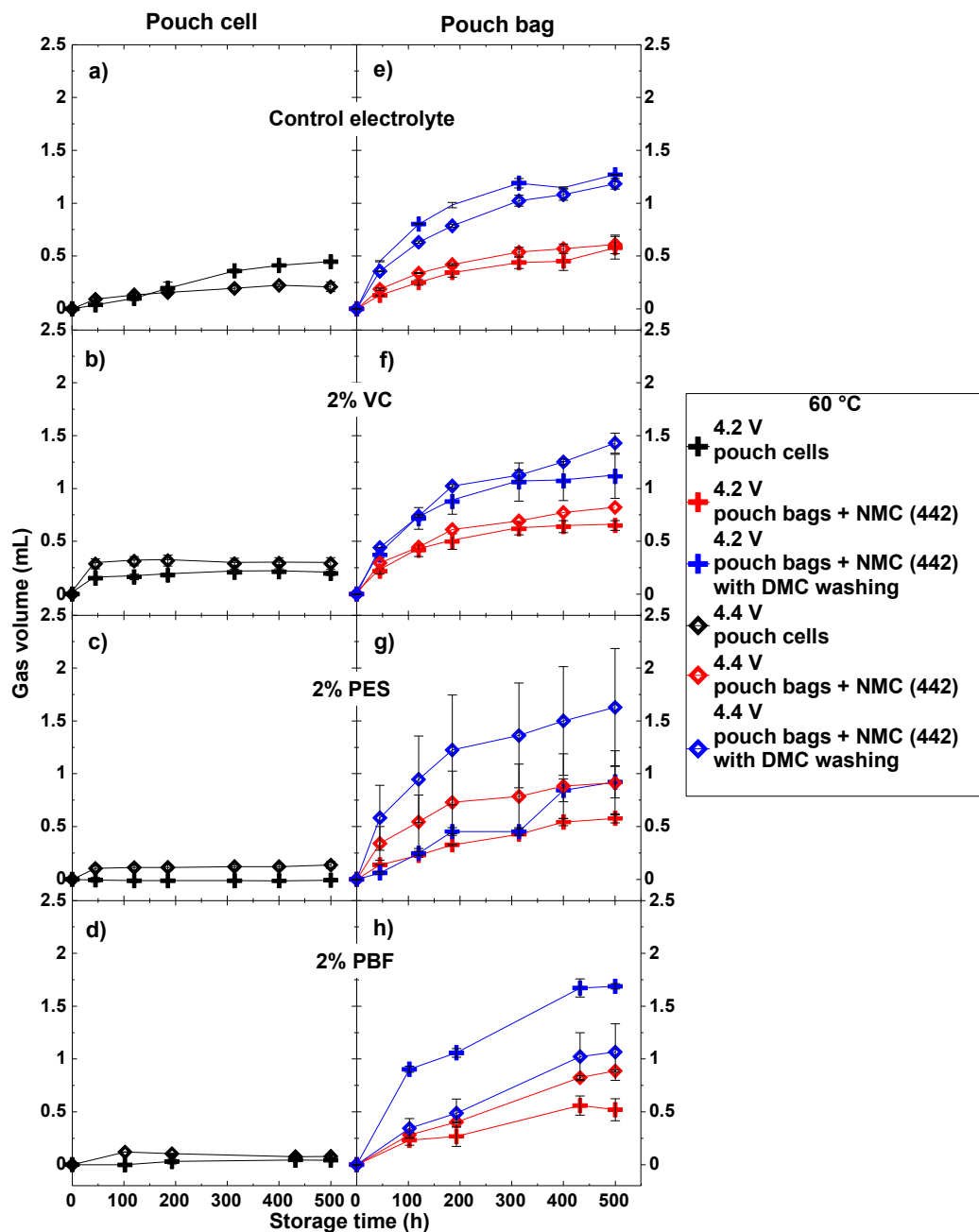
Figure 4.4 Gas volume versus time for pouch cells having an initial voltage of 4.2 V and 4.4 V, pouch bags containing the delithiated NMC442 electrode taken from pouch cells having an initial voltage of 4.2 V and 4.4 V and pouch bags containing the delithiated NMC442 plus solvent (after DMC washing) taken from pouch cells having an initial voltage of 4.2 V and 4.4 V with control electrolyte (a, e), control + 2% VC (b, f), control + 2% PES (c, g) and control + 2% PBF (d, h). The storage was done at 60°C.
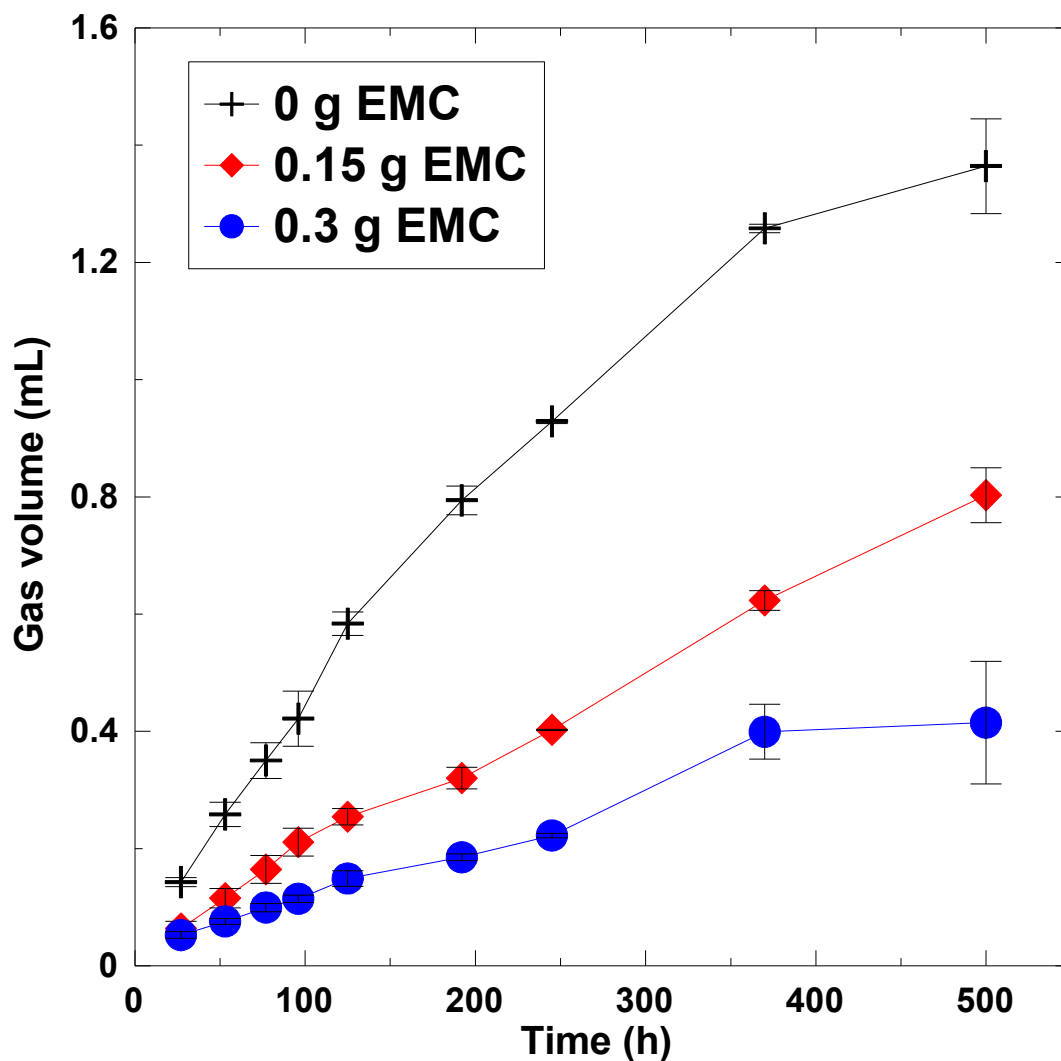
Figure 4.5 Gas volume versus time for pouch bags containing delithiated NMC442 electrodes taken from pouch cells having an initial voltage of 4.4 V with 0 g EMC, 0.15 g EMC and 0.3 g EMC added. The storage was done at 60°C.

Figures A1, A2 and A3 show chromatograms of the major gaseous products from NMC442/graphite pouch cells and pouch bags that contained charged NMC442 electrodes with control electrolyte, control + 2% VC, control + 2% PES and control + 2% PBF. A logarithmic scale on the y-axis is used for clarity. DMC and DEC come from the trans-esterification of EMC.[214] [114] In full cells with control electrolyte, the main gaseous products include $CH_2=CH_2$, CH_3CH_3, CH_3OCH_3 and $CH_3OCH_2CH_3$. These compounds

are very similar to the ones found in NMC(111)/graphite cells formed to 3.5 V as introduced by Petibon et al.[215] These compounds could be traced back to the reduction of both EC ($CH_2=CH_2$), and reduction as well as nucleophilic substitution from reduction by-products of EMC (CH_3CH_3, CH_3OCH_3, $CH_3OCH_2CH_3$). A detailed reaction mechanism can be found in reference 5. The presence of these compounds could come from an incomplete degassing step or the continuous growth of the SEI at the negative electrode. However, CH_3OCH_3 and $CH_3OCH_2CH_3$ were not detected in full cells with control + 2%VC, control + 2% PES and control + PBF. This suggest that the addition of these additives forms a better SEI at the graphite electrode to suppress the formation of these chemicals. Fluorinated alkanes such as CH_3CH_2F were also detected in all the full cells with different electrolytes which indicates the participation of $LiPF_6$ in the oxidation mechanism of the electrolyte. Most of the gaseous products in the full cells could also be found in the corresponding pouch bags except for ethane (the main gaseous product in the full cells with control electrolyte). In the pouch bags containing the delithiated NMC442 electrodes, a significant amount of CO_2 was identified while almost no CO_2 was found in the pouch cells. This means that CO_2 has almost been consumed completely by the lithiated graphite in a full cell, which explains why pouch cells produced much less gas than the corresponding pouch bags with the positive electrode by itself. This suggests that this interaction between the positive electrode and negative electrode helps to limit gassing during high temperature operation.

71
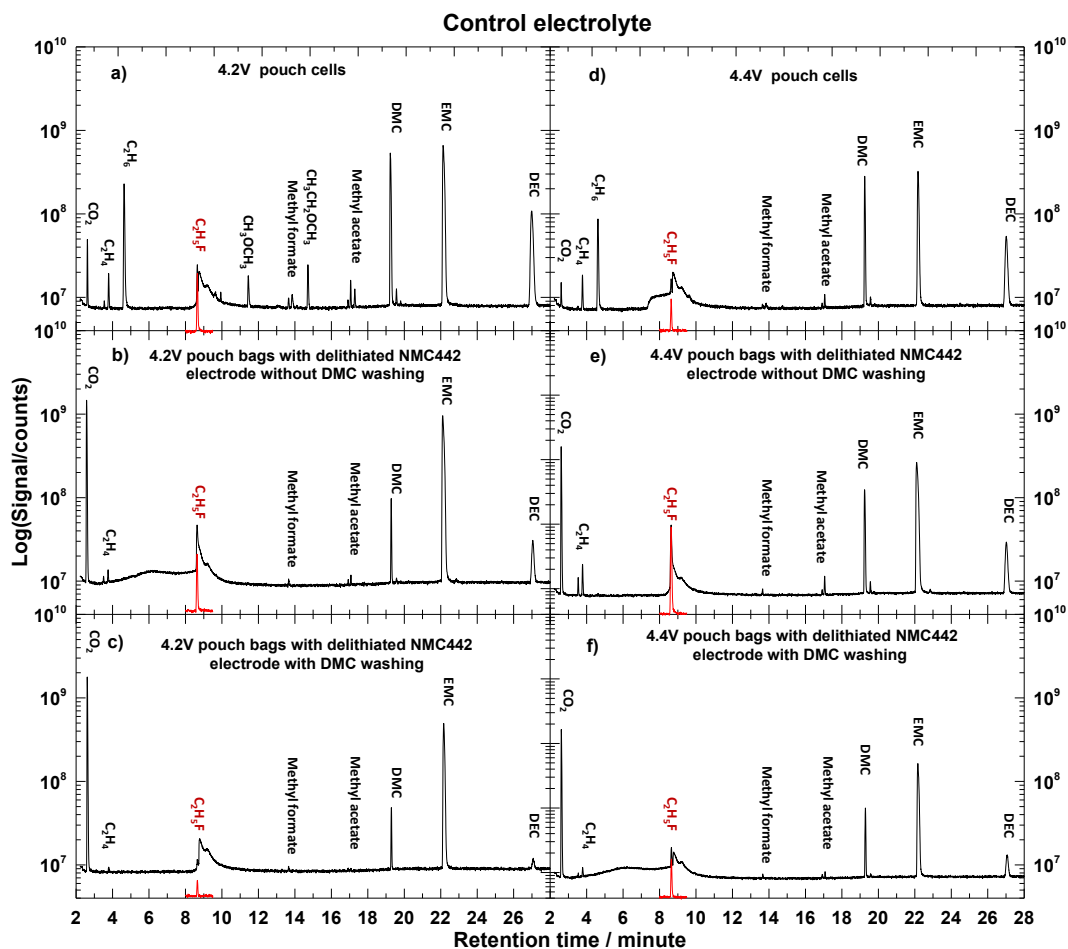
Figure 4.6 Chromatograms (total ion count), using a logarithmic scale, of the gaseous products extracted from pouch cells having an initial voltage of 4.2 V (a) and 4.4 V (d), pouch bags containing the delithiated NMC442 electrode taken from pouch cells having an initial voltage of 4.2 V (b) and 4.4 V (e), pouch bags containing the delithiated NMC442 electrode (with DMC washing) taken from pouch cells having initial voltage of 4.2 V (c) and 4.4 V (f). These pouch bags and pouch cells containing control electrolyte were stored at 60°C for approximately 500 h. The red peak shown in the Figure is assigned to CH_3CH_2F.

Sloop et al.[214] suggest a mechanism whereby CO_2 generated at the positive electrode diffuses to the negative electrode and reacts with intercalated lithium to form lithium oxalate. This formed lithium oxalate would decrease the lithium inventory and create irreversible capacity loss. Although lithium oxalate has limited solubility, Sloop et al. suggest the formed lithium oxalate can diffuse back to the positive electrode and be oxidized to CO_2 again with corresponding insertion of Li (as $Li^+ + e^-$) into the positive

72

electrode, causing self-discharge and reversible capacity loss. The lack of significant CO_2 found in the NMC442/graphite full cells compared to the pouch bags suggests that the recreation of CO_2 from lithium oxalate at the positive electrode must be very slow, compared to the rate of capture of CO_2 at the negative electrode under the conditions explored here

Figure 4.7 shows a summary of the amount of the total gas measured by Archimedes principle and the amount of CO_2 measured by the GC-MS method for these pouch cells and pouch bags. These pouch cells and pouch bags were stored at 60°C for 500 h and then at room temperature for two months. During the two month storage at room temperature, all the pouch cells shrank while the pouch bags did not shrink. This further shows that gaseous products generated at the positive electrode can be removed by the negative electrode. Figure 4.7 shows that the volume of CO_2 measured by the GC-MS method in these pouch bags exceeded the total gas volume measured by Archimedes principle. The volume of CO_2 measured by the GC-MS method is larger than that measured by Archimedes principle since some CO_2 was dissolved in the electrolyte[216]. This indicates that the majority of gas in these pouch bags is CO_2. This may also suggest that the addition of additives does not greatly suppress the reactions leading to a large amount of CO_2 generated in pouch bags. However, almost no or a small amount of CO_2 was found in pouch cells. These results indicate that CO_2 has been almost consumed by the lithiated graphite in full cells, explaining why the pouch cells produced much less gas than the corresponding pouch bag
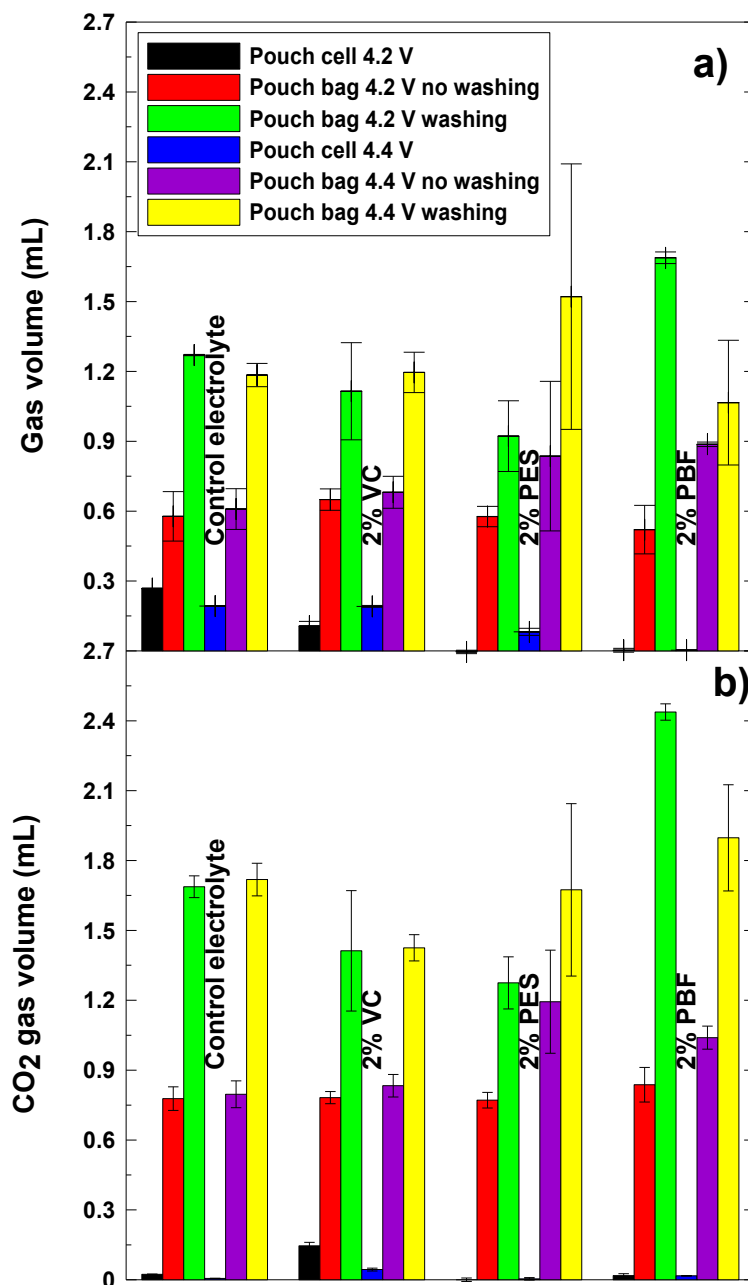
Figure 4.7 Final gas volume measured by Archimedes principle (a) and the volume of CO_2 measured by GC-MS method (b) for pouch cells and pouch bags with control electrolyte, control + 2% VC, control + 2% PES and control + 2% PBF after 500 h storage at 60°C and a two month storage at room temperature

In order to investigate how additives affect CO_2 consumption in a pouch cell, pouch bags containing lithiated graphite electrodes taken from pouch cells with different additives + intentionally added CO_2 were made. The amount of CO_2 initially added to

the pouch bags was targeted to be greater than 5 mL. According to the Henry's law constant for CO_2 in 1M $LiPF_6$ in EC/DMC (1:1 w/w) at 25°C and 1 atm measured by Dougassa et al,[216] approximately 1 mL of CO_2 can be dissolved in the electrolyte in the pouch bags. This gas dissolves rapidly once the pouch bags are filled. After that, changes in the volume of the pouch bag correspond to CO_2 that has been consumed by the lithiated graphite. Figure 4.8 shows the consumption of CO_2 vs. time for pouch bags containing a lithiated graphite electrode and added CO_2. A control sample containing EC/EMC solvent plus added CO_2 was also measured and is included in the Figure for comparison. Figure 4.8 shows that the volume of CO_2 in the pouch bag without a lithiated graphite electrode does not change significantly. This suggests that if the volume of the pouch bags with lithiated graphite and added CO_2 changes, this change is due to CO_2 consumption rather than CO_2 dissolution in electrolyte. For each curve in Figure 4.8, the average of two or three measurements on separate pouch bags were made and averaged.

Figure 4.8 shows that the addition of additives affects the rate at which CO_2 is consumed. PES-containing pouch bags shrank by approximately 2 mL. This was about twice the volume change for the other pouch bags. Therefore PES may be effective in suppressing gassing in pouch cells at high temperature because it accelerates the consumption of CO_2 at the negative electrode. The data presented in this chapter suggest that PES may not suppress gassing at high temperature at the positive electrode, but instead, suppresses the generation of ethane and accelerates CO_2 consumption at the negative electrode. Figure 4.8 shows that VC-containing pouch bags consumed CO_2 at the lowest rate compared to the other pouch bags. Figure 4.7 shows that the volume of

CO_2 for pouch cells with 2% VC at 4.2 V is larger compared to the other pouch cells at 4.2 V. These results suggest that even though VC can suppress the generation of ethane, VC slows down the CO_2 consumption at the negative electrode, resulting in increased amounts of gas in pouch cells at 4.2 V at high temperature as shown in Figure 4.4. However, the reader is cautioned that many more repeated experiments under a variety of conditions would be required to have full confidence in these statements.
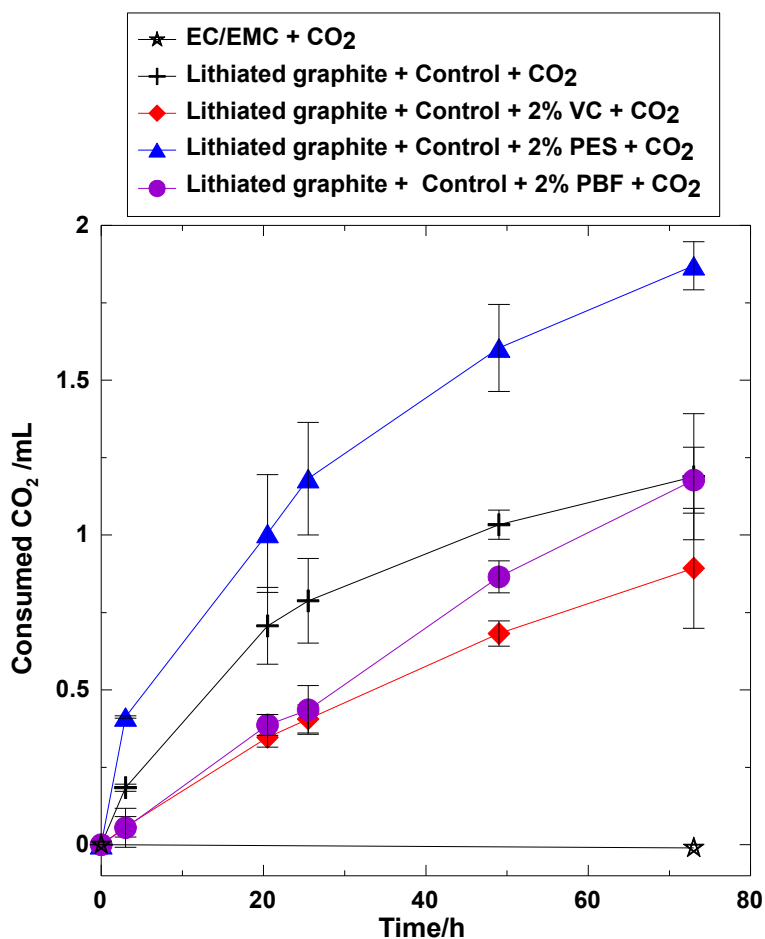
Figure 4.8 The volume change of CO_2 vs time for pouch bags containing EC/EMC solvent + intentionally added CO_2 and pouch bags containing intentionally added CO_2 + lithiated graphite electrodes taken from pouch cells with control, control + 2% VC, control + 2% PES and control + 2% PBF. The storage for lithiated graphite-containing pouch bags was done at 60 °C.

Figures 4.9, A4, A5 and A6 show the area-specific Nyquist plots of positive electrode symmetric cells reconstructed from NMC442/graphite pouch cells and NMC442-containing pouch bags with control, control + 2% VC, 2% PBF, 2% TAP stored at 40°C and 60°C. The first semicircle (high frequency) is due to the contact resistance between the double sided electrodes and the coin cell case.[111] The diameter of the second semicircle (low frequency) corresponds to twice the charge transfer impedance, R_{ct}, which is an important factor that affects cell performance. Its value is equal to $2R_{ct}$ since there are two identical positive electrodes in the symmetrical cells. Figure 4.10 shows a summary of the average values of R_{ct} measured for the electrodes taken from pouch bags and pouch cells. Figure 4.10 shows that positive electrodes taken from pouch bags have larger impedance than electrodes taken from pouch cells especially at 60°C
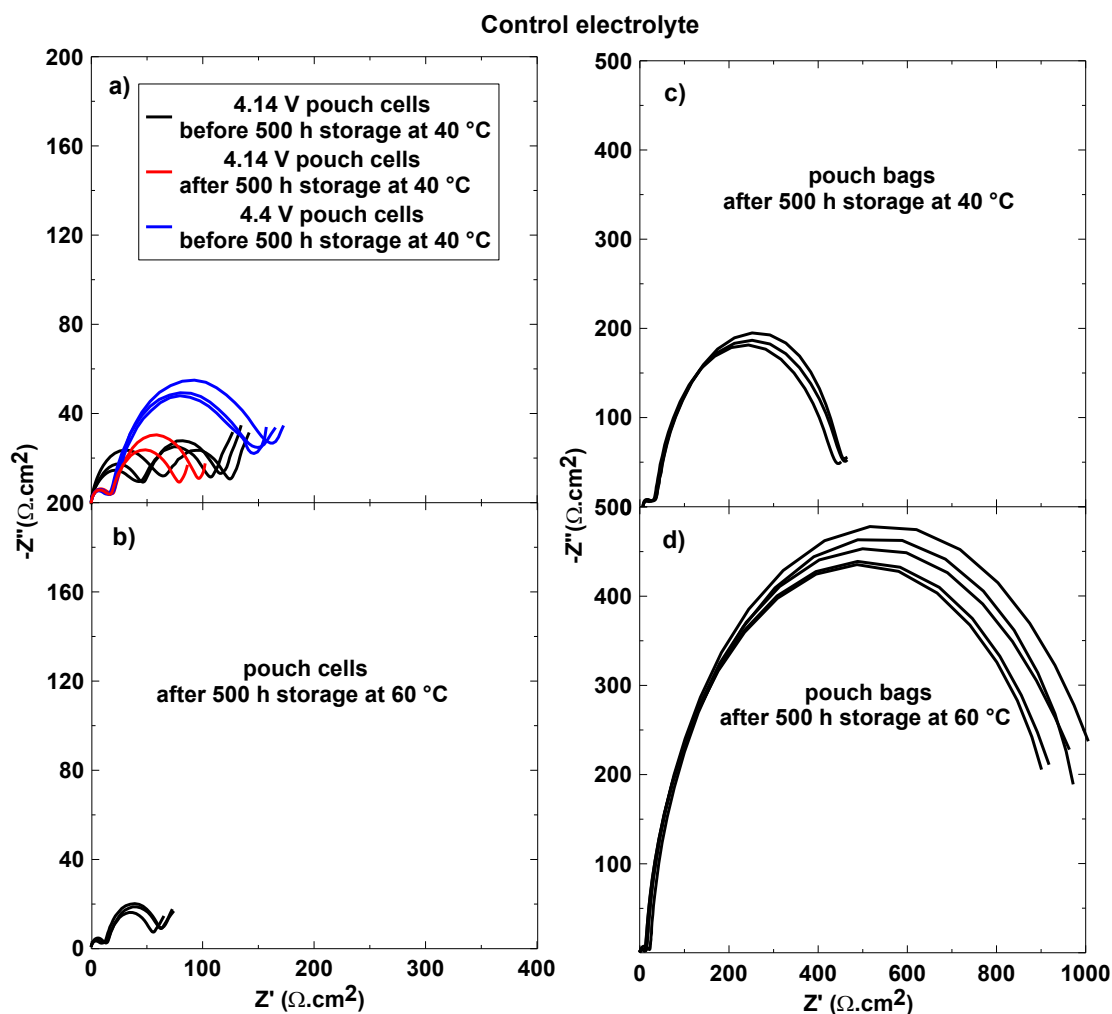
Figure 4.9 The area-specific Nyquist plots of positive electrode symmetric cells made from NMC442/graphite pouch cells at 4.14 V with control electrolyte after 500 hours of storage at 40°C (a) and 60°C (b) and from charged NMC442 electrodes taken from pouch bags with the same electrolyte after 500 hours of storage at 40°C (c) and 60°C (d).

Nelson et al. found that R_{ct} changes quasi-reversibly at high voltage in NMC442/graphite pouch cells containing EC-based electrolytes which shows that R_{ct} of the positive electrode varies with different potential (vs Li/Li$^+$) for EC-based electrolytes. [15] Therefore, it is important to compare the impedance of the positive electrode at the same potential vs Li/Li$^+$. After 500 h of storage at 40°C, the potential of pouch cells with control, control + 2% VC, 2% PBF and 2% TAP dropped from 4.4 V to 4.24, 4.25, 4.265

and 4.28 V, respectively, as shown in Figures 4.12, A7, A8 and A9. In order to gain more insight about how R_{ct} of the positive electrode changes before storage and after storage, Nyquist plots of positive electrodes taken from pouch cells before storage at both 4.4 V and 4.24 V (in the case of cells with control electrolyte, and corresponding potentials for cells with different additives) are also included in these Figures for comparison. Figures 4.9, A4, A5 and A6 show that R_{ct} of positive electrodes taken from pouch cells after 500 h storage remain almost the same as before storage when the positive electrode stays the same potential vs Li/Li$^+$.
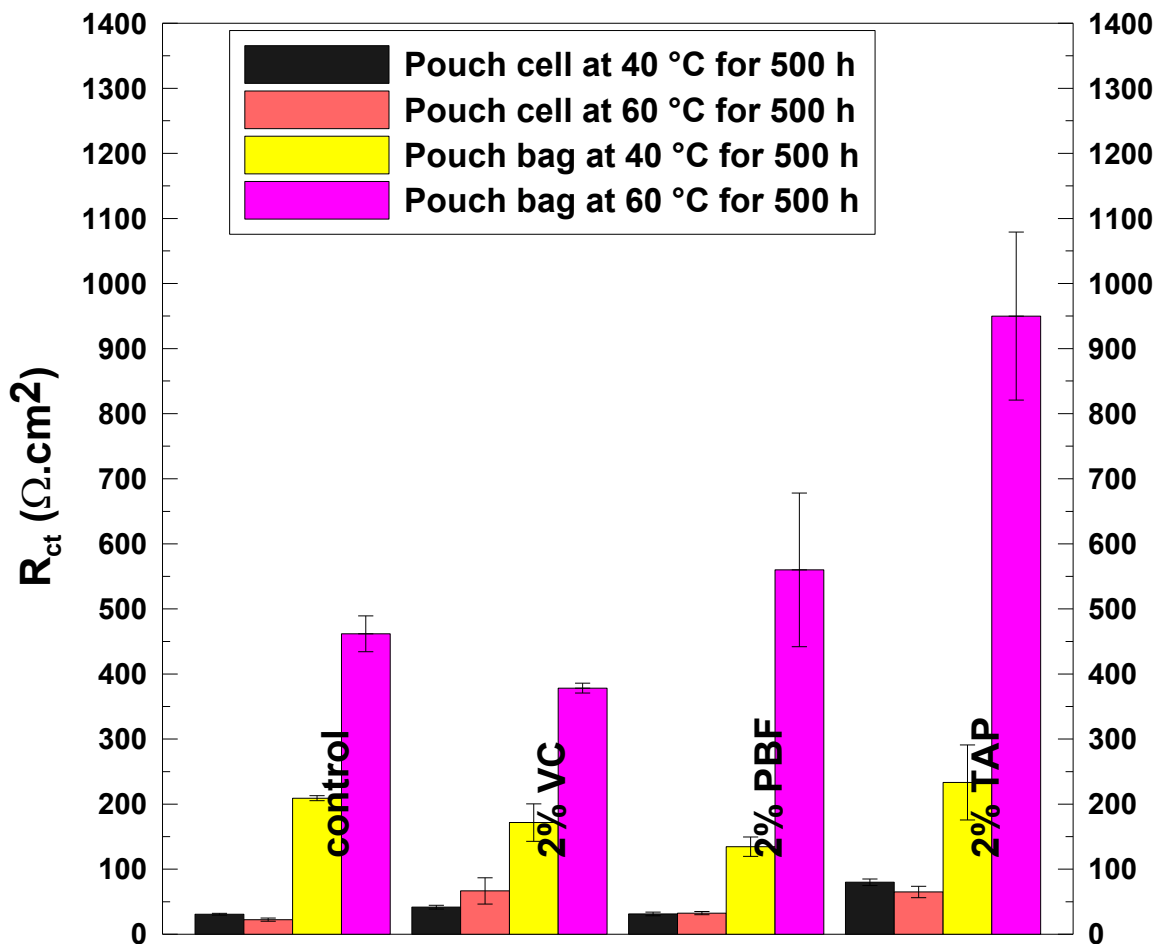
Figure 4.10 A summary of R_{ct} of the positive electrodes taken from pouch cells and pouch bags with different electrolytes after 500 h storage at 40°C and 60°C.

Figure 4.10 clearly summarizes that fact that the impedance of the positive electrode grows more rapidly during high voltage storage in a pouch bag (no negative electrode present) than in a pouch cell where there is a negative electrode present. EC and EMC-based electrolyte can be oxidized as the voltage vs Li/Li$^+$ increases above 4.2 V. [10,217] The oxidized species generated at the positive electrode in pouch bags probably remain in the electrolyte while these species could be consumed by the lithiated graphite in the pouch cells. This suggests that the consumption of oxidized species by the lithiated graphite electrode is essential for maintaining reasonable impedance in full cells to be stored at high potential (4.4 or 4.5 V), or otherwise the oxidized species apparently react with the surface of the positive electrode material leading to a high impedance film.

In order to gain insight about how R_{ct} changes over time, positive electrode symmetrical cells were reconstructed from pouch cells and pouch bags with control + 2% PBF that had been stored for 80, 300 or 500 hours at 40 and 60°C. Figure 4.11 shows a summary of R_{ct} versus time for the positive electrodes taken from these pouch cells and pouch bags. Figure 4.11 shows that R_{ct} for positive electrodes taken from pouch cells remained constant over the 500 h storage period at both 40 and 60°C. However, R_{ct} of positive electrodes taken from pouch bags stored at 40°C increased greatly at the beginning, then remained unchanged after 300 hours of storage. R_{ct} of the positive electrode taken from pouch bags stored at 60°C increased significantly with time.
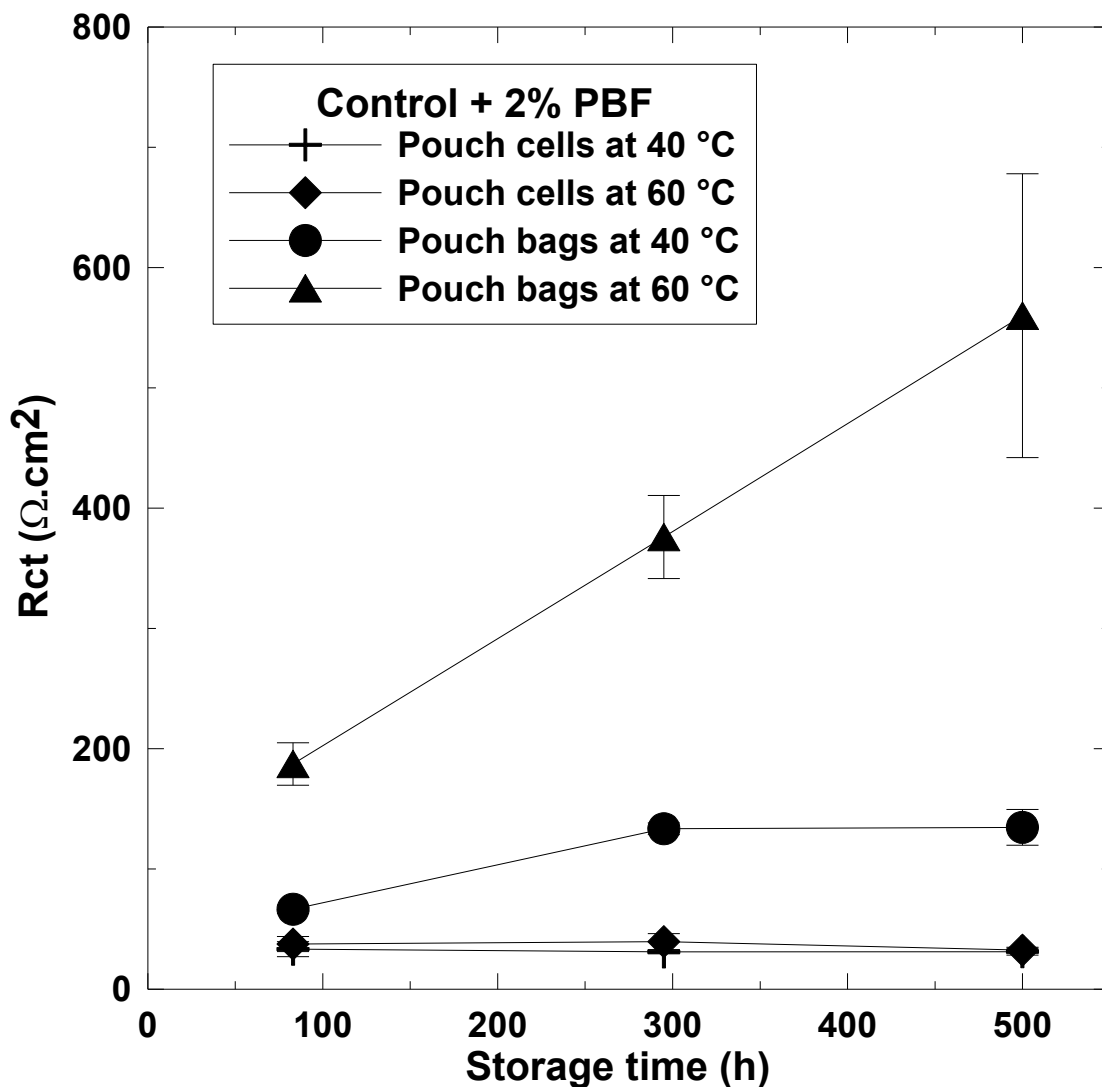
Figure 4.11 R_{ct} of positive electrode symmetric cells from NMC442/graphite pouch cells and pouch bags with control + 2% PBF plotted versus time during 500 h storage at 40°C and 60°C.

Figure 4.12 shows the potential versus time for NMC442/graphite pouch cells during storage at 40°C and at 60°C. These cells had control electrolyte. Also shown are data points collected for Li half cells constructed from electrodes recovered from the pouch bags and pouch cells at 89, 257 and 497 h at 40 °C, and 83, 275 and 490 h at 60 °C. The potential of the graphite electrode is about 0.089 ± 0.08 averaged over the six measurements shown. Therefore, a black, two-headed arrow, of length equal to 0.089 V

has been placed at different pouch cell potential-time curves. The potential of the half cells containing the NMC442 is expected to be the pouch cell potential plus the graphite potential. Figure 4.12 shows this is approximately true which suggests that no strange unexplained processes are occurring in the pouch bags, even though the potential of the positive electrode cannot be directly measured in the pouch bag during storage. It is interesting that the potential (vs Li/Li$^+$) of the electrodes in the pouch bags appears to be higher than in the pouch cells. The pouch cells were opened extremely carefully to avoid short circuit so this difference in the positive electrode potential could indicate less self-discharge for the electrodes stored in pouch bags where a negative electrode is not present. Figures A7, A8 and A9 show similar results for control + 2% VC, control + 2% PBF and control + 2% TAP, respectively. The potential of the positive electrode taken from the pouch bag (vs Li/Li$^+$) is always greater than that of the electrode taken from the pouch cell. The difference is very striking for cells and bags with control + 2% TAP at 60 °C. This is not understood at present, but is surely due to a negative electrode/positive electrode interaction which occurs in the pouch cell during storage.
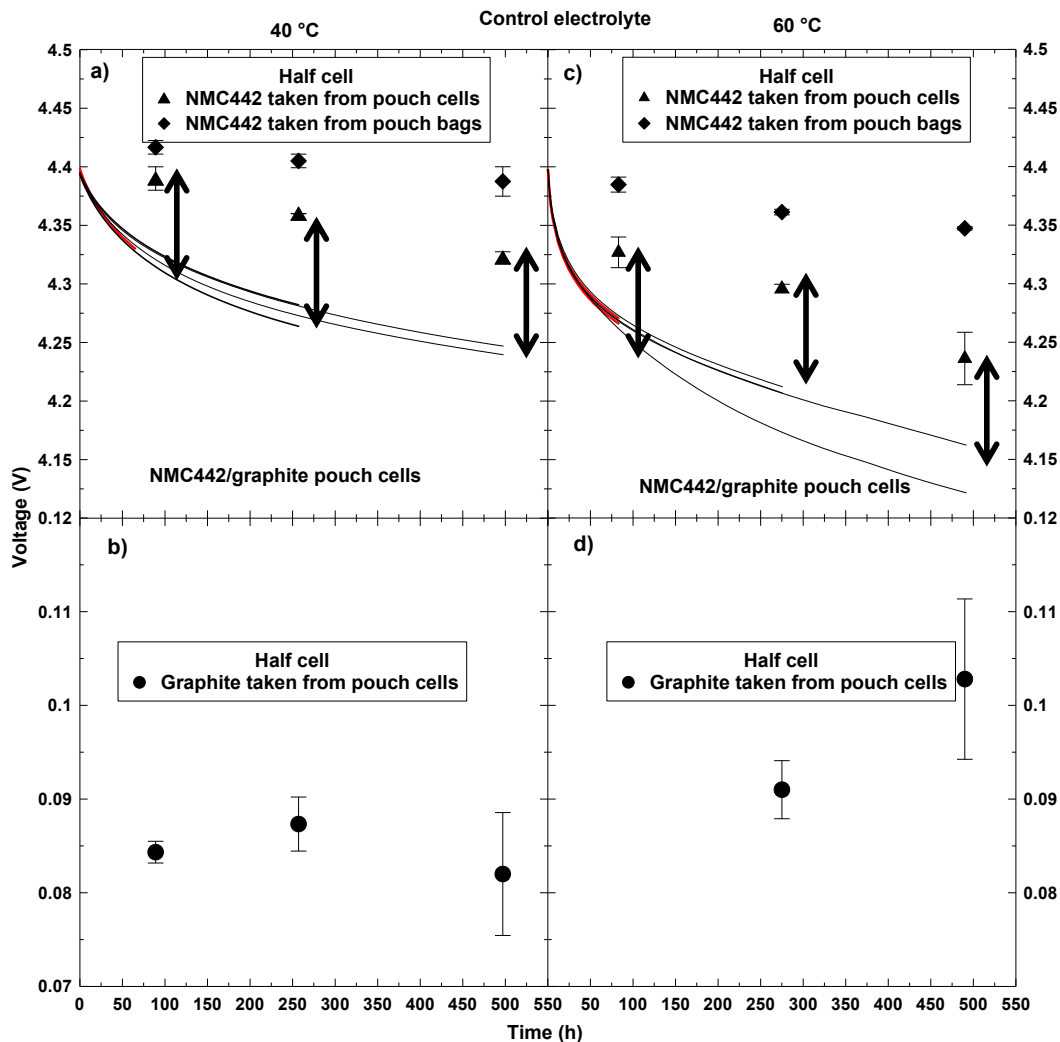
Figure 4.12 Open circuit voltage versus time for NMC442/graphite pouch cells with control electrolyte during storage at 40°C and 60°C, as well as Li/NMC442 (a, c) and Li/graphite (b, d) half cells where the electrodes were taken out of the pouch cells and pouch bags at the times indicated. The black arrows are 0.089 V long.

XPS was used to analyze the surfaces of the positive electrodes from pouch cells and pouch bags with control and control + 2% VC. Figure 4.13 shows the background-subtracted O1s spectra of positive electrodes aged in a) control electrolyte and b) control + 2% VC. In both cases, the trends are the same. The peak arising from the NMC lattice, at 529.5 eV, is larger for positive electrodes stored in bags than those stored in cells, suggesting, surprisingly, that the positive electrode SEI is **much thinner in the case of**

electrodes stored in bags. The peaks arising from SEI components containing ether and carbonyl-type environments, at 531.5 eV and 533.3 eV, are smaller for the positive electrodes stored in bags than those stored in cells. These observations indicate that the organic portion of the SEI covering the positive electrodes stored in bags is thinner than that in the SEI formed on positive electrodes stored in cells. This is surprising, as R_{ct} of positive electrodes stored in bags is much larger than those stored in cells. The thinned SEI of positive electrodes stored in bags gives evidence that a thin, non-organic, insulating phase is the dominant contributor to R_{ct} growth. This insulating phase may be the reduced layer of rocksalt structure transition metal oxide, described in several recent publications.[160,164,167] The C1s and F1s regions of the XPS spectra did not reveal significant chemical differences between positive electrodes stored in cells and bags, other than the thinning of the organic portion of the SEI
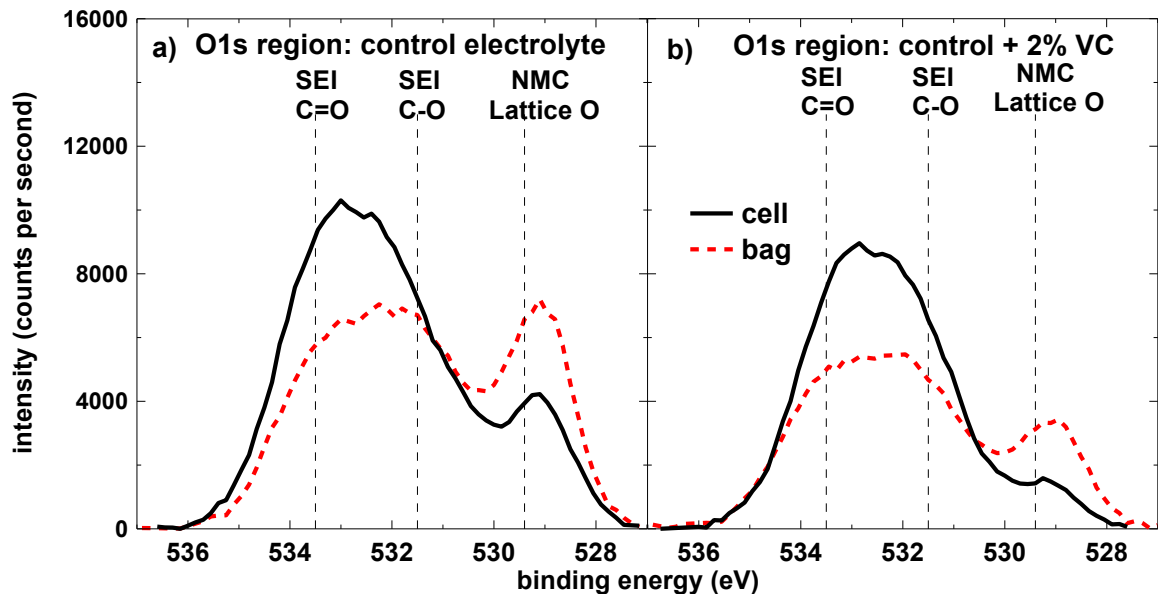
Figure 4.13 XPS O1s spectra of positive electrodes stored in cells (black) and in bags (red) with control electrolyte (a), control + 2% VC (b)
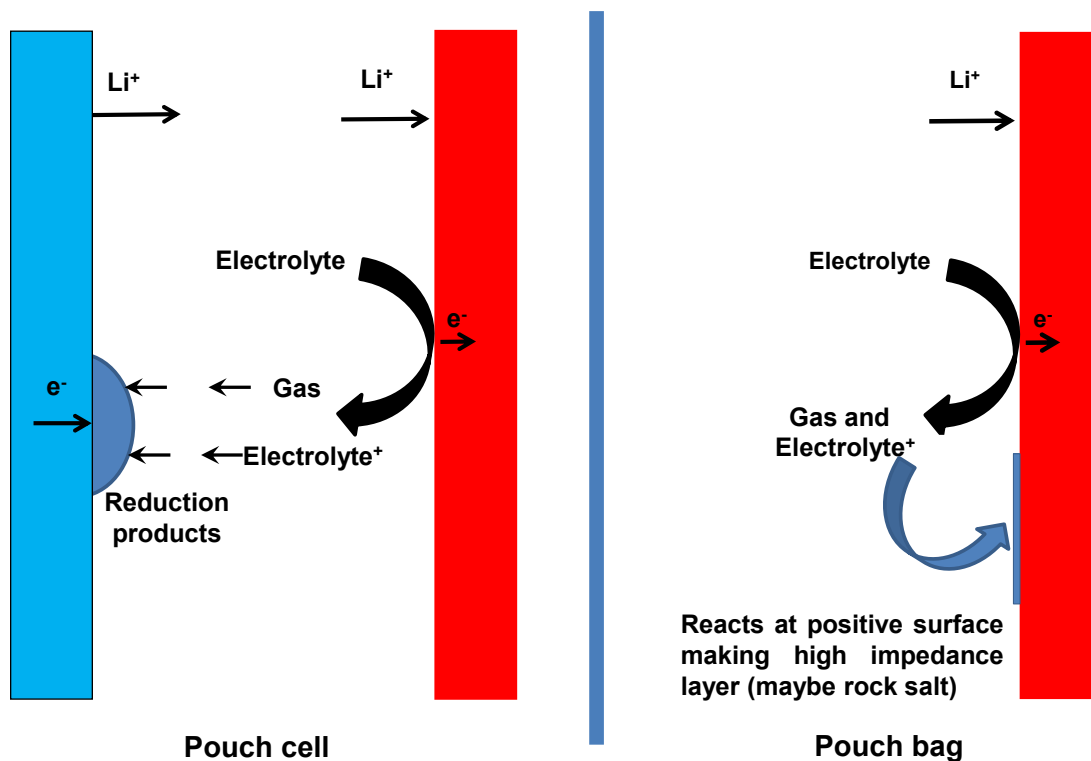
Figure 4.14 A schematic of the proposed parasitic side reactions occurring in a full cell and in a pouch bag only containing charged positive electrode and electrolyte.

Figure 4.14 shows a schematic of negative/positive electrode interactions suggested by the data presented here. In a pouch cell, electrolyte is oxidized at the positive electrode and gaseous or oxidized species as well as electrons are generated. The generated electrons combine with lithium ions and insert into the positive electrode. The released gaseous and oxidized species move to the negative electrode and are reduced there. This leads to lower cell volume increase and lower full cell impedance growth even though it can thicken the negative electrode SEI film leading to partial blocking of the path for lithium ions to insert into graphite[218]. In a pouch bag, generated gases such as CO_2 remain, other oxidized species accumulate and can react at the positive electrode again. This may produce a more resistive passivating film possibly a rock salt surface layer at

the positive electrode. These phenomena would explain the larger gas volume production and larger impedance in pouch bags compared to full pouch cells.

4.3   Summary of observations and concluding remarks

It is very useful to summarize the findings of this Chapter here:

1. NMC442 positive electrodes stored at 4.4 V at 60°C in pouch bags with electrolyte create more gas than the same electrodes stored with the same electrolyte in pouch cells. This suggests the negative electrode can consume some of the generated gas.

2. Most of the gas generated in the pouch bags during storage is CO_2 and, surprisingly, the presence of electrolyte additives known to improve high voltage storage and cycling do not affect the gas generation rate strongly.

3. CO_2 intentionally injected into pouch bags containing lithiated graphite is consumed over time.

4. NMC442 electrodes removed from pouch bags after storage at 4.4 V and elevated temperature have dramatically larger values of R_{ct} (at least double) than those removed from pouch cells.

5. Surprisingly, the positive electrode SEI is thinner (for all additives studied) on electrodes stored in pouch bags, even though their R_{ct} is much larger than electrodes extracted from pouch cells. This suggests the SEI is not thicker even though R_{ct} is larger and, instead, the surface of the NMC442 electrode may have been changed, perhaps to a rock-salt surface layer.

These observations underscore the complexity of the chemical and electrochemical reactions occurring in Li-ion cells charged to high potentials. There can be no doubt that the presence of the negative electrode "cleans" the electrolyte of harmful degradation products that otherwise adversely affect the positive electrode.

CHAPTER 5: STUDIES OF GAS GENERATION, GAS CONSUMPTION AND IMPEDANCE GROWTH IN LI-ION CELLS WITH CARBONATE OR FLUORINATED ELECTROLYTE USING THE POUCH BAG METHOD

In this chapter, the pouch cell and pouch bag method described in Chapter 4 is used to study the effect of a carbonate electrolyte containing a ternary electrolyte additive mixture and a fluorinated electrolyte on impedance growth of charged positive electrodes stored at elevated temperature. A gas chromatography method is used to identify gas compositions, including hydrogen and CO, to gain more insight about the interactions between the positive electrode and the negative electrode in the cells. The majority of this work was adapted from the following peer-reviewed article:

D.J. Xiong, L.D. Ellis, R. Petibon, T. Hynes, Q.Q. Liu, J.R. Dahn, Studies of Gas Generation, Gas Consumption and Impedance Growth in Li-Ion Cells with Carbonate or Fluorinated Electrolytes Using the Pouch Bag Method, J. Electrochem. Soc. 164 (2017) A340–A347. doi:10.1149/2.1091702jes.

Deijun Xiong prepared the pouch cells and pouch bags and also prepared the materials for the XPS studies. Toren Hynes and Qianqian Liu also prepared some cells for this study. Deijun Xiong performed the gas measurements, the impedance measurements and the electrode potential measurements. Deijun Xiong performed the GC-MS studies of gas compositions together with Remi Petibon. The XPS measurements and the analysis of

XPS spectra were performed by Leah Ellis. Deijun Xiong prepared all the figures expect for Figure 5.9 (prepared by Leah Ellis). Jeff Dahn provided guidance and participated in experimental design and the interpretation of all the data. Deijun Xiong prepared the manuscript of the article mentioned above except for the XPS section and received revisions from Leah Ellis, Remi Petibon and Jeff Dahn.

5.1   Experimental

5.1.1   Pouch Cells and Pouch Bags

The NMC442/graphite pouch cells were prepared according to the method described in Section 3.1.5 and filled with 0.76 mL of 1M $LiPF_6$ in EC:EMC (3:7 by weight) (control electrolyte) + 2% PES + 2% DTD + 2% TTSPi (called PES222 here) or 0.76 mL of 1M $LiPF_6$ in TFEC and FEC (1:1 by weight) + 1% PES (called TFEC/FEC) in an argon-filled glove box and sealed in the same glove box under vacuum. The pouch cells then experienced the pre-cycling described in Section 4.1.1. Steps and a flow path of the process used to make and test pouch cells and pouch bags were also described in Section 4.1.1.

Four pouch cells either at 4.2 V or 4.4 V were used for head-to-head comparison in the gas evolution experiments in each case. Two pouch cells were moved to a 60°C temperature box for storage. The other two pouch cells were transferred to an Ar-filled glovebox and disassembled there. The delithiated NMC442 and lithiated graphite electrodes collected from the pouch cells were inserted into different pouch bags. In order to create a similar electrolyte environment in the pouch bags as the pouch cells, 0.15 g of EMC was added to the pouch bags containing charged electrodes taken from the pouch

cells with PES222 to compensate for EMC evaporation during handling while 0.2 g of TFEC was injected into pouch bags containing charged electrodes taken from the pouch cells with TFEC/FEC to compensate for TFEC evaporation during handling. These pouch bags were also moved to a 60°C temperature box for storage. The volume of the pouch bags and pouch cells during the 500 h storage period were measured from time to time, using the *ex situ* gas volume equipment described in Section 3.4.

Eight pouch cells at 4.4 V were used for the impedance studies in each case. Two pouch cells were moved a 40°C temperature box. Another two pouch cells were moved to a 60°C temperature box. The other four identical pouch cells were transferred to the glovebox and dissected there. The four delithiated NMC442 electrodes were inserted into pouch bags with 0.15 g of EMC for PES222 electrolyte and 0.2 g of TFEC for TFEC/FEC electrolyte. Two pouch bags were moved to a 40°C temperature box. The other two pouch bags were moved to a 60°C temperature box. All these pouch cells and pouch bags were stored for a 500 h storage period.

5.1.2   Analysis of the Gas Composition in NMC442/Graphite Pouch Cells and NMC442-containing Pouch Bags

After 500 h storage at 40 or 60°C, a gas chromatograph coupled to a thermal conductivity detector (GC-TCD) was used to analyze the gas compositions in the pouch cells and pouch bags. In some cases, only one pouch cell was analyzed. A gas extraction chamber described in Section 3.5.4 was used to extract the gasses from the pouch cells and pouch bags for quantitative analysis. The procedures for quantitative analysis of gas compositions produced in pouch cells and pouch bags can be found in Section 3.5.

5.1.3 Symmetric Cell and Half Cell Construction

After the 500 h storage period, the pouch cells and pouch bags were used to construct positive/positive symmetric cells and half cells according to the method described in Section 4.1.4. 1M LiPF$_6$ in EC/EMC (3:7 w/w) was used in the half cells and symmetric cells where electrodes were taken from pouch cells and pouch bags with PES222 while 1M LiPF$_6$ in TFEC/EC (1:1 w/w) was used in the half cells and symmetric cells where electrodes were taken from pouch cells and pouch bags containing TFEC/FEC. The potential of the assembled coin half cells and AC impedance spectra of the assembled symmetric cells were measured according to the method described in Section 4.1.4.

5.1.4 XPS Analysis

The details in XPS method can be found in Section 4.1.5.

5.2 Results and Discussion

Figure 5.1 shows the gas volume vs time in the pouch cells and pouch bags with PES222 or TFEC/FEC electrolyte during the 500 h storage period at 60°C. No volume changes were detected for pouch bags containing lithiated graphite electrodes during the storage period at 60°C, which is consistent with previous results described in Chapter 4. Pouch bags with delithiated NMC442 taken from pouch cells with PES222 produced much more gas than the corresponding pouch cells while pouch bags with delithiated NMC442 taken from pouch cells with TFEC/FEC produced less gas during the first 300 h. The large error bars for the gas volume in pouch bags with TFEC/FEC electrolyte after approximately 300 h are based on 2 pair bag measurements and arise from an unknown cause.
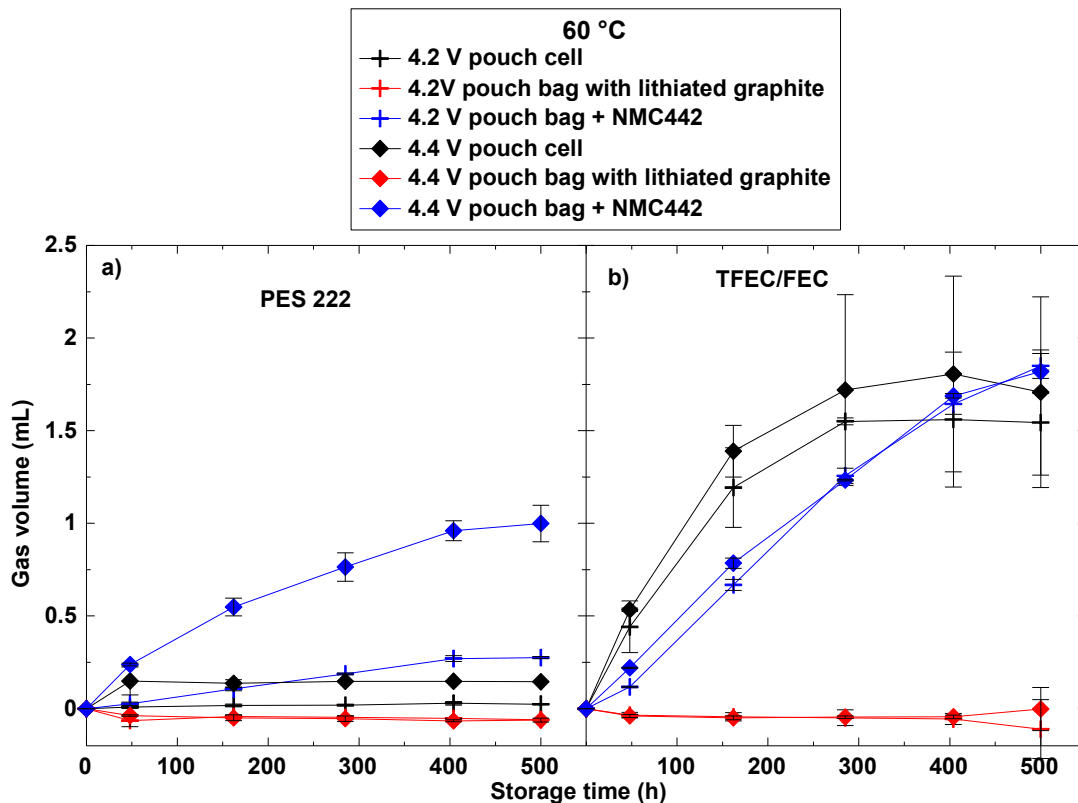
Figure 5.1 Gas volume versus time for pouch cells with PES222 or TFEC/FEC and the corresponding pouch bags containing either lithiated graphite or delithiated NMC442. These pouch cells and pouch bags were stored at 60 °C.

Figure 5.2 shows the gas compositions in the pouch cells and pouch bags determined using the GC-TCD method. Figure 5.2 shows that there is almost no CO_2 left in the pouch cells with PES222 while there is still a significant amount of CO_2 found in the pouch cells with TFEC/FEC. This suggests that the modified SEI at the graphite electrode in pouch cells with TFEC/FEC suppresses CO_2 reduction at the graphite electrode and its removal from the gas. Interestingly, hydrogen was only found in pouch cells and not in pouch bags. This suggests that the generation of hydrogen is through species created at the positive electrode which travel to the negative electrode, react and produce hydrogen there.[23,24] Figure 5.3 shows possible pathways where hydrogen can be generated from the interactions in pouch cells with carbonate electrolyte.[23,24,97] Figure 5.2 shows that there is

much more hydrogen generated in pouch cells with TFEC/FEC than in pouch cells with PES222. This explains why fluorinated electrolytes can cause severe gassing problems when used in Li-ion cells operated at elevated temperatures.
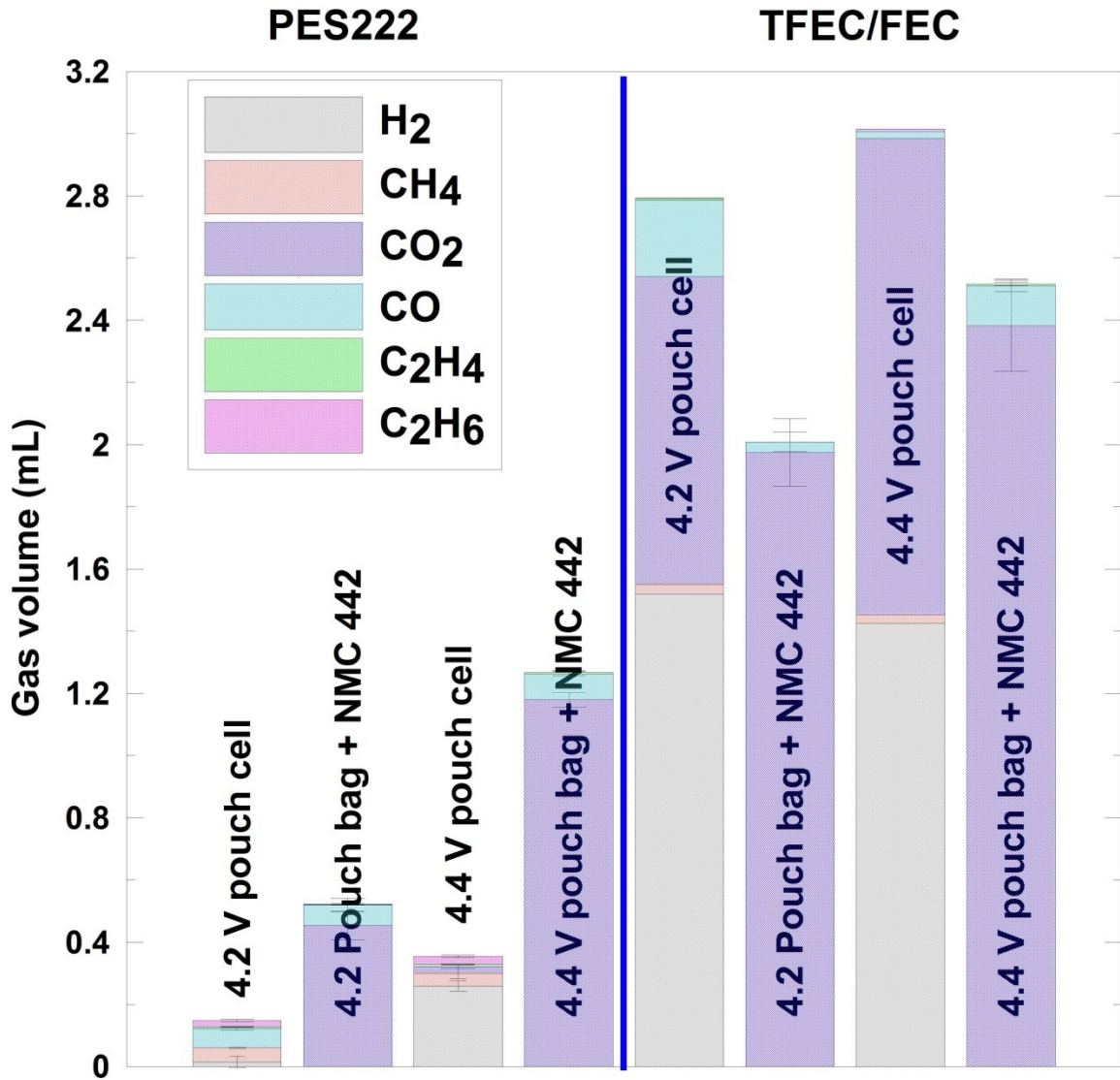
Figure 5.2 Gas compositions measured using the GC-TCD method for pouch cells and pouch bags containing charged electrodes, PES222 or TFEC/FEC.
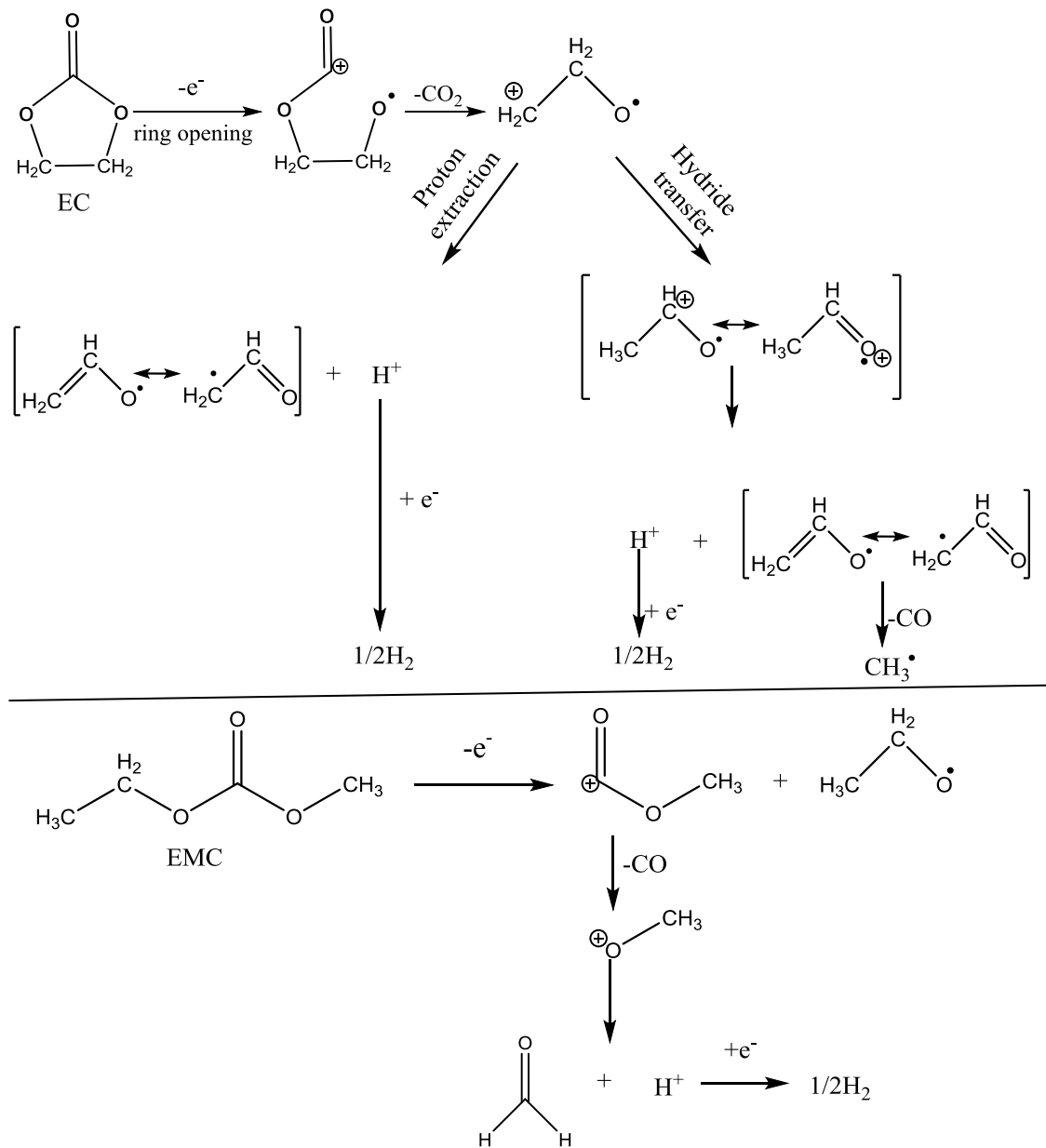
Figure 5.3 The possible pathways to generate hydrogen in pouch cells containing EC and/or EMC. [23,24,97]

Figure 5.4 shows the gas volume in the pouch cells and pouch bags measured by GC-TCD and also by Archimedes principle. Figure 5.4 shows that gas volume measured by GC-TCD is consistently larger than that measured by Archimedes principle. This is

expected since gaseous products can be dissolved in the electrolyte in the cells and bags according to Henry's law [216,219]

Figures 5.5a, 5.5b, 5.6a and 5.6b show the area-specific Nyquist plot of positive electrode symmetric cells reconstructed from NMC442/graphite pouch cells with PES222 or TFEC/FEC, respectively. Nelson et al. discovered that R_{ct} changed quasi-reversibly at high voltage in NMC442/graphite pouch cells containing EC-based electrolytes which shows that R_{ct} of the positive electrode varies with potential (vs Li/Li$^+$) in EC-based electrolytes. [15] However, Xia et al. found that R_{ct} did not change over the voltage range (3.8-4.5 V) in NMC442/graphite pouch cells containing fluorinated electrolyte indicating that R_{ct} of the positive electrode does not vary strongly with potential (vs Li/Li$^+$) in the TFEC/FEC electrolyte.[45] One must compare the impedance of the positive electrode at the same potential vs Li/Li$^+$ in EC-based electrolyte but there is no need to compare the impedance of the positive electrode at exactly the same potential vs Li/Li$^+$ in fluorinated electrolyte. After 500 h of storage at 40°C, the potential of pouch cells with control + PES222 dropped from 4.40 to 4.27 V, as shown in Figure B1. Therefore, Nyquist plots of positive electrodes taken from pouch cells with control + PES222 before storage at both 4.4 V and 4.27 V are also included in Figures 5.5 for comparison. Figure B2 shows the potential versus time of pouch cells containing TFEC/FEC electrolyte during storage for completeness.
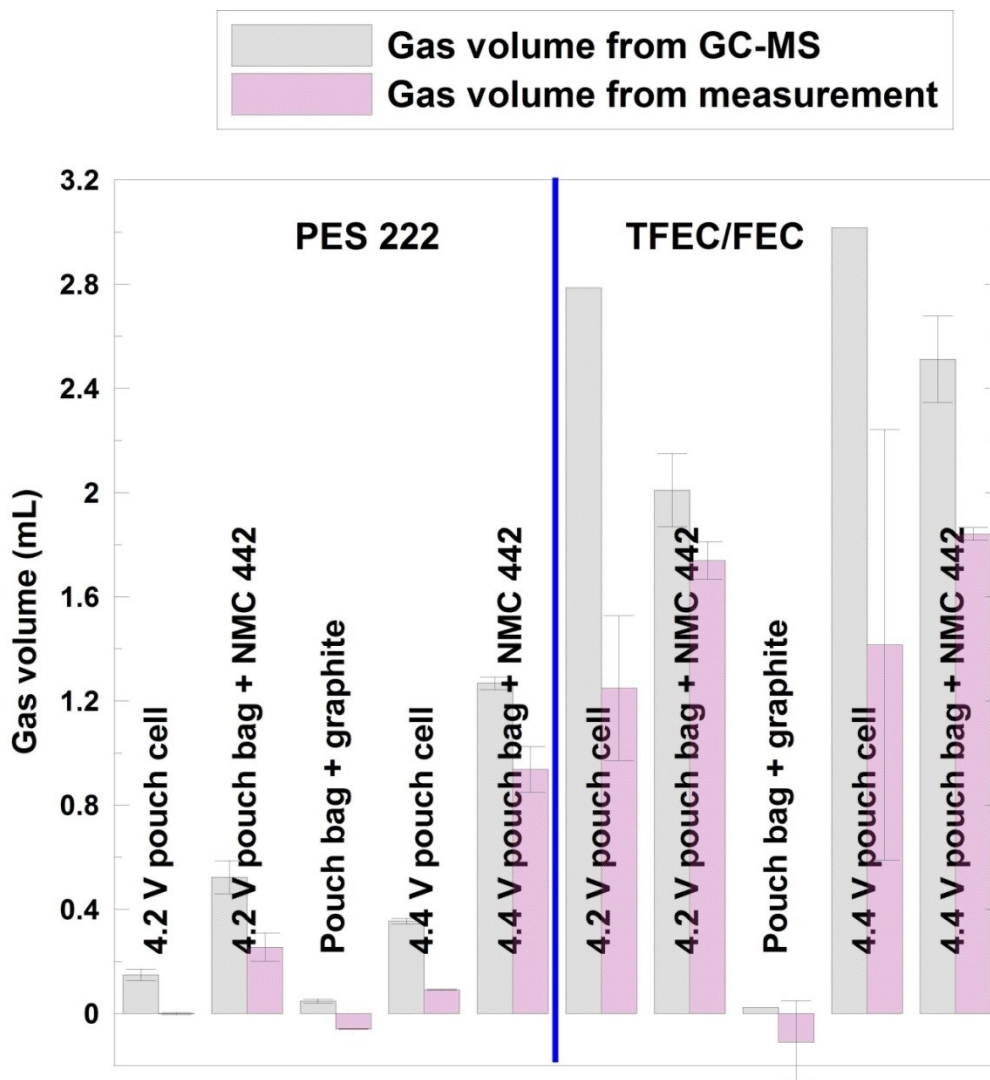
Figure 5.4 Gas volume measured after the storage period (500 h at 60°C) using GC-TCD and also using Archimedes principles for the pouch cells and pouch bags studied here

Figures 5.5 and 5.6 show that R_{ct} of the positive electrode in pouch cells does not change significantly as the storage temperature increases from 40°C to 60°C. Figure 5.5 shows that R_{ct} of positive electrodes taken from pouch bags is larger than that of positive electrodes taken from pouch cells with PES222, especially at 60°C. This is consistent with the results described in Chapter 4. This suggests that the addition of PES222 does not suppress the oxidized species from reacting with the charged positive electrode

material leading to a large increase in impedance. Figure 5.6 shows that R_{ct} of positive electrodes taken from pouch bags with TFEC/FEC is slightly larger compared to R_{ct} of positive electrodes taken from pouch cells with TFEC/FEC. Figures 5.5d and 5.6d show that R_{ct} of the electrodes stored at 60°C in pouch bags with PES222 is about an order of magnitude larger than those of electrodes stored with TFEC/FEC. This suggests that either the oxidized species from TFEC/FEC do not react with the positive electrode or that the passivating layer resulting from TFEC/FEC can prevent the oxidized species from reacting with the positive electrode resulting in less impedance growth for charged positive electrodes in contact with TFEC/FEC.
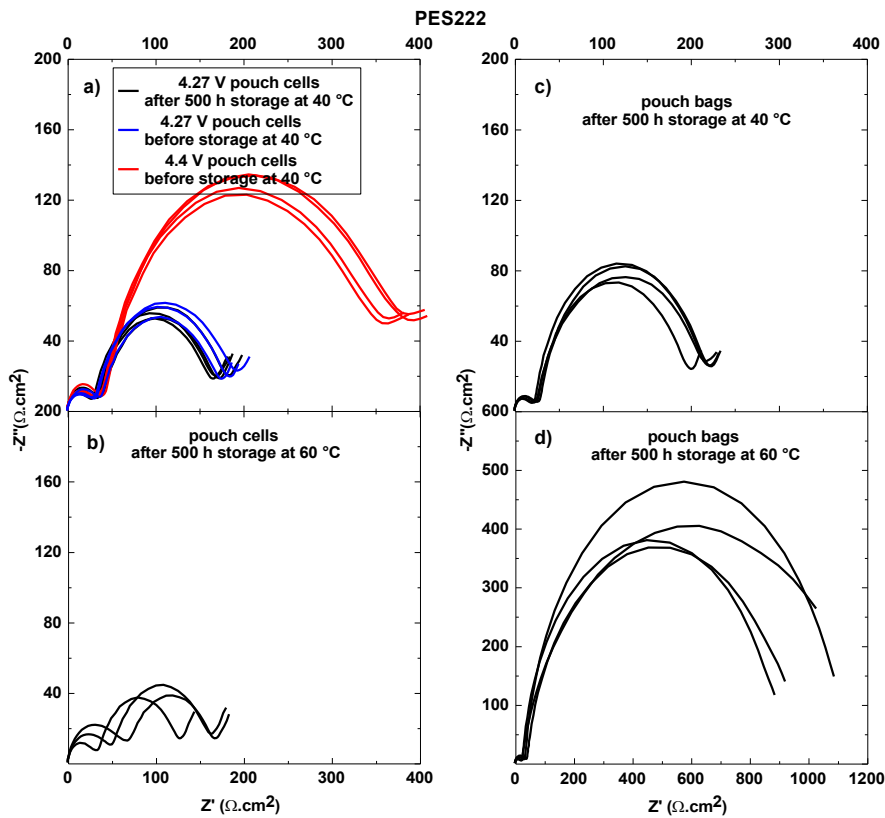
Figure 5.5 Area-specific Nyquist plots of positive electrode symmetric cells where the electrodes were taken from NMC442/graphite pouch cells with PES222 after 500 h storage at 40°C (a) and 60°C (b) and from charged NMC442-containing pouch bags with PES222 after 500 h storage at 40°C (c) and 60°C (d)

Figure 5.6 Area-specific Nyquist plot of positive electrode symmetric cells where the electrodes were taken from NMC442/graphite pouch cells with TFEC/FEC after 500 h storage at 40°C (a) and 60°C (b) and from charged NMC442-containing pouch bags with TFEC/FEC after 500 h storage at 40°C (c) and 60°C (d)

Figures 5.7 and 5.8 show the area-specific Nyquist plots of lithiated graphite electrode symmetric cells reconstructed from NMC442/graphite pouch cells and pouch bags stored with PES222 or TFEC/FEC, respectively. Figures 5.7 and 5.8 show that R_{ct} of the lithiated graphite electrodes harvested from the pouch cells is roughly the same as those from pouch bags. However, R_{ct} of the lithiated graphite electrodes harvested from pouch cells and pouch bags with TFEC/FEC (Figure 5.8) is much larger compared to R_{ct} of the lithiated graphite electrodes taken from pouch cells and pouch bags with PES222 (Figure 5.7). Large impedance at the graphite electrode is not desirable for high rate and low

temperature applications. This suggests that TFEC/FEC will not be a good choice for Li-ion cells which need to operate at high rates and low temperature.

PES222

Figure 5.7 Area-specific Nyquist plot of lithiated graphite electrode symmetric cells where the electrodes were taken from NMC442/graphite pouch cells with PES222 after 500 storage at 40 °C (a) and 60 °C (b) and from the corresponding pouch bags after 500 h storage at 40 °C (c) and 60 °C (d)
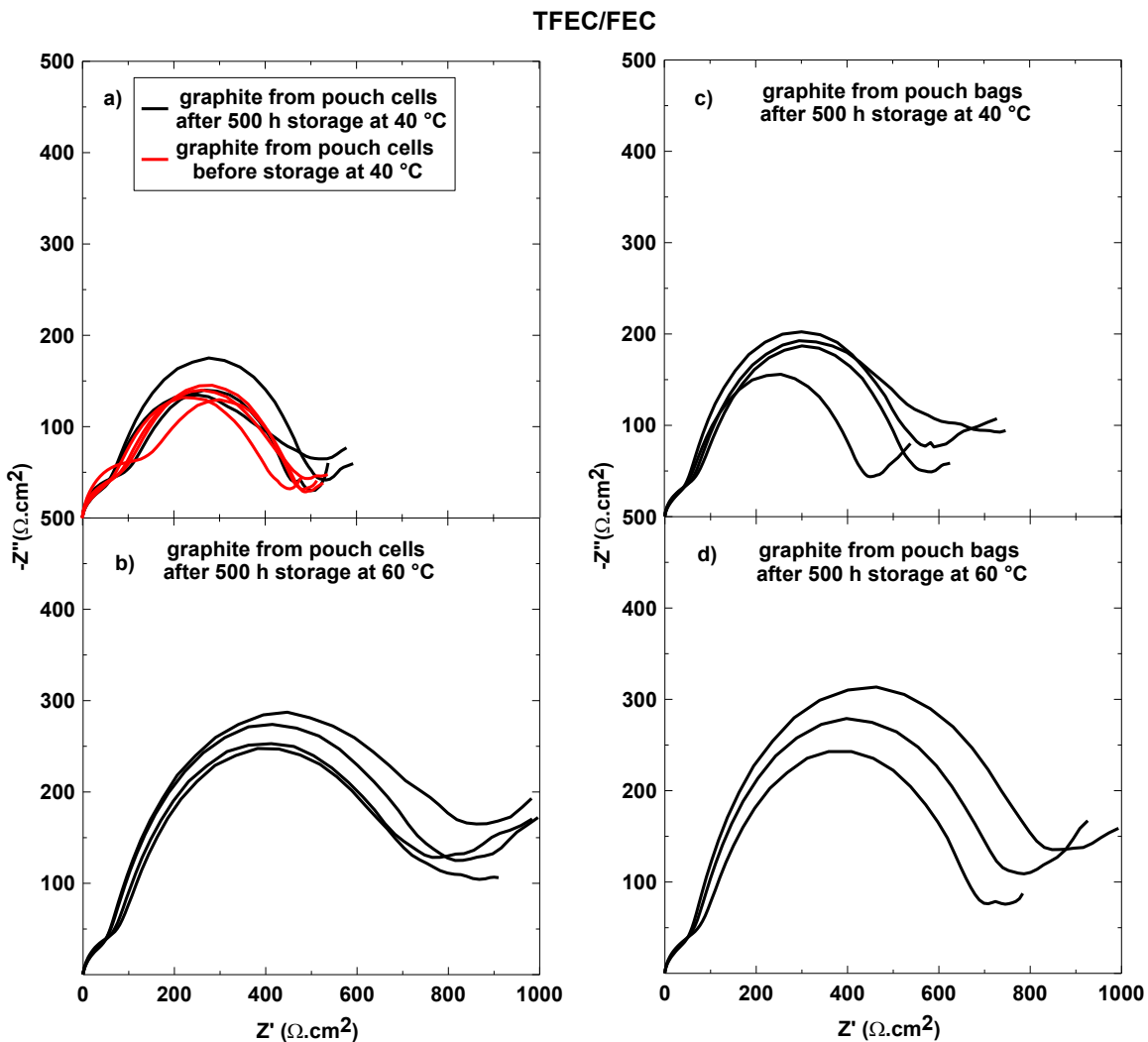
TFEC/FEC

Figure 5.8 Area-specific Nyquist plot of lithiated graphite electrode symmetric cells where the electrodes were taken from NMC442/graphite pouch cells with TFEC/FEC after 500 storage at 40 °C (a) and 60 °C (b) and from the corresponding pouch bags after 500 h storage at 40°C (c) and 60°C (d)

Figure 5.9 shows the background-subtracted O1s spectra of positive electrodes stored at 60°C for 500 h in PES 222 (Figure 5.9a) or TFEC/FEC (Figure 5.9b) containing pouch bags or pouch cells. The trends are roughly the same for both electrolytes. The peak at 529.5 eV, assigned to the NMC lattice oxygen, is larger for positive electrodes stored in pouch bags than for those stored in cells. The peaks at 531.5 eV and 533.3 eV, originating from SEI components containing ether and carbonyl-type environments, are

smaller for the positive electrodes stored in bags than those stored in cells. Both observations indicate that the SEI is much thinner for the positive electrode stored in bags than stored in cells. This is unexpected as R_{ct} of positive electrodes stored in bags containing conventional carbonate electrolyte is much larger than R_{ct} of electrodes stored in cells and R_{ct} of the positive electrode stored in bags containing fluorinated electrolyte was slightly larger than R_{ct} of electrodes stored in cells. The thinned SEI of positive electrodes stored in bags gives evidence that a thin, non-organic, insulating phase is the main contributor to R_{ct} growth. This insulating phase may be the reduced layer of rocksalt structure transition metal oxide described in several recent publications[160,162,164,167]. No significant chemical differences were revealed in the C1s and F1s regions of the XPS spectra between positive electrodes stored in cells and bags containing PES222 and TFEC/FEC, other than the thinned SEI.
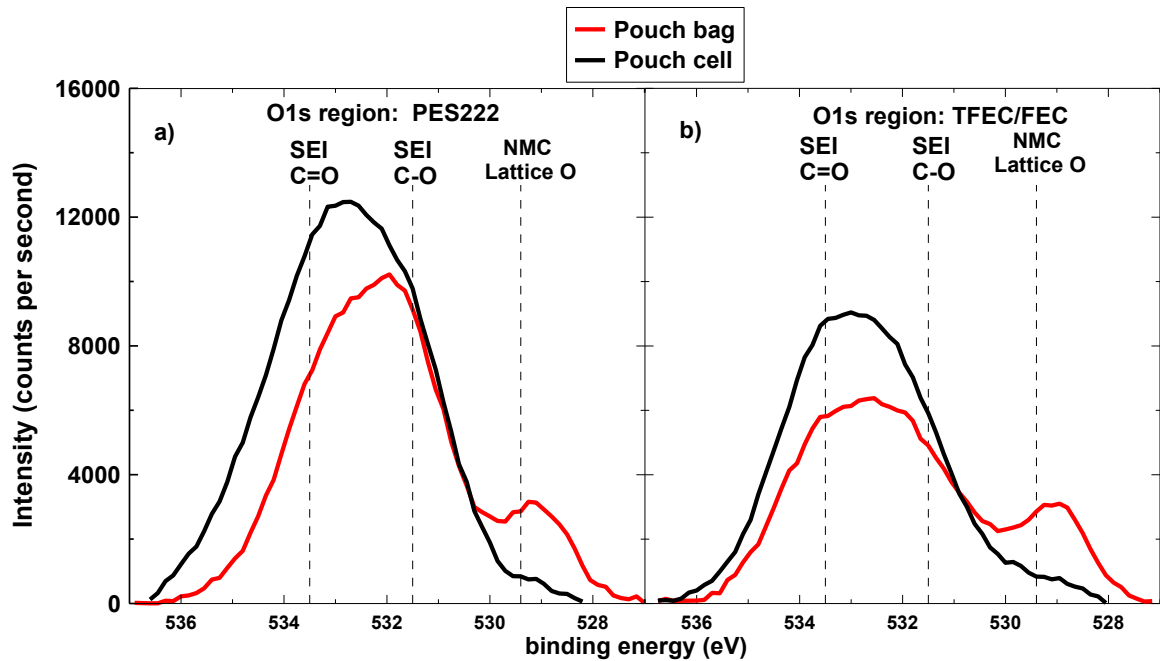
Figure 5.9 XPS O1s spectra of positive electrodes stored (500 h at 60°C) in cells (black) and in bags (red) with PES222 (a) and TFEC/FEC (b)

Figure 5.10a shows a schematic of possible reactions and crosstalk between negative and positive electrodes in the pouch cells and of reactions in the pouch bags containing conventional carbonate electrolyte suggested by the data presented here. Figure 5.10b shows a similar schematic for the cells and bags containing fluorinated electrolyte. In a pouch cell (left side of Figures 5.10a and 5.10b), both the conventional carbonate electrolyte and the fluorinated electrolyte are oxidized at the positive electrode at high voltage and elevated temperature generating gaseous or oxidized species as well as electrons. The lithium ions in the electrolyte combine with the generated electrons and insert into the positive electrode reducing the potential of the positive electrode vs Li^+/Li. The released gaseous and oxidized species move to the negative electrode and are reduced there. CO_2 is consumed at the negative electrode to produce products that coat the graphite electrode surface. It is possible that released protic species react at the graphite electrode to produce hydrogen. Much more hydrogen is produced in cells containing TFEC/FEC electrolyte than PES222 electrolyte. In a pouch bag with conventional carbonate electrolyte, generated gases such as CO_2 and other oxidized species remain and react at the positive electrode leading to a more resistive passivating film, possibly a rock salt surface layer at the positive electrode. [160,162,164,167] However, in a pouch bag with fluorinated electrolyte, the gaseous and other oxidized species are either unable to react with the positive electrode or there is a better passivating layer at the electrode which prevents reactions. Therefore, a minimal impedance growth at the positive electrode is observed in pouch bags with TFEC/FEC.
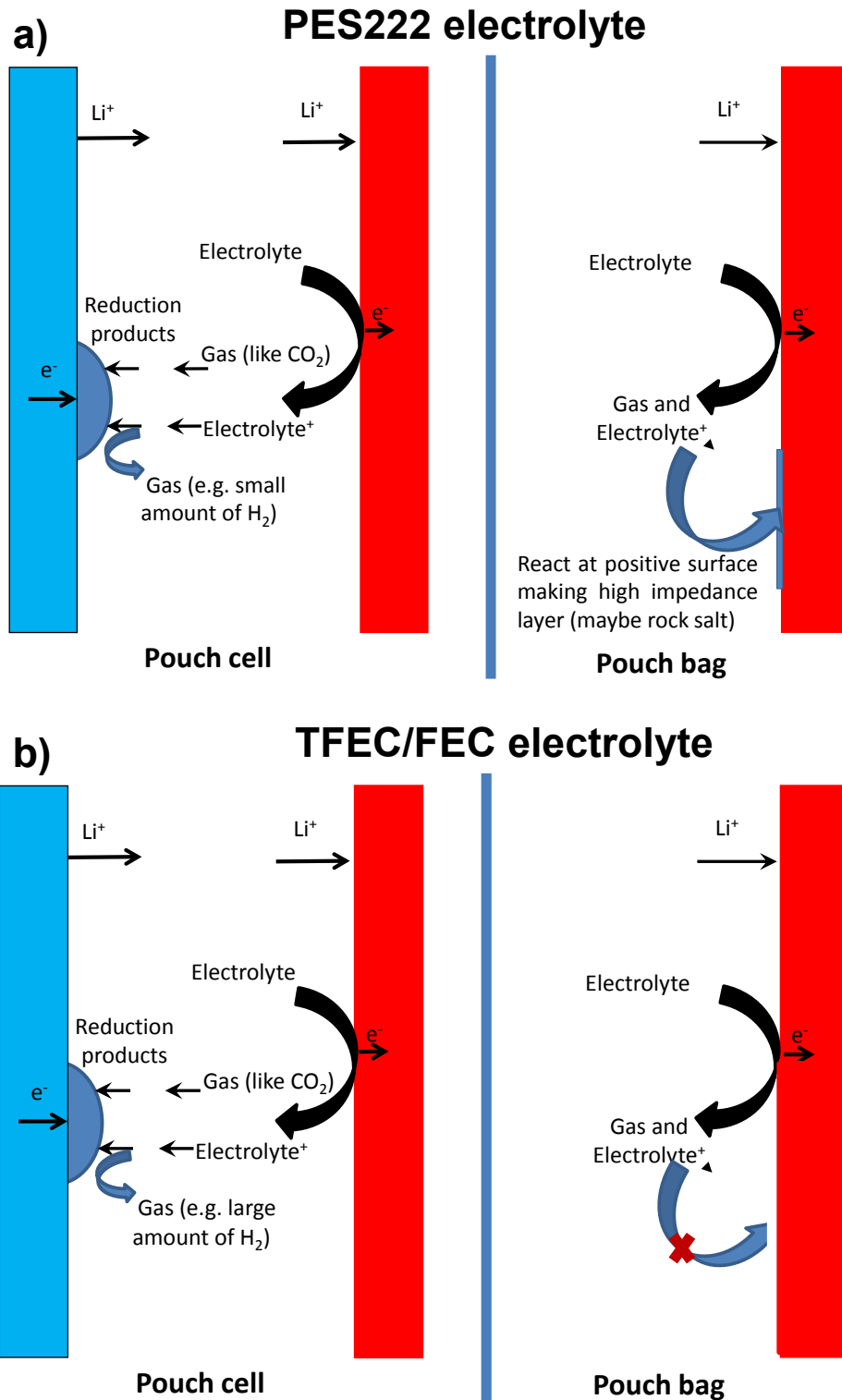
Figure 5.10 A schematic of reactions and crosstalk between negative and positive electrodes in pouch cells and of reactions occurring in pouch bags with PES222 (a) and TFEC/FEC (b)

5.3   Conclusions

EC-based and fluorinated electrolytes have been comparatively studied using NMC442/graphite pouch cells and pouch bags. The results show that the fluorinated electrolyte suppresses impedance growth of the charged NMC442 electrode but creates large initial negative electrode impedance. CO_2 is produced in pouch bags containing charged NMC422 and either electrolyte, but very little CO_2 is found in pouch cells with the EC-based electrolyte. This suggests that the SEI at the graphite electrode created by the fluorinated electrolyte limits CO_2 consumption compared to the carbonate electrolyte.

Virtually no gas was produced in pouch bags containing lithiated graphite and either electrolyte. Virtually no hydrogen was produced in pouch bags containing charged NMC442 and either electrolyte. However, hydrogen was found in pouch cells containing either electrolyte and the amount of hydrogen in the pouch cells containing the fluorinated electrolyte was very large. Therefore, the generation of hydrogen must be caused by the crosstalk between the negative electrode and the positive electrode in a cell.

CHAPTER 6: EFFECTS OF SURFACE COATING ON GAS EVOLUTION AND IMPEDANCE GROWTH AT NMC POSITIVE ELECTRODE IN LI-ION CELLS

In this chapter, the pouch bag method described in Chapter 4 is used to study the effects of surface coatings on NMC442, NMC532 and NMC622 electrodes. The majority of this work was adapted from the following manuscript:

D. J. Xiong, T. Hynes , L. Ellis, and J. R. Dahn, Effects of Surface Coating on Gas Evolution and Impedance Growth at $Li[Ni_xMn_yCo_{1-x-y}]O_2$ Positive Electrodes in Li-ion Cells, accepted by J. Electrochem. Soc.

Deijun Xiong prepared the pouch cells and pouch bags. Deijun Xiong performed the gas measurements, the impedance measurements and the electrode potential measurements. Deijun Xiong performed the GC-MS studies of gas compositions together with Toren Hynes. Deijun Xiong prepared all the figures. Jeff Dahn provided guidance and participated in experimental design and the interpretation of all the data. Deijun Xiong prepared the manuscript mentioned above and received revisions from Leah Ellis and Jeff Dahn.

6.1   Experimental

6.1.1   Pouch Cells and Pouch Bags

The uncoated NMC442/graphite, $LaPO_4$-coated NMC442/graphite, uncoated NMC532/graphite, Al_2O_3-coated NMC532/graphite, uncoated NMC622/graphite and Al_2O_3-coated NMC622/graphite cells were prepared according to the method described in

Section 3.1.5. After the cells were filled with 0.9 g of control + PES222, they then experienced the precycling described in Section 4.1.1. Steps used to make and test pouch cells and pouch bags were also described in Section 4.1.1. Four cells at 4.4 V were used for head-to-head comparison in the gas evolution experiments in each case. Two pouch cells were moved to a 60°C temperature box for storage. The other two identical pouch cells were transferred to an Ar-filled glovebox and disassembled there. Two lithiated graphite electrode and two delithiated NMC electrodes collected from the pouch cells were inserted into different pouch bags with 0.15 g EMC. The addition of 0.15 g EMC to the pouch bags created a similar electrolyte environment as in the original pouch cells. EC and $LiPF_6$ remained in the electrode and some EMC evaporated during the time (less than 5 minutes) it took to assemble the pouch bags.

Eight pouch cells at 4.4 V of each type were used for the impedance studies in the most cases. Two pouch cells were moved a 40°C temperature box. Two other pouch cells were moved to a 60°C temperature box. The other four identical pouch cells were transferred to the glovebox and opened there. Four delithiated NMC electrodes were inserted into different pouch bags with 0.15 g EMC. Two pouch bags were moved to a 40°C temperature box and the other two pouch bags were moved to a 60°C temperature box. All these pouch cells and pouch bags were stored for 500 h. The volume of all the pouch bags and pouch cells during the 500 h storage period were tracked over time using Archimedes' principle.[183] The potentials of the pouch cells were measured with an automated voltage measurement system. [110,184]

6.1.2 Symmetric Cells and Coin Half Cells

After the 500 h storage period, the pouch cells and pouch bags were used to construct positive/positive symmetric cells and half cells according to the method described in Section 4.1.4.

6.1.3 Analysis of the Gas Compositions in Pouch Cells and Pouch Bags

After 500 h storage, GC-TCD was used to analyze the gas compositions in the pouch cells and pouch bags according to the method described in Section 5.1.2.

6.2   Results and Discussion

Figure 6.1 shows the amount of gas evolved in pouch cells and pouch bags with PES222 and different types of NMC, with and without surface coating, during the 500 h storage period at 60°C. No volume changes were detected for pouch bags containing lithiated graphite electrodes during the 60°C storage period, which are consistent with previous results.[220] Pouch bags containing charged NMC electrodes produced much more gas than the corresponding pouch cells. This is also consistent with previous results.[220] Pouch cells and pouch bags containing Al_2O_3-coated NMC532 and NMC622 produced more gas than the corresponding ones containing uncoated NMC532 and NMC622 during 500 h storage. Pouch cells and pouch bags containing $LaPO_4$-coated NMC442 produced a similar amount of gas as the corresponding ones containing uncoated NMC442. This suggests that an Al_2O_3 surface coating can cause more gas generation.
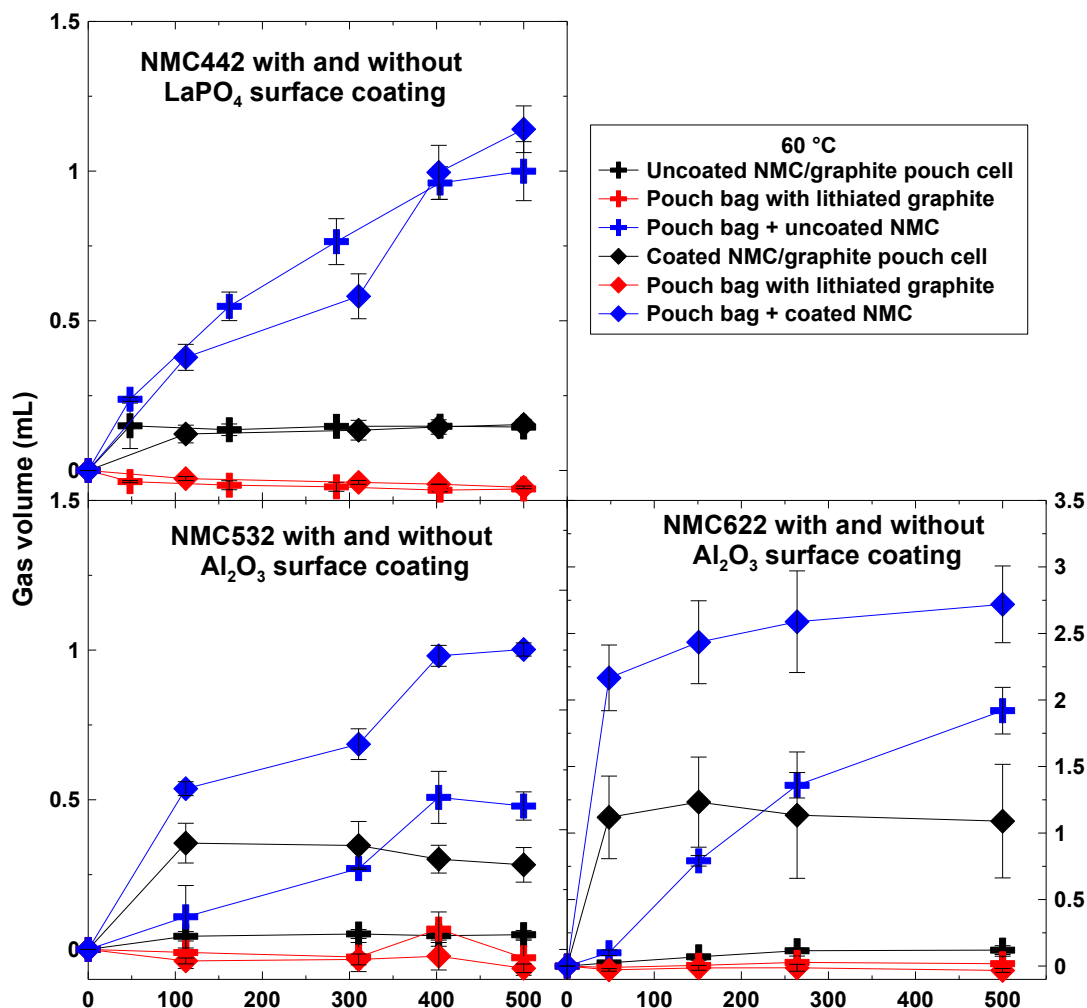
Figure 6.1 Gas volume versus time for pouch cells and pouch bags, containing lithiated graphite or delithiated NMC electrodes with and without surface coatings. PES222 electrolyte was used for these experiments in the cells and bags. Lithiated graphite electrodes in pouch bags were taken from uncoated NMC/graphite pouch cells (red crosses) and coated NMC/graphite pouch cells (red diamonds) at 4.4 V. Delithiated NMC electrodes in pouch bags were taken from uncoated NMC/graphite pouch cells (blue crosses) and coated NMC/graphite pouch cells (blue diamonds) at 4.4 V. All the pouch cells and pouch bags were stored at 60°C for 500 h.

Figure 6.2 shows the gas compositions after the storage period determined using the GC-TCD method for pouch cells and pouch bags containing different coated and uncoated NMC grade electrodes. Figure 6.2 shows that the major gases produced in the pouch cells and pouch bags are CO_2 and CO. Figure 6.2 shows that pouch bags produced much more CO_2 than the corresponding pouch cells, since gases such as CO_2 can be

consumed by the lithiated graphite electrode in pouch cells as described in Chapter 4 and 5. Figure 6.2 shows that hydrogen is only detected in pouch cells rather than pouch bags. This is further evidence that the generation of hydrogen is through species created at the positive electrode which travel to the negative electrode, react and make hydrogen.[23,24] Figure 6.2 shows that Al_2O_3-coated NMC532/graphite pouch cells produced much more hydrogen than the other pouch cells but this data appears to be anomalous. Readers should be cautioned that many more repeated experiments would be required to have full confidence in this statement.
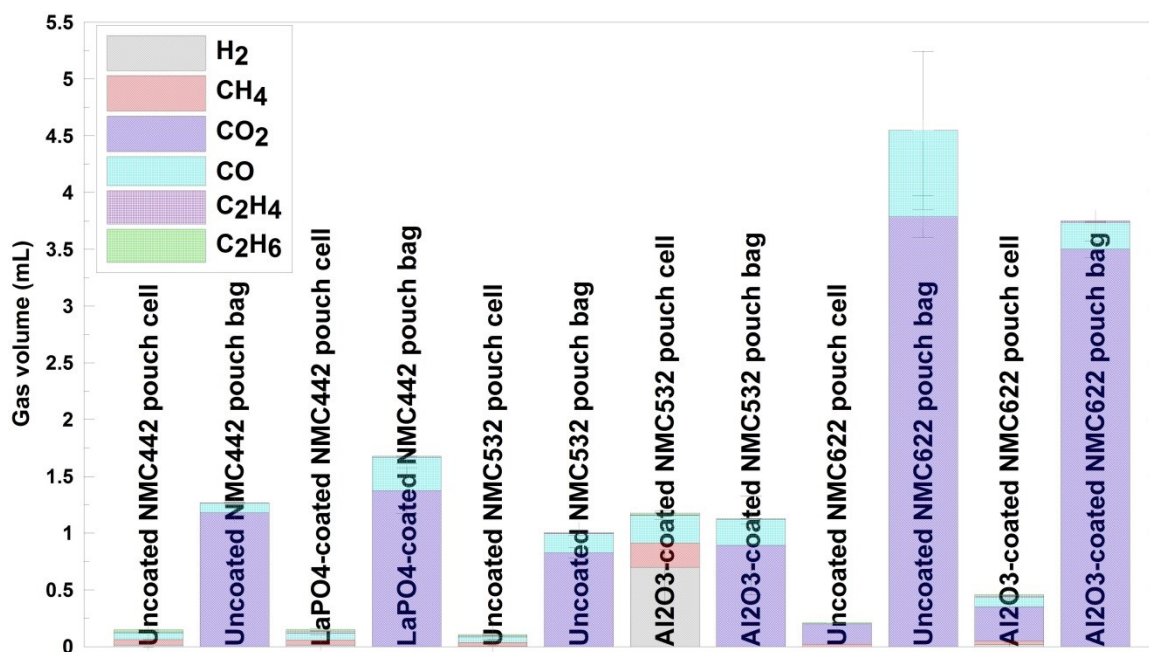
Figure 6.2 Gas compositions, measured using GC-TCD, in pouch cells and pouch bags containing PES222 stored at 60°C for 500 h. The initial voltage of these pouch cells was 4.4 V. Delithiated NMC electrodes in these pouch bags were taken from pouch cells at 4.4 V.
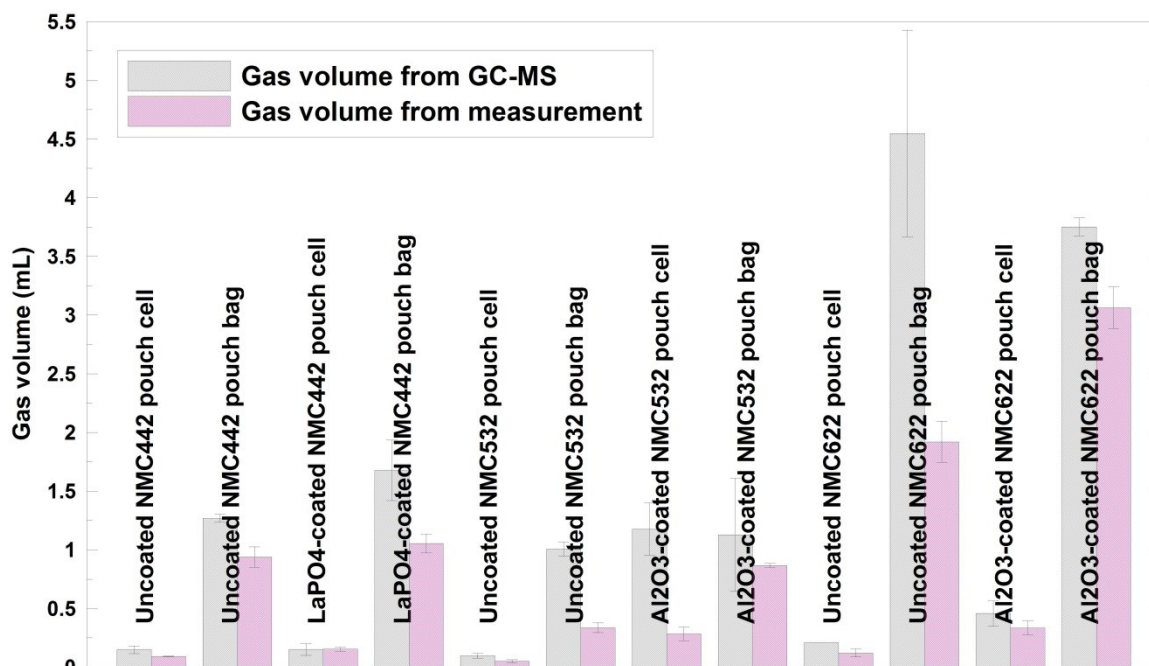
Figure 6.3 Gas volume, measured using GC-TCD and Archimedes principles, for pouch cells and pouch bags containing PES222 stored at 60°C for 500 h. The initial voltage of these pouch cells was 4.4 V. Delithiated NMC electrodes in these pouch bags were taken from pouch cells at 4.4 V.

Figure 6.3 shows the gas volumes in these pouch cells and pouch bags after the storage period as measured by both GC-TCD and Archimedes principle. Figure 6.3 shows that the gas volumes measured by GC-TCD are consistently larger than those measured by Archimedes principle. This is not surprising since many gaseous products can be dissolved in the electrolytein the cells and bags.[216,219]

Figures 6.4, 6.5, 6.6, 6.7 and 6.8 show the area-specific Nyquist plots of positive electrode symmetric cells where the electrodes were collected from uncoated NMC442/graphite, LaPO₄-coated NMC442/graphite, uncoated NMC532/graphite, Al_2O_3-coated NMC532/graphite, uncoated NMC622/graphite and coated NMC622/graphite pouch cells and pouch bags with PES222 electrolyte stored at 4.4 V at 40°C and 60°C. The first semicircle (high frequency) originates from the contact resistance between the

double sided electrodes and the coin cell case.[111] The second semicircle (low frequency) is due to the charge transfer impedance, R_{ct}, which is an important factor that affects cell performance.[111] The diameter of the second semicircle corresponds to $2R_{ct}$, since two identical positive electrodes are used in the symmetric cells. Figures 6.4, 6.6 and 6.8 show that the impedance of uncoated NMC electrodes grow more rapidly during high voltage storage at 60°C in a pouch bag than in a pouch cell where the graphite electrode is present. The oxidized species generated at the positive electrode in pouch bags can remain in the electrolyte, while these species could be consumed by the lithiated graphite in the pouch cells. The remaining oxidized species in the pouch bags could further react with the surface of the positive electrode material and thus create a high impedance film at its surface. Figures 6.4, 6.6 and 6.8 show that the impedance of uncoated NMC532 grew much less compared to uncoated NMC442 and uncoated NMC622 when these electrodes were stored in pouch bags at 60°C. Figures 6.5, 6.7 and 6.8 show that an Al_2O_3 surface coating can help suppress impedance growth while a $LaPO_4$ surface coating does not when PES222 is used. Figures 6.7 and 6.8 show that Al_2O_3-coated NMC622 has less impedance growth compared to Al_2O_3-coated NMC532 when they were stored in pouch bags at 60°C.
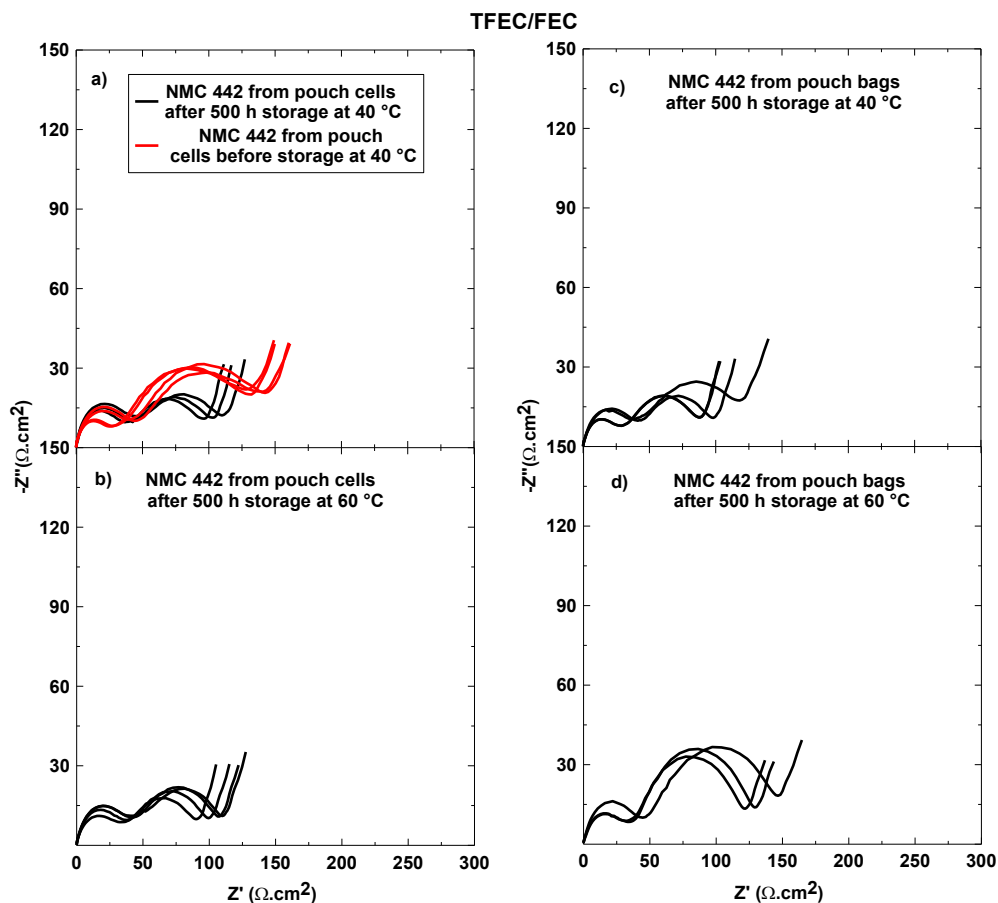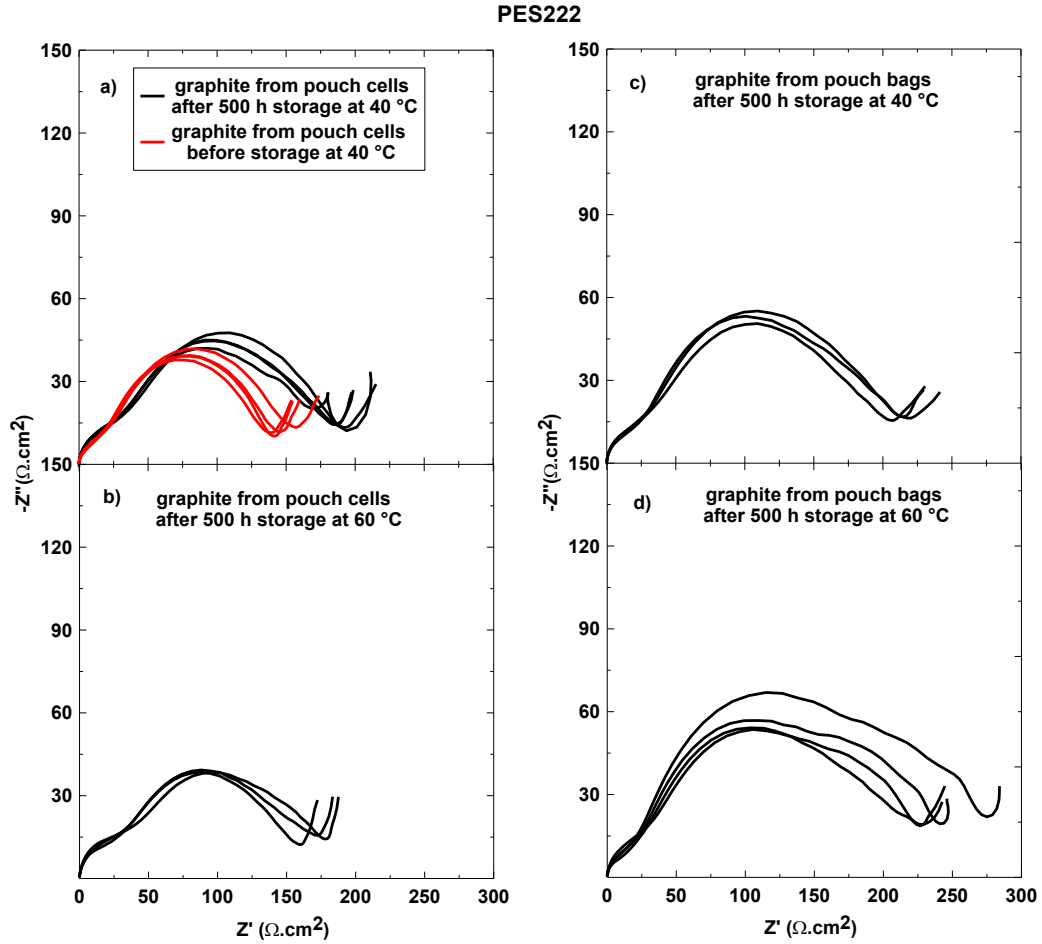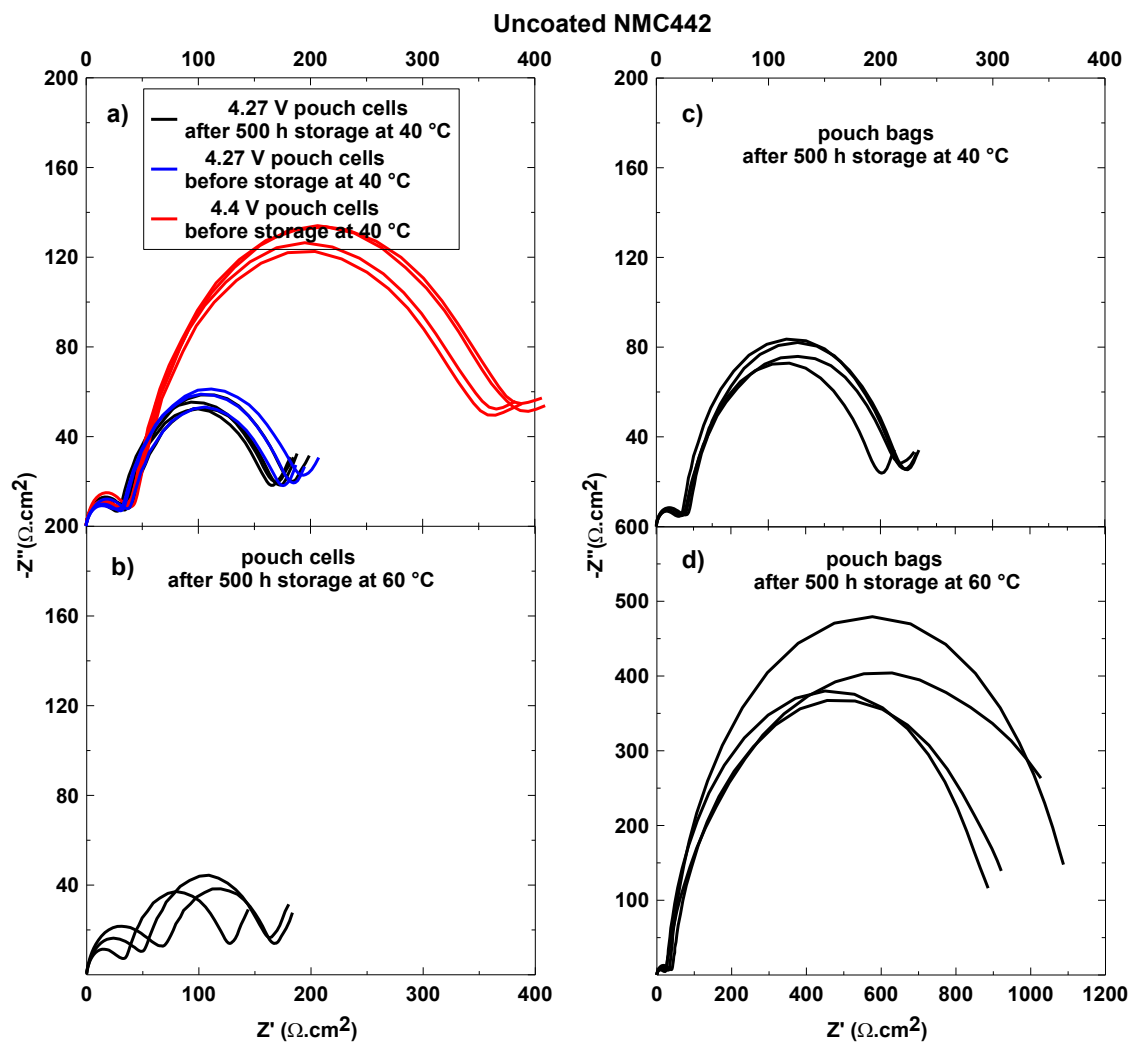
Figure 6.4 Area-specific Nyquist plots of positive electrode symmetric cells. The electrodes were taken from uncoated NMC442/graphite pouch cells containing PES222 electrolyte after 500 h storage at 40°C (a) and 60°C (b), and from charged uncoated NMC442 stored in pouch bags for 500 h at 40°C (c) and 60°C (d). The reader is cautioned to notice that the x-axis scale range in panel d) is much larger than in panels a), b) and c).
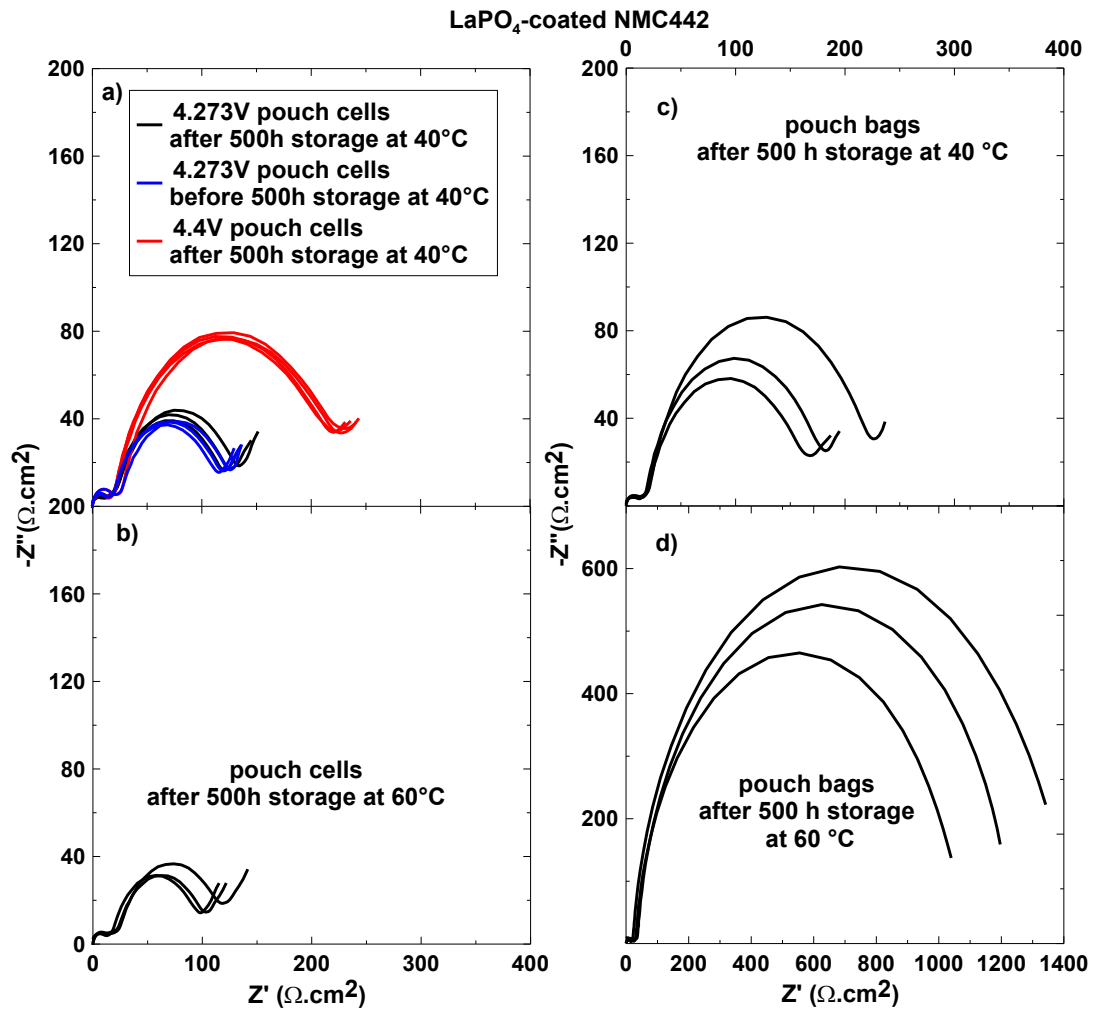
Figure 6.5 The area-specific Nyquist plot of positive electrode symmetric cells. The electrodes were taken from La$_3$PO$_4$-coated NMC442/graphite pouch cells containing PES222 electrolyte after 500 h storage at 40°C (a) and 60°C (b), and from charged LaPO$_4$-coated NMC442-stored in pouch bags for 500 h at 40°C (c) and 60°C (d). The reader is cautioned to notice that the x-axis scale range in panel d) is much larger than in panels a), b) and c).
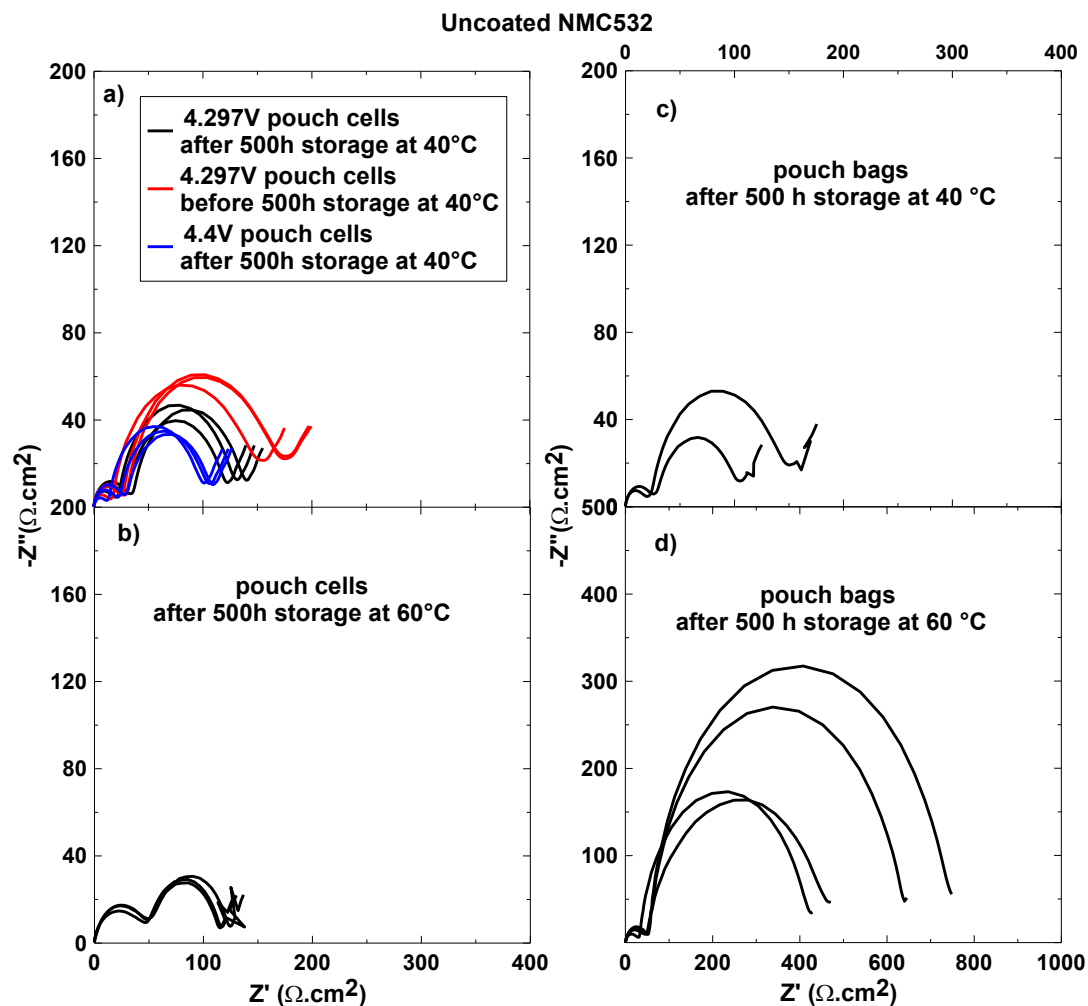
Uncoated NMC532

Figure 6.6 Area-specific Nyquist plots of positive electrode symmetric cells. The electrodes were taken from uncoated NMC532/graphite pouch cells containing PES222 electrolyte after 500 h storage at 40°C (a) and 60°C (b), and from charged uncoated NMC532 stored in pouch bags for 500 h at 40°C (c) and 60°C (d). The reader is cautioned to notice that the x-axis scale range in panel d) is much larger than in panels a), b) and c).

Al$_2$O$_3$-coated NMC532
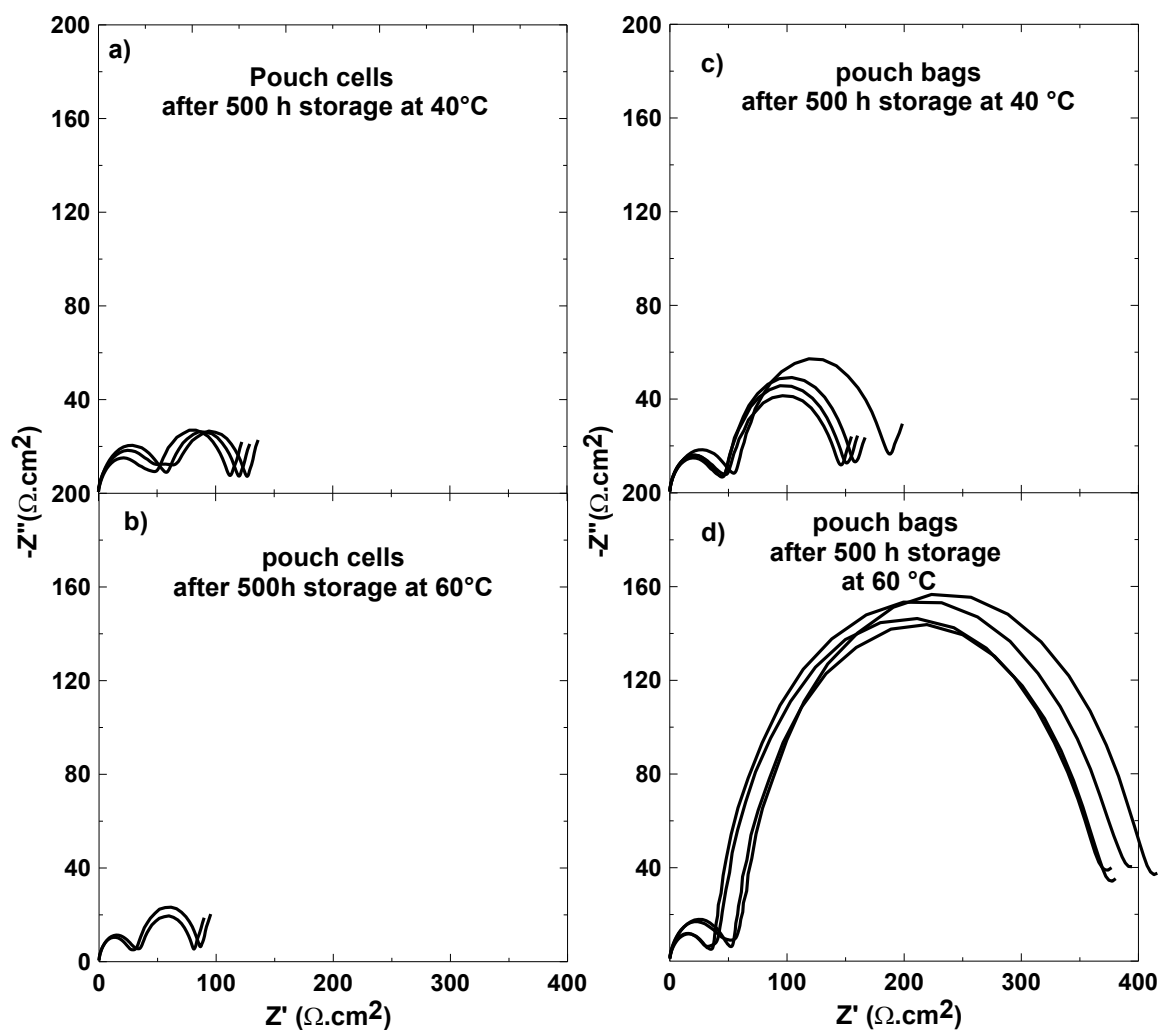
Figure 6.7 Area-specific Nyquist plots of positive electrode symmetric cells. The electrodes were taken from Al$_2$O$_3$-coated NMC532/graphite pouch cells containing PES222 electrolyte after 500 h storage at 40°C (a) and 60°C (b), and from charged Al$_2$O$_3$-coated NMC532 stored in pouch bags for 500 h at 40°C (c) and 60°C (d).
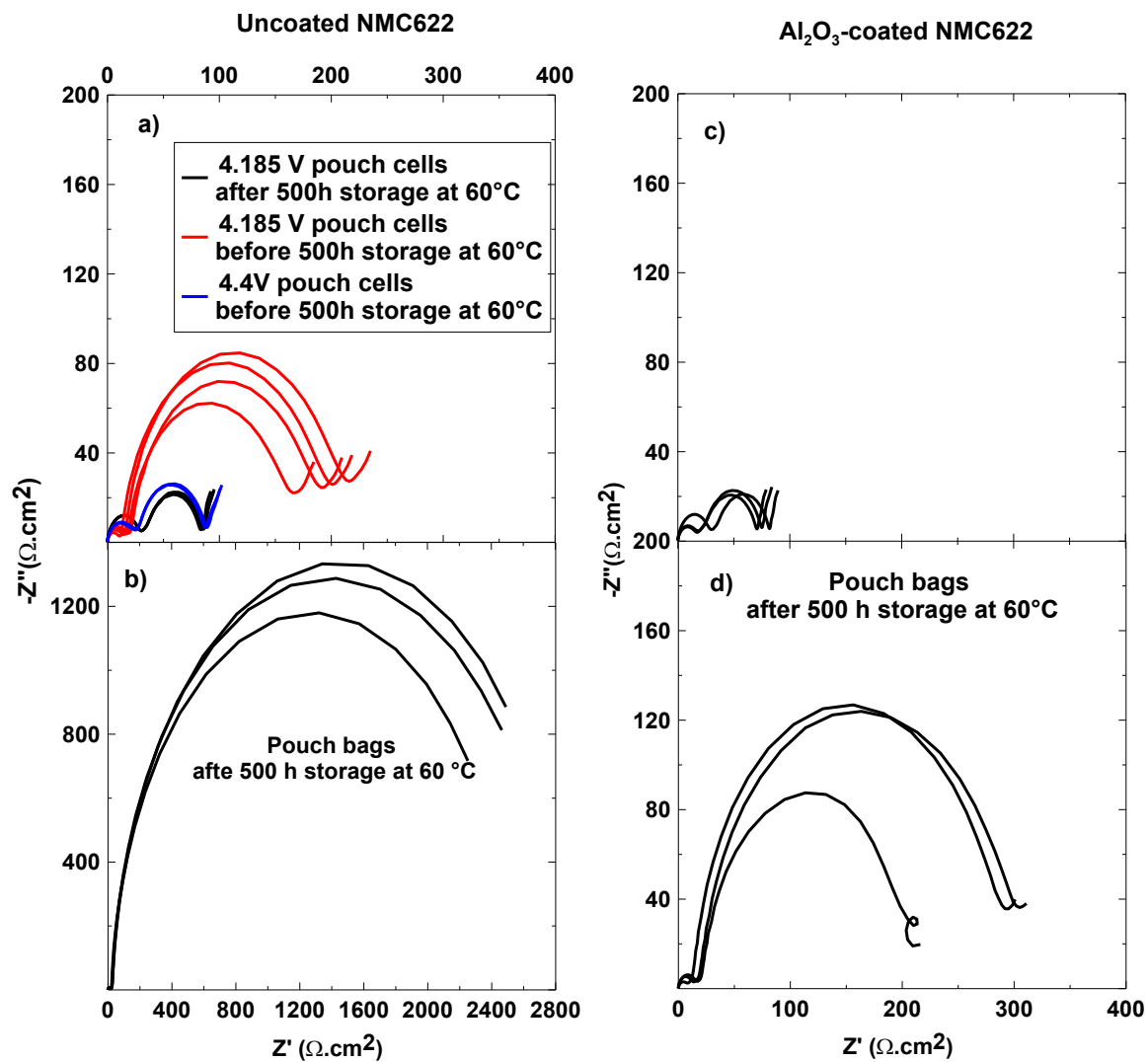
Figure 6.8 Area-specific Nyquist plots of positive electrode symmetric cells. The electrodes were taken from uncoated NMC622/graphite pouch cells (a), Al$_2$O$_3$-coated NMC622/graphite pouch cells (b), uncoated NMC622 stored in pouch bags (c) and Al$_2$O$_3$-coated NMC622 stored in pouch bags (d) after 500 h storage at 60°C. All pouch cells and pouch bags contained PES222 electrolyte. The reader is cautioned to notice that the x-axis scale range in panel b) is much larger than in panels a), c) and d).
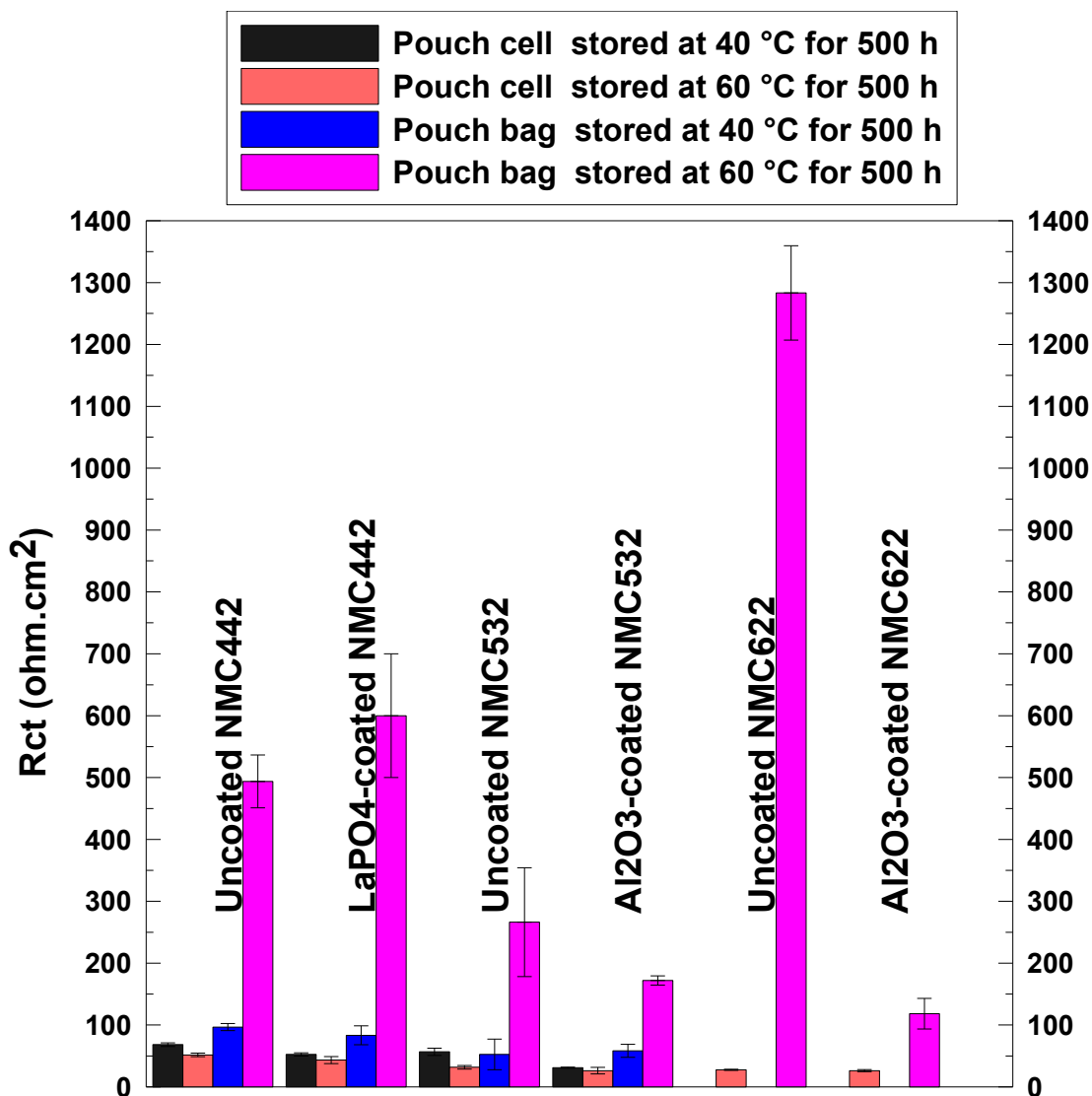
Figure 6.9 A summary of R_{ct} of the positive electrodes taken from the pouch cells and pouch bags stored with PES222 electrolyte after 500 h storage at 40°C and 60°C.

Figures C3, C4 and C5 show that Al_2O_3-coated NMC532 and Al_2O_3-coated NMC622 have roughly the same voltage drop after the storage period as do uncoated NMC532 and NMC622, respectively. These suggests that the Al_2O_3 surface coating does not dramatically suppress electrolyte oxidation occurring at the NMC electrodes but apparently hinders the oxidized species from reacting with the surface of the NMC

electrode thus limiting impedance growth at elevated temperature. The average values of R_{ct} shown in Figures 6.4, 6.5, 6.6, 6.7 and 6.8 are summarized in Figure 6.9.

R_{ct} of NMC electrodes varies with potential (vs Li/Li$^+$) in conventional carbonate electrolyte.[15] Thus it is imperative to compare the impedance of the NMC electrodes at the same potential vs Li/Li$^+$. After 500 h of storage at 40°C, the potential of uncoated NMC442/graphite, LaPO$_4$-coated NMC442/graphite and uncoated NMC532/graphite pouch cells dropped from 4.4 V to 4.27, 4.273 and 4.297, respectively, as shown in Figures C1, C2 and C3. After 500 h of storage at 60°C, the potential of uncoated NMC622/graphite dropped from 4.4 V to 4.185 V shown in Figure C5. To gain more insight about how R_{ct} of the positive electrode changes before storage and after storage, Nyquist plots of positive electrodes taken from pouch cells before storage at both 4.4 V and 4.27V for uncoated NMC442/graphite, 4.4 and 4.273 V for LaPO$_4$-coated NMC442, 4.4 and 4.297 V for uncoated NMC532, and 4.4 and 4.185 V for uncoated NMC622 are also included in Figures 6.4, 6.5, 6.6 and 6.8 for comparison. Figures 6.4a, 6.5a and 6.6a show that R_{ct} of NMC electrodes taken from pouch cells after 500 h storage are almost the same as before storage when the electrodes were taken from cells at the same voltage. Figure 6.8a shows that R_{ct} of uncoated NMC622 electrodes taken from pouch cells after 500 h storage at 60°C was roughly the same as before storage when the electrodes were taken from cells at the same voltage.

6.3 Conclusions

Different NMC electrodes, with and without surface coatings have been comparatively studied using pouch cells and pouch bags where PES222 electrolyte was used. The results

show that an Al_2O_3 surface coating can suppress impedance growth of the NMC622 electrode in pouch bags, at 60°C, more effectively than a $LaPO_4$ surface coating on a NMC442 electrode. However, the Al_2O_3 surface coating causes more gas generation at high voltage and high temperature. The pouch bag method can be used to compare the reactivity of coated positive electrode materials as a function of potential and temperature with electrolyte in the absence of a negative electrode. Using this method, it is possible that very inert positive electrode/electrolyte combinations can be found.

.

CHAPTER 7: MEASURING OXYGEN RELEASE FROM CHARGED NMC AND ITS EFFECTS ON THE PERFORMANCE OF HIGH VOLTAGE LI-ION CELLS

In this chapter, thermogravimetric analysis coupled with mass spectrometry (TGA-MS) is used to measure the release of oxygen from charged NMC electrode materials at high electrode potentials, i.e., low lithium content. This release is observed at relatively mild temperatures as low as 40°C. The amount of oxygen released may be greatly limited by utilizing larger NMC particles. Electrochemical measurements demonstrate a correlation between TGA-MS results and the cycling performance of NMC/graphite cells. X-ray photoelectron spectroscopy complements the TGA-MS results and provides evidence of the solid electrolyte interphase decomposition. The results in this work offer new support that the release of oxygen from NMC can cause oxidative decomposition of the electrolyte and is a major reason why high voltage cells generate gas and have poor capacity retention. The majority of this work was adapted from the following manuscript:

D. J. Xiong, L.D. Ellis, J. Li, H.Y. Li, T. Hynes, J.P. Allen, J. Xia, D. S. Hall, I.G. Hill and J. R. Dahn, Measuring Oxygen Release from Charged $LiNi_xMn_yCo_{1-x-y}O_2$ and its Effects on the Performance of High Voltage Li-ion Cells, accepted by J. Electrochem. Soc..

Deijun Xiong prepared the pouch cells and the materials for TGA-MS measurements together with Toren Hynes. Deijun Xiong designed and performed the TGA-MS measurements. Deijun Xiong performed *in situ* gas measurements for uncoated NMC442/graphite, uncoated NMC532/graphite, and uncoated NMC622/graphite cells

while Jenn Allen, Hongyang Li and Jing Li performed *in situ* gas measurements for the other cells. Long time cycling data were received from Jing Li and Jian Xia. Deijun Xiong designed and performed the preheated material experiment. The XPS measurements and analysis of the XPS spectra were performed by Leah Ellis. Jeff Dahn provided guidance and participated in experimental design and the interpretation of all the data. David Hall participated in preparing figures and analyzing the data. Deijun Xiong prepared the manuscript mentioned above except for the XPS section and received revisions from David Hall, Leah Ellis and Jeff Dahn.

7.1   Experimental

7.1.1   Pouch Cell Preparation

This work utilized various pouch cells which are NMC111/graphite, NMC442/graphite, NMC532/graphite, Al_2O_3-coated NMC532/graphite, HV-coated NMC532/graphite, single crystal NMC532/graphite, NMC622/graphite, Al_2O_3-coated NMC622/graphite and HV-coated NMC622/graphite. The details of these pouch cells can be found in Section 3.1.5. 0.9 g of control or control + PES211 was added to each cell. After electrolyte filling, cells experienced different pre-cycling protocols for different experimental purposes which will be given specifically in different experimental sections below.

7.1.2   Thermogravimetric Analysis/Mass Spectrometry (TGA-MS)

The cells were externally clamped to provide stack pressure (about 0.3 atm) and were first placed in a temperature box at 40°C and held at 1.5 V for 6-12 h. These cells were then charged to either 4.2, 4.4, or 4.6V at C/20 and held at that voltage for 5-10 h prior to

disassembly. One cell with control electrolyte was chosen to be discharged to 2.8 V at C/20 after it was charged to 4.6 V. These cells were then quickly transferred to an Ar-filled glove box and disassembled there with great caution. The charged positive electrodes were removed from the pouch cells and were repeatedly rinsed with dimethyl carbonate (DMC) six times to ensure that a minimal amount of electrolyte remained in the electrodes. After the electrodes were dried for half an hour in vacuum, the NMC and graphite powders were removed from the aluminum and copper foil current collectors, respectively, by gentle scraping with a stainless steel razor. The powders were then transferred in air as quickly as possible for thermogravimetric analysis coupled with mass spectroscopy (TGA/MS) experiments to minimize air exposure. Graphite and uncoated NMC442 electrodes taken from uncoated NMC442/graphite cells with control electrolyte at 2.8 V were also subjected to TGA-MS analysis after following the same rinsing treatment as the charged positive electrode. A TA-instruments SDT-Q600, coupled to a TA-instruments Discovery MS mass spectrometer was used for these experiments. In most cases, approximately 80 mg of the electrode material from each cell was used for each test. During the experiment, the sample was first set to stay at room temperature for 10 minutes with a flow of argon at 400 mL/min. Then the samples were heated from room temperature to 350°C at 10°C/min with a flow of argon at 100 mL/min while ions with $m/z = 20\text{-}80$ or only $m/z = 32$ were monitored using the mass spectrometer.

7.1.3 *In situ* Gas Measurement

After electrolyte filling, the cells with control + PES211 were first placed in a temperature box at 40°C and held at 1.5 V for 6-12 h. They were then charged to 3.5 V at C/20. After degassing in the glovebox, the cells were charged to 4.4 V at the same rate

and then degassed again. After the cells were discharged to 3.0 V at C/20, they were loaded in an in *situ* gas measurement equipment for gas measurements. This method has been described in detail in Section 3.4. The cells were charged to 4.3 V and then discharged to 2.8 V. Afterwards, the cells were charged to different cut-off voltages of 4.4, 4.5 and 4.6 V and held at each cut-off voltage for 100 h. The current used during testing was approximately C/20, where C is the measured capacity between 3.0 - 4.3 V. The tests were performed at 40°C. The changes in the volume of the cells during testing were tracked as a function of time.

7.1.4 Coin Half cells

After electrolyte filling, uncoated NMC442/graphite and single crystal NMC532/graphite pouch cells with clamps and with control + PES211 were first placed in a temperature box at $40°$C and held at 1.5 V for 6-12 h and then charged to 4.6 V at C/20 and held for 5-10 h. Cells were then transferred to an Ar-filled glovebox for disassembly. The charged electrodes were removed and washed repeatedly using DMC for six times. Before making coin half cells using these electrodes, some of them were heated intentionally at 100 °C for 3h in a vacuum chamber while the others did not receive the heat treatment. Two Celgard separators and control electrolyte were used for these coin half cells. The coin half cells were first discharged to 2.8 V and then cycled one time at C/40 at $40°$C.

7.1.5 X-Ray Photoelectron Spectroscopy (XPS)

The delithiated positive electrodes described in 7.1.4, prepared with and without heat treatment, were mounted onto a molybdenum sample holder, using double-sided, ultra-

high vacuum-compatible copper tape. The details of the XPS method can be found in Section 4.1.5. Peaks were fit with a mixed Gaussian (70%) /Lorentzian (30%) line shape. Calculations of the inelastic mean free path (IMFP) were performed using the predictive TPP-2M equation of Tanuma *et* al, with version 1.2 of the NIST EAL Database.[221,222] Leah Ellis, a third year graduate student in the Dahn lab, did these XPS measurements and calculations.

7.1.6   Long-term Cycling Tests

After uncoated NMC442/graphite and single crystal NMC532/graphite cells with control + PES211 experienced the pre-cycling protocol mentioned in section 7.1.3, they were tested (with clamps) for long-term cycling between 2.8 and 4.4 V using a C/2 rate at 40°C. In order to check how impedance affects capacity, a slow C/20 rate cycle was added every 50th cycle. Moreover, the cells were held at the top of charge until the current reached C/20 during each cycle.

7.2   Results and Discussion

It has been proposed that at low lithium content, i.e., at high electrode potentials, NMC materials release oxygen by the formation of a surface rock salt layer and that this release of oxygen can cause the observed oxidation of the electrolyte at high voltages.[160,164] Figure 7.1a shows that a large amount of O_2 (m/z = 32) is released from NMC materials when heated above ~175 °C. The peak of this oxygen release correlates well with the dm/dT peak, shown in Figure 7.1b, suggesting the main weight loss is due to this oxygen release throughout the material at high temperature. Figure 7.1c shows that the m/z=32 ion signal, which could be due to oxygen release, can also be detected

from 20 mg of the sample below 100°C. This result is consistent with the hypothesis that NMC can release oxygen atoms, presumably from its surface, at relatively mild temperatures (i.e., the onset is ~ 40°C). In order to verify that this m/z=32 ion peak was not due to some artifact from the instrument, the experiment was repeated using 76 mg of the same sample. As seen in Figure 7.1c, the area of the peak was approximately four times greater when 76 mg of NMC442 was analyzed, relative to the 20 mg sample. This result confirms that the observed m/z=32 ion peak is not spurious, but rather originates from the NMC sample.
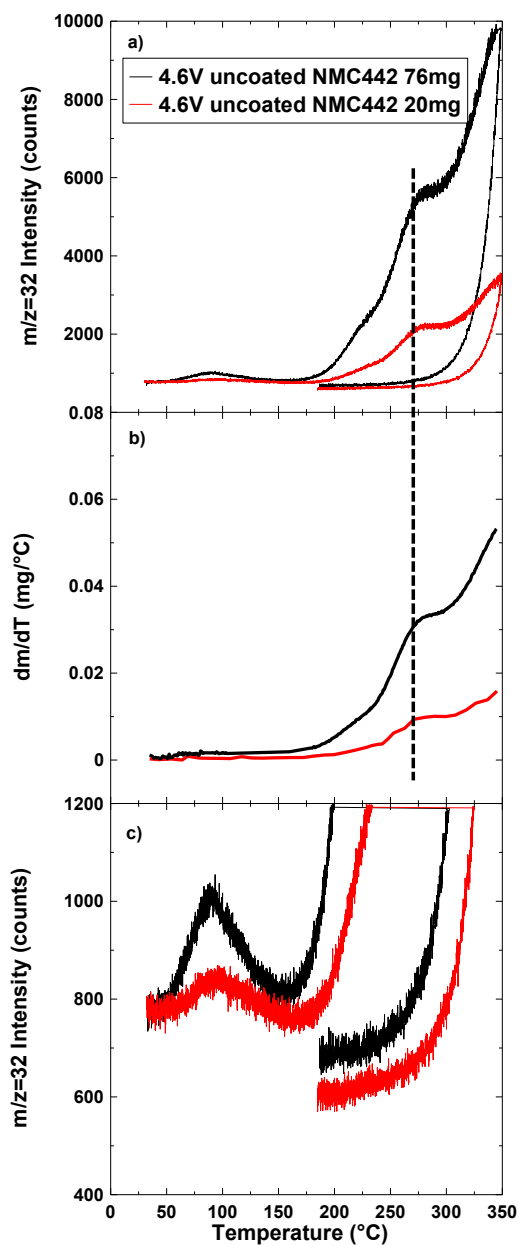
Figure 7.1 The m/z=32 ion intensity (a, c) and dm/dT (b) vs heating temperature for 20 mg and 76 mg of an uncoated NMC442 electrode taken from an uncoated NMC442/graphite cell with control + PES211 at 4.6 V. Both samples were heated from room temperature to 350 °C at 10 °C/min. A dashed line representing oxygen peak position shown in panel a and b was inserted to guide readers.

The PES211 electrolyte used here can form sulfur-containing and oxygen-containing species such as –C=O, C–O–C at the positive electrode surface. It was then considered whether the 32 ion signal may have originated from CH_3OH, SO_2 or H_2S gas molecules

that originate from decomposed SEI species. In order to exclude that a sulfur-containing SEI at the positive electrode contributes to the 32 ion signal, control electrolyte was used for most of samples measured here. Since the SEI at the graphite electrode is rich in oxygen-containing species, a graphite electrode taken from a pouch cell that was first charged to 4.6 V and then discharged to 2.8 V was analyzed by TGA-MS using total ion mode (m/z=20-80). Figure 7.2a shows that no m/z=32 signal was detected from the graphite electrode, suggesting that oxygen-containing SEI species such as –C=O and C–O–C do not measurably contribute to this signal. The most abundant ions for CH_3OH, SO_2 or H_2S gas molecules are 31, 63, and 34, respectively. Therefore, the intensities of these ions were plotted in Figure 10.2, which shows that these were not observed for the samples here. Thus, the 32 ion signal is not attributable to the CH_3OH, SO_2 and H_2S gas molecules. Figures 7.2d and 7.2e show that the 32 ion peak is present and that the peak areas are comparable for charged uncoated NMC442 electrodes taken from 4.6 V pouch cells that contained either control electrolyte or PES211 electrolyte. This suggests that the electrolyte does not significantly affect the m/z=32 signal over this heating temperature range. Figures 10.2d and 10.2e show that the onset temperature for the generation of CO_2 for uncoated NMC442 taken from 4.6 V cells is lower than that taken from lower voltage cells (2.8 V and 4.2 V) shown in Figures 7.2b and 7.2c. One interpretation is that oxygen is released from the NMC material and reacts with the SEI via a "pseudocombustion" reaction to produce CO_2. This can be supported by the XPS results which will be discussed later in detail.   Figures D1, D2, D3, D4, D5 and D6 show all the ions with signal intensities that were above the baseline threshold for any of the samples tested in this work. Compared to the instrument blank, shown in Figure D7,

the m/z=28, 32, and 44 ions are the only ones that produced a peak for the samples in Figures D1, D2, D3, D4, D5 and D6.
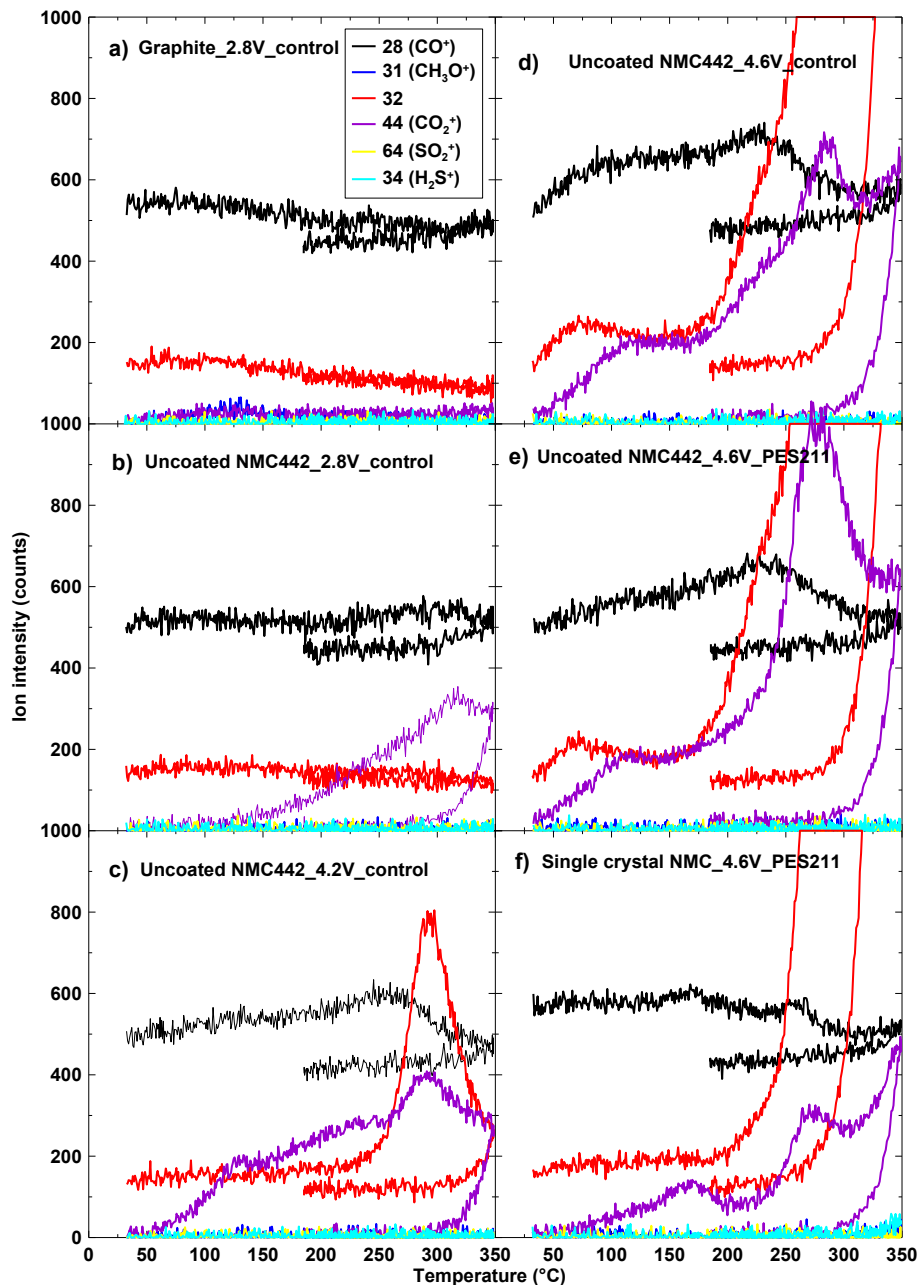
Figure 7.2 Ion intensity (m/z=28, 31, 32, 34, 44 and 64) vs heating temperature for graphite and NMC electrodes taken from pouch cells with control electrolyte at 2.8 V (a, b), 4.2 V (c) and 4.6 V (d), or with PES211 at 4.6 V (e) and (f). The samples were heated from room temperature to 350°C at 10°C/min
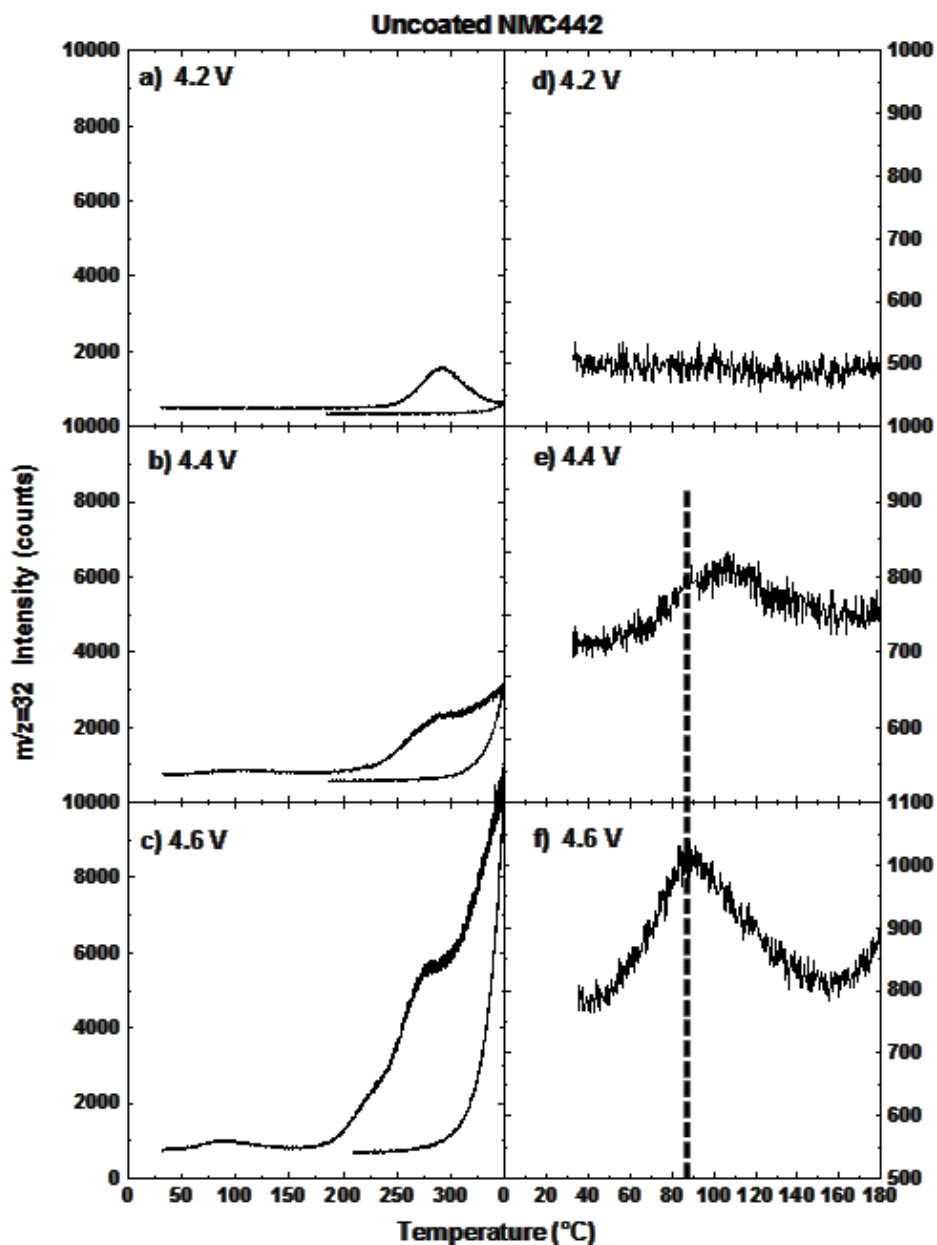
Figure 7.3 The m/z=32 ion intensity vs heating temperature for uncoated NMC442 electrodes taken from pouch cells with PES211 at 4.2V (a, d), 4.4V (b, e) and 4.6 V (c, f). The samples were heated from room temperature to 350 °C at 10°C/min. A dashed line representing the m/z=32 peak position for the 4.6 V sample was inserted to guide readers.

To investigate whether the stability of the positive electrode depends on its state of charge, uncoated NMC442 electrodes were taken from cells with PES211 that were charged to 4.2, 4.4 and 4.6 V and were used for TGA-MS analysis. Given that the

lithium content decreases as the electrode potential increases, it is expected that the material stability will be less at higher cell voltages. If it is assumed that the m/z=32 ion corresponds to oxygen, the result is consistent with the observed O_2 release behaviour shown in Figure 7.3. In general, the amount of oxygen released increased with increasing cell voltage, as evaluated semi-quantitatively from the relative peak areas, and decreased onset temperature of its release. The onset temperature for the oxygen release is approximately 40°C. Figures 7.3e and 7.3f show that the temperature for the 32 ion signal shifts to a lower temperature as the cell potential is increased. This suggests that this 32 ion release is not generated by some SEI species but from oxygen release from the surface of the positive electrode material.

Whereas the previous results provide direct evidence for O_2 release from uncoated NMC442 materials, the question arises whether this phenomenon is limited to a particular NMC stoichiometry. Guéguen *et al.* reported that charged uncoated NMC111 could release oxygen around 4.55 V vs Li/Li^+ at room temperature. [23] In order to see if the TGA-MS method used here can match their report, charged uncoated NMC111 taken from uncoated NMC111/graphite pouch cells with PES211 at 4.2, 4.4 and 4.6 V were investigated using TGA-MS. Figure 7.4 shows that the quantity of the 32 ion released from uncoated NMC111 taken from 4.2 V cells was scarcely above the instrument baseline. By contrast, the uncoated NMC111 taken from cells at 4.4 and 4.6 V clearly display the first 32 ion release peak, which onsets at ~40 °C. As observed for the uncoated NMC442 material, the average temperature of the 32 ion peak for uncoated NMC111 also decreases as the electrode potential increases. This is again consistent with the hypothesis that the material stability decreases as the NMC lithium content decreases.

130
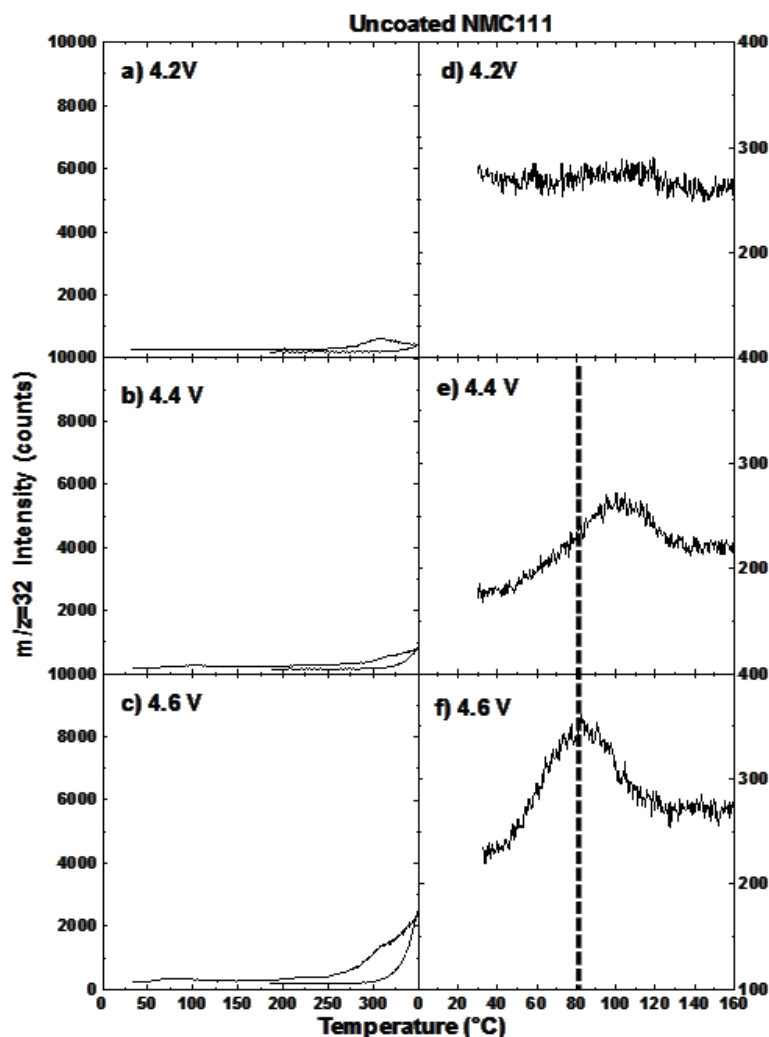
Figure 7.4 The m/z=32 ion intensity vs heating temperature for uncoated NMC111 electrodes taken from pouch cells with PES211 at 4.2V (a, d), 4.4V (b, e) and 4.6 V (c, f). The samples were heated from room temperature to 350 °C at 10°C/min. A dashed line representing the m/z=32 peak position for the 4.6 V sample was inserted to guide readers.

In order to explore whether this also occurs for other NMC materials, the method was then used for NMC532 and NMC622 electrode materials with and without surface coatings. Moreover, single crystal NMC532 materials with large particle size were also examined using the same method. This material is of particular interest because of its significantly lower surface area to volume ratio. Figures 7.5 and 7.6 show that the O_2 release can similarly occur for all of these NMC samples (uncoated NMC532, Al_2O_3-

coated NMC532 ,HV-coated NMC532, and uncoated NMC622, Al_2O_3-coated NMC622, and HV-coated NMC622 materials). However, the single crystal NMC532 materials (large particle size) taken from cells charged to 4.2, 4.4 and 4.6 V did not show the first oxygen release peak. By contrast, the application of inorganic coatings did not have a clear inhibitive effect on the tendency of delithiated NMC532 or NMC622 to release O_2.
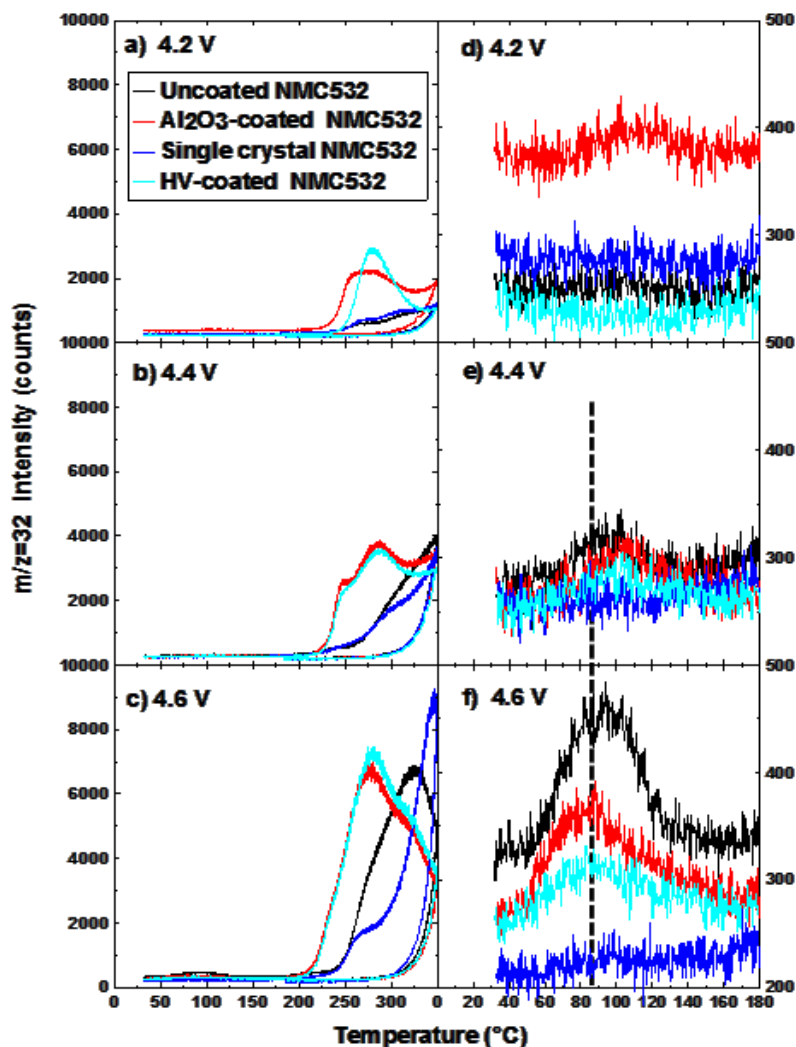
Figure 7.5 The m/z=32 ion intensity vs heating temperature for uncoated NMC532, Al_2O_3-coated NMC532, and single crystal NMC532 electrodes taken from the corresponding pouch cells with PES211 at 4.2V (a, d), 4.4V (b, e) and 4.6 V (c, f). The samples were heated from room temperature to 350 °C at 10°C/min. A dashed line representing the m/z=32 peak position for the 4.6 V sample was inserted to guide readers.
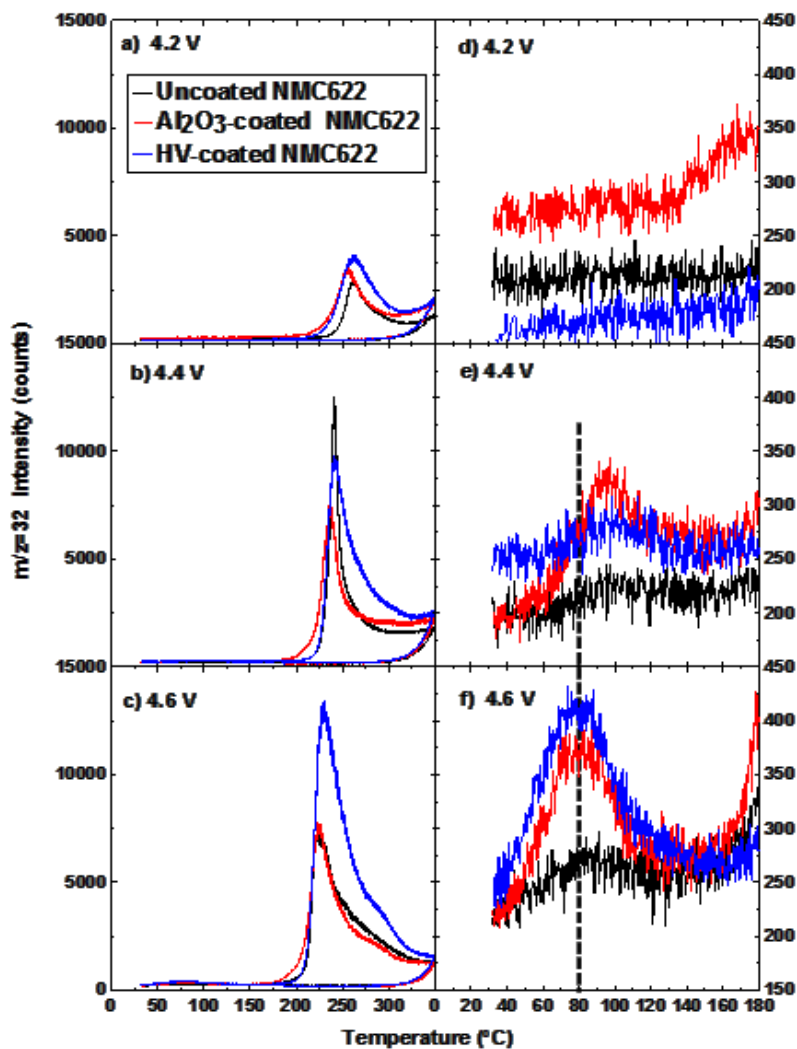
Figure 7.6 The m/z=32 ion intensity vs heating temperature range for uncoated NMC622, Al_2O_3-coated NMC622 and HV-coated NMC622 taken from the corresponding pouch cells with PES211 at 4.2V (a, d), 4.4V (b, e) and 4.6 V (c, f). The samples were heated from room temperature to 350 °C at 10°C/min. A dashing line representing the m/z=32 peak position for the 4.6 V sample was inserted to guide readers.

Bak *et al.* performed similar experiments on different grade NMC materials using TGA-MS. However, no oxygen release before 70°C was reported. The reason why Bak *et al.* failed to find this oxygen release at early temperature may have been because they only used around 4 mg of charged NMC electrode materials whose potential vs Li/Li$^+$ was 4.3 V.[223] Herein, the onset potential of NMC materials for oxygen release is about

4.48 V vs Li/Li$^+$. Therefore, the oxygen release peak, if any, in their samples was likely indistinguishable from baseline noise.
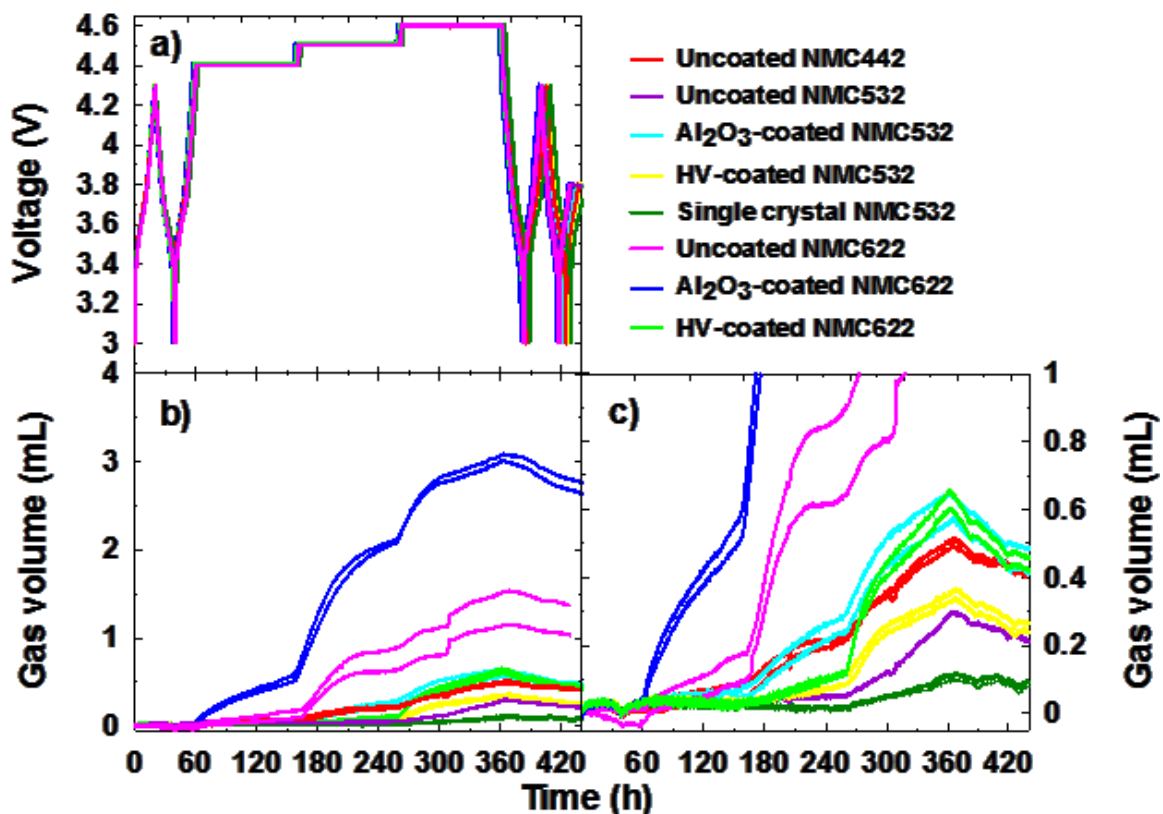
Figure 7.7 Voltage-time profile (a) and volume of gas produced (b, c) during *in situ* gas measurements of different NMC/graphite pouch cells.

During charging or storage at high voltage, gas will evolve since the released oxygen will react with electrolyte. Therefore, *in situ* gas measurements were used to probe gas evolution during a high voltage hold. The voltage-time profile is shown in Figure 7.7a, where each cell was subject to a standard formation cycling protocol followed by successive holds at 4.4, 4.5, and 4.6 V for 100 h per step. The results shown in Figures 7.7b and 7.7c and summarized in Table 1.2 demonstrate that the volume of gas released increases with the hold voltage. This trend is true for all of the NMC materials examined in this work. The single cyrstal NMC532 cells generated the least gas. This may be

attributable to the no oxygen release behavior shown in Figure 7.5 which indicates single crystal NMC532 does not release oxygen at high voltage.

For both NMC532 and NMC622, the Al_2O_3-coated materials released the most gas, followed by the HV-coated and uncoated materials, respectively. However, the effect of the proprietary HV coating was less clear, where it decreased the volume of gas released for the NMC622 material By contrast, slightly more gas was released from the HV-coated NMC532 than the uncoated material. There was also no clear trend between NMC nickel content and the volume of gas released.

Table 7.1 Volume of gas produced during 100 h constant voltage holds at 4.4, 4.5 and 4.6 V for different NMC cells (as indicated) at 40°C.

Cell type	Gas volume during 4.4 V hold (mL)	Error	Gas volume during 4.5 V hold (mL)	Error	Gas volume during 4.6 V hold (mL)	Error
Uncoated NMC442/graphite	0.059	0.026	0.154	0.015	0.266	0.026
Uncoated NMC532/graphite	0.005		0.014		0.237	
Al2O3-coated NMC532/graphite	0.024	0.013	0.201	0.013	0.332	0.026
HV-coated NMC532/graphite	0.002	0.004	0.069	0.021	0.235	0.001
Single crystal NMC532/graphite	-0.006	0.001	0.000	0.006	0.085	0.018
Uncoated NMC622/graphite	0.145	0.026	0.640	0.124	0.539	0.077
Al2O3-coated NMC622/graphite	0.521	0.050	1.543	0.032	0.909	0.073
HV-coated NMC622/graphite	-0.002	0.005	0.088	0.005	0.498	0.039

It was then considered what effect the release of oxygen has on the electrochemical behaviour of NMC materials. Uncoated NMC442 and single crystal NMC532 taken from pouch cells charged to 4.6 V were made into coin cells for electrochemical

characterisation. Further, an NMC electrode taken from the same pouch cells was thoroughly rinsed with DMC (see experimental section) then heated to 100°C for 3 h under vacuum and then made into additional coin cells. Figure 7.8 compares the cycling behaviour of the heat-treated and untreated NMC materials. The heat treatment is observed to decrease the maximum of the principle dQ/dV vs V peak at ~3.75 V. This peak is slightly shifted to lower cell voltages and has a smaller total area, representing a small loss of charge and energy densities. Although the general observations are the same between the two NMC materials, the magnitude of the effects of heating are significantly less for the single crystal NMC532 than for the uncoated NMC442. This is consistent with the TGA-MS results that show less oxygen is released from the single crystal NMC532 than the uncoated NMC442.
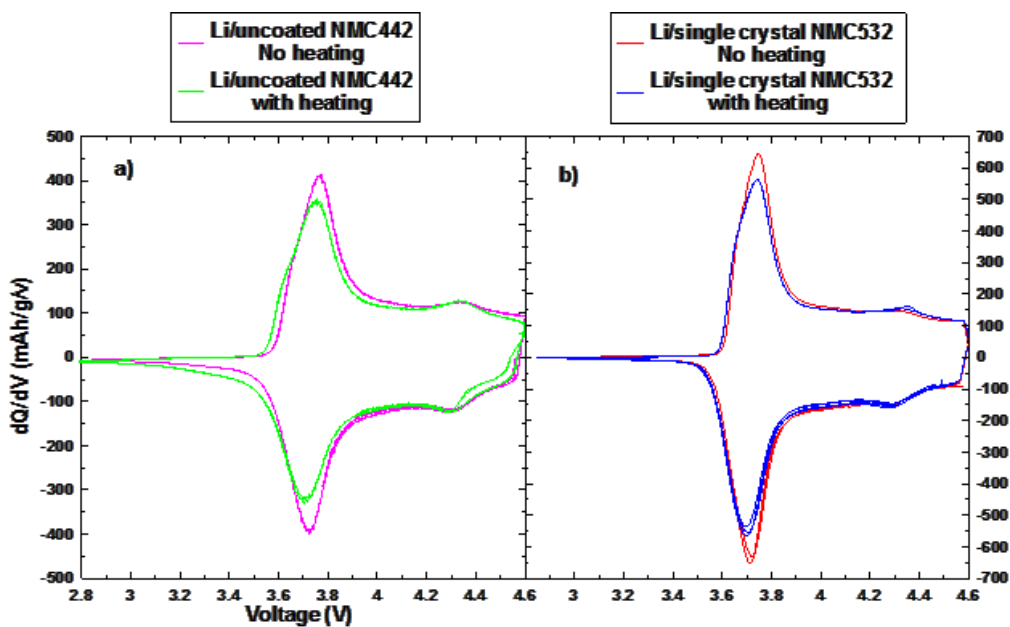
Figure 7.8 dQ/dV curves of Li/uncoated NMC442 where the electrodes were preheated and were not preheated (a) and Li/single crystal NMC532 where the electrode were preheated and were not preheated (b)

In order to gain more support for oxygen loss from NMC materials, XPS was used to analyze the samples with and without heat treatment shown in Figure 7.8. Figure 7.9 shows XPS spectra and relative chemical compositions of charged NMC442 and charged single crystal NMC532 positive electrodes, before and after prolonged exposure to 100°C. Figure 7.9a shows the O1s spectra of these electrodes. The NMC lattice oxygen peak, at 529.5 eV, is often used for determining the relative thickness of surface films on the positive electrode: a tall lattice oxygen peak indicates a thin surface coating; a small lattice oxygen peak indicates a thicker surface coating on the NMC. For both NMC442 and single crystal NMC532 electrodes, the peak at 529.2 eV is larger in the sample that was heated than in the sample which was not heated. This indicates that the positive electrode SEI is thinned upon prolonged exposure to 100°C. The lattice oxygen peaks from the single crystal NMC532 electrodes are smaller than those from the NMC442 electrodes, which is because of a proprietary surface coating, of unknown composition, on the single crystal NMC532. Figure 7.9b shows the region of the XPS spectra where 3p peaks from the transition metals (TM), Ni, Co and Mn, and the 1s peak of Li are observed. For both NMC442 and single crystal NMC532 electrodes, the transition metal peaks are taller in the samples that were heated to 100°C. This is further evidence that the SEI layer on top of the NMC positive electrodes is thinned upon heating.
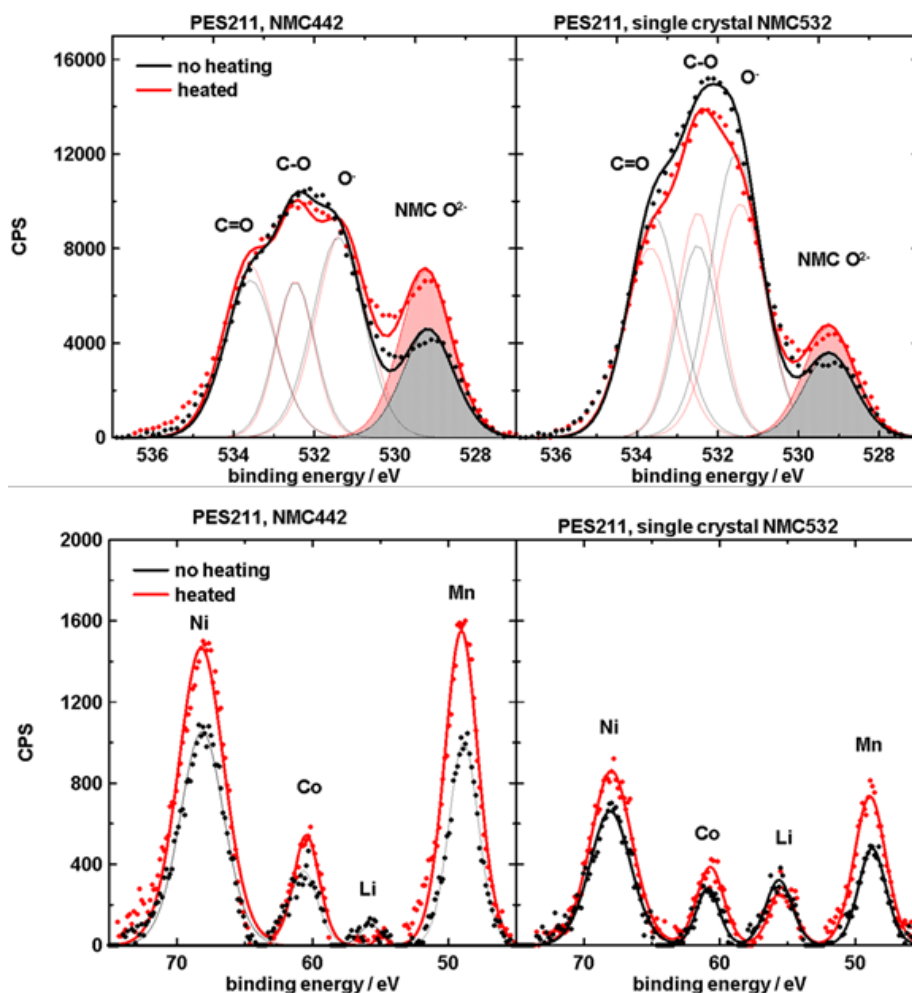
Figure 7.9 XPS spectra of charged NMC442 and charged single crystal NMC532 positive electrodes, before and after exposure to 100°C for 3 h.

Table 7.2 shows the relative atomic percent of chemical states observed by XPS analysis. The atomic species are separated in three parts: SEI and/or binder components (C, O, F and P), NMC components (TM and lattice O), and Li (which could be part of either the SEI or the NMC). Both NMC442 and single crystal NMC532 electrodes appear to lose a small amount of oxygen from the SEI region during heating, which could be a source of the observed O_2 and/or the CO_2 in the TGA-MS experiment. The ratio of the atomic percentage of lattice oxygen to the sum of atomic percentages of TM was

expected to decrease if oxygen was released from the surface of the NMC, and if the thickness of the overlaying SEI did not change. Since the thickness of the SEI appears to thin from heating, the IMFP of the O1s photoelectrons must be compared to the TM3p photoelectrons, in order to account for the change in O1s and TM3p peak areas, before conclusions about lattice oxygen loss can be made.

Table 7.2 The relative atomic percent of chemical species observed by XPS analysis

At%		NMC442		Single crystal NMC532	
		No heat	Heat	No heat	Heat
SEI + binder	C	50.1 ± 0.8	49.4 ± 0.8	49.5 ± 0.7	51 ± 0.7
	O	21.3 ± 0.5	19.3 ± 0.5	23.8 ± 0.5	21.4 ± 0.5
	F	16.4 ± 0.5	18.2 ± 0.5	14.4 ± 0.4	15.5 ± 0.4
	P	1.6 ± 0.2	1.8 ± 0.2	2.1 ± 0.2	1.6 ± 0.2
Li		3 ± 1	1 ± 1	6.1 ± 0.9	4.9 ± 0.9
NMC	O	4.8 ± 0.5	6.6 ± 0.5	3 ± 0.4	3.9 ± 0.4
	TM	2.53 ± 0.0.02	3.24 ± 0.02	1.15 ± 0.01	1.7 ± 0.01
	O:TM	1.9 ± 0.1	2.04 ± 0.08	2.6 ± 0.1	2.3 ± 0.1

Figure 7.10a shows the intensities of O1s and Mn3p photoelectrons, passing through a SEI of a thickness less than 10 nm. These were calculated using the IMFP of the O1s and Mn3p photoelectrons passing through an overlayer of organic SEI. The SEI stoichiometry was taken to be 5:2 C:O (from the XPS quantification, shown in table 7.2). The density of the SEI was assumed to be between 0.8 and 1.2 g/cm^3, and the band gap of the SEI was assumed to be between 4 and 7 eV. These values are expected to be

representative for an unconjugated organic polymer. The IMFP of the O1s photoelectron through the SEI was calculated to be between 2.2 and 2.6 nm, and the calculated IMFP of the Mn3p photoelectron through the SEI was calculated to be between 3.3 and 4.0 nm. Figure 7.10a shows that for an electrode with equal amounts of O and Mn, as the SEI thickens, the observed intensity of the O1s photoelectron would be lower than that of the Mn3p photoelectron. Figure 7.10b shows the O:TM atomic ratio that would be observed as a function of SEI overlayer thickness. Figures 7.10a and 7.10b show that thinning of an SEI overlayer would result in an increase in the observed O:TM atomic ratio. The O:TM atomic ratio of the electrodes in Figure 7.9 did not change upon heating, when the SEI was evidently thinned. This could be caused by loss of oxygen from the underlying positive electrode. However, since the precise thickness of the SEI overlayer is unknown, and the degree of its thinning is unknown, it is impossible with XPS analysis to convincingly conclude that lattice oxygen has been lost from the NMC surface.
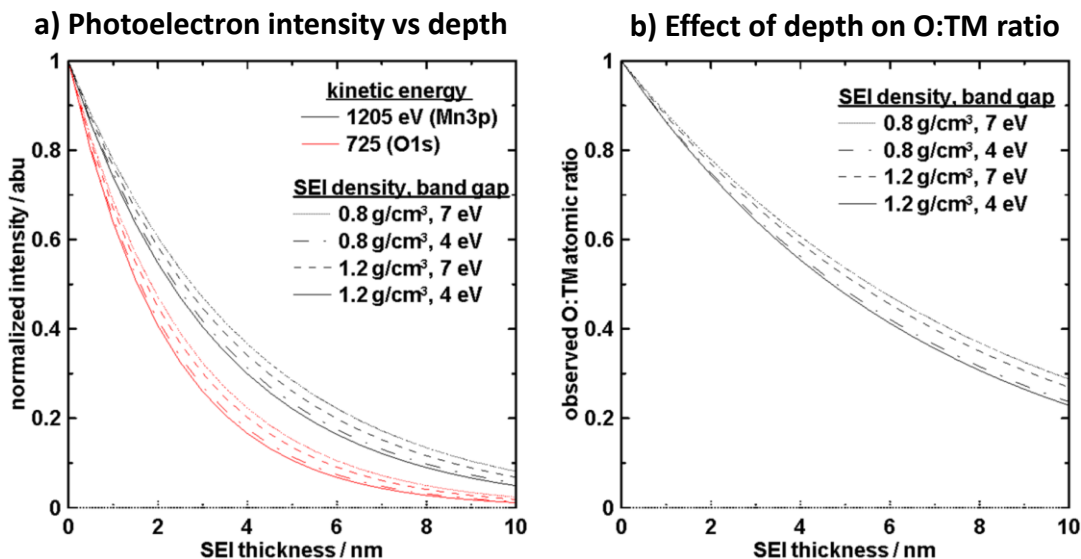
Figure 7.10 Calculated normalized photocurrents of O1s and Mn3p photoelectrons, after passing through a SEI of thickness 0 - 10 nm

It is important to compare the long term cycling between polycrystalline and single crystal NMC materials in Li-ion cells operated to 4.4 V at elevated temperature. Pouch cells were prepared from uncoated NMC442/graphite, which performed modestly in the TGA-MS measurements, and single crystal NMC532/graphite, on account of the exceptionally low oxygen release for this particular material. The results in Figure 7.11 demonstrate a clear performance difference between these two cell types. Whereas the single crystal `NMC532/graphite cell shows minimal capacity loss (< 5 %) or voltage hysteresis after more than 800 cycles, the NMC442/graphite cell shows ~15% capacity loss and significant hysteresis growth after just 400 cycles. These results are well-correlated with the predictions from the TGA-MS. This offers strong support for the hypothesis that the release of oxygen from the positive electrode material causes the deleterious effects observed at high cell voltage, especially the oxidative decomposition of the electrolyte.
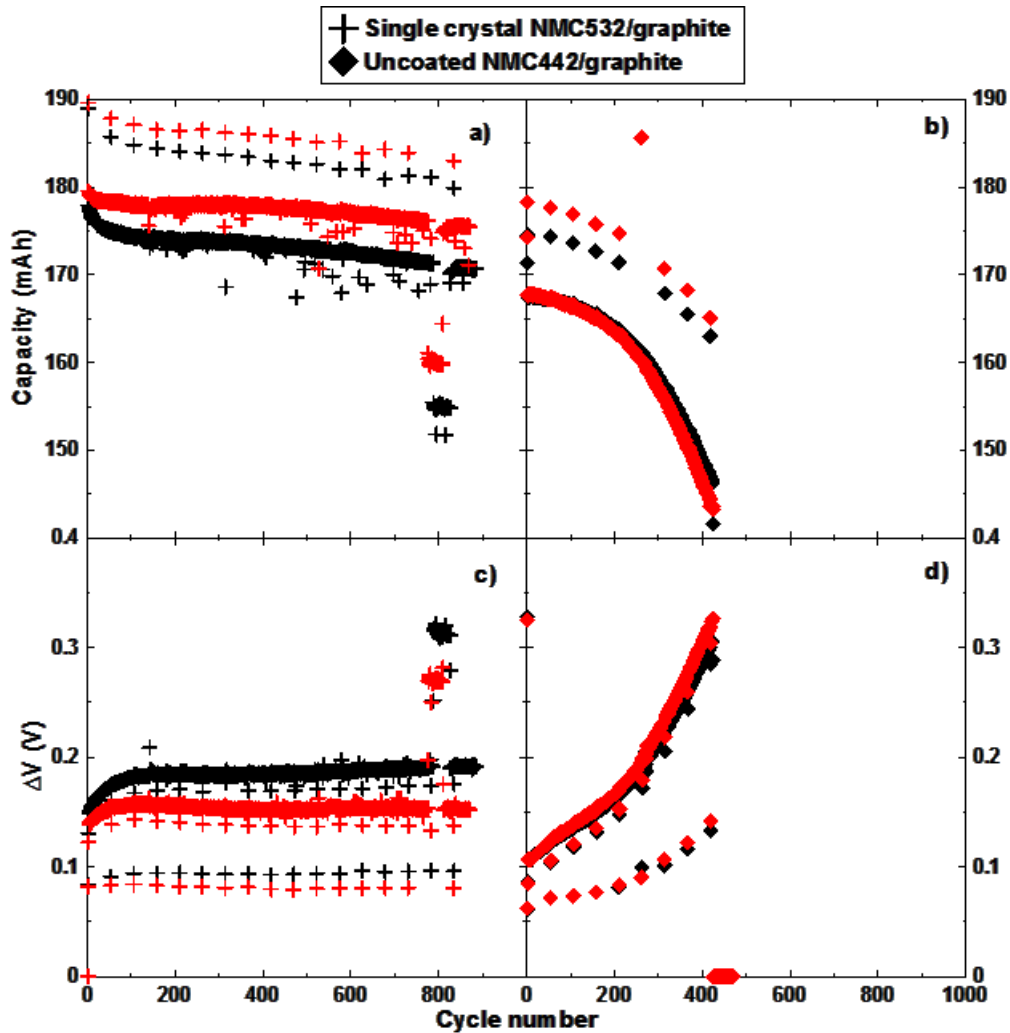
Figure 7.11 Cell capacity and difference between average charge and discharge voltages (ΔV) vs cycle number for single crystal NMC532/graphite cells (a, c) and uncoated NMC442/graphite cells (b, d) at C/2 using CCCV protocol at 40 °C between 2.8 and 4.4 V.

The main weight loss for the charged NMC electrode materials in the TGA-MS experiments is due to oxygen release above 170°C which is strongly associated with thermal runaway. Therefore, the weight loss can be used to evaluate the thermal stability of charged NMC electrodes. Figure 7.12 shows weight loss during the heating range for different NMC materials taken from the corresponding pouch cells at 4.2, 4.4 and 4.6 V. Figure 7.12 shows that higher Ni content and higher cut-off potential of NMC materials

causes more weight loss during the heating temperature range. This implies that higher cut-off potential and higher Ni content increase the reactivity between charged NMC electrode and electrolyte at elevated temperature, which is consistent with Ma et al's finding using accelerating rate calorimetry (ARC).[47]
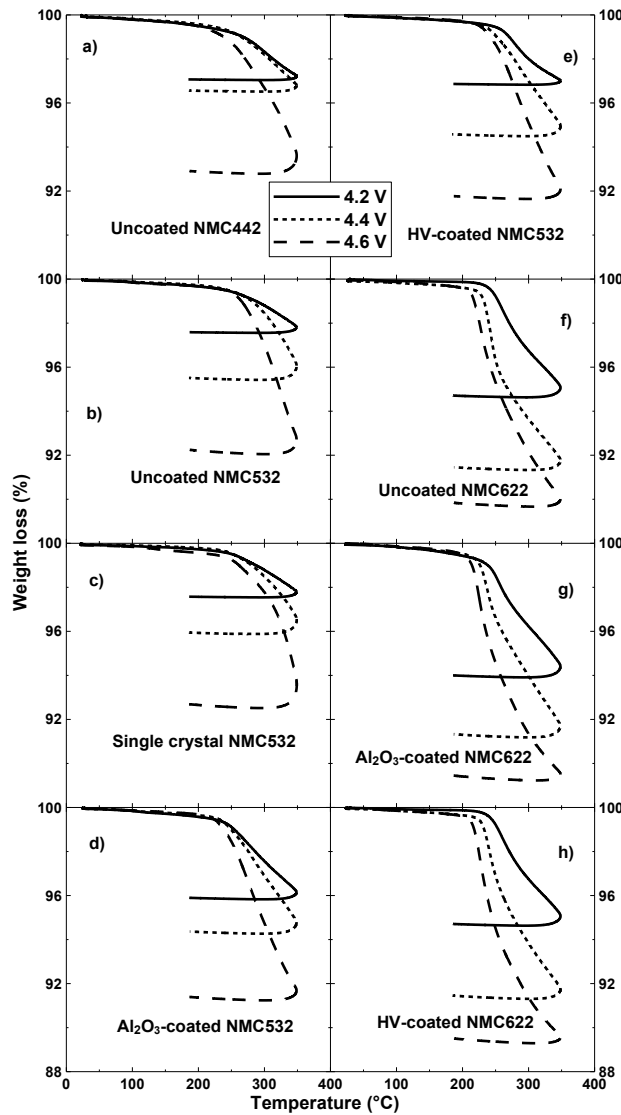
Figure 7.12 Weight loss versus temperature for uncoated NMC442 electrodes (a), uncoated NMC532 electrodes (b), single crystal NMC532 electrodes (c), Al_2O_3-coated NMC532 electrodes (d), HV-coated NMC532 electrodes (e), uncoated NMC622 electrodes (f), Al_2O_3-coated NMC622 electrodes (g) and HV-coated NMC622 electrodes (h) taken from the corresponding pouch cells at 4.2, 4.4 and 4.6 V. These samples were heated from room temperature to 350 °C at 10 °C/min in argon gas

143

7.3   Conclusions

TGA-MS measurements were used to demonstrate that oxygen is released from NMC electrode materials at high electrode potentials, i.e., low lithium content at temperatures as low as 40°C. The observation of this oxygen release offers strong support for the 'reactive electrode model,' in which the positive electrode itself acts as a reagent in the oxidative decomposition (pseudocombustion) of the electrolyte solution and the SEI. This oxidative decomposition of the solvent could be the major reason why high voltage cells generate gas and have poor capacity retention. Electrochemical measurements demonstrate a correlation between the TGA-MS results and the cycling performance of NMC/graphite cells. More surface techniques such as transmission electron microscopy should be used to investigate the underlying mechanisms of oxygen rease from NMC materials at high potentials.

.

CHAPTER 8: DRAMATIC EFFECTS OF LOW SALT CONCENTRATIONS ON LI-ION CELLS CONTAINING EC-FREE ELECTROLYTES

In this chapter, a study of different concentrations of $LiPF_6$ in EMC and EC-based electrolytes (0.3 - 2 M) was carried out. The electrolytes were used in NMC442/graphite pouch cells that were subjected to elevated temperature storage, charge-discharge and impedance spectroscopy studies. Pouch cells were taken apart so that symmetric cells could be constructed to learn at which electrode impedance increases originated. In order to achieve a fair comparison between these two different electrolyte systems at different salt concentrations, the same electrolyte additive blend with the same weight percentage was added to all electrolytes used. Ionic conductivity measurements versus salt concentration in EMC electrolyte (0.1 - 2.5 M) and EC-based electrolyte (0.002 - 0.2 M) were taken at various temperatures to gain insights on what salt concentrations should be used in EMC electrolytes to optimize cell performance and why the low salt concentrations in EMC electrolytes cause large cell impedance. The majority of this work was adapted from the following manuscript:

D.J. Xiong, T. Hynes, J.R. Dahn, Dramatic Effects of Low Salt Concentrations on Li-Ion Cells Containing EC-Free Electrolytes, J. Electrochem. Soc. 164 (2017) A2089–A2100. doi:10.1149/2.1381709jes.

Deijun Xiong prepared all the cells collaboratively with Toren Hynes. Deijun Xiong performed the conductivity measurements and the impedance measurements except the impedance measurements shown in Figure 8.8. Deijun Xiong analyzed all the data and

prepared all the figures. Jeff Dahn provided guidance and participated in experimental design and the interpretation of all the data. Deijun Xiong prepared the manuscript mentioned above and received revisions from Jeff Dahn.

8.1   Experimental

8.1.1   Electrolyte Components Used in this Work

In this chapter, various electrolytes were used for various purposes. In order to bring simplicity, a table was created to show the electrolytes used in this work and purpose of each. Furthermore, the electrolytes were labeled by convenient codes.

8.1.2   Pouch Cells, Formation and Degassing

The details of NMC442/graphite pouch cell construction, formation and degassing can be found in Section 3.1.5. However, the second degassing step for the cells in this chapter was slightly different. The cells were degassed again after they were charged to 4.5 V at C/20 and held for 1 h.

8.1.3   Storage Experiments

After cell impedance measurements, the cells with X_E_VC_TTSPi and X_EE_VC_TTSPi were discharged to 2.8 V and charged back to 4.5 V at C/20 and held at 4.5 V for 30 hours. They were then moved to a storage system and stored at 40 or 60°C for 500 h. Their open circuit voltage was monitored every 10 minutes for the first 6 h and every 6 h for the remaining 494 h.

Table 8.1 Electrolytes used in this work and purpose of each. Electrolyte are labeled by convenient code, for example: 0.3_E_VC_TTSPi means 0.3 M LiPF6 in EMC with 2% VC + 1% TTSPi; and 0.2 M_D means 0.2 M LiPF6 in DEC. Weight percentages for additives and solvents are used in this table.

Convenient codes for electrolytes used	LiPF$_6$ Molarity	Solvent 1	Solvent 2	Additive 1	Additive 2	Purpose of this electrolyte in this thesis	Cell types used in this thesis
X_E_VC_TTSPi	0.3, 0.5, 1, 1.5, 2	EMC	NA	2% VC	1% TTSPi	Storage, and various molalities of LiPF$_6$ in EMC on charge transfer resistance	Pouch cells
X_EE_VC_TTSPi	0.3, 0.5, 1, 1.5, 2	EC (30 %)	EMC (70 %)	2% VC	1% TTSPi	Storage and various molalities of LiPF$_6$ in EC/EMC on charge transfer resistance	Pouch cells
X_E_VC_TTSPi	0.5, 1, 1.5	NA	EMC	2% VC	1% TTSPi	Long time cycling	Pouch cells
X_EE_VC_TTSPi	0.5, 1, 1.5	EC	EMC	2% VC	1% TTSPi	Long time cycling	Pouch cells
X-E_VC_PPF	1	EMC	NA	2% VC	1% PPF	Precycling ten times	Pouch cells
X_E	0.1, 0.2, 0.3, 0.4, 0.6, 1, 1.5, 2, 2.5	EMC	NA	NA	NA	Ionic conductivity measurements	NA
X_E	0.2, 0.3, 2	EMC	NA	NA	NA	Impact of various molalities of LiPF$_6$ in EMC on charge transfer resistance	Coin full cells, +/+ and -/- symmetric cells
X_EE	0.002, 0.02, 0.2, 0.3, 1, 2	EC (30 %)	EMC (70 %)	NA	NA	Impact of various molalities of LiPF$_6$ in EC/EMC on charge transfer resistance	Coin full cells, +/+ and -/- symmetric cells
X_D	0.2, 1	DEC	NA	NA	NA	Impact of various molalities of LiPF$_6$ in DEC on charge transfer resistance	Coin full cells, +/+ and -/- symmetric cells
X_FT	0.2, 1	FEC (50 %)	TFEC (50 %)	NA	NA	Impact of various molalities of LiPF$_6$ in DEC on charge transfer resistance	Coin full cells, +/+ and -/- symmetric cells

8.1.4   Long Term Cycling Experiments

The NMC442/graphite pouch cells with 0.5_E_VC_TTSPi, 1_E_VC_TTSPi, 1.5_E_VC_TTSPi, 0.5_EE_VC_TTSPi, 1_EE_VC_TTSPi and 1.5_EE_VC_TTSPi after 500 h storage at 40°C were selected for long term cycling at 40°C between 2.8 and 4.4 V using a constant current of C/2.2. A constant voltage step was added at the top of charge and applied until the current dropped below C/20. A low rate C/10 cycle was also included every 50 cycles to estimate what fraction of the capacity loss was due to impedance growth during the high rate cycling.

8.1.5   Electrochemical Impedance Spectroscopy Measurements of Pouch Cells, Coin Full Cells and Symmetric Cells

NMC442/graphite pouch cells with 0.3_E_VC_TTSPi, 2_E_VC_TTSPi, 0.3_EE_VC_TTSPi and 2_EE_VC_TTSPi after 500 h storage at 40°C were first equilibrated at 3.8 V. They were then moved to an argon filled glove box and disassembled there. The harvested positive and negative electrodes from the pouch cells were used to construct NMC442/graphite coin full cells, NMC442/NMC442 and graphite/graphite symmetric cells with 0.3_E, 2_E, 0.3_EE or 2_EE electrolytes. Eight nominally identical NMC442/graphite pouch cells with 1_E_VC_PPF electrolyte underwent the two degassing steps and then were given ten charge-discharge cycles between 2.8 and 4.5 V at 40°C at a rate of C/10. Then the cells were equilibrated at 3.8 V and opened in the argon-filled glove box to make coin full cells and symmetric cells with 0.2_E, 1_E, 0.2_D, 1_D, 0.2_EE, 1_EE, 0.2_FT and 1_FT electrolytes. The harvested electrodes for symmetric cells and rebuilt coin full cells mentioned above were washed using DMC two or three times to remove the residual electrolyte from the electrodes.

Two "brother" NMC442/graphite pouch cells with 1_E_VC_PPF underwent the two degassing steps and were then equilibrated at 3.8 V. The cells were moved to the glove box and disassembled there to make coin full cells with 0.2_E, 0.2_EE, 0.02_EE and 0.002_EE. The harvested electrodes used for coin full cells with 0.02_EE and 0.002_EE were washed six times using DMC to completely remove any remaining $LiPF_6$ in the electrodes.

In most cases, more than two symmetric and coin full cells of each type were made to ensure repeatability. Most EIS measurements were conducted using a Biologic VMP-3 potentiostat, in a two wire configuration with ten points per decade from 100 kHz to 100 mHz or 10 mHz using a 10 mV input signal amplitude. The two wire configuration was used because this VMP3 is connected to a switching system that allows 16 cells to be measured automatically in sequence. The lead resisatnce (about 1 Ω) is very small compared to the impedances of the coin-type cells measured here. However, to probe the impact of low electrolyte conductivity, some EIS measurements were made using a Biologic SP150 potentiostat in 4-wire mode with ten points per decade from 100 kHz to 5.1 mHz using a 10 mV input signal amplitude. The EIS spectra for all the coin full cells were measured at 3.8 V. All EIS spectra were collected at 10°C. This temperature was chosen to magnify the difference between the impedances of the cells.

8.1.6 Determination of Gas Evolution in Pouch Cells

Procedures for *ex situ* gas measurements were described in Section 3.4.

8.1.7 Conductivity Measurements

The conductivity of EMC electrolyte with different concentrations of $LiPF_6$ was measured using a conductivity meter (METTLER TOLEDO, FE30). Three different standards (84 μS/cm, 1413 μs/cm and 12.88 mS/cm) were used for calibration. A temperature controlled bath (VWR

Scientific, Model 1157) was used to adjust the temperature. After the desired temperature was reached, the conductivity readings were recorded at least twice to ensure that the readings were stable.

8.2 Results and Discussion

Figure 8.1 shows the dQ/dV vs. V curves of NMC442/graphite cells with X_E_VC_TTSPi or X_EE_VC_TTSPi electrolytes during the formation cycle. Sinha *et al.* found that there were clear interactions between VC and TTSPi.[224] Therefore, it was difficult to assign reduction peaks for VC and TTSPi, respectively. Figure 8.1 shows that the reduction peak of the additives shifts slightly to higher voltage as the concentration of LiPF$_6$ increases in both electrolytes, which corresponds to a lower potential vs Li$^+$/Li.
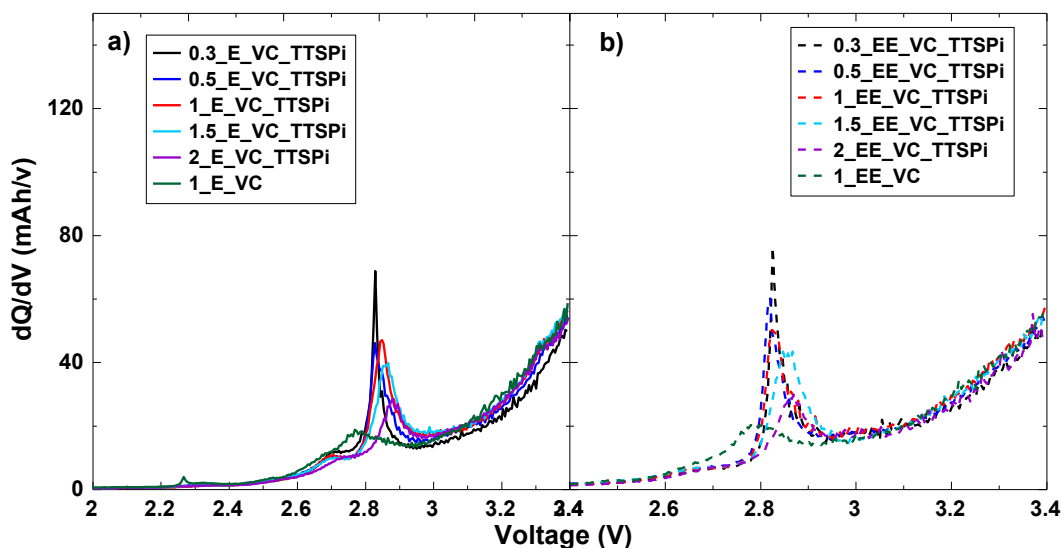
Figure 8.1 dV/dQ versus V for NMC442/graphite pouch cells with X_E_VC_TTSPi (X=0.3, 0.5, 1, 1.5 and 2 M LiPF$_6$), X_E_VC (X=1 M), X_EE_VC_TTSPi (X=0.3, 0.5, 1, 1.5 and 2 M LiPF$_6$) or X_EE_VC (X=1 M). This data was collected during the first formation step (degassing step) of the cells at C/20 and 40°C.

It is of importance to minimize gas generation in pouch cells. Figure 8.2 shows the volume of gas produced in the cells of Figure 8.1 during the two steps of formation (a, b) and during the

500 h storage periods at 4.5V at both 40 and 60°C (c, d). Figures 8.2a and 8.2b show that the concentration of $LiPF_6$ does not strongly affect gas generation during formation. Figures 8.2c and 8.2d show that the volume of gas generated during 500 h storage increases as the concentration of $LiPF_6$ increases at both temperatures, for cells containing both X_E_VC_TTSPi and X_EE_VC_TTSPi electrolytes. Much more gas was observed after 500 h of storage at 60°C compared to 40°C. This is due to more severe electrolyte oxidation at higher temperature.
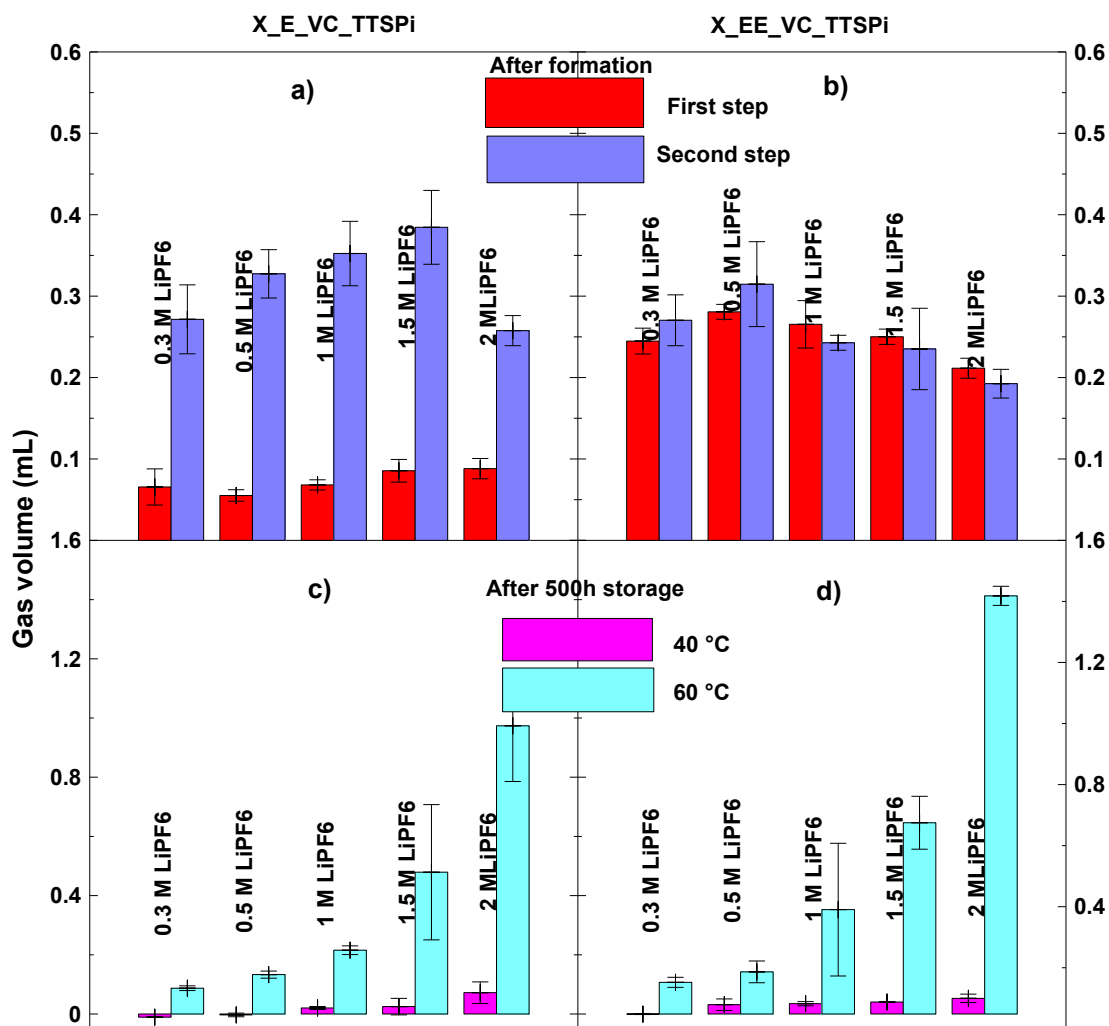
Figure 8.2 Volume of gas created in NMC442/graphite pouch cells with X_E_VC_TTSPi (X=0.3, 0.5, 1, 1.5 and 2 M $LiPF_6$) or X_EE_VC_TTSPi (X=0.3, 0.5, 1, 1.5 and 2 M $LiPF_6$) during the first formation step, the second formation step and after 500 h storage at 40 or 60°C. These open circuit storage experiments were made at an initial cell voltage of 4.5 V.

Figure 8.3 shows the open circuit voltage versus time of NMC442/graphite cells with X_E_VC_TTSPi and X_EE_VC_TTSPi electrolytes during the 500 h storage periods at 40°C and 60°C. Figure 8.4 summarizes the voltage drop during storage. The voltage drop during open circuit storage mainly originates from electrolyte oxidation at the positive electrode which causes lithium ions to intercalate into the positive electrode to combine with electrons from the electrolyte oxidation. [110] Figure 8.4 shows that higher concentrations of $LiPF_6$ cause a slightly greater voltage drop suggesting that higher concentrations of $LiPF_6$ cause slightly larger parasitic reaction rates at the positive electrode.
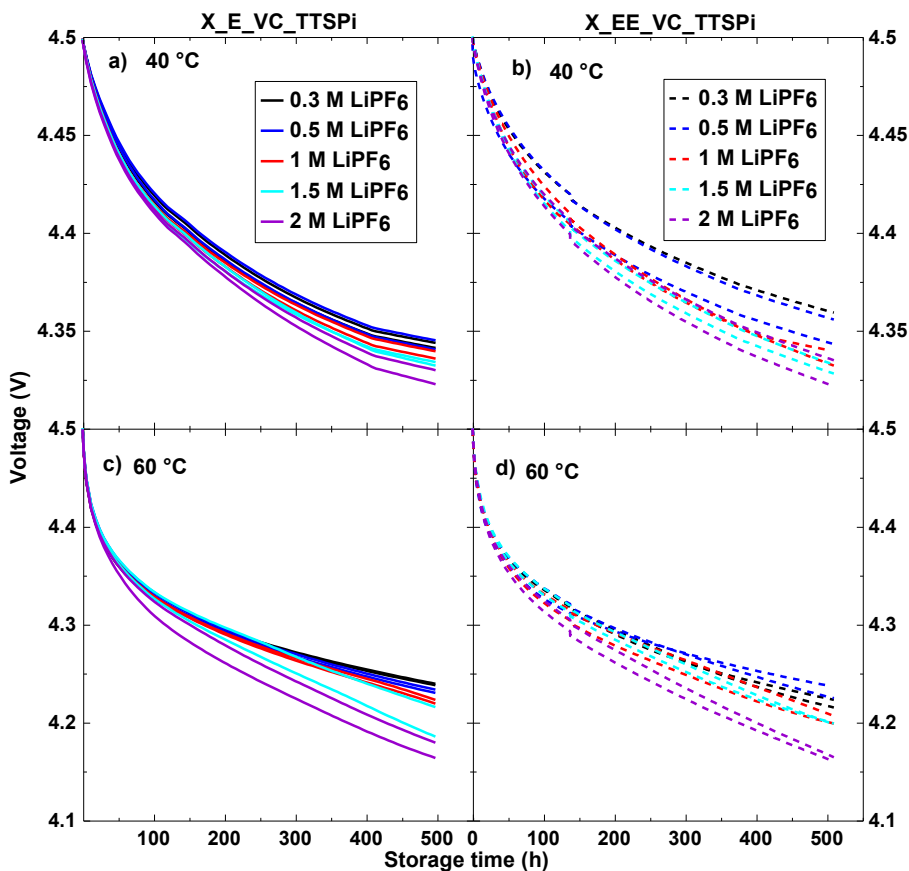
Figure 8.3 Open circuit voltage vs time for NMC442/graphite pouch cells with X_E_VC_TTSPi (0.3, 0.5, 1, 1.5 and 2M $LiPF_6$) or X_EE_VC_TTSPi (0.3, 0.5, 1, 1.5 and 2M $LiPF_6$). stored at 40 or 60°C.
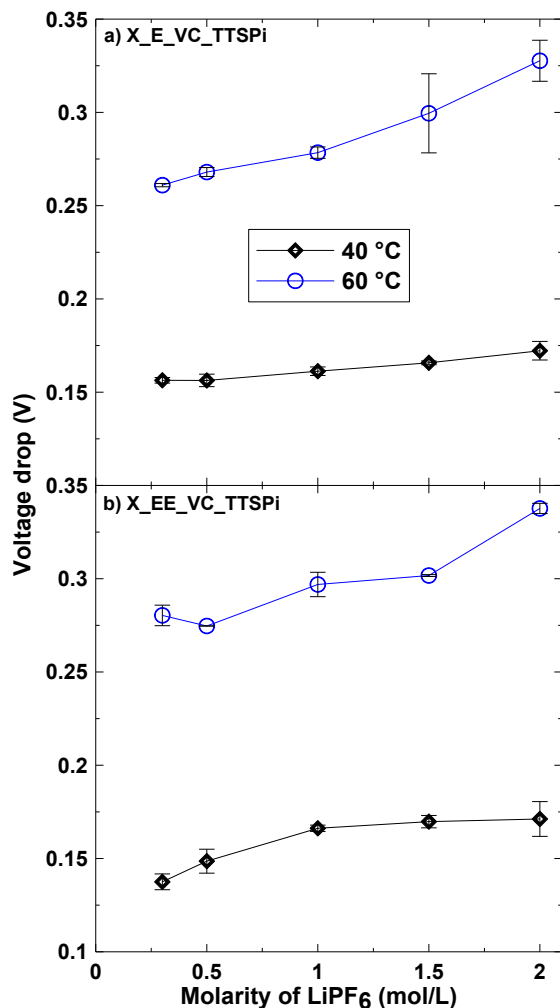
Figure 8.4 Summary of voltage drop during storage at 40°C or 60°C for NMC442/graphite pouch cells with X_E_VC_TTSPi (X=0.3, 0.5, 1, 1.5 and 2 M LiPF$_6$) or X_EE_VC_TTSPi (X=0.3, 0.5, 1, 1.5 and 2 M LiPF$_6$)

Figure 8.5 shows the area-specific Nyquist plots of NMC442/graphite pouch cells with X_E_VC_TTSPi and X_EE_VC_TTSPi electrolytes collected after formation and after the 500 h storage experiments described by Figures 8.1 and 8.3. The impedance spectra were measured at 3.8 V at 10°C. The width of the overlapping semicircles represents the sum of R_{ct} of the positive and negative electrodes. The first semicircle at higher frequency originates from the negative electrode while the second semicircle at the lower frequency range is due to the positive electrode.[111,225] Figure 8.5 shows that R_{ct} of NMC442/graphite pouch cells with

X_E_VC_TTSPi or X_EE_VC_TTSPi electrolytes decreases as the concentration of $LiPF_6$ increases. This is consistent with Wang *et al.*'s findings for LCO/graphite pouch cells.[226] Figures 8.5d and 8.5f show that R_{ct} of NMC442/graphite pouch cells after storage with 0.3_EE_VC_TTSPi is much larger compared to other concentrations of $LiPF_6$ in X_EE_VC_TTSPi. The impedance spectra in Figures 8.5d and 8.5f for cells with 0.3_EE_VC_TTSPi are well separated into two "semicircles" where the second semicircle at the lower frequency, due to the positive electrode, is much larger than the first semicircle, due to the negative electrode, at higher frequency. However, R_{ct} of NMC442/graphite pouch cells with 0.3_E_VC_TTSPi does not separate into two semicircles. This suggests that R_{ct} originating from the positive electrode does not dominate the impedance spectra of cells with 0.3_E_VC_TTSPi electrolyte. The reasons for the differences in the impedance spectra as a function of salt content in these cells will be discussed in more detail in the text pertaining to Figures 8.8, 8.9, 8.10 and 8.1
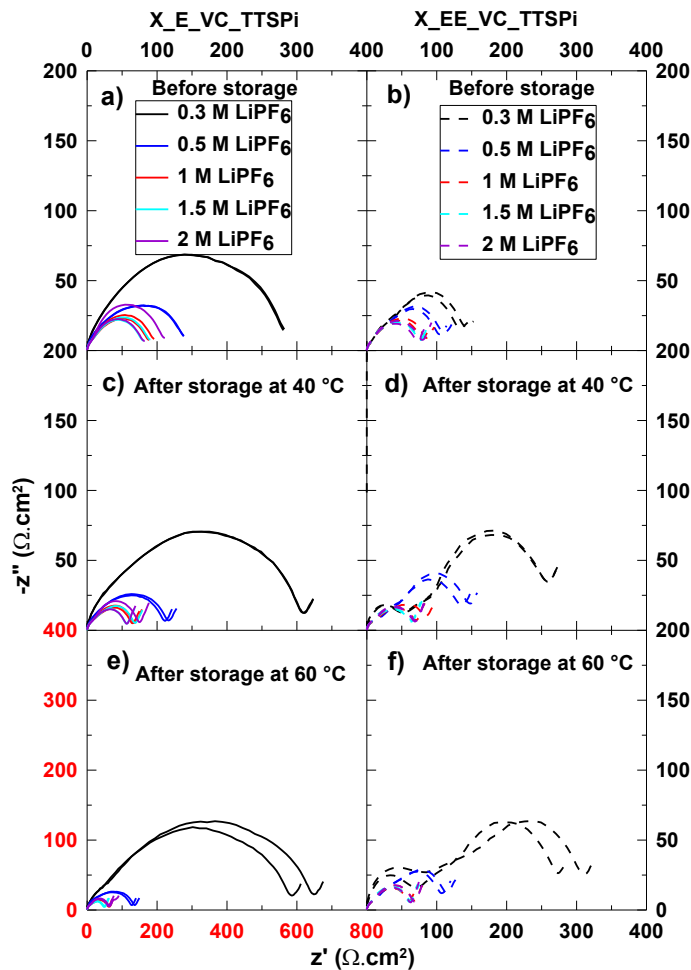
Figure 8.5 Area-specific Nyquist plots for NMC442/graphite pouch cells with X_E_VC_TTSPi (X=0.3, 0.5, 1, 1.5 and 2 M LiPF$_6$) or X_EE_VC_TTSPi (X=0.3, 0.5, 1, 1.5 and 2 M LiPF$_6$) before and after 500 h storage at 40 or 60°C. These open circuit storage experiments were made at an initial cell potential of 4.5 V. The impedance spectra of these cells were measured at 3.8 V at 10.°C.

Figure 8.6 shows discharge capacity vs cycle number for NMC442/graphite pouch cells tested at 40°C and 55°C. The cells in Figure 8.6 contained 0.5_E_VC_TTSPi, 1_E_VC_TTSPi, 1.5_E_VC_TTSPi, 0.5_EE_VC_TTSPI, 1_EE_VC_TTSPi and 1.5_EE_VC_TTSPi electrolytes. These cells were cycled between 2.8 and 4.4 V at C/2.2 using the CCCV cycling protocol described in the experimental section. At 55°C, the cells with EMC electrolyte had better capacity retention than those with the same salt concentration in EC/EMC electrolyte. The cells containing 0.5_E_VC_TTSPi or 0.5_EE_VC_TTSPi electrolyte experienced rapid capacity fade

at both testing temperatures. Nelson *et al.* [15] Ma *et al.* [14] and others [227–229] have shown that the major reason for rapid capacity loss in NMC/graphite cells tested at 55°C and to 4.4 V and above is impedance growth, not Li-inventory loss. Day *et al.* [230] showed that depletion of LiPF$_6$ salt occurred during aggressive charge-discharge cycling to 4.5 V in NMC442/graphite cells at 55°C. If this occurs, it is certainly important to know how both the electrolyte conductivity and the electrode charge transfer impedances depend on salt concentration. Increasing the salt concentration to 1.5 M improved capacity retention in both cases. This is consistent with Petibon *et al.*'s findings that higher concentrations of LiPF$_6$ help prevent impedance growth at the positive electrode when cells are cycled to 4.5 V. [201]
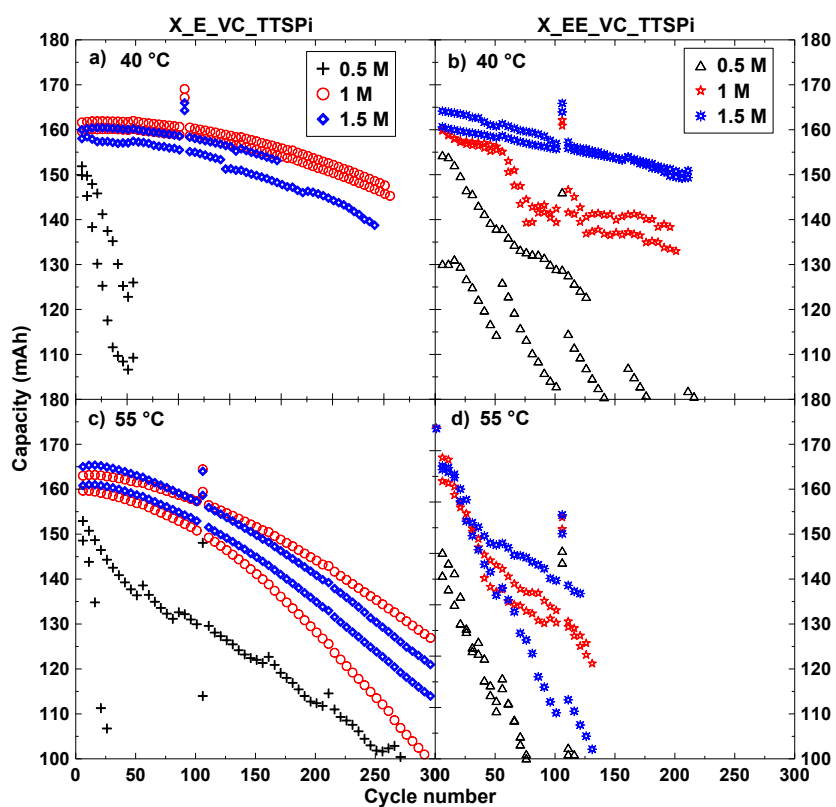
Figure 8.6 Discharge capacity versus cycle number for NMC442/graphite pouch cells with X_E_VC_TTSPi (X=0.5, 1 and 1.5 M LiPF$_6$) or X_EE_VC_TTSPi (X=0.5, 1 and 1.5 M LiPF$_6$). These cells were cycled between 2.8 and 4.4 V at C/2.2 using CCCV protocol at the temperatures indicated in the Figure legends.

Ding et al.[231,232] have measured the conductivity versus salt concentration and temperature of LiPF$_6$:EC:EMC and LiPF$_6$:PC:DEC solutions. Such solutions show "textbook" behavior, with conductivity increasing linearly with salt content at low concentration and then reaching a maximum and declining as ion pairing and viscosity increase. By contrast, a search of the literature did not reveal any measurements for the conductivity of LiPF$_6$/EMC solutions versus molarity and temperature. Therefore, measurements were made over a wide range of LiPF$_6$ (0.1 - 2.5 M) concentrations over a wide range of temperature. Figure 8.7 shows the conductivity of X_E electrolytes versus molarity and temperature. Figure 8.7 shows that the conductivity of X_E electrolyte drops dramatically when the concentration of LiPF$_6$ decreases below 0.4 M, completely unlike the results for LiPF$_6$:PC:DEC electrolytes described by Ding et al. [232]. The conductivity versus molarity results for X_E electrolytes are very similar to the results described by Doucey et al. for the conductivity of LiAsF$_6$/DMC solutions at low salt concentrations measured at 25°C.[233] Both EMC and DMC have low dielectric constants of 2.958 and 2.805, respectively [32] so the dissociation of LiPF$_6$ or LiAsF$_6$ is likely poor at low molarity which could explain the extremely low conductivity at low molarity observed in Figure 8.7. Figure 8.7 also shows that 1.5_E electrolyte has optimum conductivity over a wide temperature range, suggesting 1.5_E should be used in cells with EC-free electrolytes based on EMC.
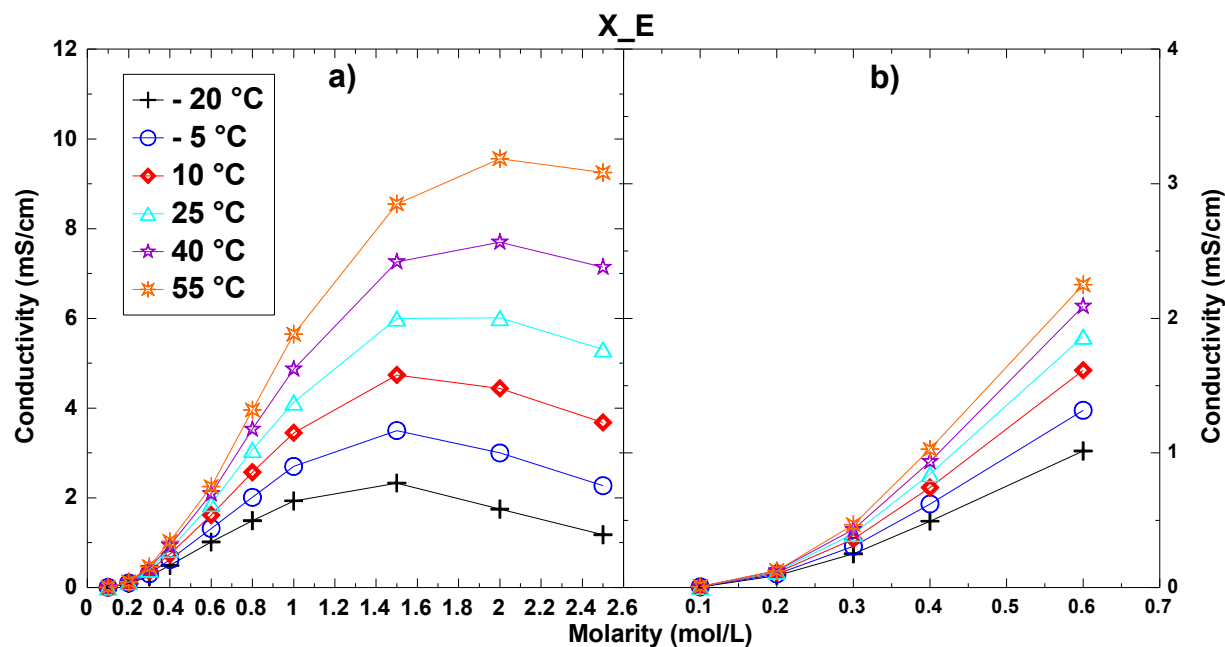
Figure 8.7 Ionic conductivity of X_E electrolytes (X=0.1, 0.2, 0.3, 0.4, 0.6, 1, 1.5, 2 and 2.5 M LiPF$_6$) measured at -20°C, -5°C , 10°C, 25°C, 40°C and 55°C using a conductivity meter.

Figure 8.8 shows the area-specific Nyquist plots of the reassembled negative/negative and positive/positive symmetric cells and coin full cells with 0.3_E (a, e, i) and 2_E (b, f, j) electrolytes where the electrodes were taken from the two "brother" pouch cells with 0.3_E_VC_TTSPi electrolytes. These two "brother" cells were stored at 40°C for 500 h and their impedance spectra, shown in Figure 8.5c, have been plotted in Figure 8.8a for comparison The symmetric cells and coin full cells with 0.3_E electrolyte had larger impedance than the corresponding ones with 2_E. Figure 8.8 shows the impedance spectra of the reassembled negative/negative and positive/positive symmetric cells and coin full cells with 0.3_E (c, g, k) and 2_E (d, h, l) electrolytes where the electrodes were taken from brother pouch cells with 2_EE_VC_TTSPi electrolyte. These two "brother" cells were stored at 40°C for 500 h and their impedance spectra, shown in Figure 8.5c, have been plotted in Figure 8.8d for comparison. The symmetric cells and coin full cells with 0.3_E electrolyte had much larger impedance than the

corresponding ones with 2_E as well. The coin full cells and symmetric cells using 0.3_E electrolyte (compare Figures 8.8a and 8.8c; compare Figures 8.8e and 8.8g; compare Figures 8.8i and 8.8k) had roughly the same impedance even though the electrodes were taken from pouch cells that initially had very different LiPF$_6$ concentration electrolytes. This clearly demonstrates that the LiPF$_6$ concentration in EMC can greatly affect R$_{ct}$ in symmetric cells even when the electrodes used for the symmetric cells have very different histories.

Figure 8.8 Area-specific Nyquist plots of reassembled NMC442/graphite full cells, NMC442/NMC442 and graphite/graphite symmetric cells where the electrodes were taken from pouch cells with 0.3_E_VC_TTSPi or 2_E_VC_TTSPi electrolytes equilibrated at 3.8 V. The impedance of the NMC442/NMC442 and graphite/graphite symmetric cells has been divided by two. The pouch cells were stored at 4.5 V for 500 h at 40°C prior to disassembly. The reassembled cells either contained 0.3_E or 2_E electrolyte.

Figure 8.9 shows the area-specific Nyquist plot of reassembled negative/negative symmetric cells, positive/positive symmetric cells and coin full cells with 0.3_EE and 2_EE electrolytes where the electrodes were taken from the "brother" pouch cells with 0.3_EE_VC_TTSPi electrolyte. These two "brother" pouch cells were stored at 40°C for 500 h and their impedance spectra, shown in Figure 8.5d, have been plotted in Figure 8.9a for comparison. Figure 8.9 shows that the positive electrode contributes most to the full cell impedance. Corresponding symmetric cells and coin full cells with 0.3_EE had roughly the same impedance as those with 2_EE (Compare Figures 8.9a and 8.9b; compare Figures 8.9e and 8.9f; compare Figures 9.8i and 9.8j). Figure 8.9 also shows the area-specific Nyquist plot of negative/negative symmetric cells, positive/positive symmetric cells and coin full cells with 0.3_EE and 2_EE electrolytes where the electrodes were taken from brother pouch cells with 2_EE_VC_TTSPi electrolyte. These two "brother" pouch cells were stored at 40°C for 500 h and their impedance spectra, shown in Figure 8.9d, have been plotted in Figure 8.9d for comparison. The symmetric cells and coin full cells with 0.3_EE had roughly the same impedance as the corresponding ones with 2_EE (Compare Figures 8.9c and 8.9d; compare Figures 8.9g and 8.9h; compare Figures 8.9k and 8.9l). Figures 8.9a, 8.9b, 8.9i and 8.9j show that the large R_{ct} in the full cells with 0.3_EE_VC_TTSPi after storage is caused by the large positive electrode impedance and that this is not affected by the salt concentration used in the symmetric cells during the impedance measurement. Similarly, Figures 8.9c, 8.9d, 8.9k and 8.9l show that the modest R_{ct} in the full cells with 2_EE_VC_TTSPi after storage is mirrored by modest positive electrode impedance and that this is not affected by the salt concentration used in the symmetric cells during the impedance measurement.

Figure 8.8 is important because it shows that charge transfer resistance at either electrode is always large when measured in pouch cells, coin full cells or symmetric cells when the cells

contain 0.3_E or 0.3_VC_TTSPi electrolytes, no matter the prior history of the pouch cells prior to symmetric cell construction. Figure 8.8 also shows that that charge transfer resistance at either electrode is always small when measured in pouch cells, coin full cells or symmetric cells when the cells contain 2_E or 2_E_VC_TTSPi electrolytes, no matter the prior history of the pouch cells prior to symmetric cell construction. Figure 8.9 shows that the charge transfer resistance is only high for the positive electrodes taken after storage from pouch cells containing 0.3_EE_VC_TTSPi while it is not high if the positive electrodes were extracted after storage from a pouch cells containing 2_EE_VC_TTSPi. Therefore, in EC-free, EMC based electrodes, the large charge transfer resistance appears to be caused by the presence of low salt concentration during measurement, which is a surprising result while in EC:EMC electrolyte low salt concentration during elevated temperature storage at 4.5 V leads to high positive electrode charge transfer resistance, no matter how it is measured afterwards, provided EC:EMC electrolytes are used in the symmetric cells. To further confirm these observations, the experiments below were performed.
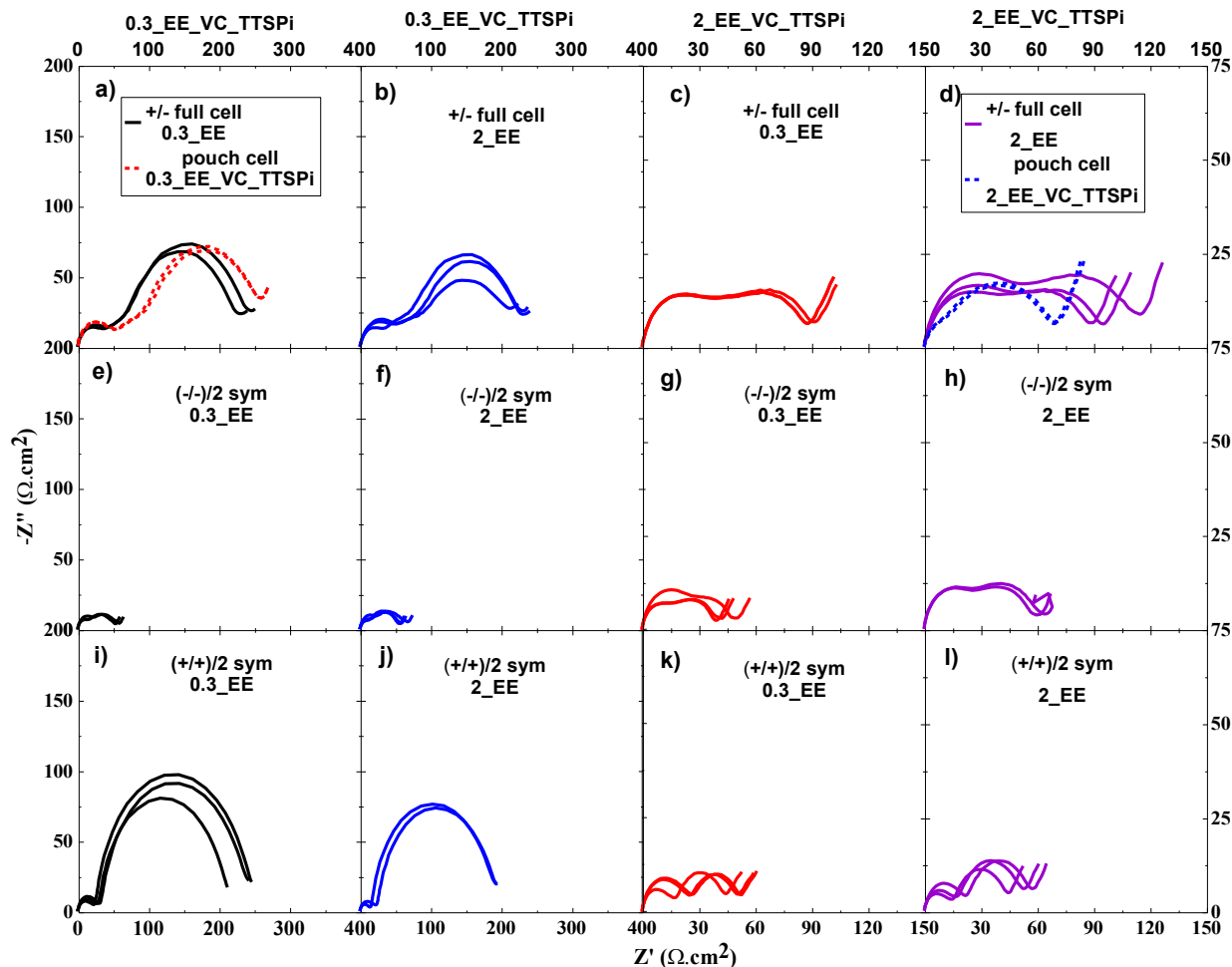
Figure 8.9 Area-specific Nyquist plots of reassembled NMC442/graphite full cells, NMC442/NMC442 and graphite/graphite symmetric cells where the electrodes were taken from pouch cells with 0.3_EE_VC_TTSPi or 2_EE_VC_TTSPi electrolytes equilibrated at 3.8 V. The impedance of the NMC442/NMC442 and graphite/graphite symmetric cells has been divided by two. The pouch cells were stored at 4.5 V for 500 h at 40°C prior to disassembly. The reassembled cells either contained 0.3_EE or 2_EE electrolyte.

Figure 8.10 shows the area-specific Nyquist plots of reassembled full cells, positive/positive symmetric cells and negative/negative symmetric cells filled with 0.2_E, 0.2_D, 0.2_EE and 0.2_TF electrolytes. Figure 8.11 shows the area-specific Nyquist plots of reassembled full cells, positive/positive symmetric cells and negative/negative symmetric cells filled with 1_E, 1_D, 1_EE and 1_TF electrolytes. The electrodes used to make the various coin cells in Figures 8.10 and 8.11 were harvested from "brother" pouch cells that contained 1_E_VC_PPF electrolyte

after ten charge discharge cycles. Figure 8.10 shows that the charge transfer impedance of both the positive and negative electrodes are much larger when measured in 0.2_E or 0.2_D electrolytes than in 0.2_EE or 0.2_TF electrolyte. The reader should note the large differences in horizontal scale between those of Figures 8.10a, 8.10b, 8.10e, 8.10f, 8.10i and 8.10j compared to those of Figures 8.10c, 8.10d, 8.10g, 8.10h, 8.10k and 8.10l. By contrast, Figure 8.11 shows that all the charge transfer impedances of symmetric and coin full cells with 1_E, 1_D, 1_EE and 1_TF electrolytes are roughly the same. The electrodes for all the reassembled symmetric cells and coin full cells in Figures 8.10 and 8.11 were taken from "brother" cells and experienced the same rinsing procedure, so the SEI at these electrodes were roughly the same before coin cell construction. This further verifies that low $LiPF_6$ concentration in EC-free linear alkyl carbonate electrolytes, based on EMC or DEC, causes large charge transfer impedance.
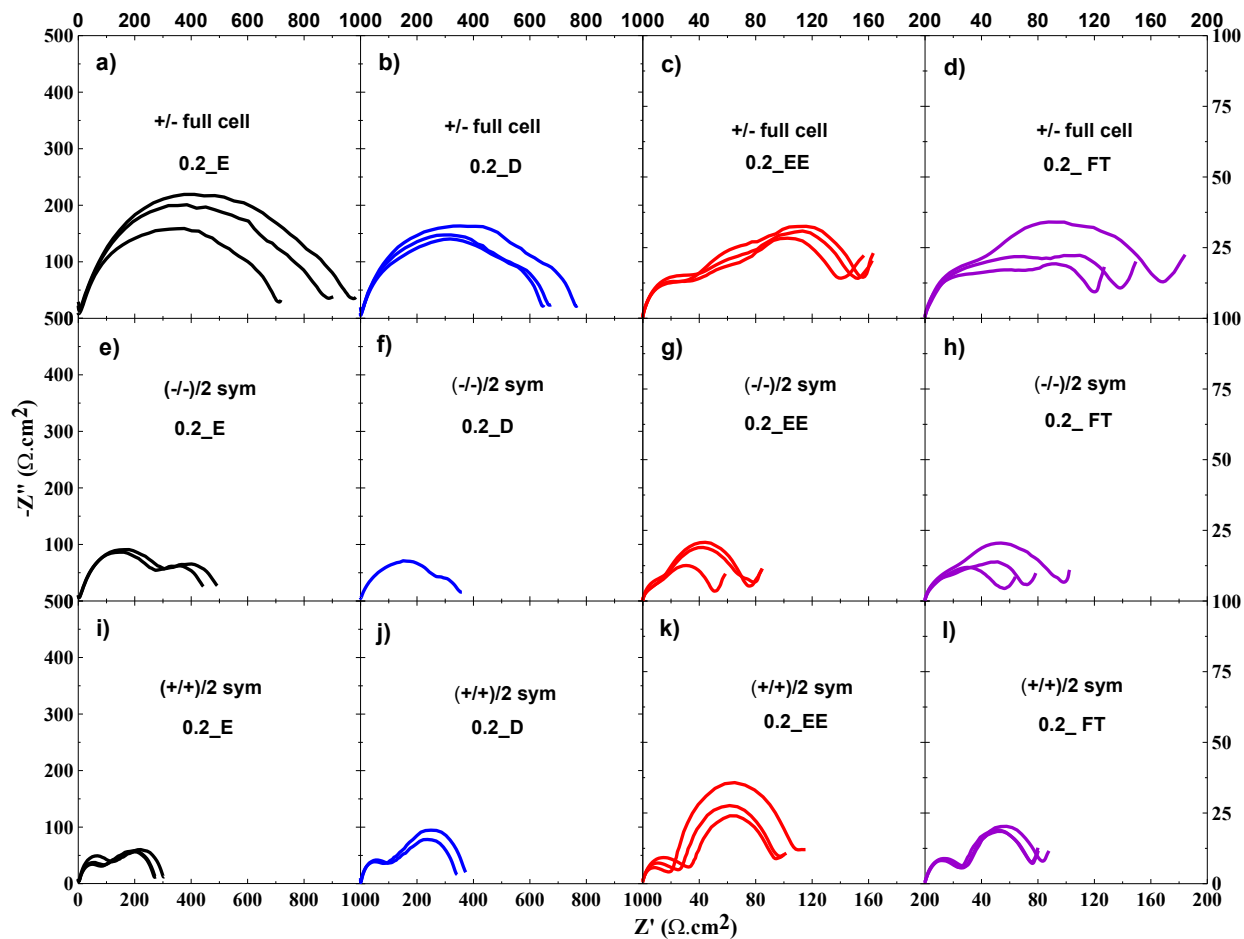
Figure 8.10 Area-specific Nyquist plots of reassembled NMC442/graphite full cells, NMC442/NMC442 and graphite/graphite symmetric cells where the electrodes were taken from pouch cells with 1_E_VC_PPF which had 10 charge-discharge cycles between 2.8 and 4.5 V at C/10 and 40°C. The cells were equilibrated at 3.8 V prior to disassembly. The impedance of the NMC442/NMC442 and graphite/graphite symmetric cells has been divided by two. The reassembled coin cells either contained 0.2_E, 0.2_D, 0.2_EE or 0.2_TF electrolytes as indicated in the legend
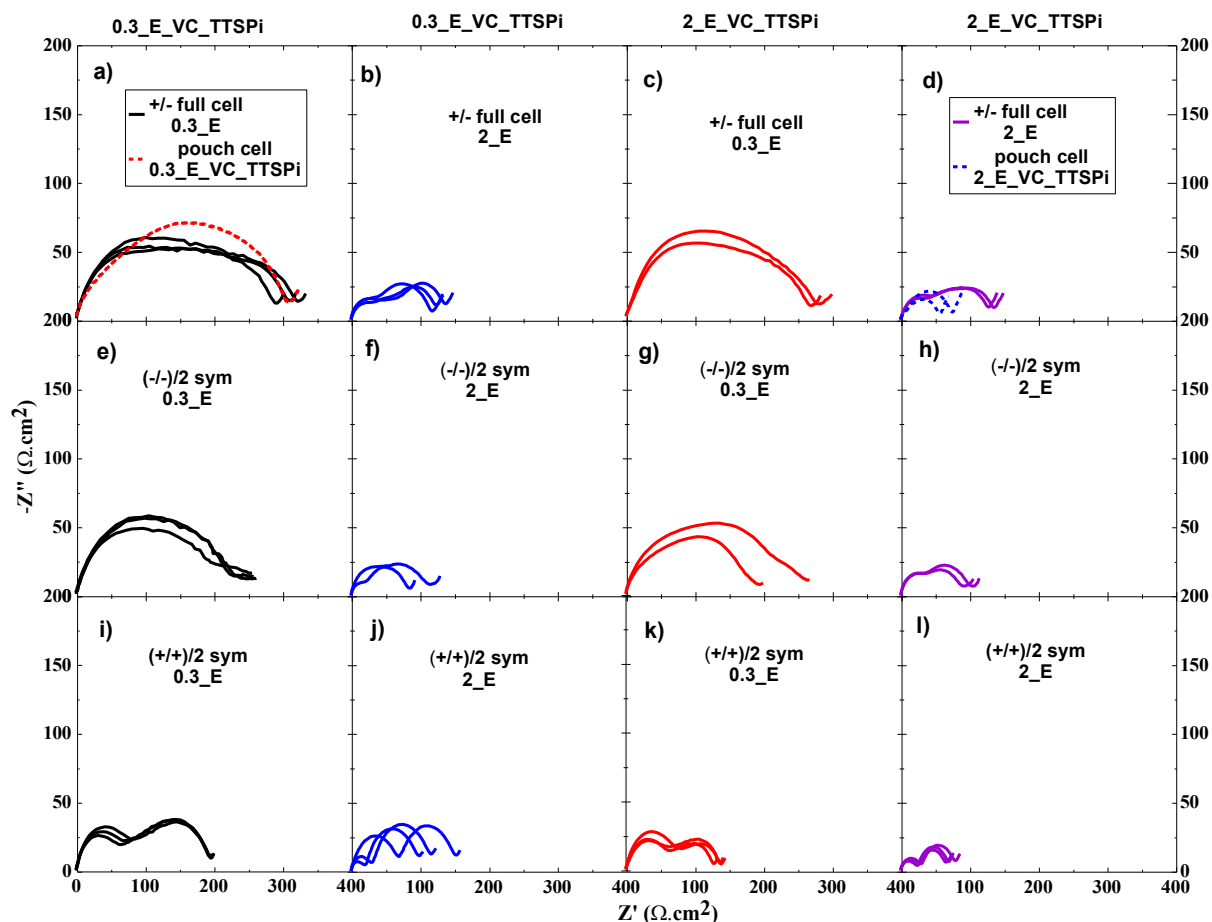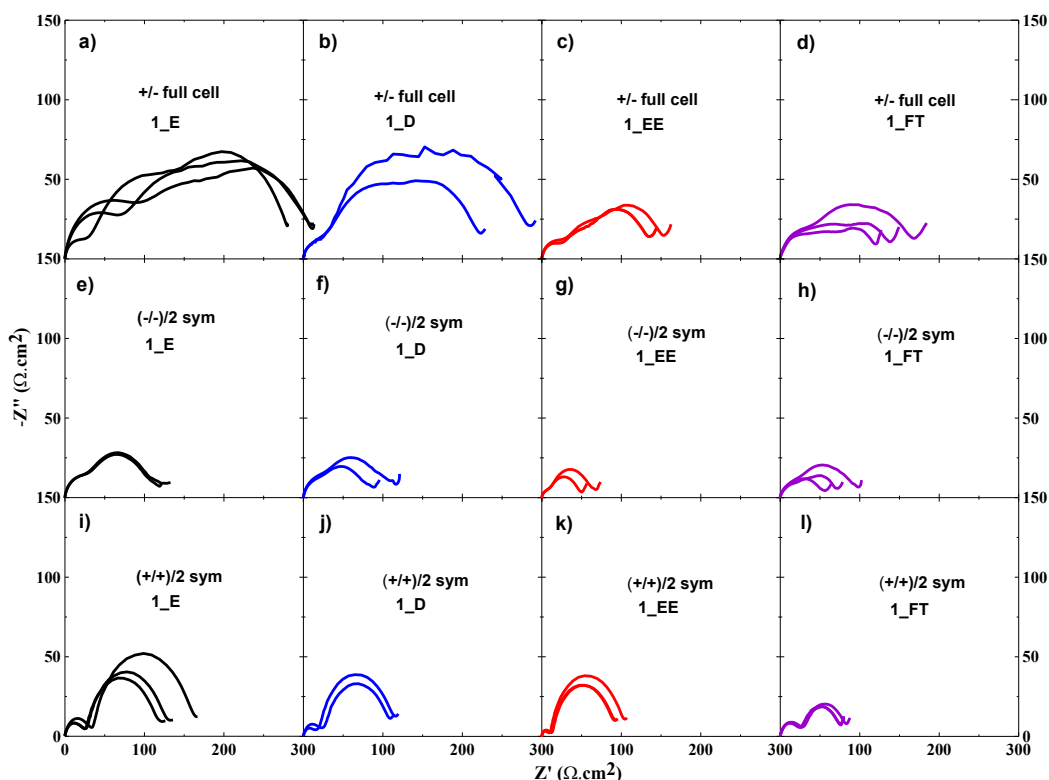
Figure 8.11 Area-specific Nyquist plots of reassembled NMC442/graphite full cells, NMC442/NMC442 and graphite/graphite symmetric cells where the electrodes were taken from pouch cells with 1_E_VC_PPF which had 10 charge-discharge cycles between 2.8 and 4.5 V at C/10 and 40°C. The cells were equilibrated at 3.8 V prior to disassembly. The impedance of the NMC442/NMC442 and graphite/graphite symmetric cells has been divided by two. The reassembled coin cells either contained 1_E, 1_D, 1_EE or 1_TF electrolytes as indicated in the legends.

In order to convince readers of the robustness of these results, it is important to use Bode plots to demonstrate that the impedances of the reassembled coin full cells are equal to the sum of the impedances of the negative/negative symmetric cells divided by two and the impedance of positive/positive symmetric cells divided by two.[111]   Figures E1, E2, E3, and E4 are the corresponding Bode plots to the Nyquist plots in Figures 8.8, 8.9, 8.10 and 8.11. Figures E2, E3 and E4 show good agreement between the impedances of the reassembled full cells and the sum of the impedances of the symmetric cells while Figure E1 does not. It is not known why this is the case, so the reader is cautioned that the results in Figure 8.8 are less robust than those in the other Figures.

To further investigate how low molarity EC-free and EC:EMC electrolyte affects impedance spectra of Li-ion cells and charge transfer impedance, coin full cells were made from electrodes extracted from pouch cells at 3.8 V. The coin full cells used 0.2_E, 0.2_EE, 0.02_EE and 0.002_EE electrolytes. Figure 8.12a and Figure 8.12b shows the area-specific Nyquist plots of the reassembled coin full cells obtained using four wire EIS measurements at 10 °C, while Figure 8.12c shows the conductivity of the same electrolytes also measured at 10.°C. Since four-wire measurements were used, the high frequency intercept is meaningful and represents the ionic resistance due to the electrolyte. Figure 8.12 shows that the diameter of the impedance "semicircle", R_{ct}, increases as the LiPF$_6$ concentration in EC/EMC electrolyte decreases from 0.2 M to 0.002 M. However, R_{ct} for 0.2_E is much larger than R_{ct} for 0.2_EE and still larger than that of 0.002_EE.
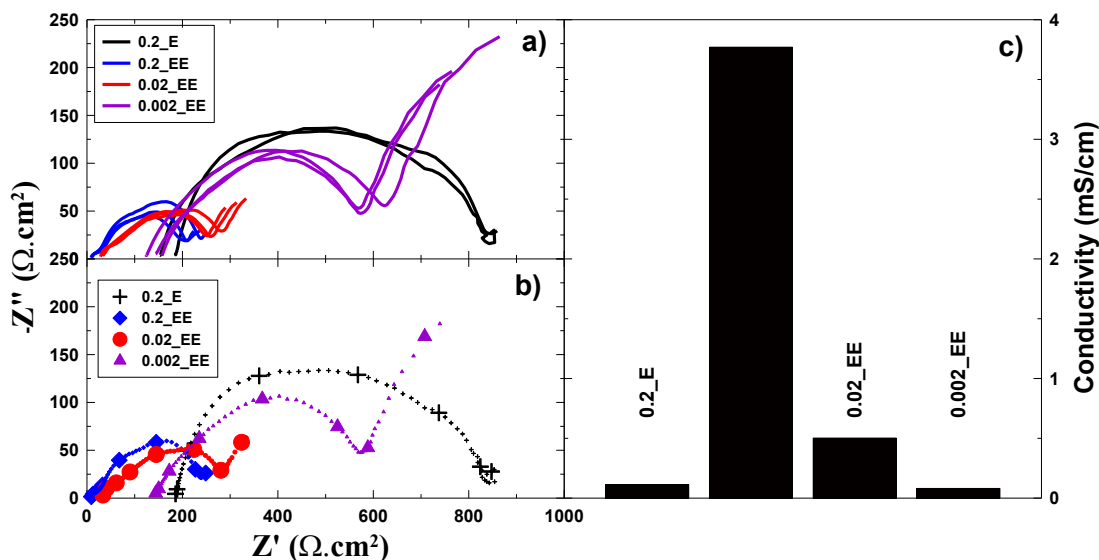
Figure 8.12 Area-specific Nyquist plots of NMC442/graphite coin full cells measured at 10 °C with 0.2_E, 0.2_EE, 0.02_EE and 0.002_EE electrolytes where the positive and negative electrodes were harvested from the same pouch cell at 3.8 V. Panel a) shows the impedance spectra as continuous curves (a) while panel b) shows the spectra with one point per decade highlighted. All the impedance spectra were collected using a 4-wire EIS instrument. Panel c) shows the conductivity of each of these electrolytes measured at 10 °C.
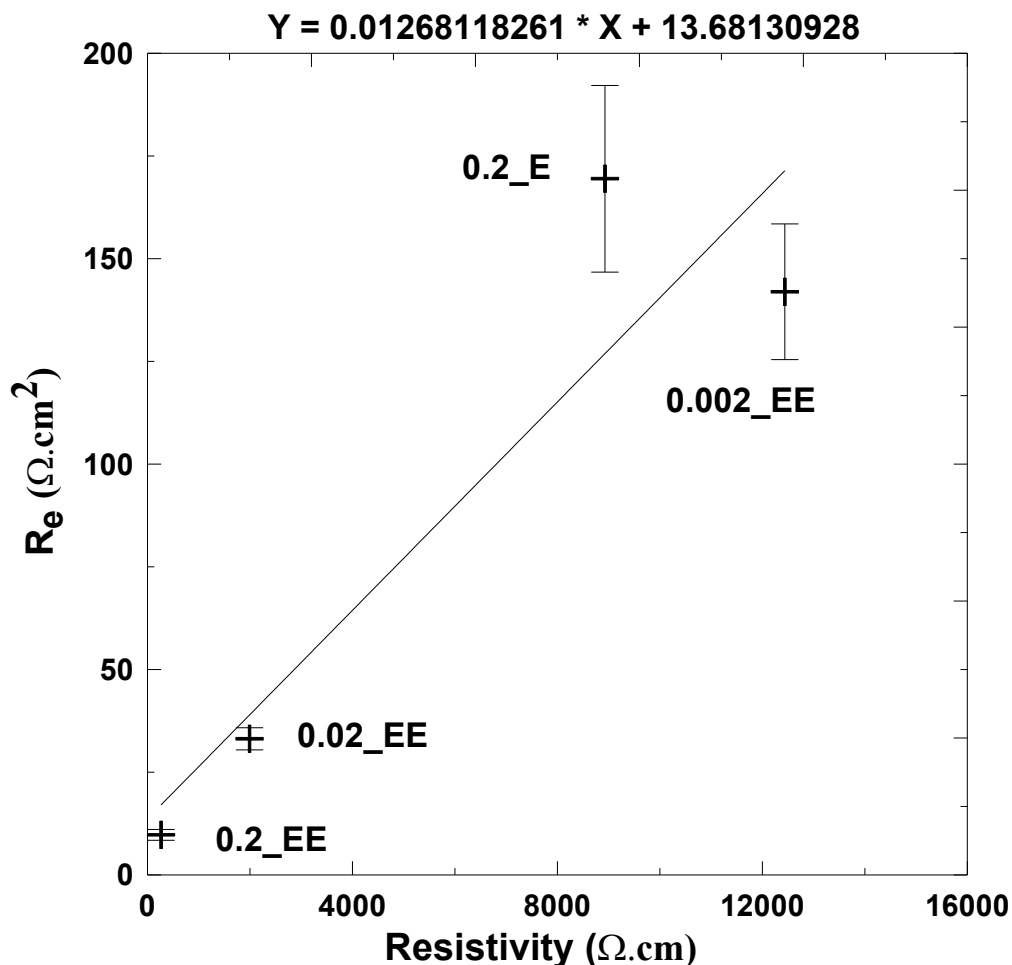
Figure 8.13 The area-specific electrolyte resistance of the coin full cells described by Figure 8.12a and Figure 8.12b extracted from the four-wire EIS measurement plotted vs. the electrolyte resistivity obtained using the data in Figure 8.12c

Figure 8.13 shows the electrolyte resistivity (the reciprocal of the conductivity plotted in Figure 8.12c) plotted versus the high frequency intercept of the impedance spectra of Figures 8.12a and 8.12b. Figure 8.13 shows a good correlation, as expected since the high frequency intercept is primarily due to the electrolyte resistance in the cell. [192]

Why is the charge transfer resistance for electrodes so large in low molarity solutions of $LiPF_6$ in EMC and DEC? Xu *et al.* reported that the extraction of the lithium ion from its solvation sheath is the rate determining step for lithium intercalation into graphite.[234] In dilute $LiPF_6$

solutions in EMC or DMC, by analogy to LiAsF$_6$ in DMC, as reported by Doucey et al.[233] the salt is not well-dissociated at low concentration, which is why the conductivity is so small. Doucey *et al.* state that in PC solutions, the lithium salt is well dissociated, while in DMC solutions the ion pair Li$^+$•••AsF$_6^-$ exists at very low concentrations, while the ion pairs [Li(DMC)$_4$]$^+$•••AsF$_6^-$ and dissociated [Li(DMC)$_4$]$^+$ exist at intermediate concentrations. Other researchers [235–239] have come to similar conclusions about electrolytes made with low dielectric constant solvents. It is our belief that the large charge transfer impedance at the electrodes of NMC442/graphite cells which use 0.2_E (Figure 8.10), 0.2_D (Figure 8.10) or 0.3_E (Figure 8.8) electrolyte stems from the difficulty of extracting a Li$^+$ cation from the ion pairs that predominate at low concentrations. When the salt concentration is large enough, i.e. 1 M as in Figure 8.11, then sufficient dissociated Li$^+$ cations exist and the charge transfer impedance in EMC-based electrolytes becomes comparable to that in EC/EMC-based electrolytes.

8.3   Conclusions

The effects of LiPF$_6$ concentration in EMC and EMC/EC electrolytes were studied in NMC442/graphite pouch cells. Low concentrations of LiPF$_6$ in EMC electrolyte lead to large charge transfer resistance at both electrodes of NMC442/graphite cells. This is because the LiPF$_6$ salt is poorly dissociated at low concentration, which also leads to extremely low electrolyte conductivity. At higher concentrations, e.g. 1 M, the charge transfer resistance at electrodes in EMC-based electrolytes becomes similar to that of electrodes in EC/EMC electrodes.

There are significant consequences of these findings for the possible application of EC-free electrolytes based on EMC in Li-ion cells designed for high voltage operation. Any time a Li-ion cell is operated at high rate, concentration polarization in the electrolyte develops. Figure 8.7 shows that the electrolyte conductivity drops precipitously near 0.4 M and this would be a

concern if large concentration polarization developed. In addition, at the same time, the charge transfer impedance at the electrode surfaces also rises dramatically as the salt concentration decreases which would also limit the rate capability of cells. Based on these findings, it is important to select an initial electrolyte concentration that minimizes the possibility that low concentration would develop at some portions of the electrodes when high currents are demanded from the cell. Based on Figure 8.7, 1.5 M rather than 1 M $LiPF_6$ in EMC should be used. However, based on the voltage drop during storage (Figure 8.3 and 8.4) and gas evolution during storage (Figure 8.2), there may be applications where it is desirable to limit $LiPF_6$ concentration to 1 M. Tradeoffs need to be considered

.

CHAPTER 9: SOME PHYSICAL PROPERTIES OF ETHYLENE CARBONATE-FREE ELECTROLYTES

In this chapter, some physical properties of LiPF$_6$ in ethyl methyl carbonate (EMC) and dimethyl carbonate (DMC) electrolytes were studied by conductivity measurements, Fourier transform infrared spectroscopy (FT-IR) and differential thermal analysis (DTA). Conductivity measurements show that the addition of additive levels of FEC to EMC electrolyte can dramatically increase the conductivity of EC-free EMC electrolytes at low salt concentrations below 0.4 M. FT-IR results show that the added FEC hinders ion pair formation by competing with EMC to dissociate LiPF$_6$ resulting in increased conductivity in EMC electrolytes. Conductivity measurements show that the conductivity of DMC electrolytes decreases significantly below 0°C due to the high melting point of DMC. Differential thermal analysis was used to determine the LiPF$_6$-DMC phase diagram which then can be used to explain the conductivity results. The results presented here identify avenues by which EC-free electrolytes can be improved for use in practical Li-ion cells. The majority of this work was adapted from the following manuscript:

D. J. Xiong, M. Bauer, T. Hynes, S. Hyatt, D.S. Hall and J. R. Dahn, Some Physical Properties of Ethylene Carbonate-free Electrolytes, submitted to J. Electrochem. Soc..

Deijun Xiong performed the conductivity measurements for the LiPF$_6$:EMC electrolytes while Toren Hynes under Deijun Xiong's supervision performed the conductivity measurements for the LiPF$_6$:EMC:FEC electrolytes. Michael Bauer performed the conductivity measurement of 1M LiPF$_6$ in DMC. Deijun Xiong performed the FT-IR measurements together with Toren Hynes. Michael Bauer performed the DTA measurements of the LiPF$_6$:DMC electrolytes while

Sarah Hyatt carried out the DTA measurements of the LiPF$_6$:EMC electrolytes. Deijun Xiong prepared all the FT-IR and conductivity figures. Michael Bauer prepared all the DTA figures. Deijun Xiong received assistance from David Hall for interpreting the FT-IR data. Jeff Dahn provided guidance and participated in experimental design and the interpretation of the data. Deijun Xiong prepared the manuscript mentioned above except for the DTA section (prepared by Michael Bauer) and received revisions from David Hall and Jeff Dahn.

9.1 Experimental Methods

9.1.1 Conductivity measurements

The conductivity of EMC, FEC/EMC(5:95), FEC/EMC (10:90) with different concentrations of LiPF$_6$ were measured using a Mettler Toledo FiveGo conductivity meter. The solvents were mixed by weight percentage. Details about conductivity measurements can be found in Section 8.1.7.

9.1.2 FT-IR analysis

Measurements were taken on an Agilent Technologies Cary 630 FT-IR, equipped with a diamond attenuated total reflectance (ATR) accessory, in an Ar-filled glove box. The electrolytes analyzed were the same as those used for conductivity measurements in addition to pure EMC, FEC:EMC (5:95) and FEC:EMC (10:90) solvents. 0.1 mL of each solution was placed directly on the ATR crystal. Sixteen scans were taken for each sample, at 2 cm^{-1} resolution over the frequency range from 600 to 4000 cm^{-1}.

9.1.3 Differential Thermal Analysis

Differential thermal analysis (DTA) measurements were taken with a custom built cryostat and software setup, using a Model 336 LakeShore temperature controller. The details of the construction of DTA have been reported by Day et al.[230] The samples measured here were LiFUN NMC/graphite pouch cells (402030 size) filled with 0.8 ml of electrolyte (0M – 1.5M LiPF$_6$ in EMC and 0M – 2.0M LiPF$_6$ in DMC). The cells with EMC electrolytes were cooled from 25°C to -105°C at a rate of -2.5 K/min and then heated back up to 25°C at 2.0 K/min. The cells that contained DMC-based electrolytes were cooled from 25 C to -45 C at a rate of -1.5 C min^{-1} and then heated back up to 25 C at 1.0 C min^{-1}.

9.2 Results and Discussion

The conductivities of EMC-based electrolytes were measured as a function of the salt concentration and the solution temperature. Figure 9.1 shows that, in general, the conductivity increases as the salt concentration (below 1.5M) or the temperature increases. This is expected since the concentration or the mobility of free ions (i.e., Li$^+$ and PF$_6^-$) increases as the salt concentration or temperature increases, respectively. The increase of conductivity with salt concentration is not linear at low molarity as has been found by Doucy et al. for solutions of LiAsF$_6$ in DMC.[233] In addition, even at high salt concentrations, the solution conductivity is relatively low for a Li-ion electrolyte. It is well-known that in non-polar solvents, such as EMC, LiPF$_6$ tends to form ion pairs that do not contribute to ionic conduction in the solution. It is for this reason, in part, that EC, a very polar co-solvent, is commonly used in Li-ion cell electrolytes (the second reason being its tendency to form a passive SEI on graphite electrode surfaces).[32] Therefore, it is desirable to consider how alternative co-solvents like FEC, which have been

shown to improve the properties of Li-ion cells with EC-free electrolytes,[31] affect the conductivity of EC-free electrolytes.

Solutions were prepared with 5% or 10% FEC, an SEI-forming additive, a highly polar molecule, and a demonstrated 'enabler' for EC-free solutions.[31] Figure 9.1 shows that the addition of FEC to EMC electrolytes indeed improves the electrolyte conductivity. This matches the expectation that the relative permittivity (dielectric constant) of EMC-based electrolytes increases when FEC is added. Table 9.1 shows the permittivity of an FEC:EMC mixture as calculated using a simple model described by Prakongpan et al.[240] The permittivity of the EMC-based electrolytes decreases significantly at low $LiPF_6$ concentrations, notably below 0.4 M, completely unlike the results for EMC electrolytes with just 5 – 10 % FEC. This behavior has been observed before in electrolyte solutions prepared with non-polar (low dielectric constant) solvents.[235,241] Consequently, at low salt concentrations, the low dielectric constant of the solution results in the formation of electrically neutral ion pairs or aggregates.

Table 9.1 The static permittivity of FEC/EMC binary mixture calculated using a simple model

FEC:EMC mixture (w/w)	relative permittivity
0:100	2.96
5:95	7.30
10:90	11.64
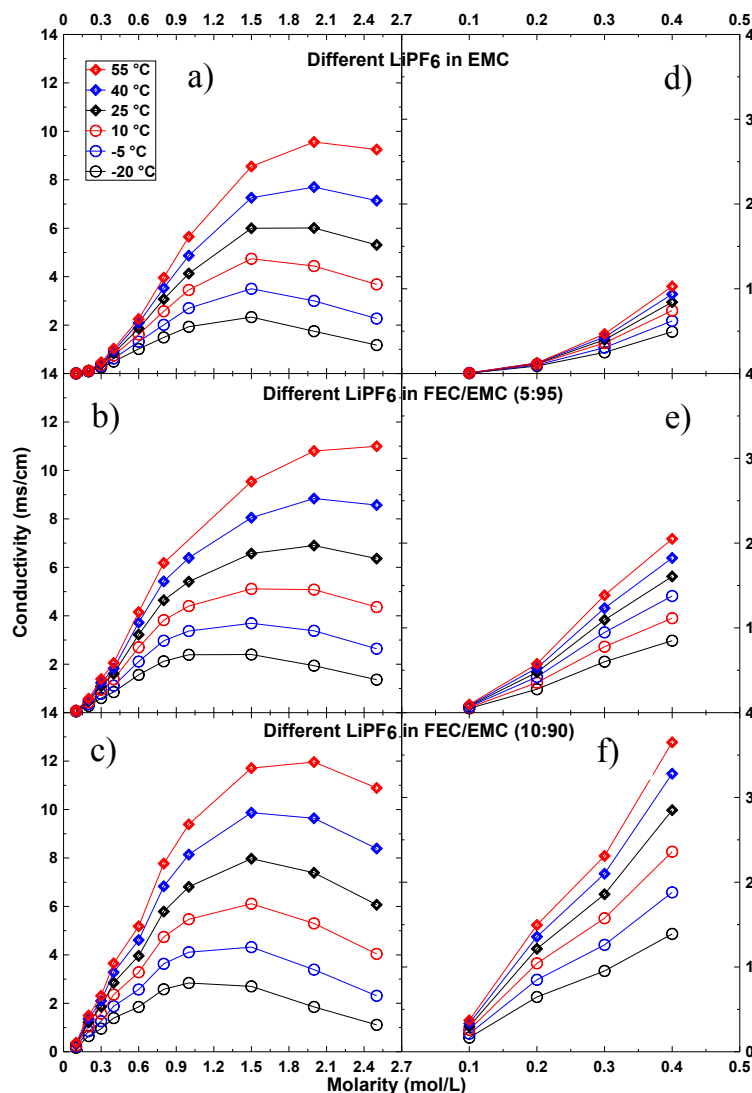
Figure 9.1 Conductivity vs molarity of LiPF$_6$ in EMC (a, d), FEC:EMC (5:95 w/w) (b, e) and FEC:EMC (10:90 w/w) (c, f) in the temperature range from -20 to 55°C.

It is therefore desirable to examine the interactions between the ions and the solvent (or solvents). FT-IR is a good tool that has been applied to investigate solvation behaviour and ion pair formation for a wide variety of salts and solvents.[233,242–246] Figures 9.2 and 9.3 show FT-IR spectra (800-900 and 1600-1900 cm^{-1}) of EMC and mixed FEC:EMC (10:90) electrolyte containing different concentrations of LiPF$_6$. Figure F1 shows FT-IR spectra of mixed FEC:EMC (5:95) electrolyte containing different concentrations of LiPF$_6$. The IR-active t$_{1u}$

174

absorption of the free, octahedrally symmetric PF_6^- anion is observed at 843 cm^{-1}.[244,245] The formation of contact and/or solvation ion pairs lowers the symmetry of the anion, causing the absorption frequency to shift and split into two bands, approximately centred at 877 and 834 cm^{-1}. EMC has an absorption band at 878 cm^{-1} that overlaps with this region, complicating any quantitative analysis of the PF_6^- ion pair or aggregates, consistent with the behaviour in diethyl carbonate (DEC) solvent, as described by Seo et al.[244] Nonetheless, the relative absorbance of the free (843 cm^{-1}) and ion-paired (834 cm^{-1}) PF_6^- may be evaluated qualitatively from the spectra shown in Figures 9.2 and 9.3. Examination of these peaks reveals that in mixed FEC:EMC electrolytes, there is a lower degree of ion-pairing than is observed in the EMC-based electrolytes. This can be seen from the absorbance of the free (843 cm^{-1}) PF_6^- relative to the ion-paired (834 cm^{-1}) PF_6^-. For a given salt concentration and solution temperature, it is observed that the free PF_6^- peak increases as FEC is added. By inhibiting the interaction between Li^+ cations and PF_6^- anions, it is expected that the addition of FEC should increase the concentration of ion carriers in solution. This is indeed consistent with the measured conductivity results, as described above.
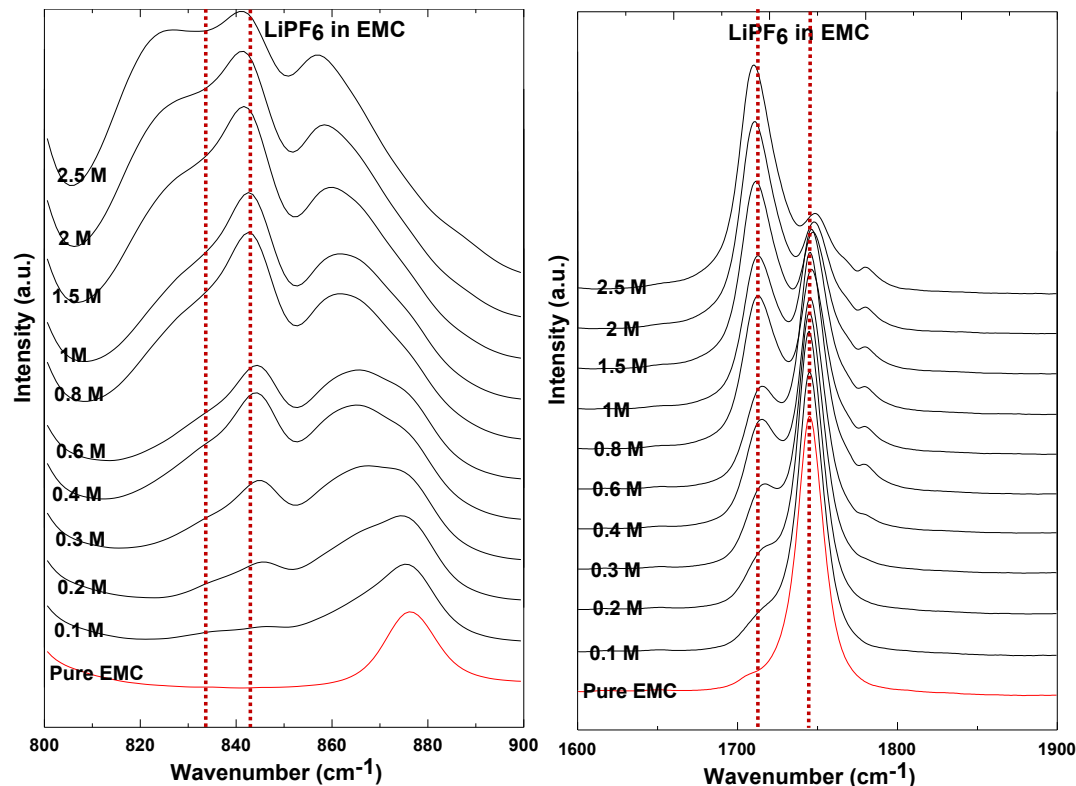
Figure 9.2 FT-IR (800-900 and 1600-1900 cm^{-1}) spectra of LiPF$_6$:EMC electrolytes of different molarities. Dashed lines indicating the 834, 843, 1710 and 1745 cm^{-1} positions have been inserted into the Figures to guide readers.

The C=O bond of the carbonate functional group has a very strong IR absorption in the carbonyl region (1650-1850 cm^{-1}). The carbonyl shift depends on the local environment and is typically shifted to a higher wavenumber upon coordination to the Li$^+$ cation. The uncoordinated C=O stretching frequencies for EMC and FEC occurs at 1745 cm^{-1} and 1835 cm^{-1}, respectively, while the stretching frequencies for a C=O group coordinated to Li$^+$ appear at 1710 cm^{-1} and 1810 cm^{-1}, respectively. [244] As the FEC concentration is increased, the ratio between uncoordinated and coordinated C=O groups belonging to EMC decreases while the ratio between uncoordinated and coordinated C=O groups belonging to FEC increases. This result may be interpreted that FEC competes with EMC to associate with the Li$^+$ cations in solution, as may be expected from the significantly larger dipole moment of the FEC molecule. The significance of

this result is that FEC can indeed serve as both an SEI-forming additive and as a polar co-solvent, even at very low concentrations.
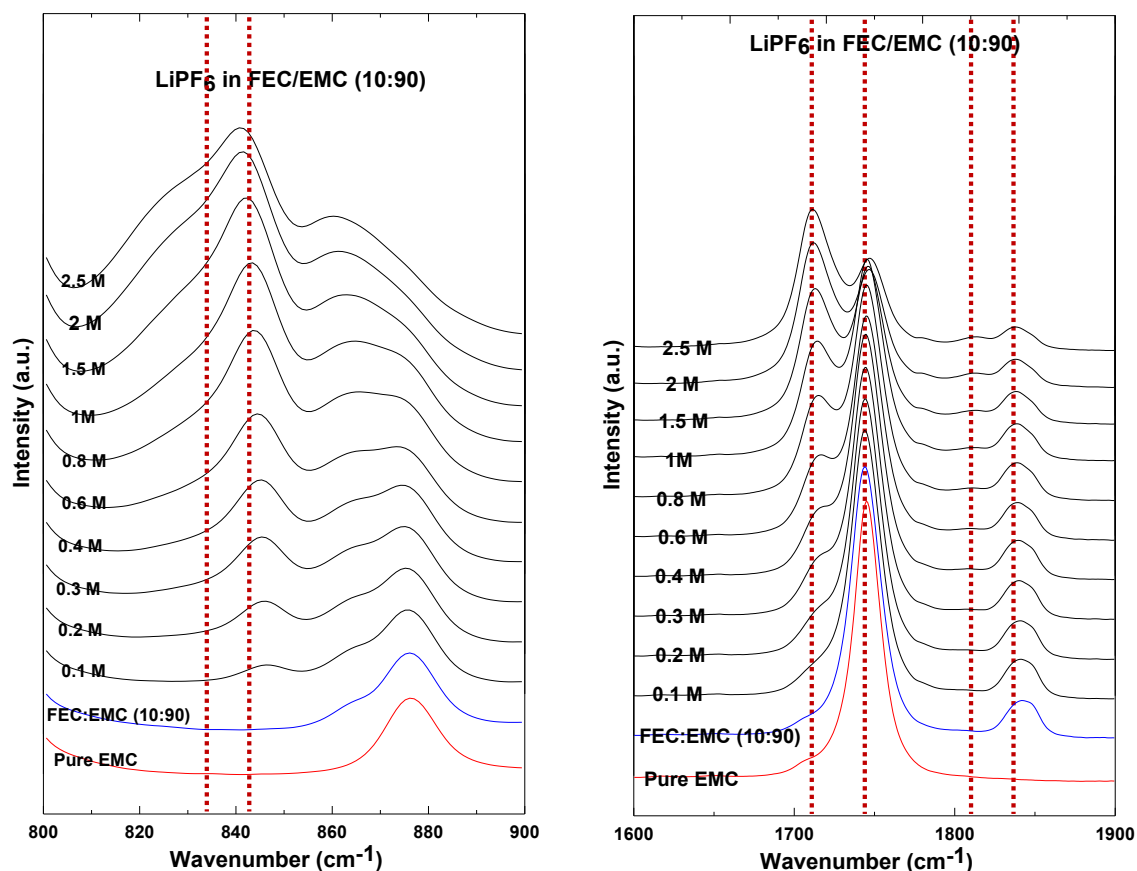
Figure 9.3 FT-IR (800-900 and 1600-1900 cm^{-1}) spectra of LiPF$_6$:FEC:EMC (10:90) electrolytes of various molarities and of pure EMC. Dashed lines indicating the 834, 843, 1710, 1745, 1810 and 1845 cm^{-1} positions have been inserted into the Figures to guide readers.

DTA can be used to examine the state of the electrolyte in a cell and generate phase diagrams of electrolyte systems as well.[230] Here, this method was used to examine the phase transition behaviour of EMC and DMC electrolytes with various salt concentrations. The phase diagram can, among other things, show the liquidus point of the solution, which marks a sharp decrease in electrolyte conductivity. Thus, the method can be used to determine the lowest temperature that a cell can be expected to function properly.
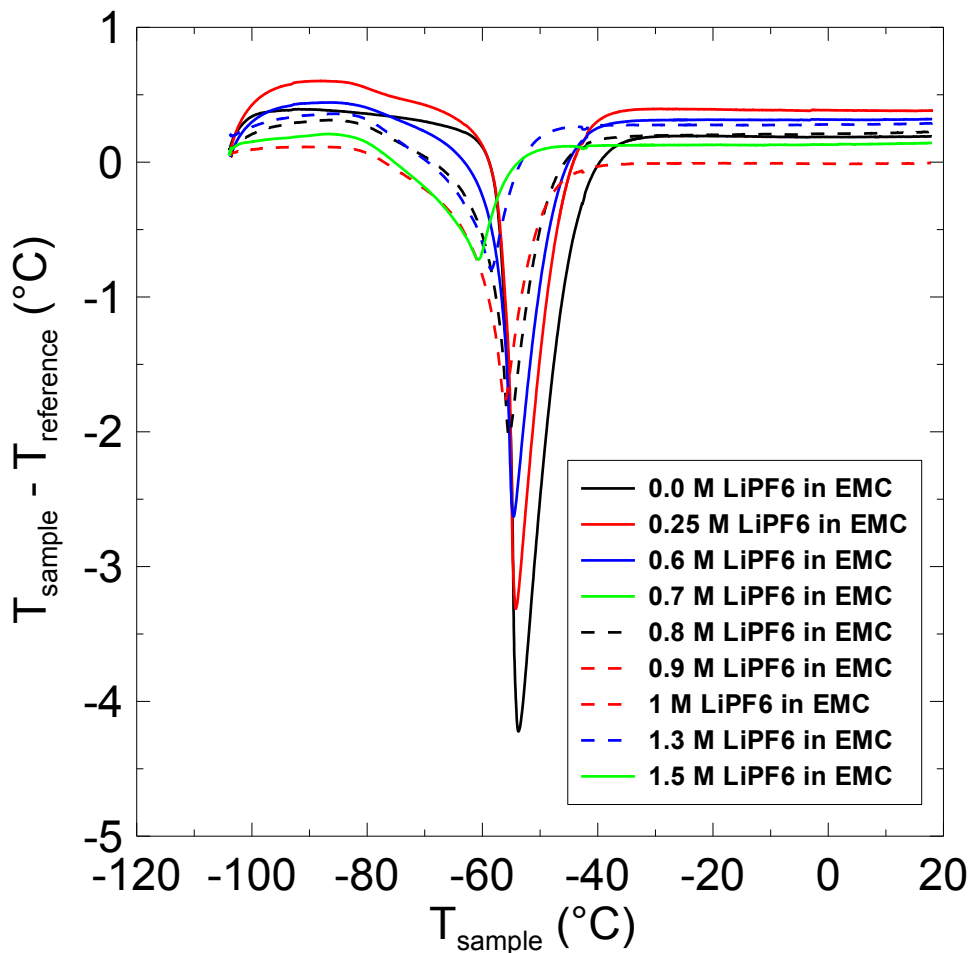
Figure 9.4 DTA curves for various molarities (0, 0.25, 0.6, 0.8, 1.3 and 1.5M) of LiPF$_6$ in EMC electrolyte

Figure 9.4 shows the DTA traces for NMC/graphite cells containing LiPF$_6$:EMC electrolytes with various LiPF$_6$ concentrations. This figure shows that the freezing point of the electrolyte decreases as salt concentration increases. This data can then be used to construct a phase diagram showing the relationship between the melting points and the salt compositions of the LiPF$_6$:EMC system. The phase diagrams are created by plotting the onset of the solidus feature and peak of the liquidus features, as shown by Ding et al..[247] In the case of the LiPF$_6$:EMC system, the solidus and liquidus features are very close in temperature, which makes the eutectic point and the other finer points of the phase diagram very difficult to discern. This issue could perhaps be

178

overcome with lower heating rates, which would give more precise measurements, but these rates might be experimentally impractical for testing a large number of samples.
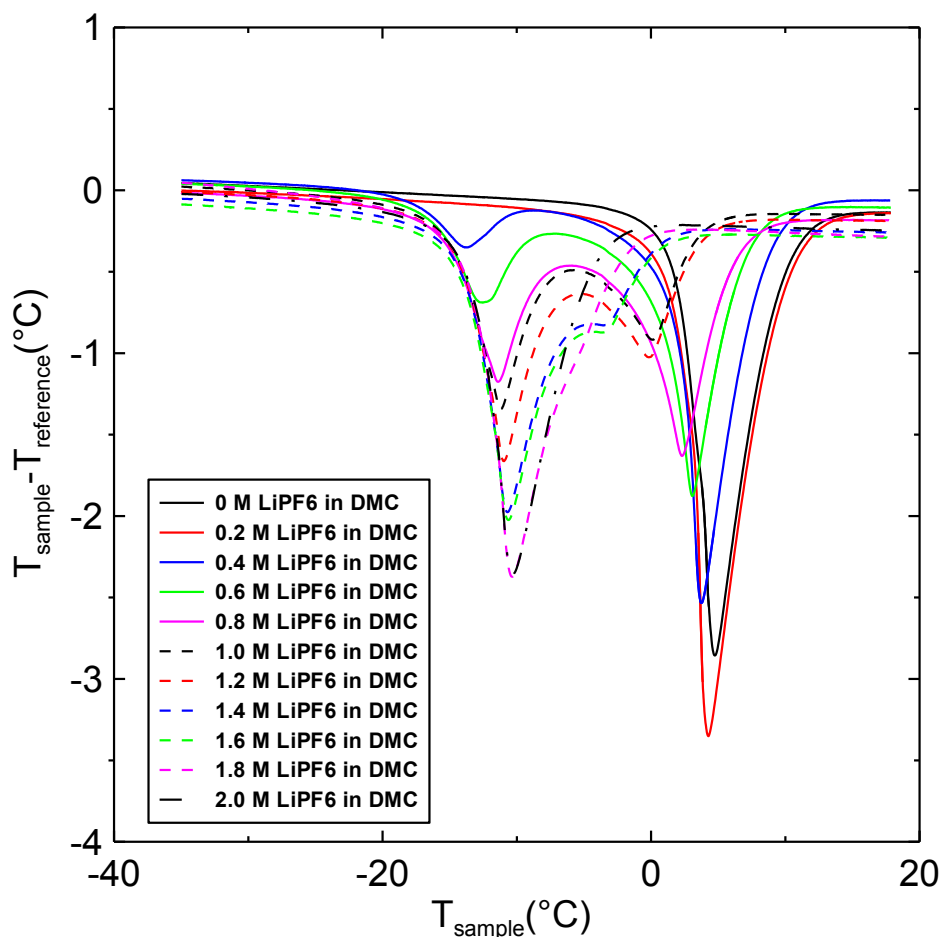
Figure 9.5 DTA curves for various molarities of $LiPF_6$ in DMC electrolyte.

Other solvents, such as DMC, freeze at higher temperatures than EMC (4°C vs. -53°C, respectively, for the pure compounds). The $LiPF_6$:DMC system also has a greater temperature difference between the solidus and liquidus features, which allows for more clarity in generating the associated phase diagram. Furthermore, some commercial cells have electrolytes containing large proportions of DMC (>70% of the solvents by weight). The phase diagram of $LiPF_6$:DMC is considerably easier to construct, and could provide valuable data when considering cells to be

179

used for low temperature applications. Figure 9.5 shows the DTA traces for cells containing LiPF$_6$:DMC electrolytes. This figure more clearly shows the liquidus (higher temperature) and solidus (lower temperature) features present in DTA signals. Using the same liquidus/solidus convention as described by Ding et al.,[247] this diagram can be used to construct the phase diagram shown in Figure 9.6.
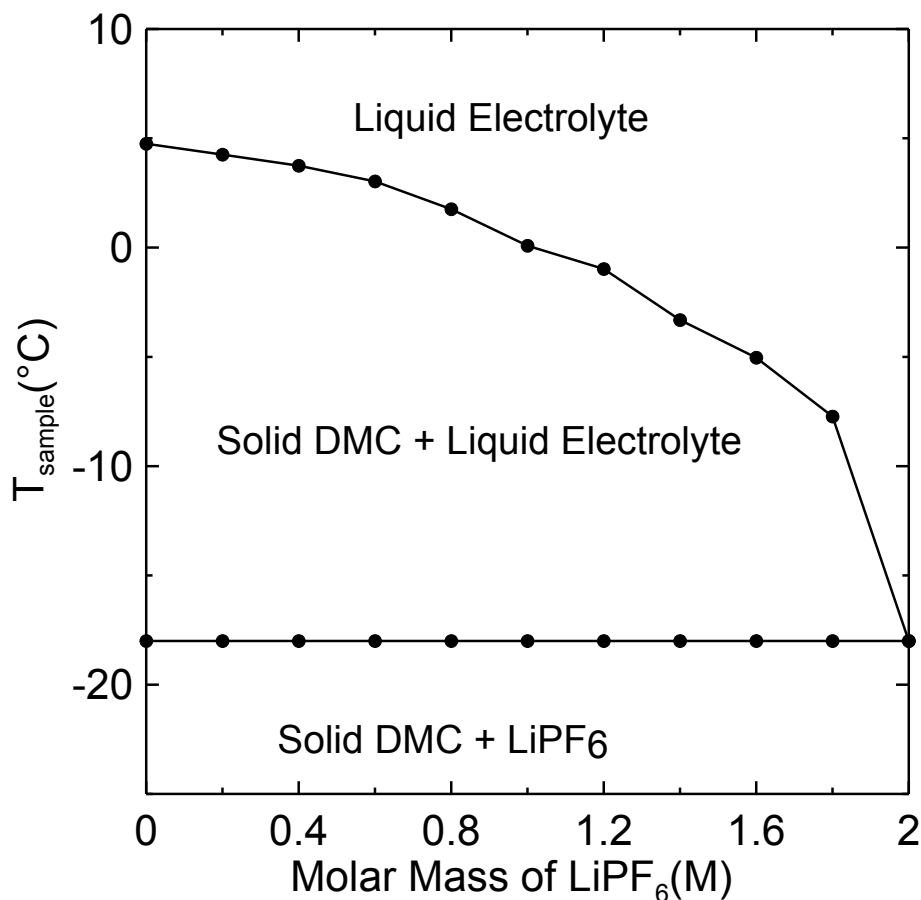
Figure 9.6 The DMC-LiPF$_6$ phase diagram, generated using the data shown in Figure 9.5

The DTA curve for a particular electrolyte can help explain the conductivity vs. temperature curve for the same electrolyte. These data can then be used to determine relationship between conductivity and phase change. Figure 9.7 shows the DTA trace and conductivity vs. temperature of the 1M LiPF$_6$ in DMC electrolyte. Figure 9.7 shows that a change of state from liquid to solid

in the electrolyte will drastically reduce its conductivity. Though the electrolytes does not completely freeze until -18°C, DMC will begin to freeze out of the electrolyte at the liquidus point, 3°C. The solid DMC crystals then increase the molarity of the remaining liquid, while also significantly reducing the mobility of the rest of the DMC. As the presence of DMC in a solvent mixture will increase the freezing point, cells that are to be used for low temperature applications should not have DMC in large quantities, in order to optimize low temperature performance.
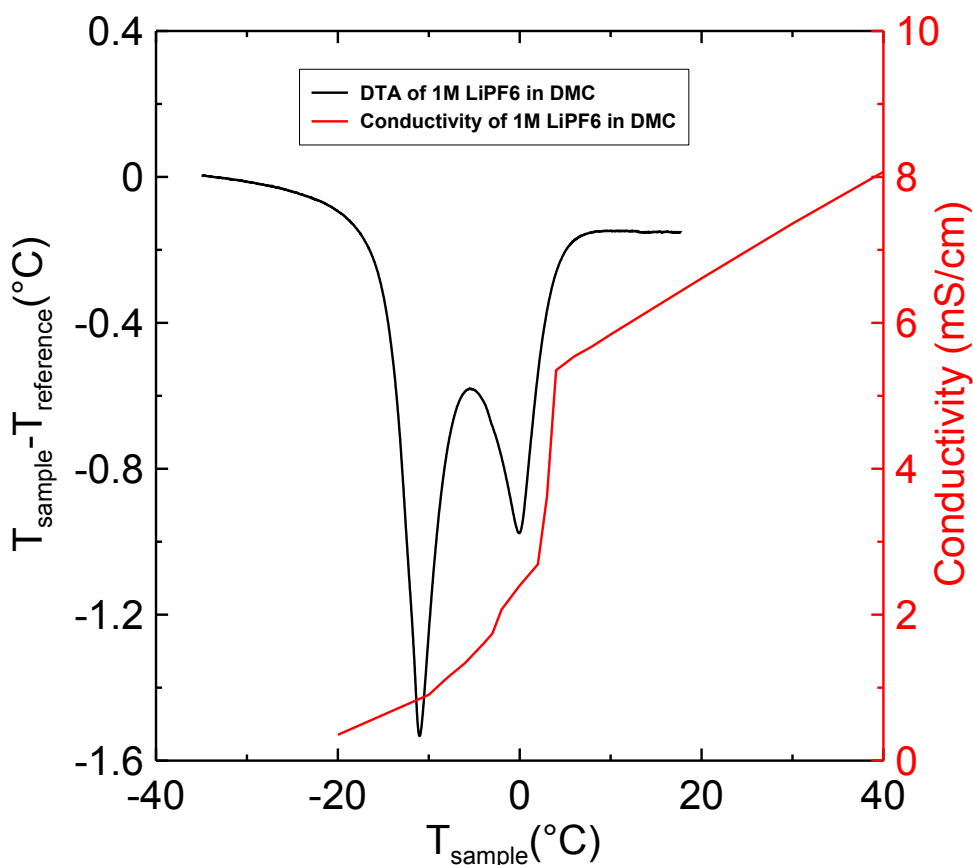
Figure 9.7 The DTA curve (black) and conductivity versus temperature (red) of 1M LiPF$_6$ in DMC

9.3   Conclusions

In this report, EC-free electrolytes were studied by conductivity measurements, FT-IR and DTA. The results show that LiPF$_6$:EMC electrolytes have low conductivity compared to

conventional EC:EMC electrolytes due to the formation of non-conducting ion pairs and/or aggregates. The addition of additive quantities (5 – 10 %) of FEC significantly improve EMC electrolyte conductivity especially at low salt concentrations. The phase diagram of the LiPF$_6$:DMC system has been determined for the first time. Anomalies in the conductivity versus temperature behaviour of 1M LiPF$_6$ in DMC can be understood based on the determined phase diagram. The results suggest that a large portion of DMC should not be used in electrolytes when cell performance at low temperature is important.

CHAPTER 10:   CONCLUSIONS AND FUTURE WORK

10.1   Conclusions

In this thesis, high voltage NMC cell failure mechanisms were studied using a variety of analytical techniques, especially a newly developed pouch bag method and a newly developed TGA-MS method. The effects of various salt concentrations in EC-free linear carbonate electrolytes on cell performance and electrolyte physical properties were also studied. Many surprising chemistries were discovered. These findings could guide to further improve high voltage NMC cell performance.

In Chapter 4, a simple pouch bag method was developed to explore the origin of gas production and impedance growth, and the negative/positive electrode interactions. NMC442 positive electrodes taken from pouch cells at 4.4 V and stored at 60°C in pouch bags with EC-based electrolyte created more gas than the same electrodes stored with the same electrolyte in pouch cells. Most of the gas generated in the pouch bags during storage was CO_2. Surprisingly, the presence of electrolyte additives known to improve high voltage storage and cycling did not affect the gas generation rate strongly. CO_2 intentionally injected into pouch bags containing lithiated graphite was consumed over time. Electrolyte additives used could greatly affect the CO_2 consumption rate. Unexpectedly, NMC442 electrodes removed from pouch bags after storage at 4.4 V and elevated temperature had dramatically larger values of R_{ct} (at least double) than those removed from pouch cells. Curiously, the positive electrode SEI was thinner on electrodes stored in pouch bags, even though their R_{ct} was much larger than electrodes extracted from pouch cells. These results underscore the complexity of the chemical and electrochemical reactions occurring in Li-ion cells charged to high voltages and operated at elevated temperature.

Furthermore, these results undoubtedly demonstrate that oxidized species created at the positive electrode can migrate to the negative electrode and be "consumed" there. Without the consumption of these harmful degradation species, the positive electrode would be greatly affected.

In Chapter 5, EC-based and fluorinated electrolytes were comparatively studied using the pouch bag method. The results show that the fluorinated electrolyte greatly suppresses impedance growth of the charged NMC442 electrode but create large initial negative electrode impedance. The results also suggest that the SEI formed by the fluorinated electrolyte at the graphite electrode hinders the consumption of CO_2 generated at the delithiated NMC442 electrode, leading to more CO_2 in pouch cells with fluorinated electrolyte than in cells with carbonate electrolyte. Surprisingly, hydrogen gas was only observed in pouch cells after storage and not in pouch bags which contained either a single negative electrode plus electrolyte or a single positive electrode plus electrolyte. This implies that the H_2 results from a species created at the positive electrode that subsequently reacts at the negative electrode in a pouch cell.

In Chapter 6, different NMC electrodes, with and without surface coatings were comparatively studied using the pouch bag method. The results show that an Al_2O_3 surface coating can greatly suppress impedance growth of the NMC622 electrode, in pouch bags, at 60°C, more effectively than a $LaPO_4$ surface coating on an NMC442 electrode. However, the Al_2O_3 surface coating caused more gas generation at high voltage and high temperature.

In Chapter 7, TGA-MS was used to measure the release of oxygen from charged NMC electrode materials at high electrode potentials, i.e., low lithium content. This oxygen release was observed at relatively mild temperatures as low as 40°C. Unexpectedly, the results showed that

the amount of oxygen released can be greatly limited by utilizing larger NMC particles. The results offer new support that the release of oxygen from NMC can cause oxidative decomposition of the electrolyte and was a major reason why high voltage cells generate gas and have poor capacity retention.

In Chapter 8, the effects of $LiPF_6$ concentration in EMC and EC/EMC electrolytes on cell performance were studied in NMC442/graphite pouch cells. Surprisingly, low concentrations of $LiPF_6$ in EMC electrolyte caused large charge transfer resistance at both electrodes of NMC442/graphite cells. This is because the $LiPF_6$ salt is poorly dissociated at low concentration, which also leads to extremely low electrolyte conductivity. At higher concentrations, e.g. 1 M, the charge transfer resistance at electrodes in EMC-based electrolytes became similar to that of electrodes in EC/EMC electrolytes. There are significant consequences of these findings for the possible application of EC-free EMC-based electrolytes in Li-ion cells designed for high voltage operation. Any time a Li-ion cell is operated at high rate, concentration polarization in the electrolyte develops. Therefore, it is important to select an initial electrolyte concentration that minimizes the possibility that low salt concentration would develop at some portions of the electrodes when high currents are applied for the cells.

In Chapter 9, the effects of salt concentrations and electrolyte additives in EC-free electrolytes on electrolyte physical properties were studied. The results show that the addition of additive levels of FEC to EMC electrolyte can dramatically increase the conductivity of EC-free EMC electrolytes at low salt concentrations below 0.4 M. The results show that the added FEC limits ion pair formation more effectively by dissociating $LiPF_6$ resulting in increased conductivity in EMC electrolytes. Anomalies in the conductivity versus temperature behavior of 1M $LiPF_6$ in DMC can be understood based on the $LiPF_6$:DMC phase diagram, which was determined in this

work for the first time. The results suggest that a large portion of DMC should not be used in electrolytes when cell performance at low temperature matters. Overall, the results presented here identify avenues by which EC-free electrolytes can be improved for use in practical Li-ion cells

10.2 Future work

10.2.1 Investigate the Reactivity between Additional Electrode Materials and Electrolyte Formulations using the Pouch Bag Method

The pouch bag method introduced in this thesis is a useful tool to investigate the reactivity of charged electrode materials with electrolyte. More specifically, this method can provide considerable insight about the origin of gas production and the origin of impedance growth in Li-ion cells at high voltage and at elevated temperature. In a future study, the reactivity of many other positive electrode materials, such as single crystal NMC532, NMC811, NCA and LCO, with conventional carbonate electrolytes can be explored using the pouch bag method. Additionally, DMC and ester solvents such as MA are commonly added as co-solvents in commercial cells to improve cell rate capability or performance at low temperature. However, it was found in the Dahn lab that these added co-solvents can cause more gas production in cells at elevated temperature. It is important to carry out the pouch bag experiments to understand why this occurs. EC-free linear carbonate electrolyte and sulfone-based electrolyte have been reported to improve high voltage NMC442 cell performance. As a future work, pouch bag experiments could be useful to gain insight why this occurs.

10.2.2   Identify the Chemical Origins of Impedance Growth of Charged Positive Electrodes

It was found in this thesis that the charge transfer impedance of a charged NMC electrode that is stored in a pouch bag with a carbonate-based electrolyte and at an elevated temperature will grow more rapidly than that of an electrode that is stored in a pouch cell. This suggests that an oxidized species is a "criminal" and causes the impedance growth of a charged positive electrode. In pouch bag experiments, the main gaseous oxidation products generated were CO_2 and CO. The question therefore arose whether CO_2 or CO are responsible for the impedance growth at the positive electrode. To explore this question, pouch bags containing charged NMC442 electrodes and either CO_2 or CO gas were prepared. The electrodes used for these pouch bag experiments were taken from NMC442/graphite pouch cells charged to 4.4 V. Before these electrodes were inserted into the pouch bags, they were rinsed six times with DMC and dried under vacuum. CO_2 or CO was then injected into the pouch bags. After 500 h storage at 60°C, the electrodes were taken from these pouch bags to construct NMC442/NMC442 symmetric cells and the impedance growth was measured. Figure 10.1 shows that the charge transfer impedance for the materials stored with injected CO_2 is roughly the same as for those stored without any injected gas. This may indicate that CO_2 gas is not the chemical origin of impedance growth of the positive electrode. Figure 10.1 shows that the charge transfer impedance for the materials stored with injected CO is slightly larger compared to those stored without any injected gas. This may imply that CO causes impedance growth of the positive electrode. However, in the other experiments presented in this thesis, the pouch bags also contained an electrolyte of interest. It is therefore worth repeating this experiment using both injected gas and an electrolyte, rather than dry electrode materials. As a future work, it is suggested that CO_2 and CO should be directly injected

187

into NMC442/graphite pouch cells. It is hoped that by continuing to study the chemical origins of the impedance growth of charged NMC electrodes, ways to suppress impedance growth of charged positive electrodes at high voltage could be developed.
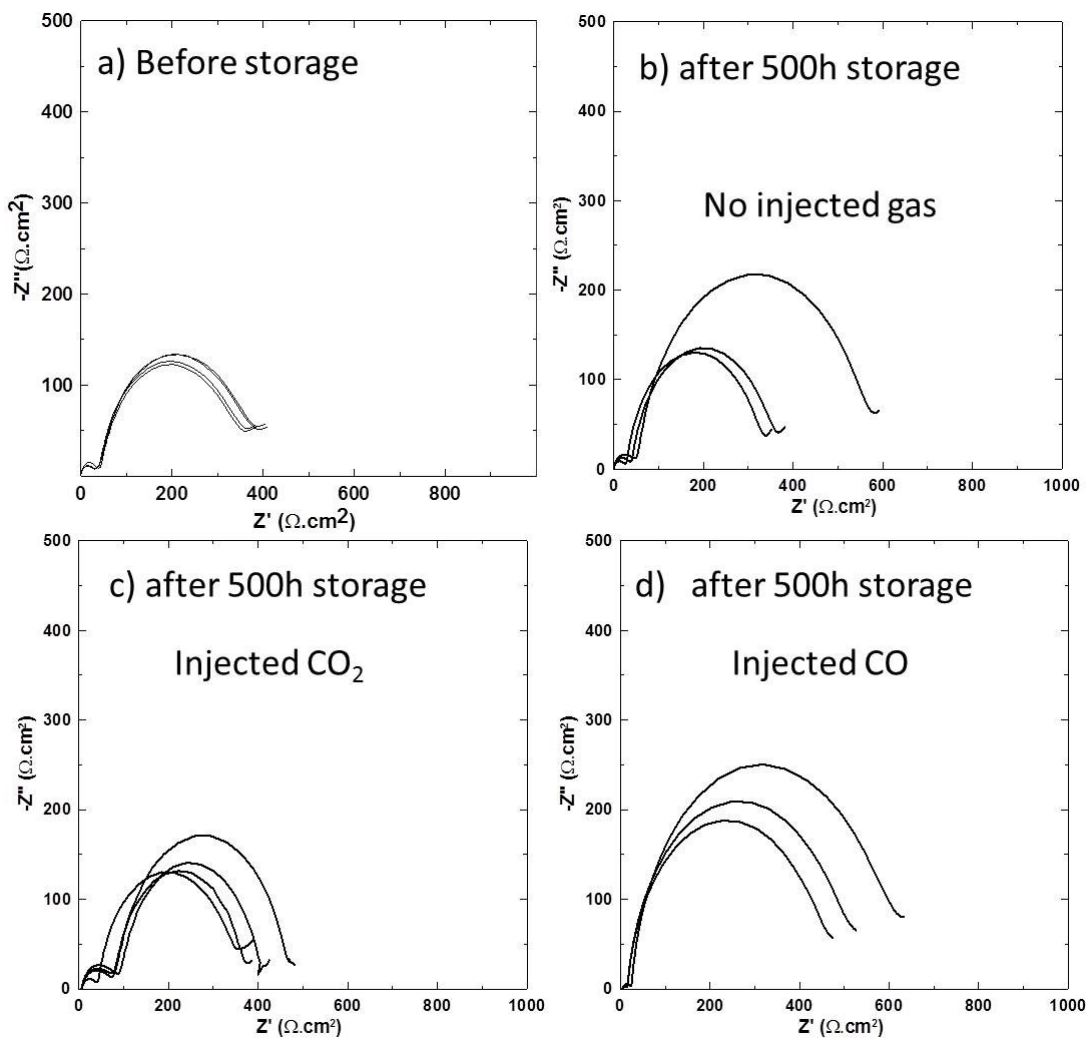
Figure 10.1 The Nyquist plot of the delithiated NMC442 electrodes before storage (a) and taken from pouch bags with dry and rinsed delithiated NMC442 electrodes plus no injected gas (a), CO_2 (b) and CO (c) after 500 h storage at 60°C

10.2.3   Identify Transition Metal Dissolution in Pouch Bags

The TGA-MS experiments show that oxygen can be released from charged NMC positive electrodes at high voltage at elevated temperature. This released oxygen can oxidize the SEI

and/or the electrolyte and it has been suggested this may generate water.[248] Due to the hydrolysis of LiPF$_6$ by reacting with the released water, HF is generated.[23,249–252] HF can then corrode NMC positive electrode materials and cause dissolution of the transition metals. As a future work, it could be useful to measure for this transition metal dissolution. Charged positive electrode-containing pouch bags could be prepared and studied as a function of the initial electrode potential and of the storage time.

10.2.4   Investigate Electrolyte Oxidation Occurring at the Positive Electrode at High Voltage

GC-MS is a powerful tool to probe volatile by-products from electrolyte oxidation occurring in high voltage NMC cells.[65,114] This thesis shows that oxidized species can move from the positive to the negative electrode and subsequently get reduced. This suggests that the analysis of the electrolyte extracted from full cells cannot reflect the true products of electrolyte oxidation at the positive electrode. Furthermore, it was reported that transesterification was initiated by lithium alkoxides[30,117,253] while other researchers argued that the NMC positive electrode could catalyze transesterification.[254] As a future work, it could be useful to analyze the electrolyte extracted from pouch bags with only charged positive electrode and electrolyte using the GC-MS method reported by Petibon et al..[114] Thus, the true electrolyte oxidation pathway at the positive electrode could be determined and the truth about how transesterification occurs in the cells can be determined.

10.2.5   Use the Pouch Bag Method to Screen Electrolytes and Electrolyte Additives

Sodium- and potassium-ion batteries are promising alternatives to lithium-ion batteries for grid storage application due to their potential low cost. In the laboratory, half cells are normally

used to evaluate electrode materials for sodium- and potassium-based applications. However, due to the unstable SEIs that tend to form on sodium and potassium metal electrodes in conventional carbonate electrolytes, the impedance of sodium and potassium metal in half cells changes over time.[255–257] Therefore, the electrochemical performance of the tested sodium and potassium electrode materials using half cells cannot reflect their reliability. It was shown in chapter 5 that the pouch bag can be used as a powerful tool to screen the stability of electrolytes. As a future work, the pouch bags could be used to evaluate new electrolytes and electrolyte additives which are good for testing sodium and potassium electrode materials. Specifically, pouch bags containing sodium or potassium metal plus an electrolyte of interest would be stored at a certain temperature (e.g. 50°C) for a certain time (e.g. 500 h). After storage, the gas volume and composition would be measured and symmetric cells constructed to measure the charge transfer impedance. Good electrolytes or electrolyte additives would be the ones that cause the least gas production and impedance growth.

10.2.6 Use TGA-MS and Pouch Bags to Compare Positive Electrode Materials at High Voltage

In chapter 7, it was demonstrated that TGA-MS is a powerful tool to identify oxygen release from NMC electrodes charged to high voltages. As a future work, it could be useful to test other positive electrode materials such as LCO, NCA and LMO to discover if these materials release oxygen at a charged state below 100°C. Single crystal NMC could be the next generation positive electrode material due to its high inertness to the electrolyte. Presently, only single crystal NMC532 is available in the market. Single crystal NMC622, NMC811 and NCA positive electrodes may be available in the future. As a future work, it is recommended to test these single crystal materials using this method.

In the laboratory, coin cells are normally used to test the performance of materials. However, this cell format cannot be used to monitor gas generation. Figure 10.2 shows that charged uncoated NMC532 electrodes produce less gas and have less impedance growth compared to uncoated NMC442 and uncoated NMC622 electrodes when they are stored in the pouch bags at 60°C after 500 h. These impedance and gas volume results were extracted from Chapter 6. This suggests that pouch bags could be a good tool to evaluate synthesized positive electrode materials in the laboratory where materials are normally produced at a small scale. The charged electrode materials can be obtained by charging the pellet coin cells to high voltage. The pellet coin cell here refers to a half coin cell where the positive electrode has been compressed into a pellet and the counter electrode is lithium metal. The charged positive electrode materials are then removed and included in pouch bags. The best positive electrode materials could be the materials generating the least gas during storage at elevated temperature.
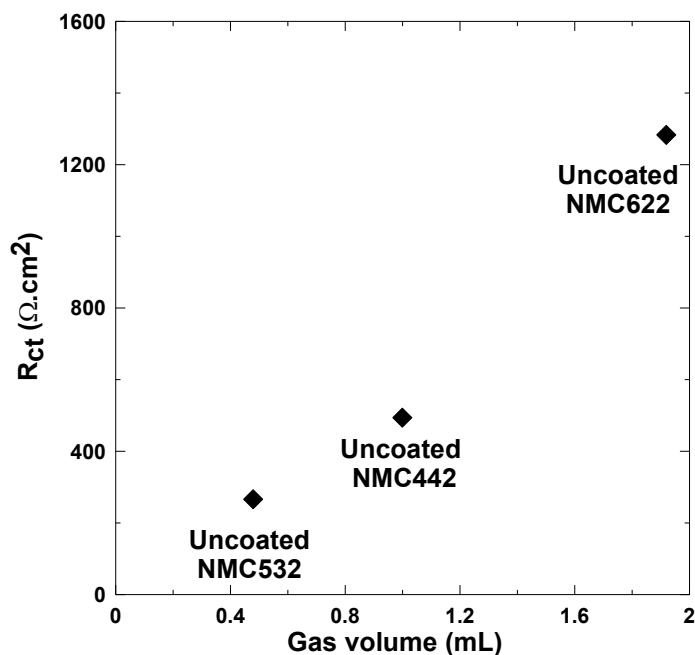
Figure 10.2 Charge transfer impedance vs gas volume for pouch bags containing uncoated NMC442, uncoated NMC532 and uncoated NMC622 stored at 60°C for 500h.

10.2.7 Use FTIR to Probe the Change of Salt Concentration during Cell Operation

During cell operation, especially at high voltages and at elevated temperature, the salt and solvents in the electrolyte can slowly be consumed due to unwanted parasitic reaction pathways. Day et al. reported a method that differential thermal analysis (DTA) may be used to measure the consumption of $LiPF_6$ and the carbonate co-solvents in intact cells. However, the DTA apparatus is not a universal device used in the laboratory. Figure 10.3 shows the area of uncoordinated EMC and coordinated EMC vs salt concentration in $LiPF_6$/EMC electrolytes. Figure 10.3 shows that there is a linear relationship between the relative peak areas corresponding to free EMC and EMC that is coordinated to a Li^+ cation, and the salt concentration. These peak area results were extracted from FT-IR data shown in Chapter 9. This suggests that FT-IR can be used to identify the salt concentration. Although this method cannot be applied to an intact cell, FT-IR instruments are more widely available in the average laboratory. Therefore, it is suggested that an FT-IR method could be developed to measure the salt consumption in Li-ion cells.
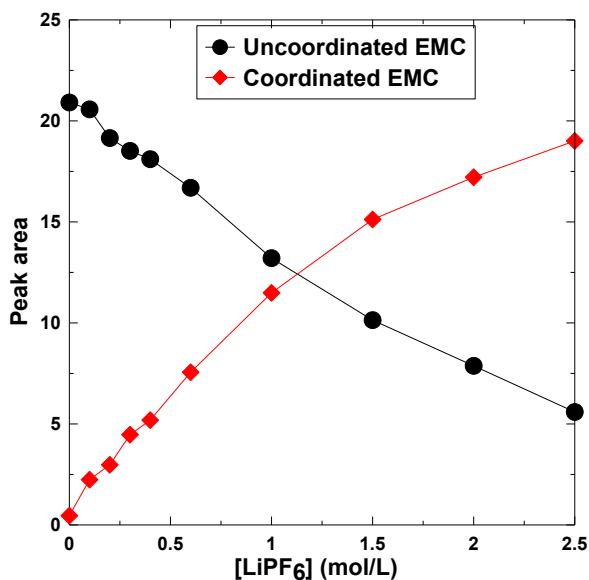
Figure 10.3 The peak areas for the C=O group of free EMC (1845 cm^{-1}) and EMC that is coordinated to Li^+ (1810 cm^{-1}) vs the concentration of $LiPF_6$ in EMC electrolytes.

REFERENCES

1. D. Andre, S.-J. Kim, P. Lamp, S. F. Lux, F. Maglia, O. Paschos, and B. Stiaszny, *J. Mater. Chem. A*, **3**, 6709–6732 (2015).

2. G. E. Blomgren, *J. Electrochem. Soc.*, **164**, A5019–A5025 (2017).

3. D. D. MacNeil and J. R. Dahn, *J. Electrochem. Soc.*, **149**, A912–A919 (2002).

4. D. D. MacNeil, L. Christensen, J. Landucci, J. M. Paulsen, and J. R. Dahn, *J. Electrochem. Soc.*, **147**, 970–979 (2000).

5. D. D. MacNeil, Z. Lu, and J. R. Dahn, *J. Electrochem. Soc.*, **149**, A1332–A1336 (2002).

6. Z. Lu, D. D. MacNeil, and J. R. Dahn, *Electrochem. Solid-State Lett.*, **4**, A200–A203 (2001).

7. T. Ohzuku and Y. Makimura, *Chem. Lett.*, **30**, 642–643 (2001).

8. J. Li, R. Petibon, S. Glazier, N. Sharma, W. K. Pang, V. K. Peterson, and J. R. Dahn, *Electrochimica Acta*, **180**, 234–240 (2015).

9. L. E. Downie, K. J. Nelson, R. Petibon, V. L. Chevrier, and J. R. Dahn, *ECS Electrochem. Lett.*, **2**, A106–A109 (2013).

10. L. E. Downie, S. R. Hyatt, and J. R. Dahn, *J. Electrochem. Soc.*, **163**, A35–A42 (2016).

11. L. Ma, D. Y. Wang, L. E. Downie, J. Xia, K. J. Nelson, N. N. Sinha, and J. R. Dahn, *J. Electrochem. Soc.*, **161**, A1261–A1265 (2014).

12. J. Xia, J. Self, L. Ma, and J. R. Dahn, *J. Electrochem. Soc.*, **162**, A1424–A1431 (2015).

13. J. Im, J. Lee, M.-H. Ryou, Y. M. Lee, and K. Y. Cho, *J. Electrochem. Soc.*, **164**, A6381–A6385 (2017).

14. L. Ma, J. Xia, and J. R. Dahn, *J. Electrochem. Soc.*, **161**, A2250–A2254 (2014).

15. K. J. Nelson, G. L. d'Eon, A. T. B. Wright, L. Ma, J. Xia, and J. R. Dahn, *J. Electrochem. Soc.*, **162**, A1046–A1054 (2015).

16. R. S. Arumugam, L. Ma, J. Li, X. Xia, J. M. Paulsen, and J. R. Dahn, *J. Electrochem. Soc.*, **163**, A2531–A2538 (2016).

17. Y.-S. Lee, W.-K. Shin, A. G. Kannan, S. M. Koo, and D.-W. Kim, *ACS Appl. Mater. Interfaces*, **7**, 13944–13951 (2015).

18. S. L. Glazier, K. J. Nelson, J. P. Allen, J. Li, and J. R. Dahn, *J. Electrochem. Soc.*, **164**, A1203–A1212 (2017).

19. Y.-K. Sun, S.-W. Cho, S.-W. Lee, C. S. Yoon, and K. Amine, *J. Electrochem. Soc.*, **154**, A168–A172 (2007).

20. C. P. Aiken, J. Self, R. Petibon, X. Xia, J. M. Paulsen, and J. R. Dahn, *J. Electrochem. Soc.*, **162**, A760–A767 (2015).

21. J. Self, C. P. Aiken, R. Petibon, and J. R. Dahn, *J. Electrochem. Soc.*, **162**, A796–A802 (2015).

22. M. Metzger, C. Marino, J. Sicklinger, D. Haering, and H. A. Gasteiger, *J. Electrochem. Soc.*, **162**, A1123–A1134 (2015).

23. A. Guéguen, D. Streich, M. He, M. Mendez, F. F. Chesneau, P. Novák, and E. J. Berg, *J. Electrochem. Soc.*, **163**, A1095–A1100 (2016).

24. M. Metzger, B. Strehle, S. Solchenbach, and H. A. Gasteiger, *J. Electrochem. Soc.*, **163**, A798–A809 (2016).

25. K. J. Nelson, D. W. Abarbanel, J. Xia, Z. Lu, and J. R. Dahn, *J. Electrochem. Soc.*, **163**, A272–A280 (2016).

26. J. A. Gilbert, J. Bareño, T. Spila, S. E. Trask, D. J. Miller, B. J. Polzin, A. N. Jansen, and D. P. Abraham, *J. Electrochem. Soc.*, **164**, A6054–A6065 (2017).

27. S. L. Glazier, L. E. Downie, J. Xia, A. J. Louli, and J. R. Dahn, *J. Electrochem. Soc.*, **163**, A2131–A2138 (2016).

28. L. E. Downie and J. R. Dahn, *J. Electrochem. Soc.*, **161**, A1782–A1787 (2014).

29. J. Xia, R. Petibon, D. Xiong, L. Ma, and J. R. Dahn, *J. Power Sources*, **328**, 124–135 (2016).

30. R. Petibon, J. Xia, L. Ma, M. K. G. Bauer, K. J. Nelson, and J. R. Dahn, *J. Electrochem. Soc.*, **163**, A2571–A2578 (2016).

31. L. Ma, S. L. Glazier, R. Petibon, J. Xia, J. M. Peters, Q. Liu, J. Allen, R. N. C. Doig, and J. R. Dahn, *J. Electrochem. Soc.*, **164**, A5008–A5018 (2017).

32. K. Xu, *Chem. Rev.*, **104**, 4303–4418 (2004).

33. P. Arora and Z. (John) Zhang, *Chem. Rev.*, **104**, 4419–4462 (2004).

34. http://www.avicenne.com/pdf/Fort_Lauderdale_Tutorial_C_Pillot_March2015.pdf.

35. A. K. Padhi, K. S. Nanjundaswamy, and J. B. Goodenough, *J. Electrochem. Soc.*, **144**, 1188–1194 (1997).

36. C. Sun, S. Rajasekhara, J. B. Goodenough, and F. Zhou, *J. Am. Chem. Soc.*, **133**, 2132–2135 (2011).

37. J. Jiang and J. R. Dahn, *Electrochem. Commun.*, **6**, 39–43 (2004).

38. C. Delacourt, L. Laffont, R. Bouchet, C. Wurm, J.-B. Leriche, M. Morcrette, J.-M. Tarascon, and C. Masquelier, *J. Electrochem. Soc.*, **152**, A913–A921 (2005).

39. C. M. Julien, K. Zaghib, A. Mauger, M. Massot, A. Ait-Salah, M. Selmane, and F. Gendron, *J. Appl. Phys.*, **100**, 063511 (2006).

40. M. M. Doeff, Y. Hu, F. McLarnon, and R. Kostecki, *Electrochem. Solid-State Lett.*, **6**, A207–A209 (2003).

41. R. Dominko, M. Bele, M. Gaberscek, M. Remskar, D. Hanzel, S. Pejovnik, and J. Jamnik, *J. Electrochem. Soc.*, **152**, A607–A610 (2005).

42. C. Delacourt, P. Poizot, S. Levasseur, and C. Masquelier, *Electrochem. Solid-State Lett.*, **9**, A352–A355 (2006).

43. K. Mizushima, P. C. Jones, P. J. Wiseman, and J. B. Goodenough, *Mater. Res. Bull.*, **15**, 783–789 (1980).

44. K. Ozawa, *Solid State Ion.*, **69**, 212–221 (1994).

45. J. Xia, M. Nie, J. C. Burns, A. Xiao, W. M. Lamanna, and J. R. Dahn, *J. Power Sources*, **307**, 340–350 (2016).

46. H.-J. Noh, S. Youn, C. S. Yoon, and Y.-K. Sun, *J. Power Sources*, **233**, 121–130 (2013).

47. L. Ma, M. Nie, J. Xia, and J. R. Dahn, *J. Power Sources*, **327**, 145–150 (2016).

48. Y. Wang, J. Jiang, and J. R. Dahn, *Electrochem. Commun.*, **9**, 2534–2540 (2007).

49. I. Belharouak, W. Lu, D. Vissers, and K. Amine, *Electrochem. Commun.*, **8**, 329–335 (2006).

50. D. D. MacNeil, T. D. Hatchard, and J. R. Dahn, *J. Electrochem. Soc.*, **148**, A663–A667 (2001).

51. G. Amatucci and J.-M. Tarascon, *J. Electrochem. Soc.*, **149**, K31–K46 (2002).

52. M. Wohlfahrt-Mehrens, C. Vogler, and J. Garche, *J. Power Sources*, **127**, 58–64 (2004).

53. J. Vetter, P. Novák, M. R. Wagner, C. Veit, K.-C. Möller, J. O. Besenhard, M. Winter, M. Wohlfahrt-Mehrens, C. Vogler, and A. Hammouche, *J. Power Sources*, **147**, 269–281 (2005).

54. A. D. Pasquier, A. Blyr, P. Courjal, D. Larcher, G. Amatucci, B. Gérand, and J.-M. Tarascon, *J. Electrochem. Soc.*, **146**, 428–436 (1999).

55. A. Banerjee, Y. Shilina, B. Ziv, J. M. Ziegelbauer, S. Luski, D. Aurbach, and I. C. Halalay, *J. Electrochem. Soc.*, **164**, A6315–A6323 (2017).

56. M. N. Obrovac and V. L. Chevrier, *Chem. Rev.*, **114**, 11444–11502 (2014).

57. K. Zaghib, M. Dontigny, A. Guerfi, P. Charest, I. Rodrigues, A. Mauger, and C. M. Julien, *J. Power Sources*, **196**, 3949–3954 (2011).

58. N. Takami, H. Inagaki, Y. Tatebayashi, H. Saruwatari, K. Honda, and S. Egusa, *J. Power Sources*, **244**, 469–475 (2013).

59. N. Takami, H. Inagaki, T. Kishi, Y. Harada, Y. Fujita, and K. Hoshina, *J. Electrochem. Soc.*, **156**, A128–A132 (2009).

60. A. Jaiswal, C. R. Horne, O. Chang, W. Zhang, W. Kong, E. Wang, T. Chern, and M. M. Doeff, *J. Electrochem. Soc.*, **156**, A1041–A1046 (2009).

61. Y. Wang and J. Dahn, *Electrochem. Solid-State Lett.*, **9**, A340–A343 (2006).

62. V. A. Sethuraman, A. Nguyen, M. J. Chon, S. P. V. Nadimpalli, H. Wang, D. P. Abraham, A. F. Bower, V. B. Shenoy, and P. R. Guduru, *J. Electrochem. Soc.*, **160**, A739–A746 (2013).

63. U. Kasavajjula, C. Wang, and A. J. Appleby, *J. Power Sources*, **163**, 1003–1039 (2007).

64. M. N. Obrovac and L. Christensen, *Electrochem. Solid-State Lett.*, **7**, A93–A96 (2004).

65. R. Petibon, V. L. Chevrier, C. P. Aiken, D. S. Hall, S. R. Hyatt, R. Shunmugasundaram, and J. R. Dahn, *J. Electrochem. Soc.*, **163**, A1146–A1156 (2016).

66. M. C. Smart, B. V. Ratnakumar, S. Surampudi, Y. Wang, X. Zhang, S. G. Greenbaum, A. Hightower, C. C. Ahn, and B. Fultz, *J. Electrochem. Soc.*, **146**, 3963–3969 (1999).

67. M. C. Smart, B. V. Ratnakumar, and S. Surampudi, *J. Electrochem. Soc.*, **149**, A361–A370 (2002).

68. S. S. Zhang, K. Xu, and T. R. Jow, *J. Electrochem. Soc.*, **149**, A586–A590 (2002).

69. G. G. Eshetu, S. Grugeon, G. Gachot, D. Mathiron, M. Armand, and S. Laruelle, *Electrochimica Acta*, **102**, 133–141 (2013).

70. H.-B. Han, S.-S. Zhou, D.-J. Zhang, S.-W. Feng, L.-F. Li, K. Liu, W.-F. Feng, J. Nie, H. Li, X.-J. Huang, M. Armand, and Z.-B. Zhou, *J. Power Sources*, **196**, 3623–3632 (2011).

71. A. Abouimrane, J. Ding, and I. J. Davidson, *J. Power Sources*, **189**, 693–696 (2009).

72. K. Xu, S. Zhang, and T. R. Jow, *Electrochem. Solid-State Lett.*, **6**, A117–A120 (2003).

73. K. Xu, S. Zhang, T. R. Jow, W. Xu, and C. A. Angell, *Electrochem. Solid-State Lett.*, **5**, A26–A29 (2002).

74. K. Xu, S. Zhang, B. A. Poese, and T. R. Jow, *Electrochem. Solid-State Lett.*, **5**, A259–A262 (2002).

75. J. Jiang, H. Fortier, J. N. Reimers, and J. R. Dahn, *J. Electrochem. Soc.*, **151**, A609–A613 (2004).

76. J. L. Nowinski, P. Lightfoot, and P. G. Bruce, *J. Mater. Chem.*, **4**, 1579–1580 (1994).

77. S. S. Zhang and T. R. Jow, *J. Power Sources*, **109**, 458–464 (2002).

78. T. Kawamura, A. Kimura, M. Egashira, S. Okada, and J.-I. Yamaki, *J. Power Sources*, **104**, 260–264 (2002).

79. C. L. Campion, W. Li, and B. L. Lucht, *J. Electrochem. Soc.*, **152**, A2327–A2334 (2005).

80. P. Arora, R. E. White, and M. Doyle, *J. Electrochem. Soc.*, **145**, 3647–3667 (1998).

81. J. C. Burns, N. N. Sinha, G. Jain, H. Ye, C. M. VanElzen, E. Scott, A. Xiao, W. M. Lamanna, and J. R. Dahn, *J. Electrochem. Soc.*, **160**, A2281–A2287 (2013).

82. J. C. Burns, N. N. Sinha, G. Jain, H. Ye, C. M. VanElzen, E. Scott, A. Xiao, W. M. Lamanna, and J. R. Dahn, *J. Electrochem. Soc.*, **161**, A247–A255 (2014).

83. J. C. Burns, G. Jain, A. J. Smith, K. W. Eberman, E. Scott, J. P. Gardner, and J. R. Dahn, *J. Electrochem. Soc.*, **158**, A255–A261 (2011).

84. C. Täubert, M. Fleischhammer, M. Wohlfahrt-Mehrens, U. Wietelmann, and T. Buhrmester, *J. Electrochem. Soc.*, **157**, A721–A728 (2010).

85. S. S. Zhang, K. Xu, and T. R. Jow, *J. Power Sources*, **156**, 629–633 (2006).

86. M. Nie, D. Chalasani, D. P. Abraham, Y. Chen, A. Bose, and B. L. Lucht, *J. Phys. Chem. C*, **117**, 1257–1267 (2013).

87. P. He, X. Zhang, Y.-G. Wang, L. Cheng, and Y.-Y. Xia, *J. Electrochem. Soc.*, **155**, A144–A150 (2008).

88. A. Würsig, H. Buqa, M. Holzapfel, F. Krumeich, and P. Novák, *Electrochem. Solid-State Lett.*, **8**, A34–A37 (2005).

89. D. Aurbach, M. D. Levi, E. Levi, H. Teller, B. Markovsky, G. Salitra, U. Heider, and L. Heider, *J. Electrochem. Soc.*, **145**, 3024–3034 (1998).

90. D. Aurbach, *J. Power Sources*, **89**, 206–218 (2000).

91. T. Eriksson, A. M. Andersson, A. G. Bishop, C. Gejke, T. Gustafsson, and J. O. Thomas, *J. Electrochem. Soc.*, **149**, A69–A78 (2002).

92. A. M. Andersson, D. P. Abraham, R. Haasch, S. MacLaren, J. Liu, and K. Amine, *J. Electrochem. Soc.*, **149**, A1358–A1369 (2002).

93. D. Aurbach, K. Gamolsky, B. Markovsky, G. Salitra, Y. Gofer, U. Heider, R. Oesten, and M. Schmidt, *J. Electrochem. Soc.*, **147**, 1322–1331 (2000).

94. Z. Wang, X. Huang, and L. Chen, *J. Electrochem. Soc.*, **151**, A1641–A1652 (2004).

95. Z. Wang, Y. Sun, L. Chen, and X. Huang, *J. Electrochem. Soc.*, **151**, A914–A921 (2004).

96. L. Yang, B. Ravdel, and B. L. Lucht, *Electrochem. Solid-State Lett.*, **13**, A95–A97 (2010).

97. D. Aurbach, B. Markovsky, G. Salitra, E. Markevich, Y. Talyossef, M. Koltypin, L. Nazar, B. Ellis, and D. Kovacheva, *J. Power Sources*, **165**, 491–499 (2007).

98. H. Ota, Y. Sakata, A. Inoue, and S. Yamaguchi, *J. Electrochem. Soc.*, **151**, A1659–A1669 (2004).

99. D. Aurbach, K. Gamolsky, B. Markovsky, Y. Gofer, M. Schmidt, and U. Heider, *Electrochimica Acta*, **47**, 1423–1439 (2002).

100. Y. Wang, S. Nakamura, K. Tasaki, and P. B. Balbuena, *J. Am. Chem. Soc.*, **124**, 4408–4421 (2002).

101. Y. Hu, W. Kong, H. Li, X. Huang, and L. Chen, *Electrochem. Commun.*, **6**, 126–131 (2004).

102. R. McMillan, H. Slegr, Z. X. Shu, and W. Wang, *J. Power Sources*, **81**–**82**, 20–26 (1999).

103. R. Mogi, M. Inaba, S.-K. Jeong, Y. Iriyama, T. Abe, and Z. Ogumi, *J. Electrochem. Soc.*, **149**, A1578–A1583 (2002).

104. L. Xing, W. Li, M. Xu, T. Li, and L. Zhou, *J. Power Sources*, **196**, 7044–7047 (2011).

105. A. Sano and S. Maruyama, *J. Power Sources*, **192**, 714–718 (2009).

106. D. Aurbach, K. Gamolsky, B. Markovsky, Y. Gofer, M. Schmidt, and U. Heider, *Electrochimica Acta*, **47**, 1423–1439 (2002).

107. H. Ota, Y. Sakata, A. Inoue, and S. Yamaguchi, *J. Electrochem. Soc.*, **151**, A1659–A1669 (2004).

108. H. Ota, K. Shima, M. Ue, and J. Yamaki, *Electrochimica Acta*, **49**, 565–572 (2004).

109. D. Xiong, J. C. Burns, A. J. Smith, N. Sinha, and J. R. Dahn, *J. Electrochem. Soc.*, **158**, A1431–A1435 (2011).

110. N. N. Sinha, A. J. Smith, J. C. Burns, G. Jain, K. W. Eberman, E. Scott, J. P. Gardner, and J. R. Dahn, *J. Electrochem. Soc.*, **158**, A1194–A1201 (2011).

111. R. Petibon, C. P. Aiken, N. N. Sinha, J. C. Burns, H. Ye, C. M. VanElzen, G. Jain, S. Trussler, and J. R. Dahn, *J. Electrochem. Soc.*, **160**, A117–A124 (2013).

112. J. C. Burns, G. Jain, A. J. Smith, K. W. Eberman, E. Scott, J. P. Gardner, and J. R. Dahn, *J. Electrochem. Soc.*, **158**, A255–A261 (2011).

113. J. C. Burns, R. Petibon, K. J. Nelson, N. N. Sinha, A. Kassam, B. M. Way, and J. R. Dahn, *J. Electrochem. Soc.*, **160**, A1668–A1674 (2013).

114. R. Petibon, L. Rotermund, K. J. Nelson, A. S. Gozdz, J. Xia, and J. R. Dahn, *J. Electrochem. Soc.*, **161**, A1167–A1172 (2014).

115. R. Petibon, J. Xia, J. C. Burns, and J. R. Dahn, *J. Electrochem. Soc.*, **161**, A1618–A1624 (2014).

116. J. Xia, L. Ma, C. P. Aiken, K. J. Nelson, L. P. Chen, and J. R. Dahn, *J. Electrochem. Soc.*, **161**, A1634–A1641 (2014).

117. L. Madec, R. Petibon, J. Xia, J.-P. Sun, I. G. Hill, and J. R. Dahn, *J. Electrochem. Soc.*, **162**, A2635–A2645 (2015).

118. M. Broussely, P. Biensan, F. Bonhomme, P. Blanchard, S. Herreyre, K. Nechev, and R. J. Staniewicz, *J. Power Sources*, **146**, 90–96 (2005).

119. G. Yan, X. Li, Z. Wang, H. Guo, and C. Wang, *J. Power Sources*, **248**, 1306–1311 (2014).

120. Y.-M. Song, J.-G. Han, S. Park, K. T. Lee, and N.-S. Choi, *J. Mater. Chem. A*, **2**, 9506–9513 (2014).

121. A. von Cresce and K. Xu, *J. Electrochem. Soc.*, **158**, A337–A342 (2011).

122. J. Xia, N. N. Sinha, L. P. Chen, G. Y. Kim, D. J. Xiong, and J. R. Dahn, *J. Electrochem. Soc.*, **161**, A84–A88 (2014).

123. X. Zuo, C. Fan, X. Xiao, J. Liu, and J. Nan, *J. Power Sources*, **219**, 94–99 (2012).

124. M. Xu, D. Lu, A. Garsuch, and B. L. Lucht, *J. Electrochem. Soc.*, **159**, A2130–A2134 (2012).

125. M. Hu, X. Pang, and Z. Zhou, *J. Power Sources*, **237**, 229–242 (2013).

126. Y. S. Jung, A. S. Cavanagh, A. C. Dillon, M. D. Groner, S. M. George, and S.-H. Lee, *J. Electrochem. Soc.*, **157**, A75–A81 (2010).

127. N. Kosova, E. Devyatkina, A. Slobodyuk, and V. Kaichev, *Solid State Ion.*, **179**, 1745–1749 (2008).

128. Z. Chen and J. R. Dahn, *Electrochem. Solid-State Lett.*, **6**, A221–A224 (2003).

129. Z. Chen and J. R. Dahn, *Electrochimica Acta*, **49**, 1079–1090 (2004).

130. Y. Zhou, Y. Lee, H. Sun, J. M. Wallas, S. M. George, and M. Xie, *ACS Appl. Mater. Interfaces*, **9**, 9614–9619 (2017).

131. Y.-K. Sun, J.-M. Han, S.-T. Myung, S.-W. Lee, and K. Amine, *Electrochem. Commun.*, **8**, 821–826 (2006).

132. Y.-K. Sun, C. S. Yoon, S.-T. Myung, I. Belharouak, and K. Amine, *J. Electrochem. Soc.*, **156**, A1005–A1010 (2009).

133. H. G. Song, K.-S. Park, and Y. J. Park, *Solid State Ion.*, **225**, 532–537 (2012).

134. A. M. Wise, C. Ban, J. N. Weker, S. Misra, A. S. Cavanagh, Z. Wu, Z. Li, M. S. Whittingham, K. Xu, S. M. George, and M. F. Toney, *Chem. Mater.*, **27**, 6146–6154 (2015).

135. K. Yang, L.-Z. Fan, J. Guo, and X. Qu, *Electrochimica Acta*, **63**, 363–368 (2012).

136. X. Zhang, R. Kostecki, T. J. Richardson, J. K. Pugh, and P. N. Ross, *J. Electrochem. Soc.*, **148**, A1341–A1345 (2001).

137. E. Peled, *J. Electrochem. Soc.*, **126**, 2047–2051 (1979).

138. A. J. Smith, J. C. Burns, X. Zhao, D. Xiong, and J. R. Dahn, *J. Electrochem. Soc.*, **158**, S23–S23 (2011).

139. D. Xiong, J. C. Burns, A. J. Smith, N. Sinha, and J. R. Dahn, *J. Electrochem. Soc.*, **158**, A1431–A1435 (2011).

140. E. Peled, D. Golodnitsky, and G. Ardel, *J. Electrochem. Soc.*, **144**, L208–L210 (1997).

141. P. Verma, P. Maire, and P. Novák, *Electrochimica Acta*, **55**, 6332–6341 (2010).

142. A. J. Smith, J. C. Burns, D. Xiong, and J. R. Dahn, *J. Electrochem. Soc.*, **158**, A1136–A1142 (2011).

143. M. Broussely, S. Herreyre, P. Biensan, P. Kasztejna, K. Nechev, and R. J. Staniewicz, *J. Power Sources*, **97–98**, 13–21 (2001).

144. M. Winter, G. H. Wrodnigg, J. O. Besenhard, W. Biberacher, and P. Novák, *J. Electrochem. Soc.*, **147**, 2427–2431 (2000).

145. M. Hahn, H. Buqa, P. W. Ruch, D. Goers, M. E. Spahr, J. Ufheil, P. Novák, and R. Kötz, *Electrochem. Solid-State Lett.*, **11**, A151–A154 (2008).

146. P. Arora, R. E. White, and M. Doyle, *J. Electrochem. Soc.*, **145**, 3647–3667 (1998).

147. R. Fathi, J. C. Burns, D. A. Stevens, H. Ye, C. Hu, G. Jain, E. Scott, C. Schmidt, and J. R. Dahn, *J. Electrochem. Soc.*, **161**, A1572–A1579 (2014).

148. P. Lu, C. Li, E. W. Schneider, and S. J. Harris, *J. Phys. Chem. C*, **118**, 896–903 (2014).

149. I. Bloom, B. W. Cole, J. J. Sohn, S. A. Jones, E. G. Polzin, V. S. Battaglia, G. L. Henriksen, C. Motloch, R. Richardson, T. Unkelhaeuser, D. Ingersoll, and H. L. Case, *J. Power Sources*, **101**, 238–247 (2001).

150. H. J. Ploehn, P. Ramadass, and R. E. White, *J. Electrochem. Soc.*, **151**, A456–A462 (2004).

151. M. Moshkovich, M. Cojocaru, H. E. Gottlieb, and D. Aurbach, *J. Electroanal. Chem.*, **497**, 84–96 (2001).

152. D. Aurbach, B. Markovsky, A. Rodkin, M. Cojocaru, E. Levi, and H.-J. Kim, *Electrochimica Acta*, **47**, 1899–1911 (2002).

153. A. Jarry, S. Gottis, Y.-S. Yu, J. Roque-Rosell, C. Kim, J. Cabana, J. Kerr, and R. Kostecki, *J. Am. Chem. Soc.*, **137**, 3533–3539 (2015).

154. L. Xing, W. Li, C. Wang, F. Gu, M. Xu, C. Tan, and J. Yi, *J. Phys. Chem. B*, **113**, 16596–16602 (2009).

155. S. E. Sloop, J. B. Kerr, and K. Kinoshita, *J. Power Sources*, **119**–**121**, 330–337 (2003).

156. R. Spotnitz, *J. Power Sources*, **113**, 72–80 (2003).

157. J. C. Burns, A. Kassam, N. N. Sinha, L. E. Downie, L. Solnickova, B. M. Way, and J. R. Dahn, *J. Electrochem. Soc.*, **160**, A1451–A1456 (2013).

158. R. Dedryvère, D. Foix, S. Franger, S. Patoux, L. Daniel, and D. Gonbeau, *J. Phys. Chem. C*, **114**, 10999–11008 (2010).

159. S. R. Li, C. H. Chen, X. Xia, and J. R. Dahn, *J. Electrochem. Soc.*, **160**, A1524–A1528 (2013).

160. F. Lin, I. M. Markus, D. Nordlund, T.-C. Weng, M. D. Asta, H. L. Xin, and M. M. Doeff, *Nat. Commun.*, **5**, 3529 (2014).

161. J. Self, D. S. Hall, L. Madec, and J. R. Dahn, *J. Power Sources*, **298**, 369–378 (2015).

162. D. P. Abraham, R. D. Twesten, M. Balasubramanian, I. Petrov, J. McBreen, and K. Amine, *Electrochem. Commun.*, **4**, 620–625 (2002).

163. D. P. Abraham, R. D. Twesten, M. Balasubramanian, J. Kropf, D. Fischer, J. McBreen, I. Petrov, and K. Amine, *J. Electrochem. Soc.*, **150**, A1450–A1456 (2003).

164. S.-K. Jung, H. Gwon, J. Hong, K.-Y. Park, D.-H. Seo, H. Kim, J. Hyun, W. Yang, and K. Kang, *Adv. Energy Mater.*, **4**, n/a-n/a (2014).

165. N. Y. Kim, T. Yim, J. H. Song, J.-S. Yu, and Z. Lee, *J. Power Sources*, **307**, 641–648 (2016).

166. J. Li, H. Liu, J. Xia, M. Nie, G. Botton, and J. R. Dahn, *Meet. Abstr.*, **MA2016-03**, 893–893 (2016).

167. Y. Makimura, S. Zheng, Y. Ikuhara, and Y. Ukyo, *J. Electrochem. Soc.*, **159**, A1070–A1073 (2012).

168. D. H. Jang, Y. J. Shin, and S. M. Oh, *J. Electrochem. Soc.*, **143**, 2204–2211 (1996).

169. D. H. Jang and S. M. Oh, *J. Electrochem. Soc.*, **144**, 3342–3348 (1997).

170. A. D. Robertson, S. H. Lu, and W. F. Howard, *J. Electrochem. Soc.*, **144**, 3505–3512 (1997).

171. K. Takahashi, M. Saitoh, N. Asakura, T. Hibino, M. Sano, M. Fujita, and K. Kifune, *J. Power Sources*, **136**, 115–121 (2004).

172. W. Choi and A. Manthiram, *J. Electrochem. Soc.*, **153**, A1760–A1764 (2006).

173. R. Benedek and M. M. Thackeray, *Electrochem. Solid-State Lett.*, **9**, A265–A267 (2006).

174. L. Yunjian, L. Xinhai, G. Huajun, W. Zhixing, H. Qiyang, P. Wenjie, and Y. Yong, *J. Power Sources*, **189**, 721–725 (2009).

175. M. Saulnier, A. Auclair, G. Liang, and S. B. Schougaard, *Solid State Ion.*, **294**, 1–5 (2016).

176. J. Choa and M. M. Thackeray, *J. Electrochem. Soc.*, **146**, 3577–3581 (1999).

177. Y. Xia, Y. Zhou, and M. Yoshio, *J. Electrochem. Soc.*, **144**, 2593–2600 (1997).

178. C. Zhan, J. Lu, A. J. Kropf, T. Wu, A. N. Jansen, Y.-K. Sun, X. Qiu, and K. Amine, *Nat. Commun.*, **4**, 2437 (2013).

179. H.-C. Wu, C.-Y. Su, D.-T. Shieh, M.-H. Yang, and N.-L. Wu, *Electrochem. Solid-State Lett.*, **9**, A537–A541 (2006).

180. D. Li, D. L. Danilov, L. Gao, Y. Yang, and P. H. L. Notten, *J. Electrochem. Soc.*, **163**, A3016–A3021 (2016).

181. J. Kasnatscheew, M. Evertz, B. Streipert, R. Wagner, S. Nowak, I. Cekic Laskovic, and M. Winter, *J. Phys. Chem. C*, **121**, 1521–1529 (2017).

182. B. Gyenes, D. A. Stevens, V. L. Chevrier, and J. R. Dahn, *J. Electrochem. Soc.*, **162**, A278–A283 (2015).

183. C. P. Aiken, J. Xia, D. Y. Wang, D. A. Stevens, S. Trussler, and J. R. Dahn, *J. Electrochem. Soc.*, **161**, A1548–A1554 (2014).

184. N. N. Sinha, T. H. Marks, H. M. Dahn, A. J. Smith, J. C. Burns, D. J. Coyle, J. J. Dahn, and J. R. Dahn, *J. Electrochem. Soc.*, **159**, A1672–A1681 (2012).

185. T. Momma, M. Matsunaga, D. Mukoyama, and T. Osaka, *J. Power Sources*, **216**, 304–307 (2012).

186. A. Eddahech, O. Briat, N. Bertrand, J.-Y. Delétage, and J.-M. Vinassa, *Int. J. Electr. Power Energy Syst.*, **42**, 487–494 (2012).

187. W. Waag, S. Käbitz, and D. U. Sauer, *Appl. Energy*, **102**, 885–897 (2013).

188. D. Andre, M. Meiler, K. Steiner, C. Wimmer, T. Soczka-Guth, and D. U. Sauer, *J. Power Sources*, **196**, 5334–5341 (2011).

189. U. Tröltzsch, O. Kanoun, and H.-R. Tränkler, *Electrochimica Acta*, **51**, 1664–1672 (2006).

190. D. Andre, M. Meiler, K. Steiner, H. Walz, T. Soczka-Guth, and D. U. Sauer, *J. Power Sources*, **196**, 5349–5356 (2011).

191. K. J. Nelson, J. Xia, and J. R. Dahn, *J. Electrochem. Soc.*, **161**, A1884–A1889 (2014).

192. D. W. Abarbanel, K. J. Nelson, and J. R. Dahn, *J. Electrochem. Soc.*, **163**, A522–A529 (2016).

193. J. Xia, J. E. Harlow, R. Petibon, J. C. Burns, L. P. Chen, and J. R. Dahn, *J. Electrochem. Soc.*, **161**, A547–A553 (2014).

194. J. Xia, L. Madec, L. Ma, L. D. Ellis, W. Qiu, K. J. Nelson, Z. Lu, and J. R. Dahn, *J. Power Sources*, **295**, 203–211 (2015).

195. M. Dollé, F. Orsini, A. S. Gozdz, and J.-M. Tarascon, *J. Electrochem. Soc.*, **148**, A851–A857 (2001).

196. G. Nagasubramanian, *J. Power Sources*, **87**, 226–229 (2000).

197. J. Y. Song, H. H. Lee, Y. Y. Wang, and C. C. Wan, *J. Power Sources*, **111**, 255–267 (2002).

198. S. Klink, E. Madej, E. Ventosa, A. Lindner, W. Schuhmann, and F. La Mantia, *Electrochem. Commun.*, **22**, 120–123 (2012).

199. C. H. Chen, J. Liu, and K. Amine, *J. Power Sources*, **96**, 321–328 (2001).

200. R. Petibon, N. N. Sinha, J. C. Burns, C. P. Aiken, H. Ye, C. M. VanElzen, G. Jain, S. Trussler, and J. R. Dahn, *J. Power Sources*, **251**, 187–194 (2014).

201. R. Petibon, L. Madec, D. W. Abarbanel, and J. R. Dahn, *J. Power Sources*, **300**, 419–429 (2015).

202. C. Pastor-Fernández, K. Uddin, G. H. Chouchelamane, W. D. Widanage, and J. Marco, *J. Power Sources*, **360**, 301–318 (2017).

203. Y. Xie, J. Li, and C. Yuan, *Electrochimica Acta*, **127**, 266–275 (2014).

204. T. Momma, T. Yokoshima, H. Nara, Y. Gima, and T. Osaka, *Electrochimica Acta*, **131**, 195–201 (2014).

205. J. G. Zhu, Z. C. Sun, X. Z. Wei, and H. F. Dai, *RSC Adv.*, **4**, 29988–29998 (2014).

206. A. Mertens, I. C. Vinke, H. Tempel, H. Kungl, L. G. J. de Haart, R.-A. Eichel, and J. Granwehr, *J. Electrochem. Soc.*, **163**, H521–H527 (2016).

207. U. Westerhoff, K. Kurbach, F. Lienesch, and M. Kurrat, *Energy Technol.*, **4**, 1620–1630 (2016).

208. T. Hang, D. Mukoyama, H. Nara, N. Takami, T. Momma, and T. Osaka, *J. Power Sources*, **222**, 442–447 (2013).

209. D. C. Harris, *Quantitative chemical anaalysis*, 6 th., W. H. Freeman and Company, (2003).

210. B. M. Ham and A. MaHam, *Analytical chemistry: a chemist and laboratory technician's toolkit*, 2015 John Wiley and Sons.

211. L. Madec, J. Xia, R. Petibon, K. J. Nelson, J.-P. Sun, I. G. Hill, and J. R. Dahn, *J. Phys. Chem. C*, **118**, 29608–29622 (2014).

212. Y. Kim, *J. Solid State Electrochem.*, **17**, 1961–1965 (2013).

213. O. Borodin, W. Behl, and T. R. Jow, *J. Phys. Chem. C*, **117**, 8661–8682 (2013).

214. S. E. Sloop, J. B. Kerr, and K. Kinoshita, *J. Power Sources*, **119–121**, 330–337 (2003).

215. R. Petibon, L. M. Rotermund, and J. R. Dahn, *J. Power Sources*, **287**, 184–195 (2015).

216. Y. R. Dougassa, C. Tessier, L. El Ouatani, M. Anouti, and J. Jacquemin, *J. Chem. Thermodyn.*, **61**, 32–44 (2013).

217. K. Kanamura, *J. Power Sources*, **81–82**, 123–129 (1999).

218. J. C. Burns, A. Kassam, N. N. Sinha, L. E. Downie, L. Solnickova, B. M. Way, and J. R. Dahn, *J. Electrochem. Soc.*, **160**, A1451–A1456 (2013).

219. Y. R. Dougassa, J. Jacquemin, L. El Ouatani, C. Tessier, and M. Anouti, *J. Chem. Thermodyn.*, **79**, 49–60 (2014).

220. D. J. Xiong, R. Petibon, M. Nie, L. Ma, J. Xia, and J. R. Dahn, *J. Electrochem. Soc.*, **163**, A546–A551 (2016).

221. S. Tanuma, C. J. Powell, and D. R. Penn, *Surf. Interface Anal.*, **17**, 927–939 (1991).

222. C. J. Powell and A. Jablonski, *NIST Electron Inelastic-Mean-Free-Path Database-Version 1.2*, National Institute of Standards and Technology, Gaithersburg, MD, USA, (2010).

223. S.-M. Bak, E. Hu, Y. Zhou, X. Yu, S. D. Senanayake, S.-J. Cho, K.-B. Kim, K. Y. Chung, X.-Q. Yang, and K.-W. Nam, *ACS Appl. Mater. Interfaces*, **6**, 22594–22601 (2014).

224. N. N. Sinha, J. C. Burns, and J. R. Dahn, *J. Electrochem. Soc.*, **161**, A1084–A1089 (2014).

225. J.-M. Atebamba, J. Moskon, S. Pejovnik, and M. Gaberscek, *J. Electrochem. Soc.*, **157**, A1218–A1228 (2010).

226. D. Y. Wang, J. C. Burns, and J. R. Dahn, *J. Electrochem. Soc.*, **161**, A1278–A1283 (2014).

227. S. H. Ju, I.-S. Kang, Y.-S. Lee, W.-K. Shin, S. Kim, K. Shin, and D.-W. Kim, *ACS Appl. Mater. Interfaces*, **6**, 2546–2552 (2014).

228. Y. Zhang and C.-Y. Wang, *J. Electrochem. Soc.*, **156**, A527–A535 (2009).

229. J. Xia, L. Ma, K. J. Nelson, M. Nie, Z. Lu, and J. R. Dahn, *J. Electrochem. Soc.*, **163**, A2399–A2406 (2016).

230. R. P. Day, J. Xia, R. Petibon, J. Rucska, H. Wang, A. T. B. Wright, and J. R. Dahn, *J. Electrochem. Soc.*, **162**, A2577–A2581 (2015).

231. M. S. Ding, K. Xu, S. S. Zhang, K. Amine, G. L. Henriksen, and T. R. Jow, *J. Electrochem. Soc.*, **148**, A1196–A1204 (2001).

232. M. S. Ding and T. R. Jow, *J. Electrochem. Soc.*, **150**, A620–A628 (2003).

233. L. Doucey, M. Revault, A. Lautié, A. Chaussé, and R. Messina, *Electrochimica Acta*, **44**, 2371–2377 (1999).

234. K. Xu, A. von Cresce, and U. Lee, *Langmuir*, **26**, 11538–11543 (2010).

235. M. Delsignore, H. Farber, and S. Petrucci, *J. Phys. Chem.*, **89**, 4968–4973 (1985).

236. Z. Chen and M. Hojo, *J. Phys. Chem. B*, **101**, 10896–10902 (1997).

237. D. Ekka and M. N. Roy, *J. Phys. Chem. B*, **116**, 11687–11694 (2012).

238. R. Dewan and M. N. Roy, *Phys. Chem. Liq.*, **49**, 145–154 (2011).

239. Y. Marcus and G. Hefter, *Chem. Rev.*, **106**, 4585–4621 (2006).

240. A. Jouyban, S. Soltanpour, and H.-K. Chan, *Int. J. Pharm.*, **269**, 353–360 (2004).

241. M. Delsignore, H. E. Maaser, and S. Petrucci, *J. Phys. Chem.*, **88**, 2405–2411 (1984).

242. N. Chapman, O. Borodin, T. Yoon, C. C. Nguyen, and B. L. Lucht, *J. Phys. Chem. C*, **121**, 2135–2148 (2017).

243. M. Nie, D. P. Abraham, D. M. Seo, Y. Chen, A. Bose, and B. L. Lucht, *J. Phys. Chem. C*, **117**, 25381–25389 (2013).

244. D. M. Seo, S. Reininger, M. Kutcher, K. Redmond, W. B. Euler, and B. L. Lucht, *J. Phys. Chem. C*, **119**, 14038–14046 (2015).

245. C. M. Burba and R. Frech, *J. Phys. Chem. B*, **109**, 15161–15164 (2005).

246. X. Xuan, J. Wang, J. Tang, G. Qu, and J. Lu, *Phys. Chem. Liq.*, **39**, 327–342 (2001).

247. M. S. Ding, K. Xu, and T. R. Jow, *J. Electrochem. Soc.*, **147**, 1688–1694 (2000).

248. R. Jung, M. Metzger, F. Maglia, C. Stinner, and H. A. Gasteiger, *J. Electrochem. Soc.*, **164**, A1361–A1377 (2017).

249. D. J. Xiong, R. Petibon, L. Madec, D. S. Hall, and J. R. Dahn, *J. Electrochem. Soc.*, **163**, A1678–A1685 (2016).

250. L. Terborg, S. Weber, F. Blaske, S. Passerini, M. Winter, U. Karst, and S. Nowak, *J. Power Sources*, **242**, 832–837 (2013).

251. R. Wagner, M. Korth, B. Streipert, J. Kasnatscheew, D. R. Gallus, S. Brox, M. Amereller, I. Cekic-Laskovic, and M. Winter, *ACS Appl. Mater. Interfaces*, **8**, 30871–30878 (2016).

252. A. V. Plakhotnyk, L. Ernst, and R. Schmutzler, *J. Fluor. Chem.*, **126**, 27–31 (2005).

253. J.-Y. Eom, I.-H. Jung, and J.-H. Lee, *J. Power Sources*, **196**, 9810–9814 (2011).

254. M. He, C.-C. Su, C. Peebles, Z. Feng, J. G. Connell, C. Liao, Y. Wang, I. A. Shkrob, and Z. Zhang, *ACS Appl. Mater. Interfaces*, **8**, 11450–11458 (2016).

255. K. Kubota and S. Komaba, *J. Electrochem. Soc.*, **162**, A2538–A2550 (2015).

256. D. I. Iermakova, R. Dugas, M. R. Palacín, and A. Ponrouch, *J. Electrochem. Soc.*, **162**, A7060–A7066 (2015).

257. R. Dugas, A. Ponrouch, G. Gachot, R. David, M. R. Palacin, and J. M. Tarascon, *J. Electrochem. Soc.*, **163**, A2333–A2339 (2016).
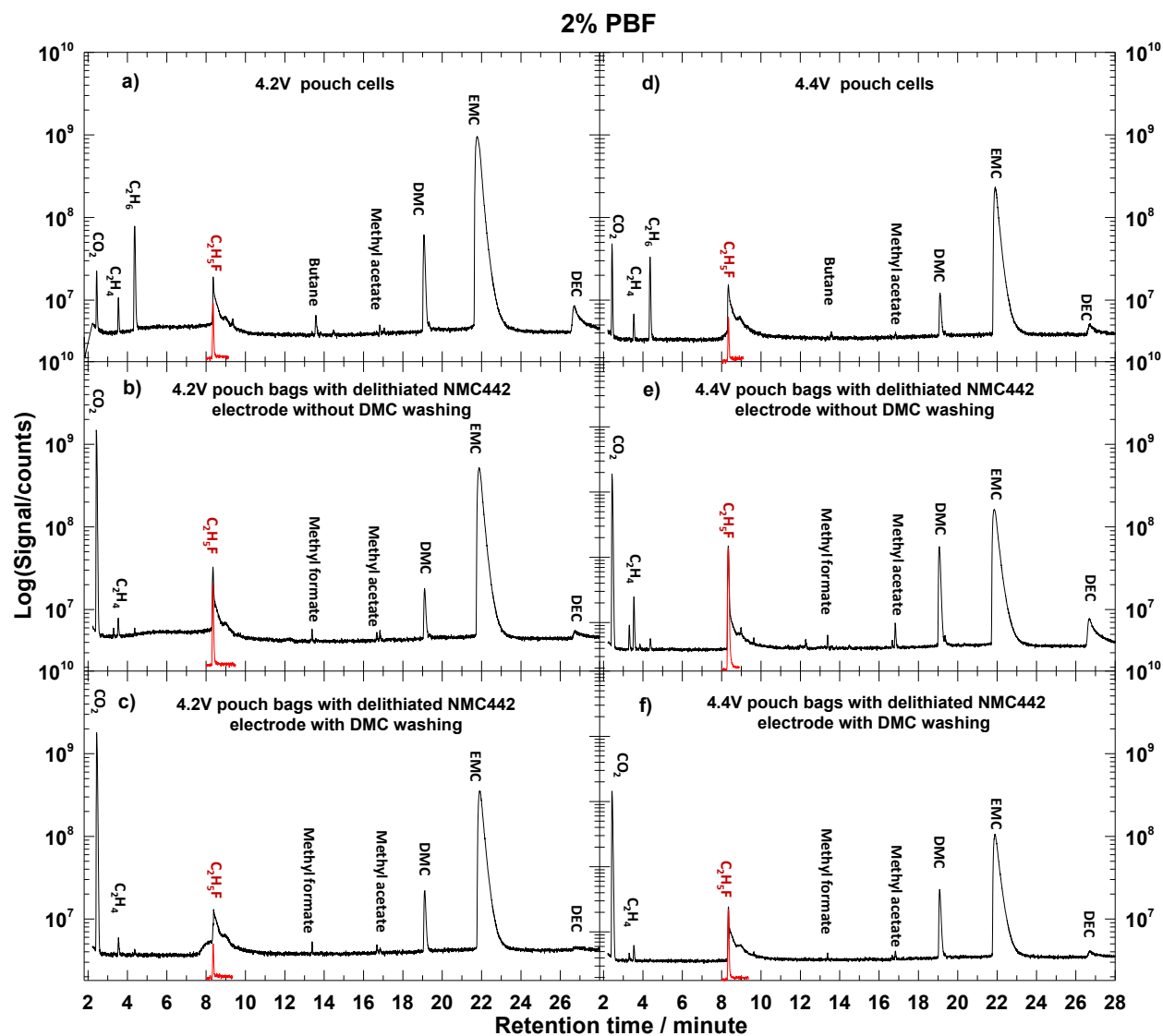
APPENDIX A

2% VC
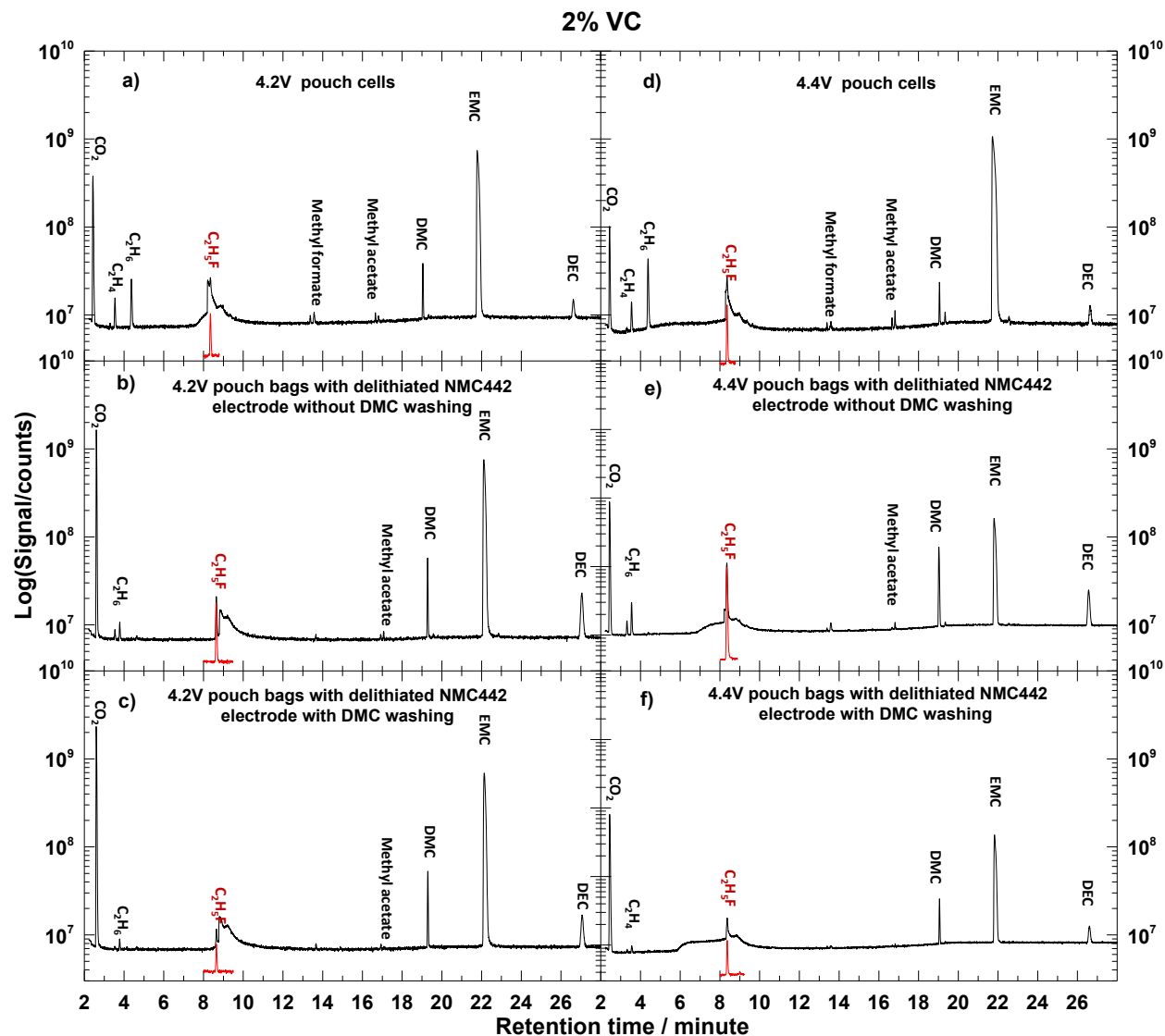
Figure A1 Chromatograms (total ion count) , using a logarithmic scale, of the gaseous products extracted from pouch cells having an initial voltage of 4.2 V (a) and 4.4 V (d), pouch bags containing the delithiated NMC442 electrode taken from pouch cells having an initial voltage of 4.2 V (b) and 4.4 V (e), pouch bags containing the delithiated NMC442 electrode (with DMC washing) taken from pouch cells having initial voltage of 4.2 V (c) and 4.4 V (f). These pouch bags and pouch cells containing control + 2% VC were stored at 60°C for approximately 500 h. The red peak shown in the Figure is assigned to CH_3CH_2F.
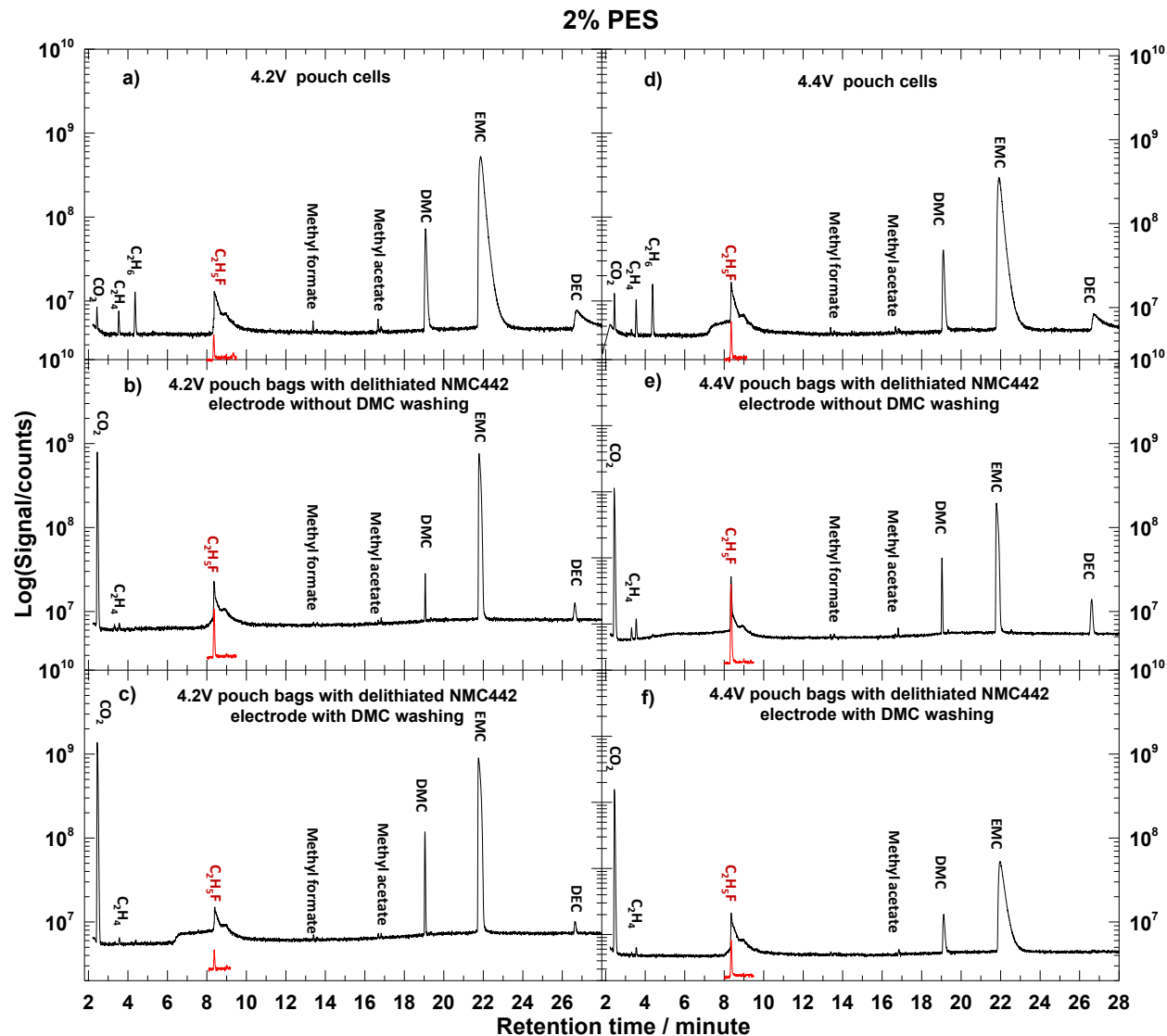
Figure A2 Chromatograms (total ion count) , using a logarithmic scale, of the gaseous products extracted from pouch cells having an initial voltage of 4.2 V (a) and 4.4 V (d), pouch bags containing the delithiated NMC442 electrode taken from pouch cells having an initial voltage of 4.2 V (b) and 4.4 V (e), pouch bags containing the delithiated NMC442 electrode (with DMC washing) taken from pouch cells having initial voltage of 4.2 V (c) and 4.4 V (f). These pouch bags and pouch cells containing control + 2% PES were stored at 60°C for approximately 500 h. The red peak shown in the Figure is assigned to CH_3CH_2F.

Figure A3 Chromatograms (total ion count) , using a logarithmic scale, of the gaseous products extracted from pouch cells having an initial voltage of 4.2 V (a) and 4.4 V (d), pouch bags containing the delithiated NMC442 electrode taken from pouch cells having an initial voltage of 4.2 V (b) and 4.4 V (e), pouch bags containing the delithiated NMC442 electrode (with DMC washing) taken from pouch cells having initial voltage of 4.2 V (c) and 4.4 V (f). These pouch bags and pouch cells containing control + 2% PBF were stored at 60°C for approximately 500 h. The red peak shown in the Figure is assigned to CH_3CH_2F.
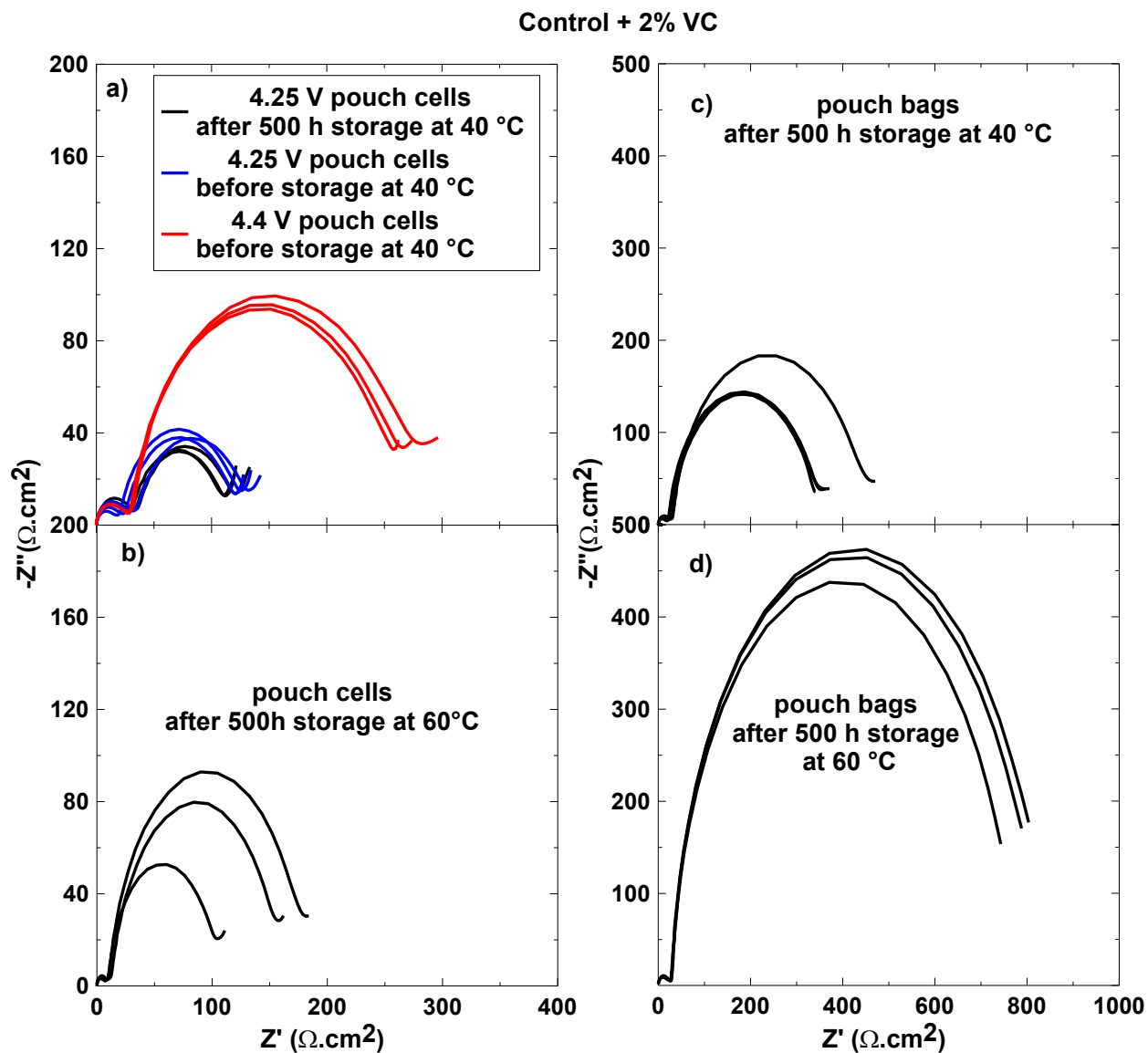
Figure A4 The area-specific Nyquist plots of positive electrode symmetric cells made from NMC442/graphite pouch cells at 4.25 V with control + 2% VC after 500 hours of storage at 40°C (a) and 60°C (b) and from charged NMC442 electrodes taken from pouch bags with the same electrolyte after 500 hours of storage at 40°C (c) and 60°C (d).
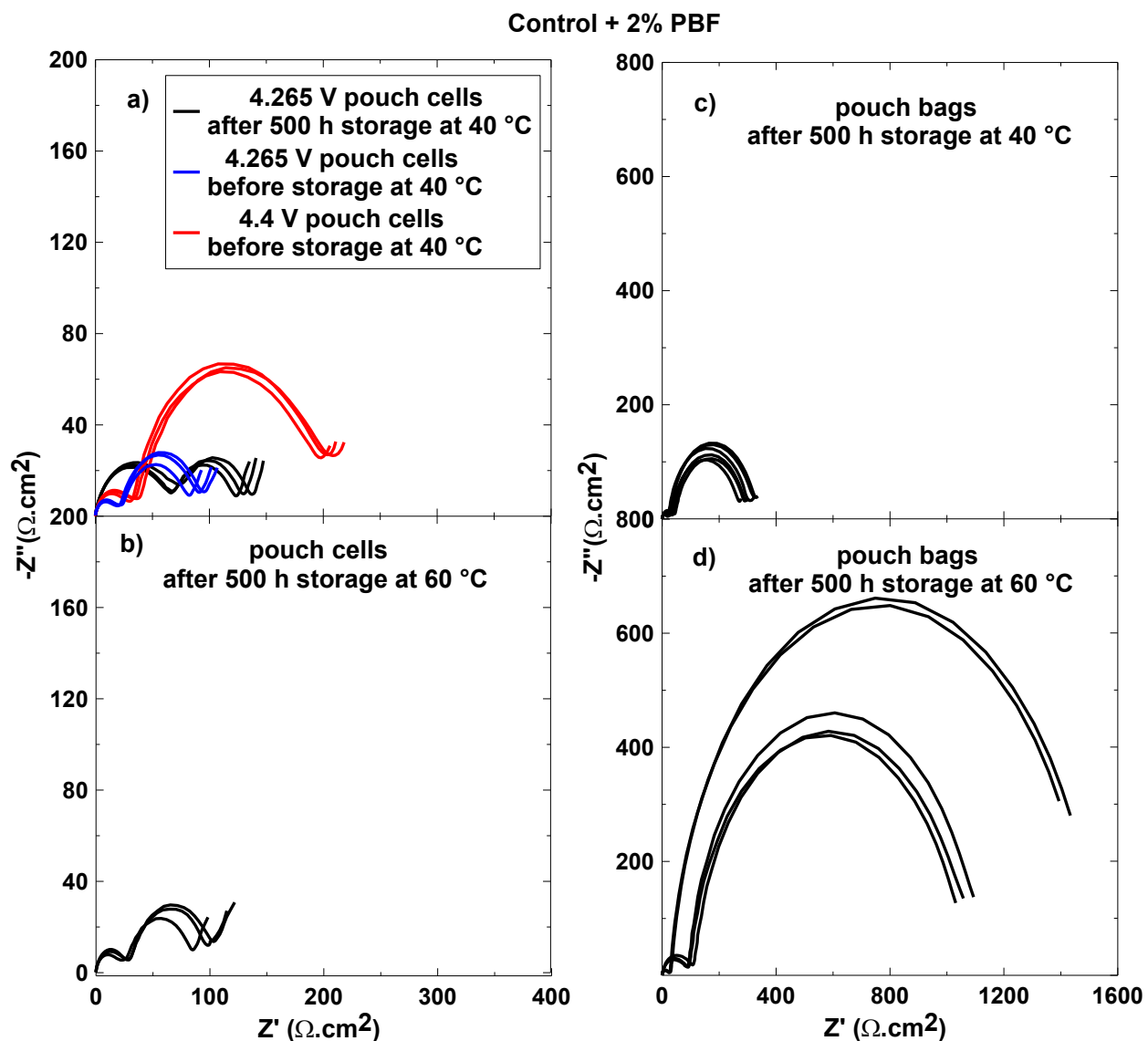
Figure A5 The area-specific Nyquist plots of positive electrode symmetric cells made from NMC442/graphite pouch cells at 4.265 V with control + 2% PBF after 500 hours of storage at 40°C (a) and 60°C (b) and from charged NMC442 electrodes taken from pouch bags with the same electrolyte after 500 hours of storage at 40°C (c) and 60°C (d)
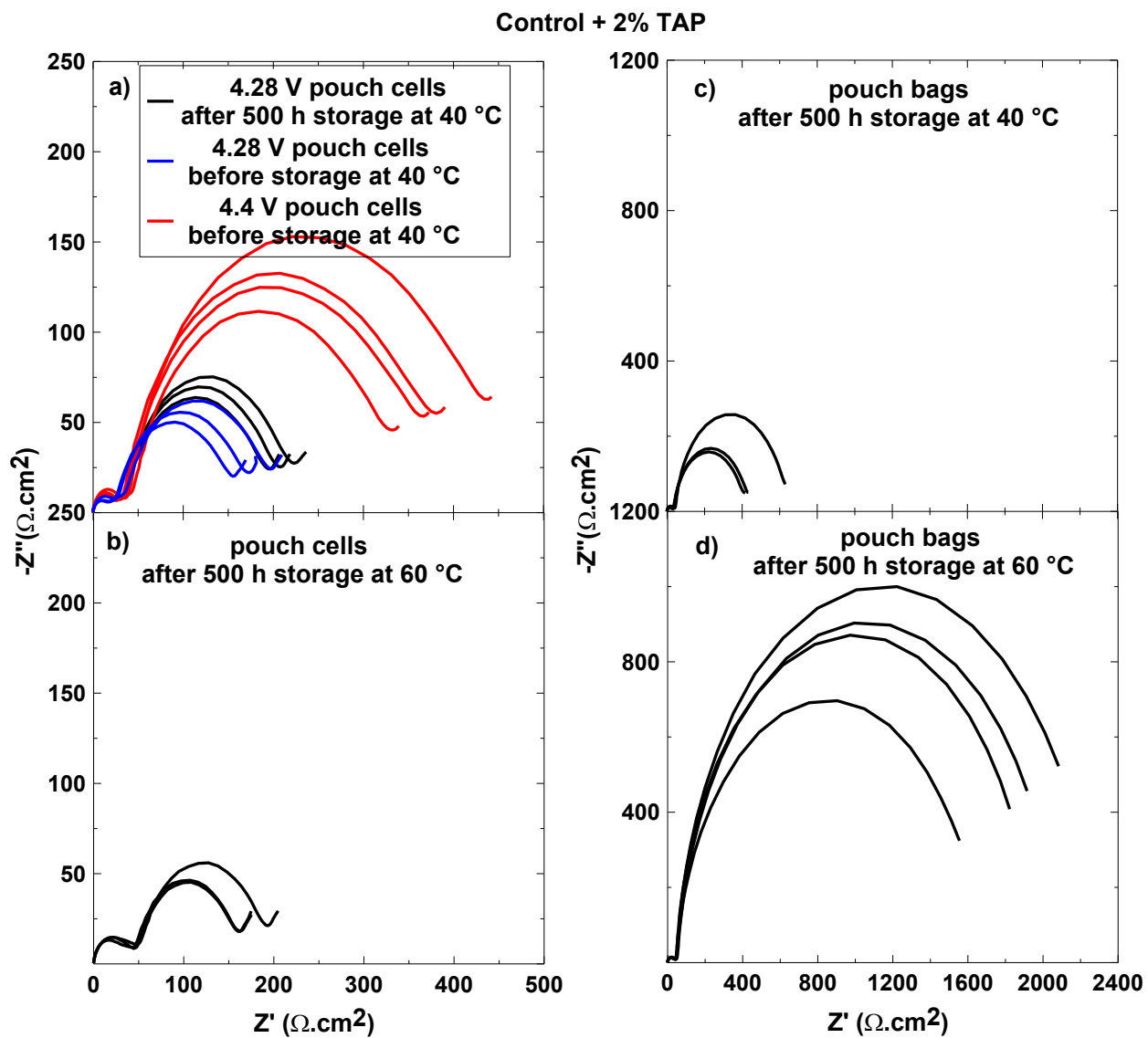
Control + 2% TAP

Figure A6 The area-specific Nyquist plots of positive electrode symmetric cells made from NMC442/graphite pouch cells at 4.28 V with control + 2% TAP after 500 h of storage at 40°C (a) and 60°C (b) and from charged NMC442 electrodes taken from pouch bags with the same electrolyte after 500 hours of storage at 40°C (c) and 60°C (d)
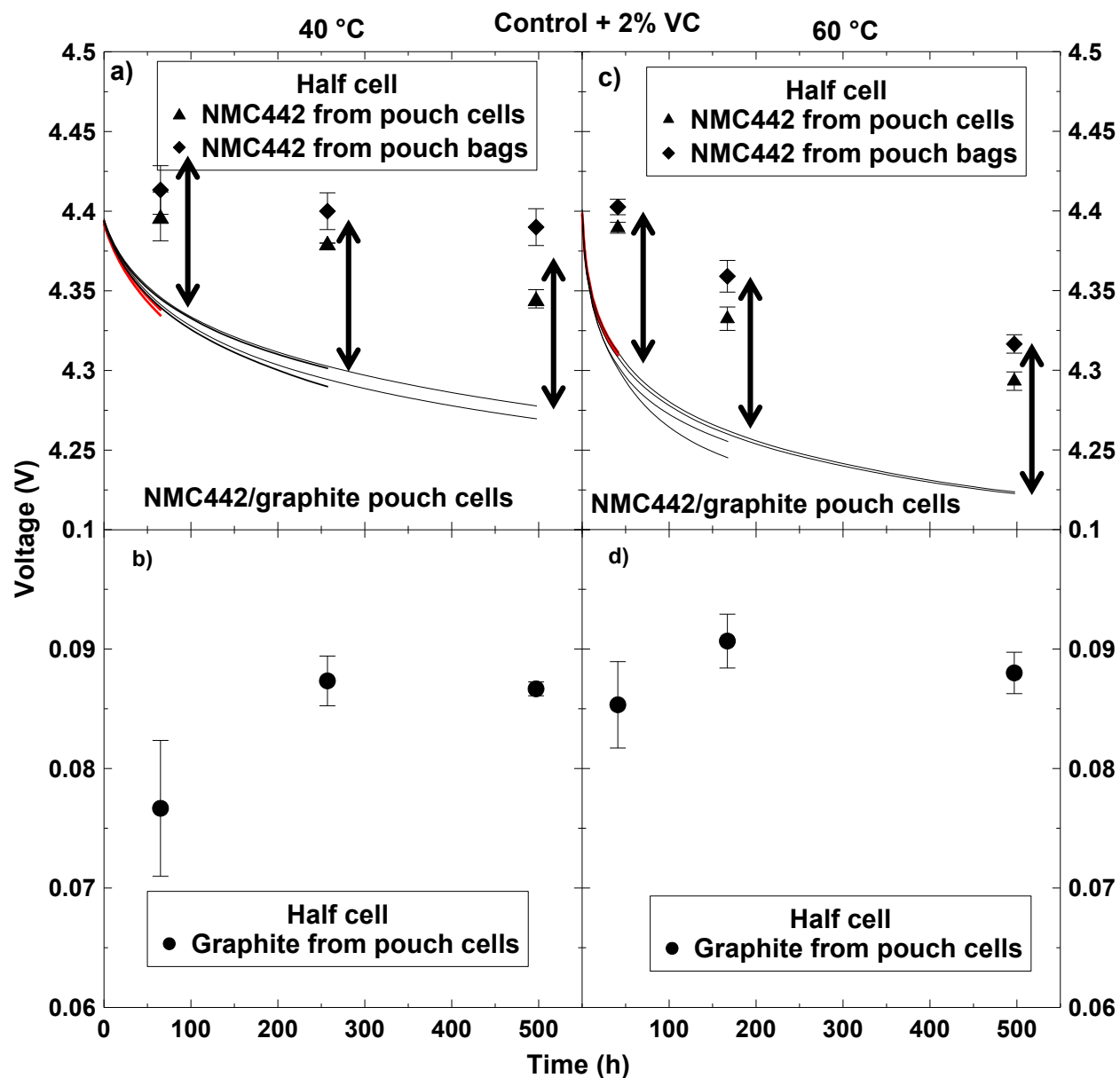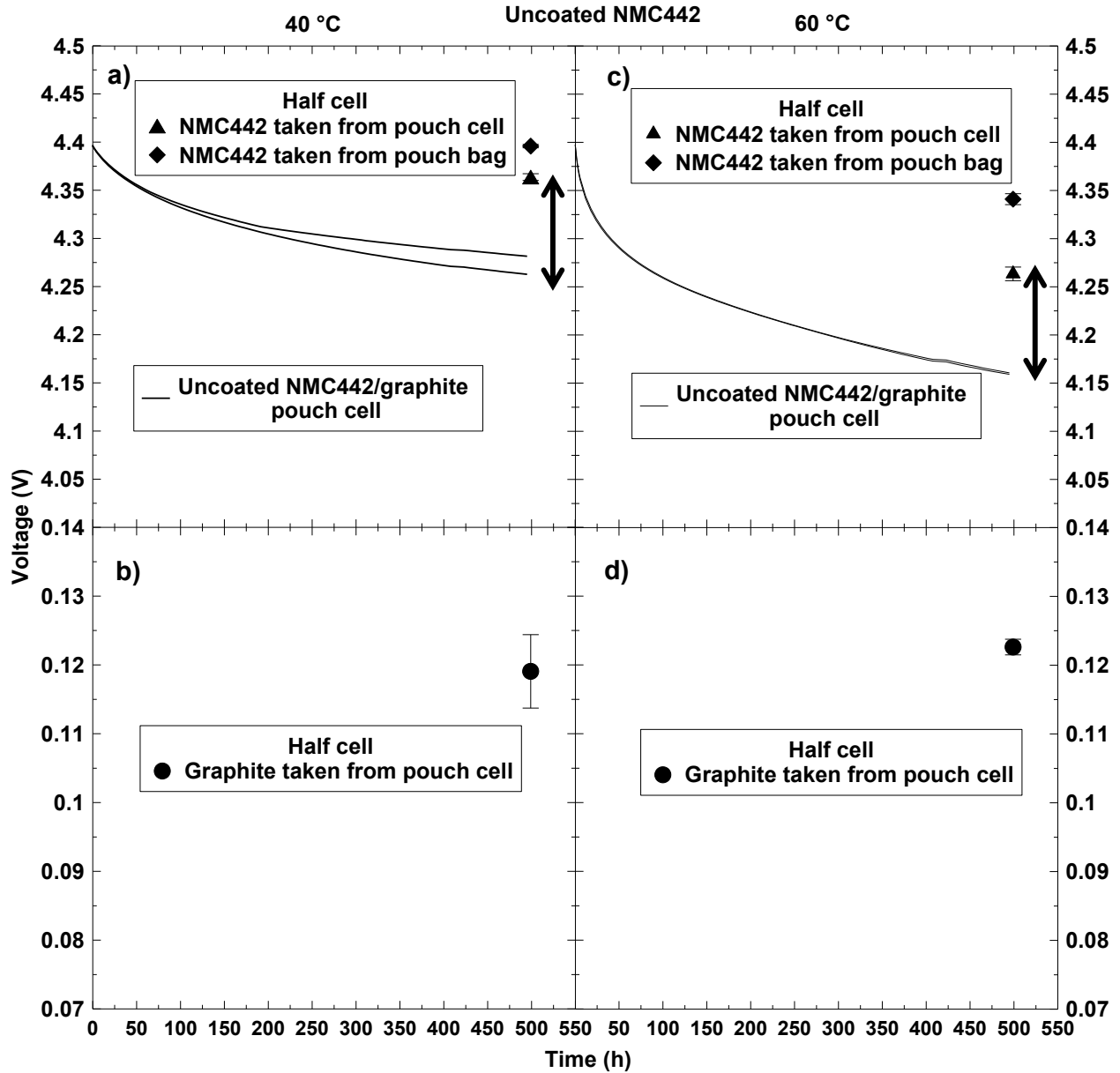
Figure A7 Open circuit voltage versus time for NMC442/graphite pouch cells with 2% VC during storage at 40°C and 60°C, as well as Li/NMC442 (a, c) and Li/graphite (b, d) half cells where the electrodes were taken out of the pouch cells and pouch bags at the times indicated. The black arrows are 0.085 V long.
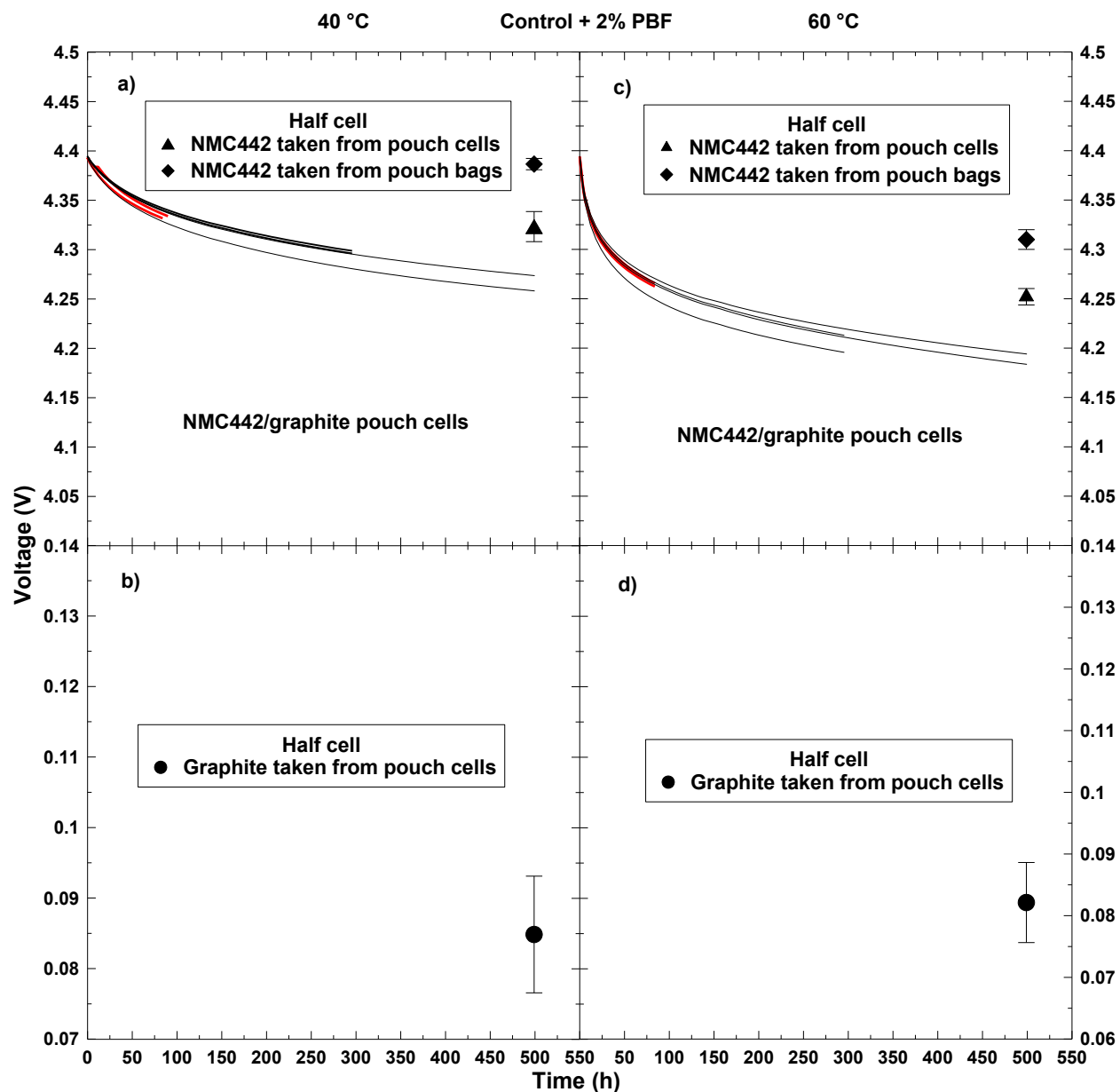
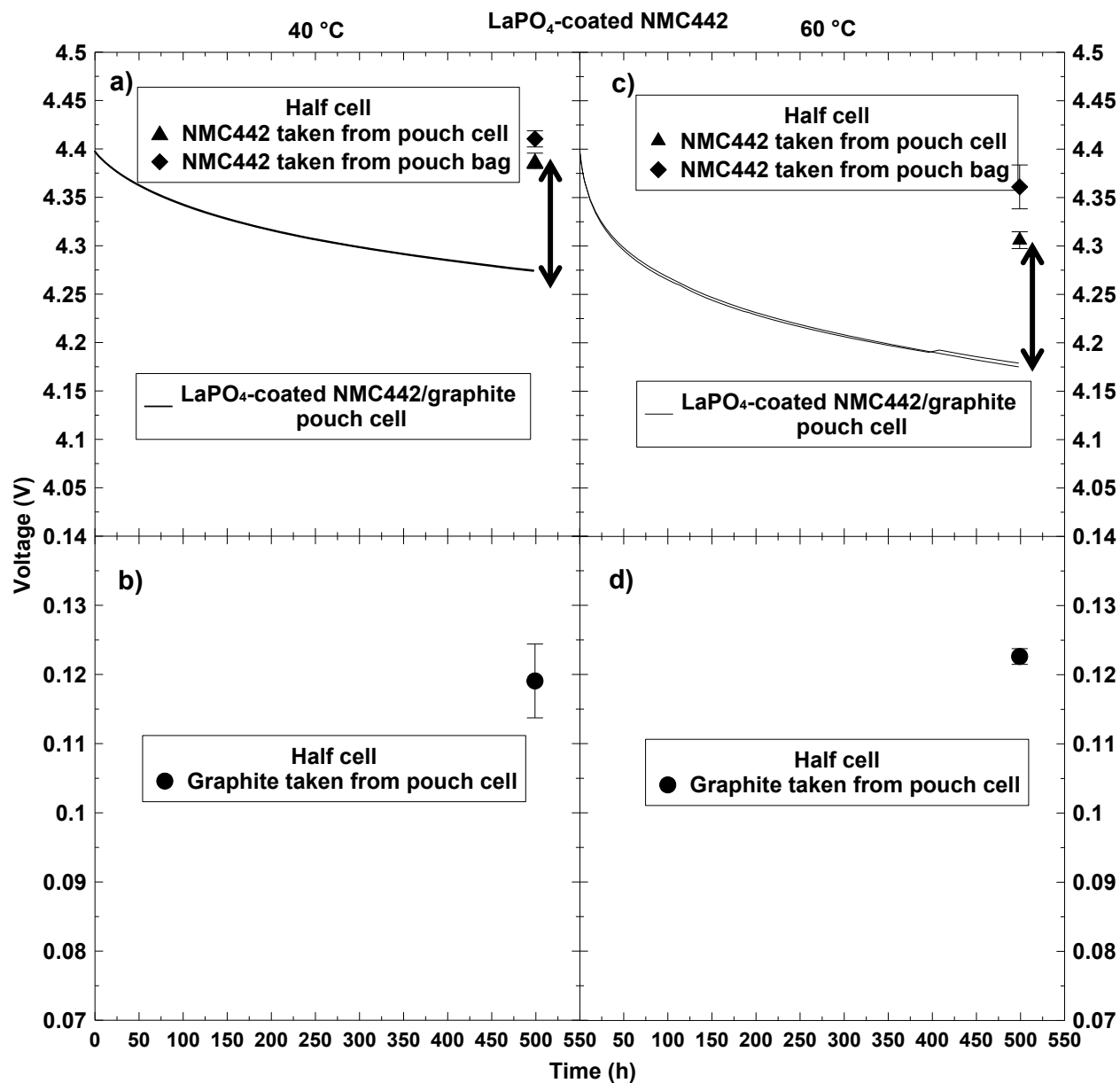Figure A8 Open circuit voltage versus time for NMC442/graphite pouch cells with control + 2% PBF during storage at 40°C and 60 °C, as well as Li/NMC442 (a, c) and Li/graphite (b, d) half cells where the electrodes were taken out of the pouch cells and pouch bags at the times indicated
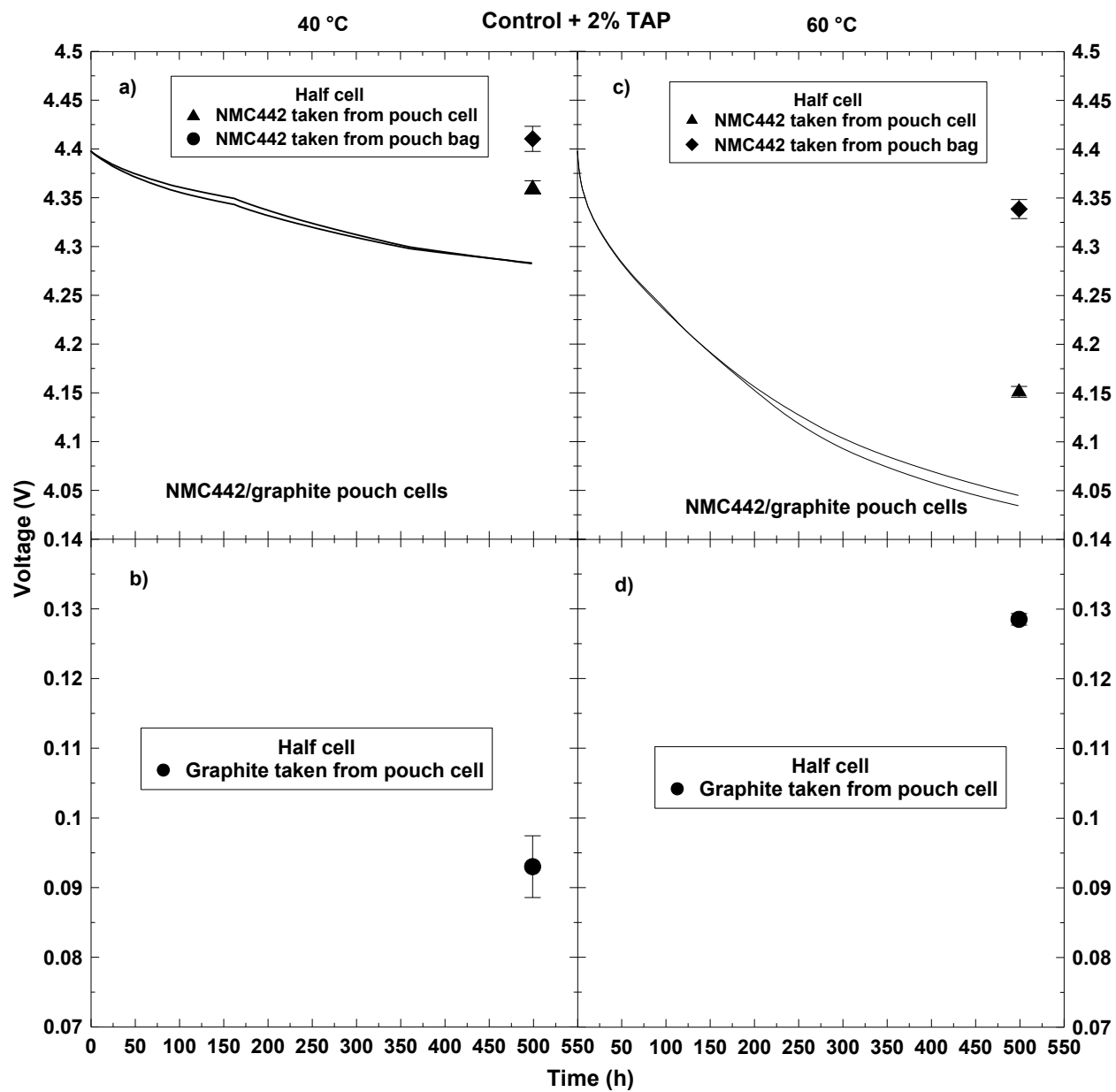
Figure A9 Open circuit voltage versus time for NMC442/graphite pouch cells with control + 2% TAP during storage at 40°C and 60 °C, as well as Li/NMC442 (a, c) and Li/graphite (b, d) half cells where the electrodes were taken out of the pouch cells and pouch bags at the times indicated
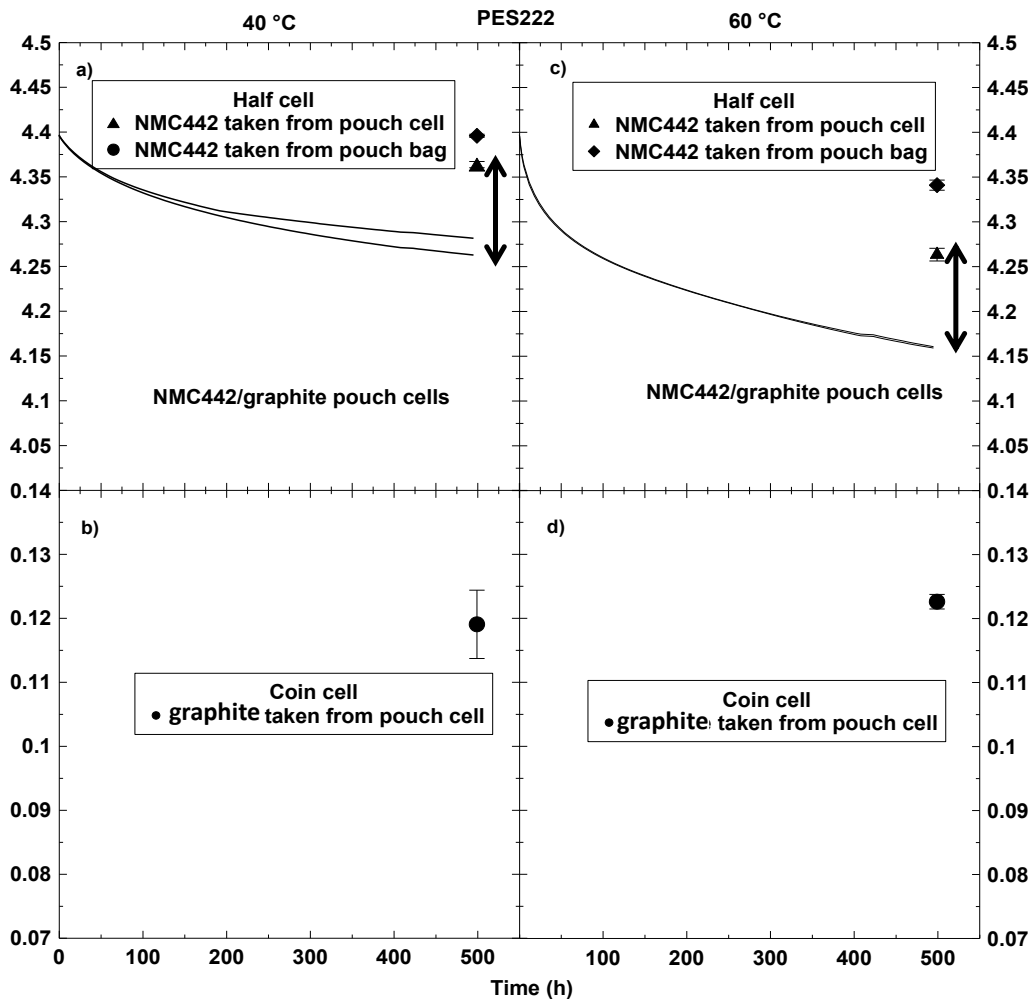
Figure B1   Open circuit voltage versus time for NMC442/graphite pouch cells with PES222 during storage at 40 and 60°C, as well as Li/NMC442 (a, c) and Li/graphite (b, d) half cells where the electrodes were taken out of the pouch cells and pouch bags at the times indicated. The black two-headed arrow is 0.012 V long.
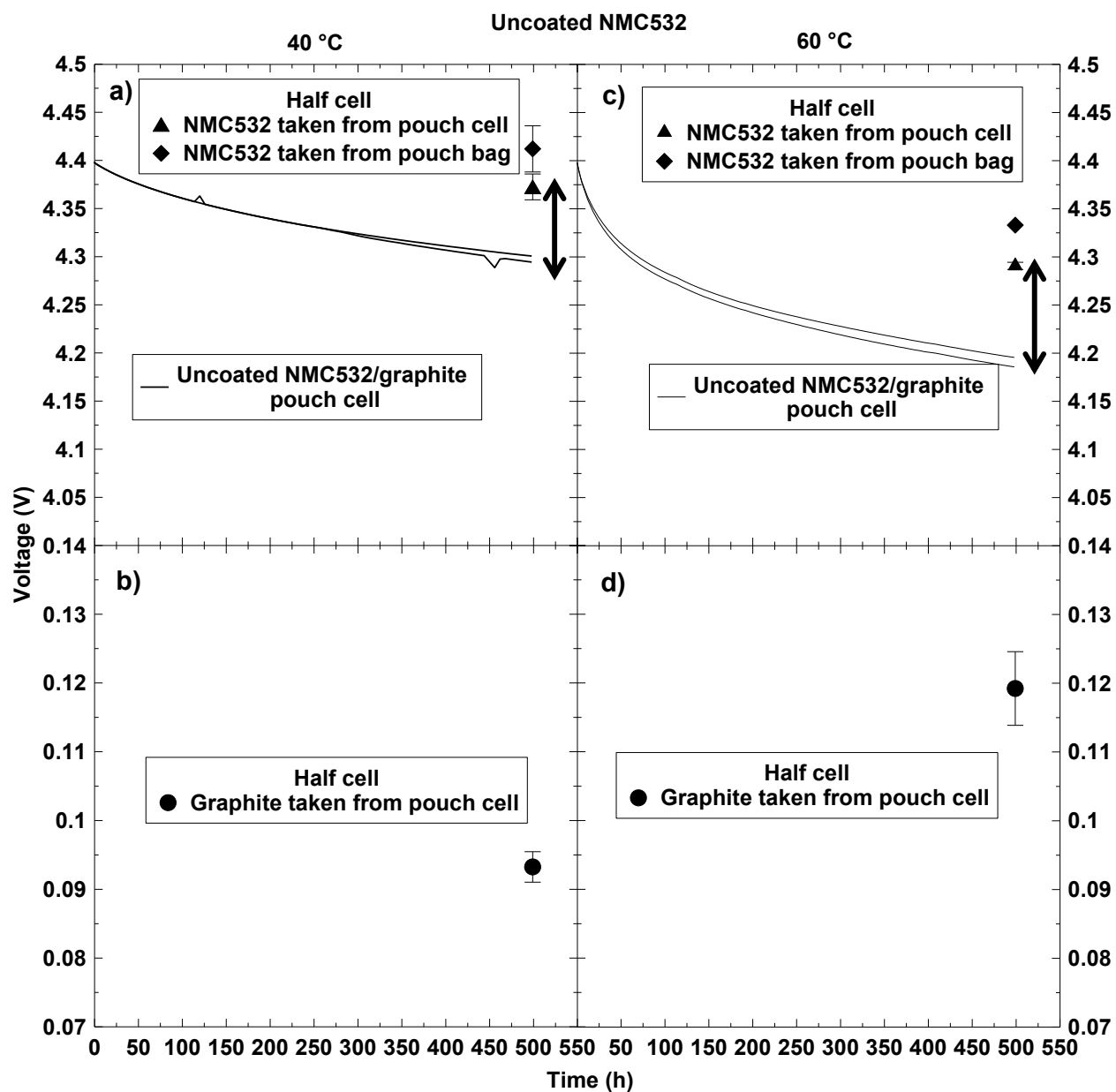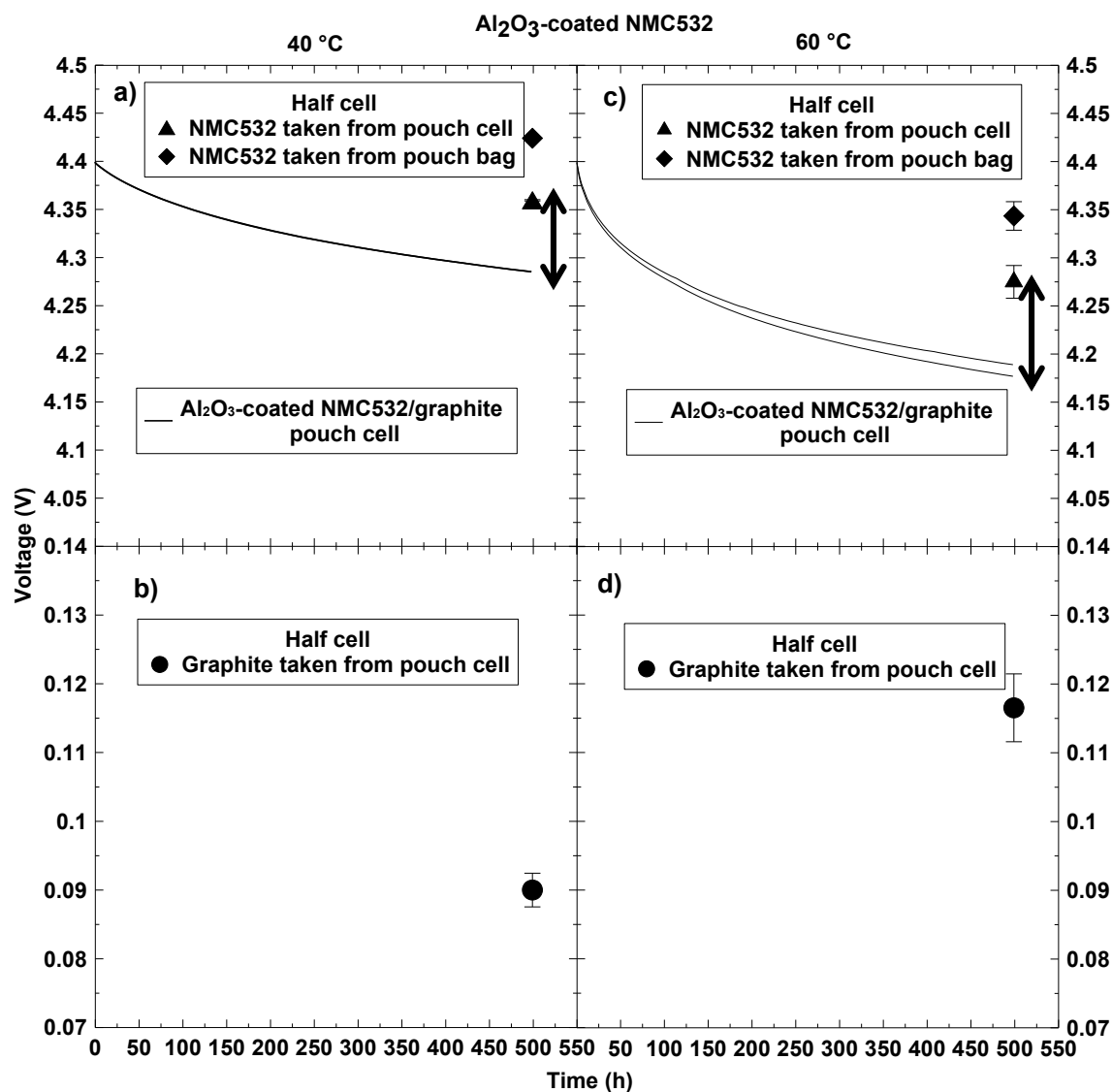
.
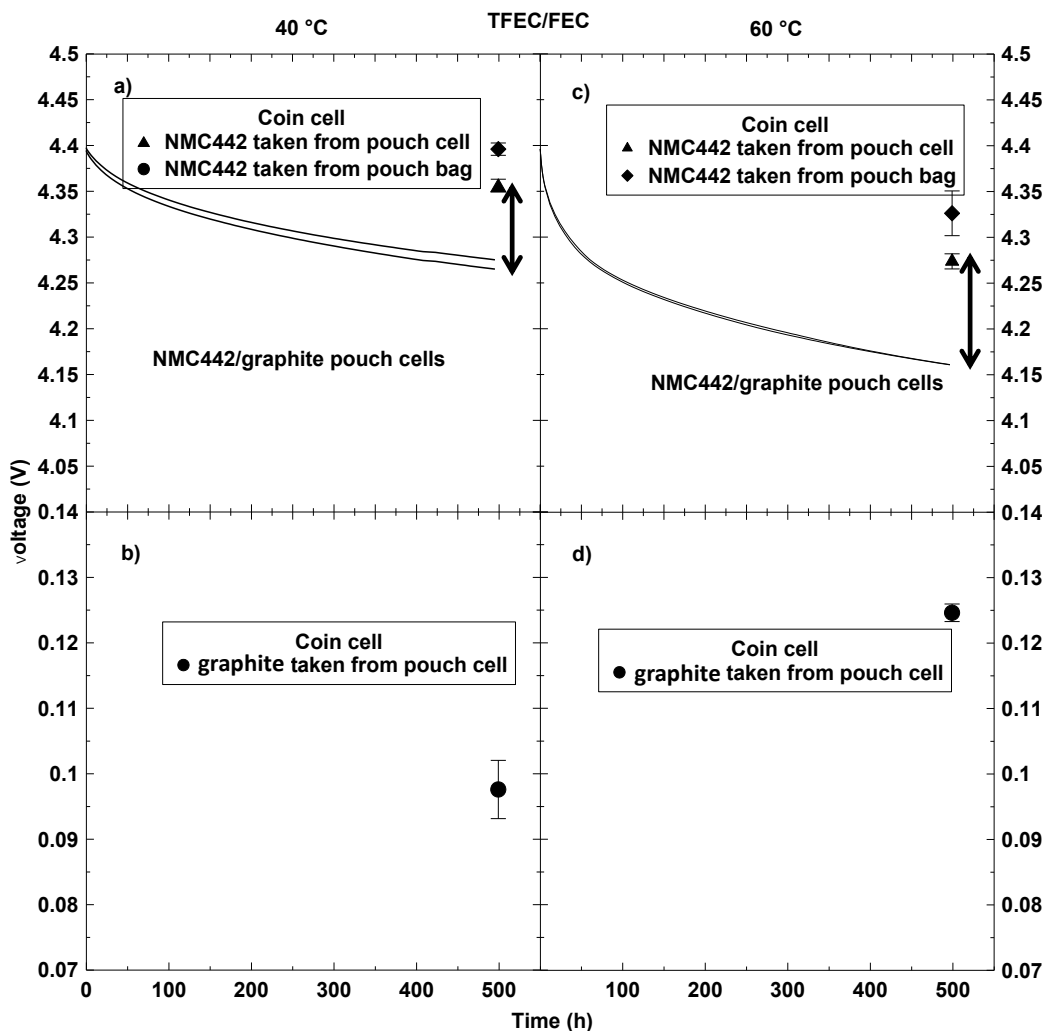
Figure B2 Open circuit voltage versus time for NMC442/graphite pouch cells with TFEC/FEC during storage at 40°C and 60°C, as well as Li/NMC442 (a, c) and Li/graphite (b, d) half cells where the electrodes were taken out of the pouch cells and pouch bags at the times indicated. The black two-headed arrows in panel a and panel b are 0.097 V and 0.125 V long, respectively.

219

Figure C1 Open circuit voltage versus time for uncoated NMC442/graphite pouch cells with PES222 during storage at 40 and 60°C, as well as Li/NMC442 (a, c) and Li/graphite (b, d) half cells where the electrodes were taken out of the pouch cells and pouch bags at the times indicated. The black two-headed arrow is 0.12 V long.
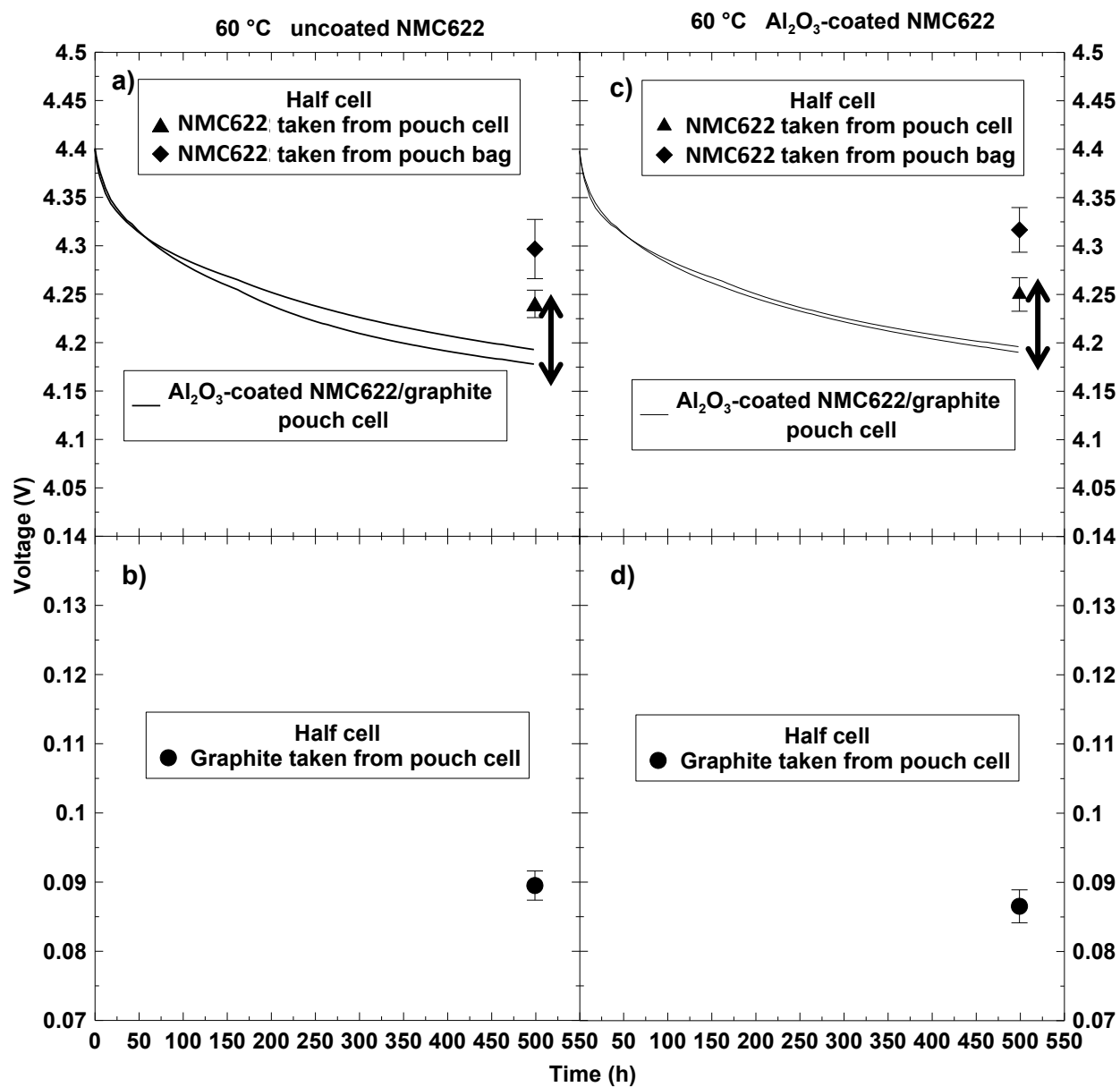
Figure C2 Open circuit voltage versus time for LaPO$_4$-coated NMC442/graphite pouch cells with PES222 during storage at 40 and 60°C, as well as Li/LaPO$_4$-coated NMC442 (a, c) and Li/graphite (b, d) half cells where the electrodes were taken out of the pouch cells and pouch bags at the times indicated. The black two-headed arrow is 0.12 V long.

Figure C3 Open circuit voltage versus time for uncoated NMC5322/graphite pouch cells with PES222 during storage at 40 and 60°C, as well as Li/uncoated NMC532 (a, c) and Li/graphite (b, d) half cells where the electrodes were taken out of the pouch cells and pouch bags at the times indicated. The black two-headed arrows are 0.09 V (a) 0.12 V (c) long.

Figure C4 Open circuit voltage versus time for Al$_2$O$_3$-coated NMC532/graphite pouch cells with PES222 during storage at 40 and 60°C, as well as Li/ Al$_2$O$_3$-coated NMC532 (a, c) and Li/graphite (b, d) half cells where the electrodes were taken out of the pouch cells and pouch bags at the times indicated. The black two-headed arrows are 0.09 V (a) 0.12 V (b) long.

Figure C5 Open circuit voltage versus time for uncoated NMC622/graphite and Al$_2$O$_3$-coated NMC622/graphite pouch cells (a, c) with PES222 during storage 60°C, as well as Li/uncoated NMC622 and Li/Al$_2$O$_3$-coated NMC622 (a, c) and Li/graphite (b, d) half cells where the electrodes were taken out of the pouch cells and pouch bags at the times indicated. The black two-headed arrow is 0.09 V long.
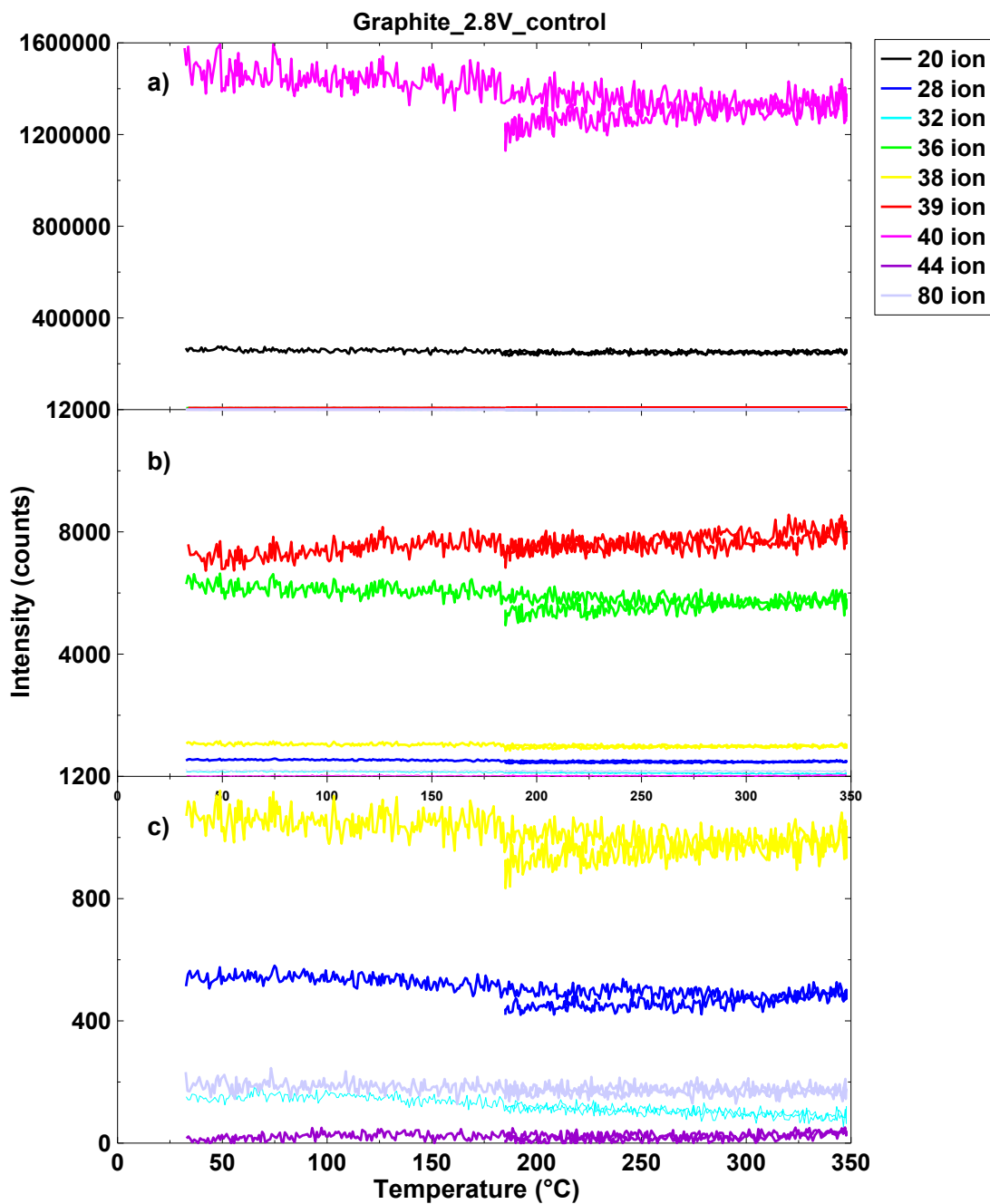
Figure D1 The intensity of all the ions whose intensity is above the baseline threshold (a, b, c) vs heating temperature range for a graphite electrode taken from an uncoated NMC442/graphite pouch cell with control electrolyte at 2.8 V. The scanned m/z ranges were from 20 to 80.
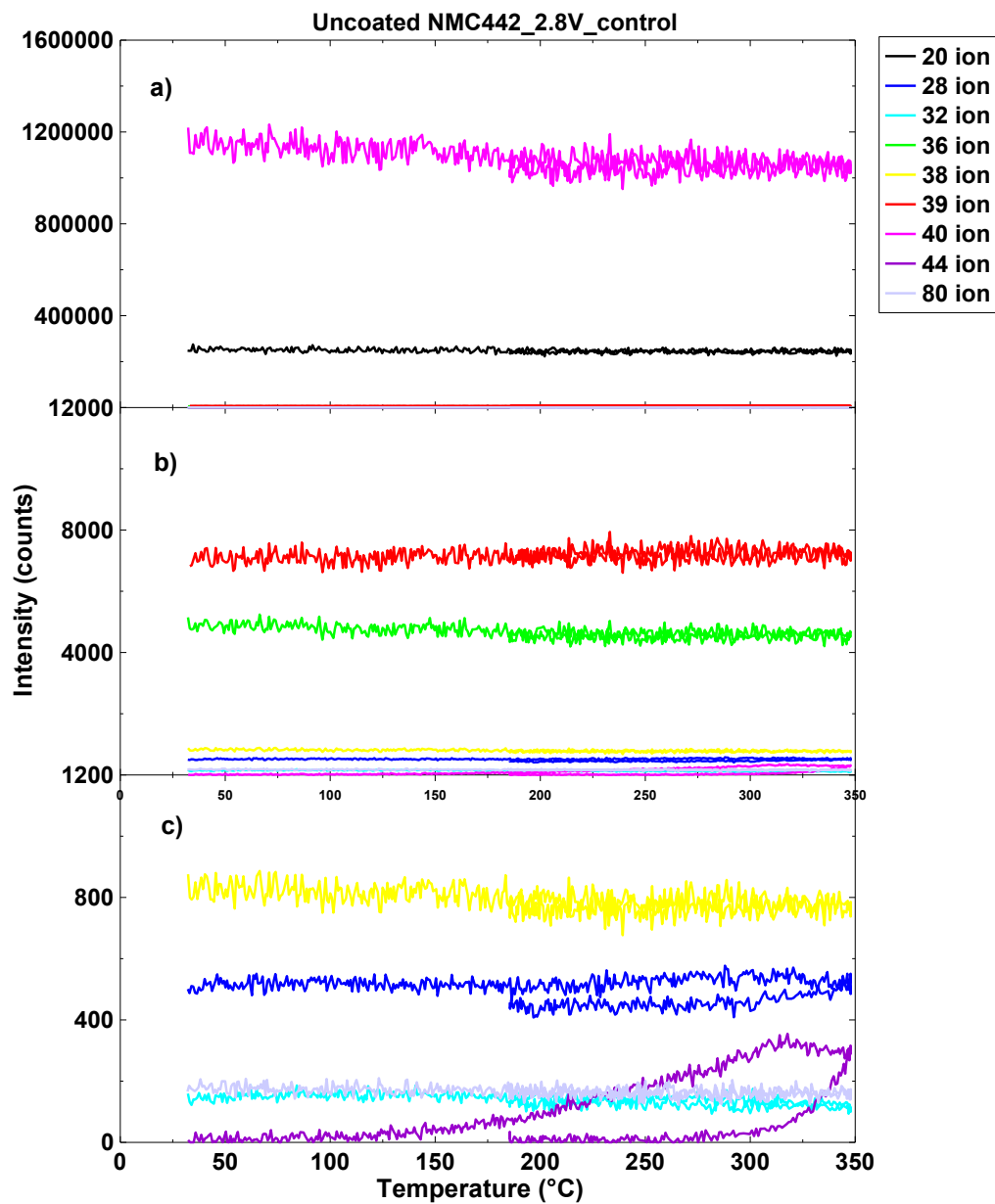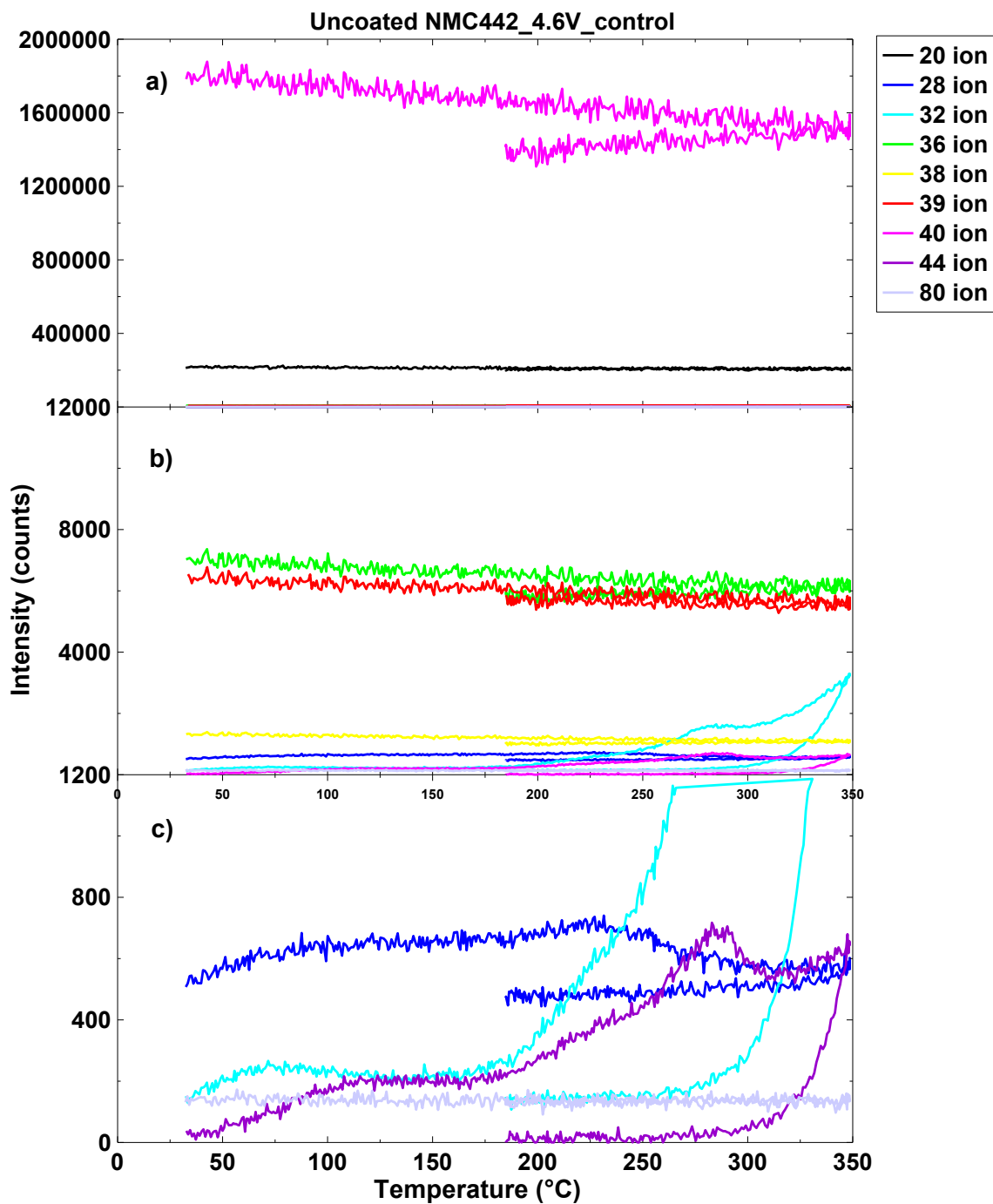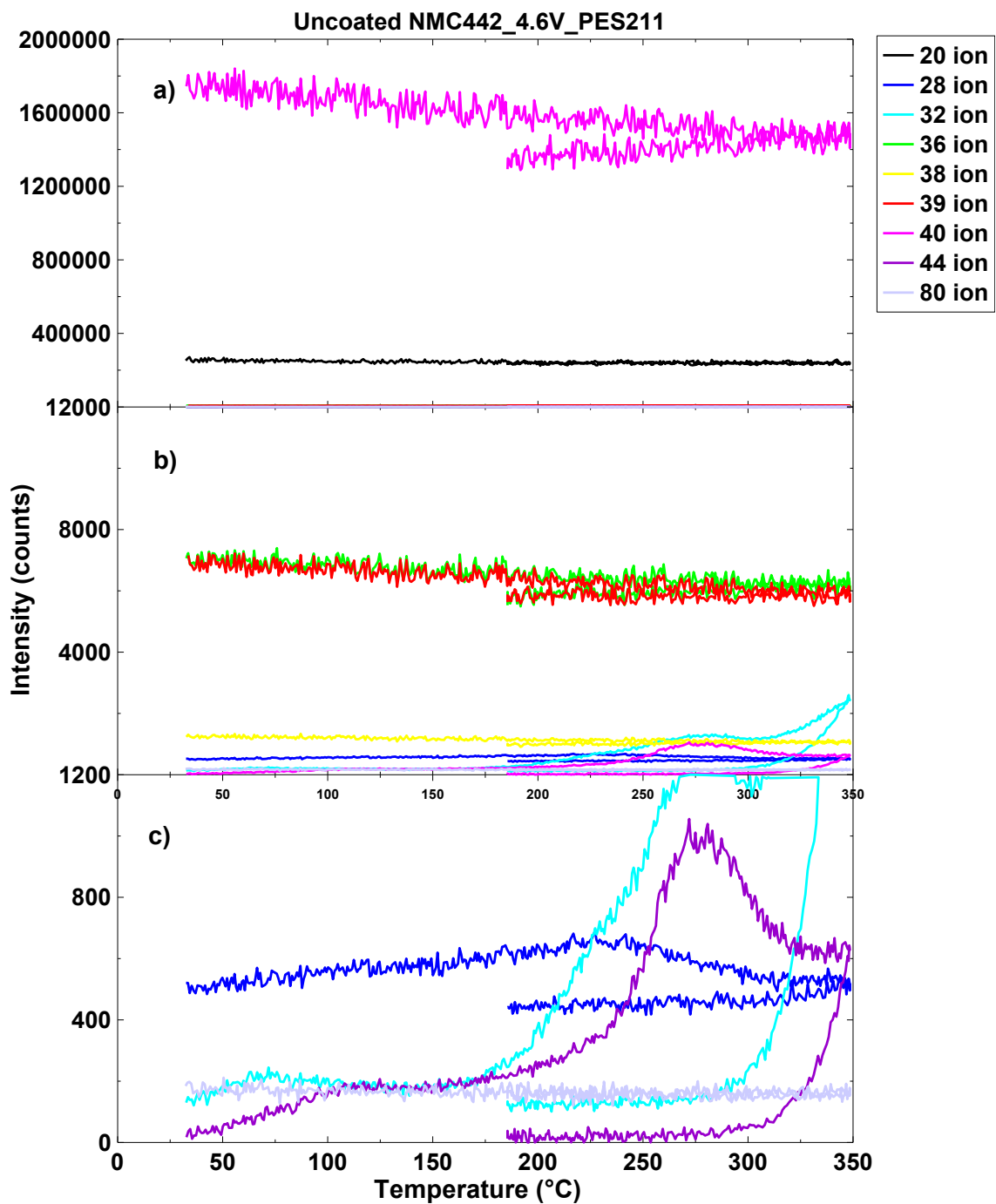
Figure D2 The intensity of all the ions whose intensity is above the baseline threshold (a, b, c) vs heating temperature range for a uncoated NMC442 electrode taken from an uncoated NMC442/graphite pouch cell with control electrolyte at 2.8 V. The scanned m/z ranges were from 20 to 80.
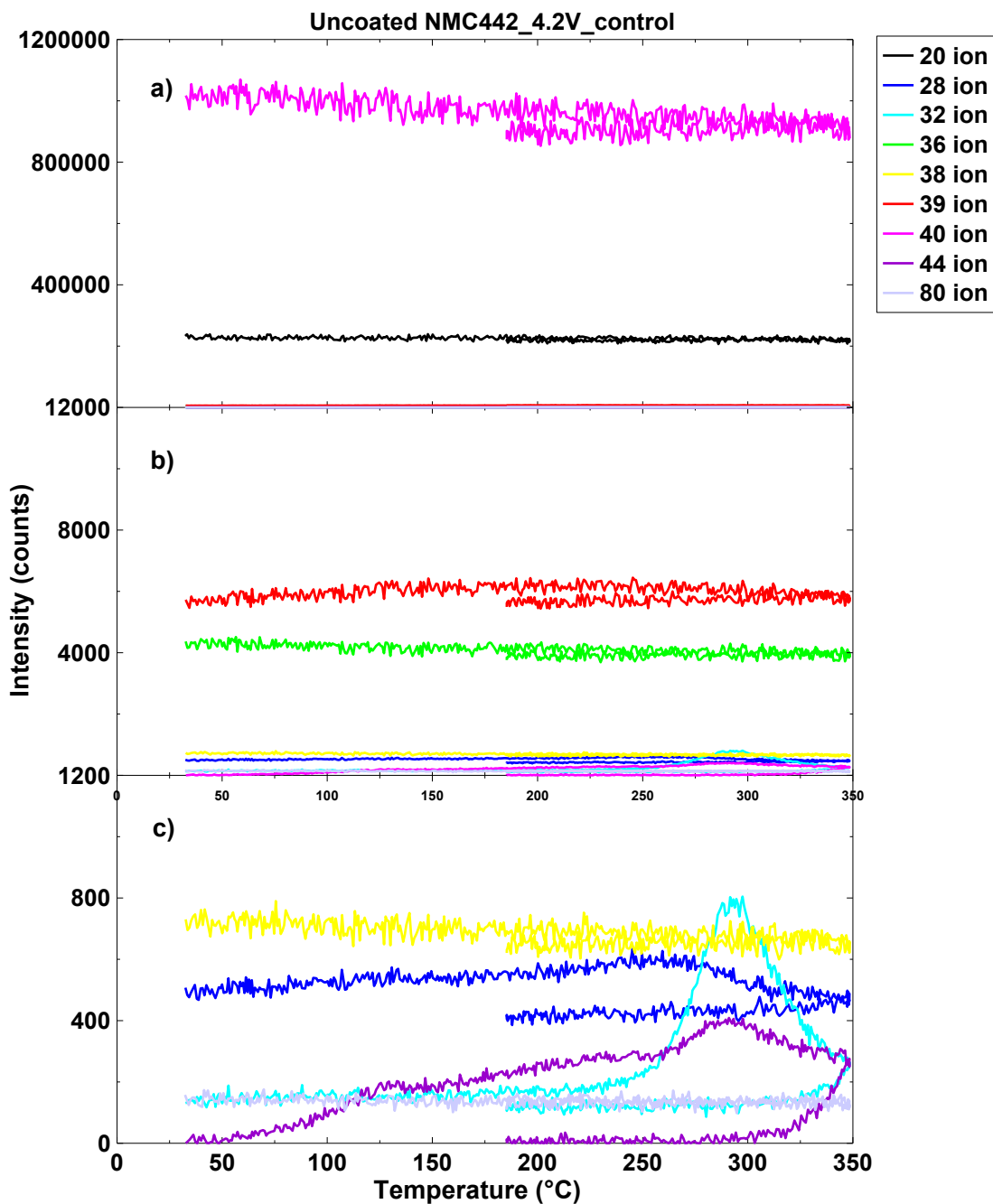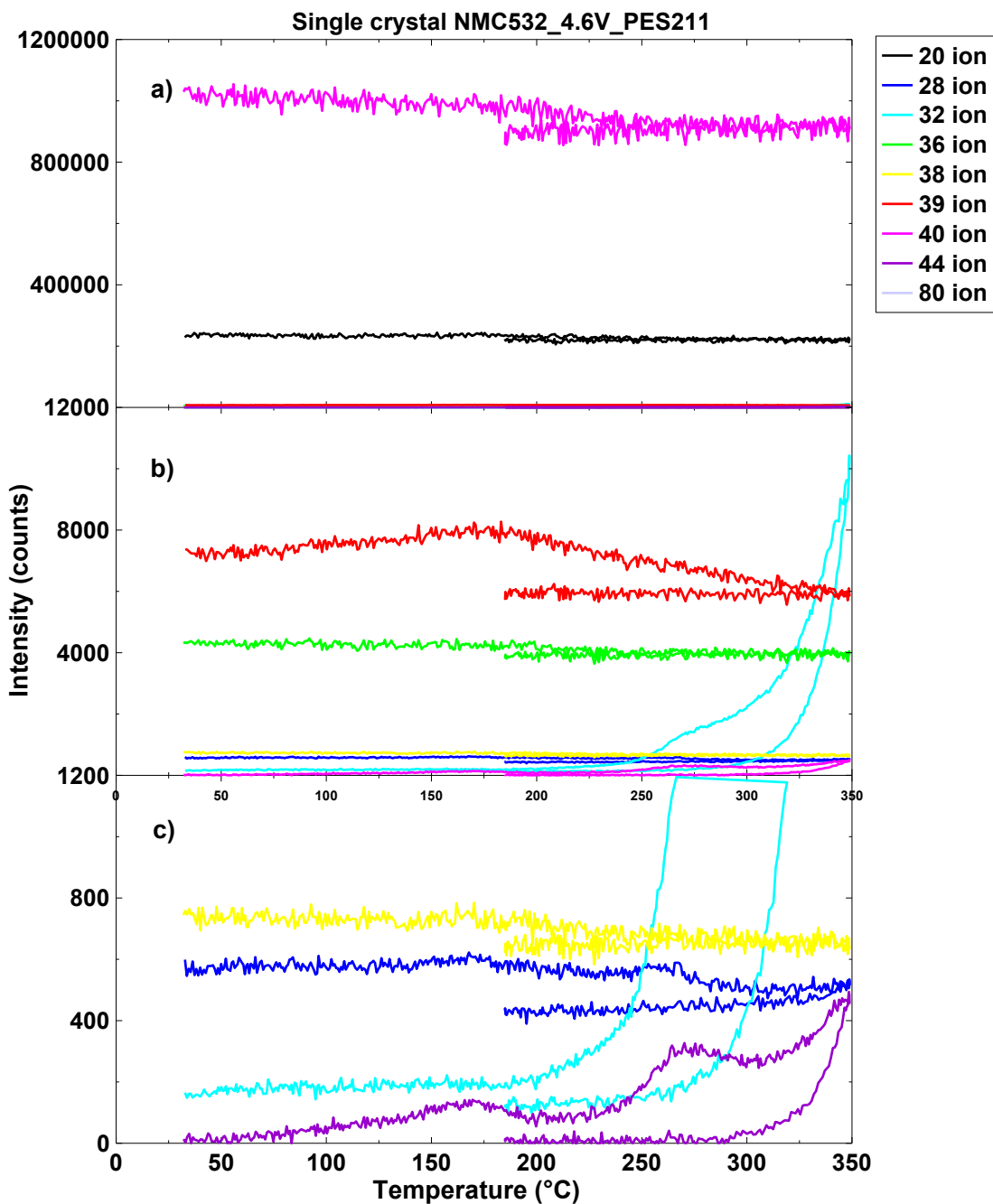
Figure D3 The intensity of all the ions whose intensity is above the baseline threshold (a, b, c) vs heating temperature range for a uncoated NMC442 electrode taken from an uncoated NMC442/graphite pouch cell with control electrolyte at 4.2 V. The scanned m/z ranges were from 20 to 80.

Figure D4 The intensity of all the ions whose intensity is above the baseline threshold (a, b, c) vs heating temperature range for a uncoated NMC442 electrode taken from an uncoated NMC442/graphite pouch cell with control electrolyte at 4.6 V. The scanned m/z ranges from 20 to 80.
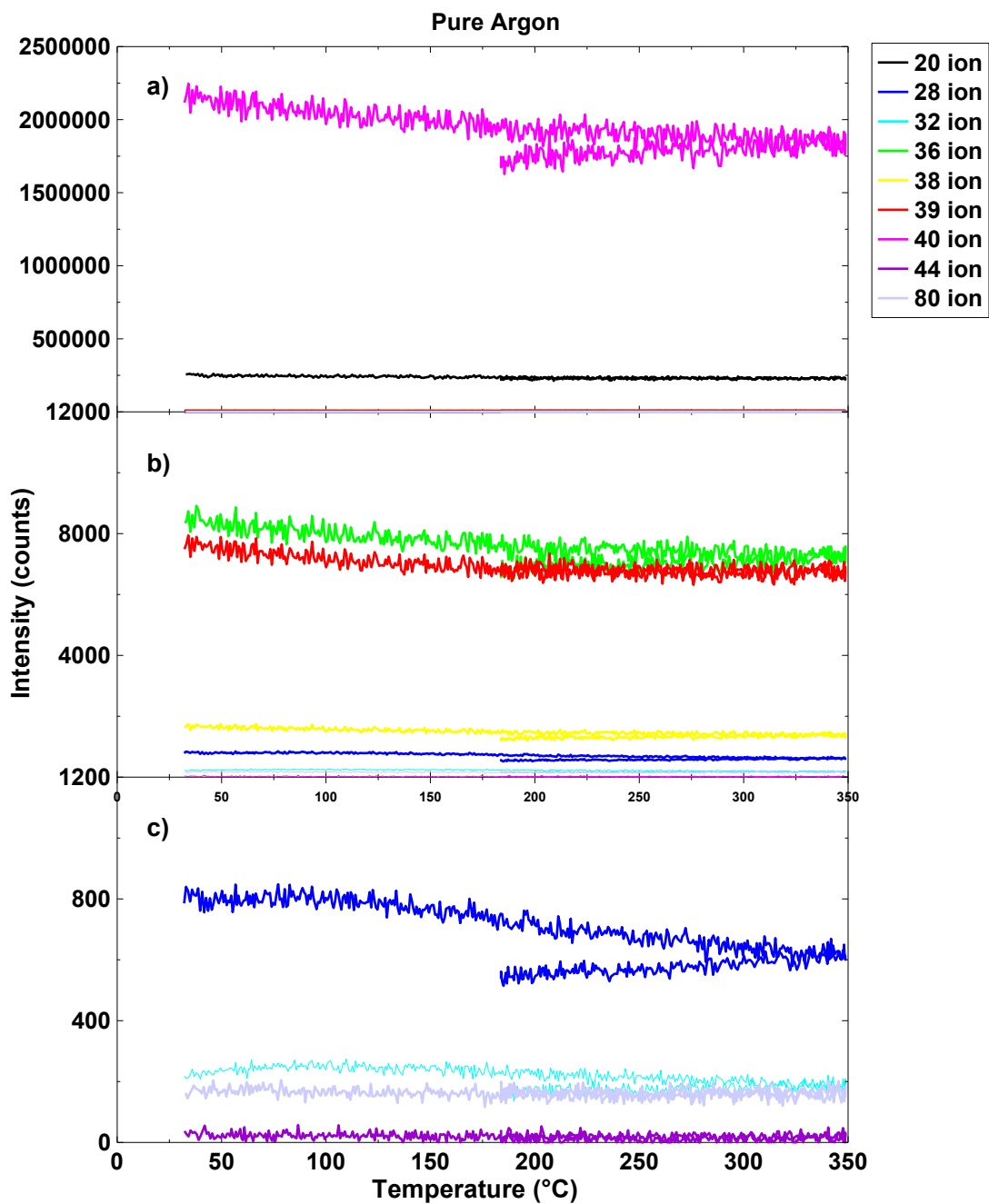
Figure D5 The intensity of all the ions whose intensity is above the baseline threshold (a, b, c) vs heating temperature range for a uncoated NMC442 electrode taken from an uncoated NMC442/graphite pouch cell with control + PES211 at 4.6 V. The scanned m/z ranges were from 20 to 80.

Figure D6 The intensity of all the ions whose intensity is above the baseline threshold (a, b, c) vs heating temperature range for a single crystal NMC532 electrode taken from a single crystal NMC532/graphite pouch cell with control + PES211 at 4.6 V. The scanned m/z ranges were from 20 to 80.

Figure D7 The intensity of all the ions whose intensity is above the baseline threshold (a, b, c) vs. heating temperature range for pure argon. The scanned m/z ranges were from 20 to 80.
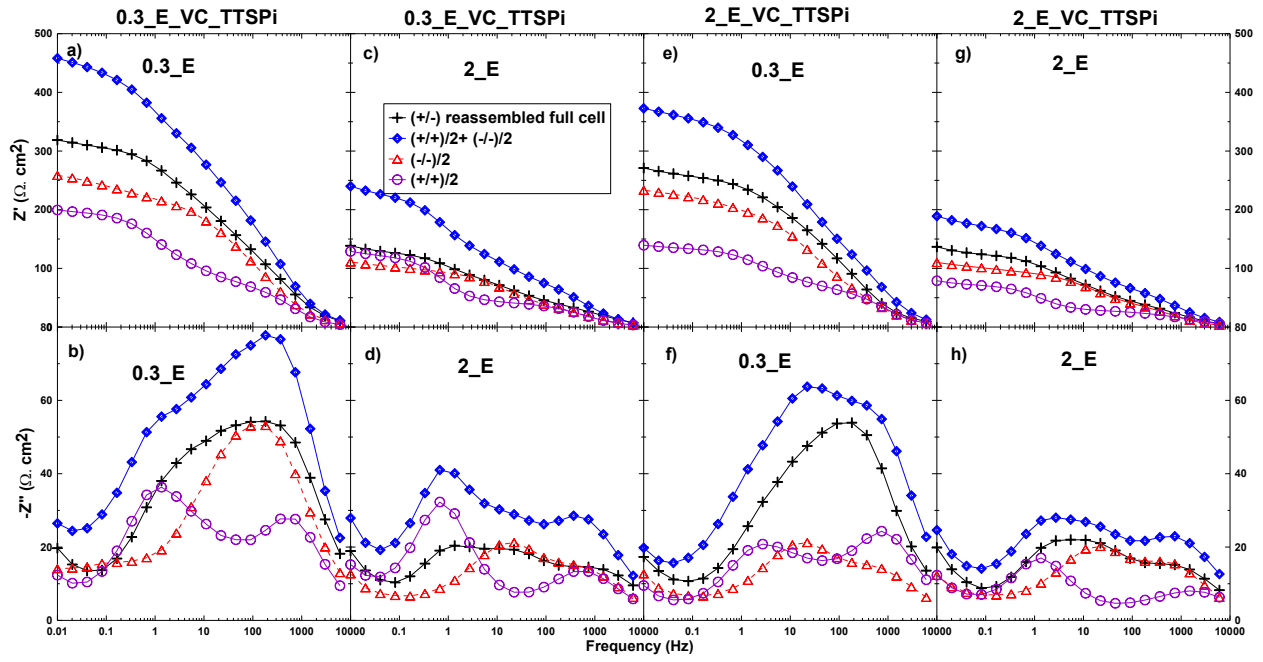
Figure E1 The area-specific Bode plot spectra of the data corresponding to the Nyquist plots in Figure 8.8 in the main thesis.
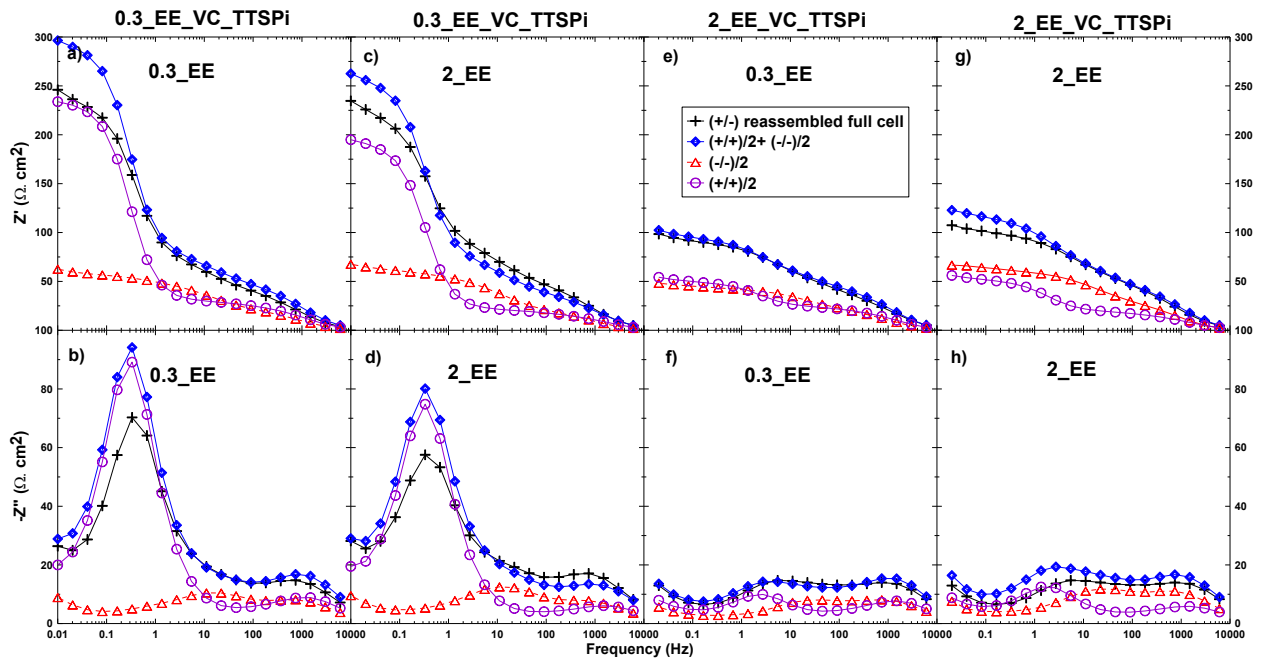
Figure E2 The Area Specific Bode plot spectra corresponding to the Nyquist plots shown in Figure 8.9 in the main thesis
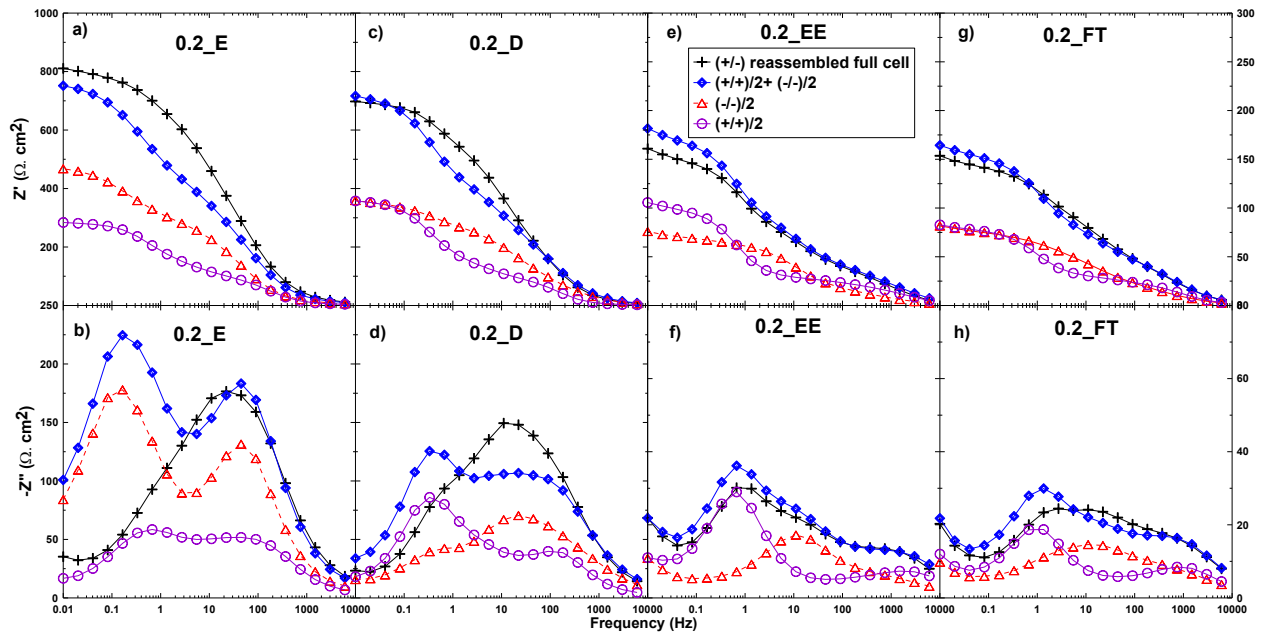
Figure E3 The Area Specific Bode plot spectra corresponding to the Nyquist plots shown in Figure 8.10 in the main thesis.
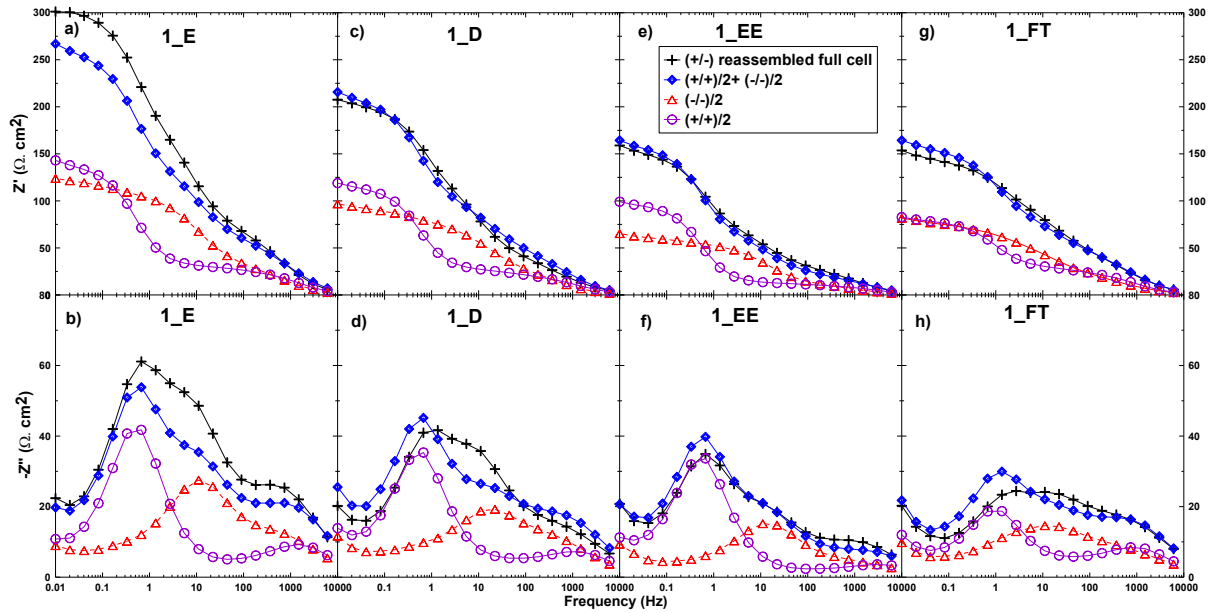
Figure E4. The Area Specific Bode plot spectra corresponding to the Nyquist plots shown in Figure 8.11 in the main thesis.
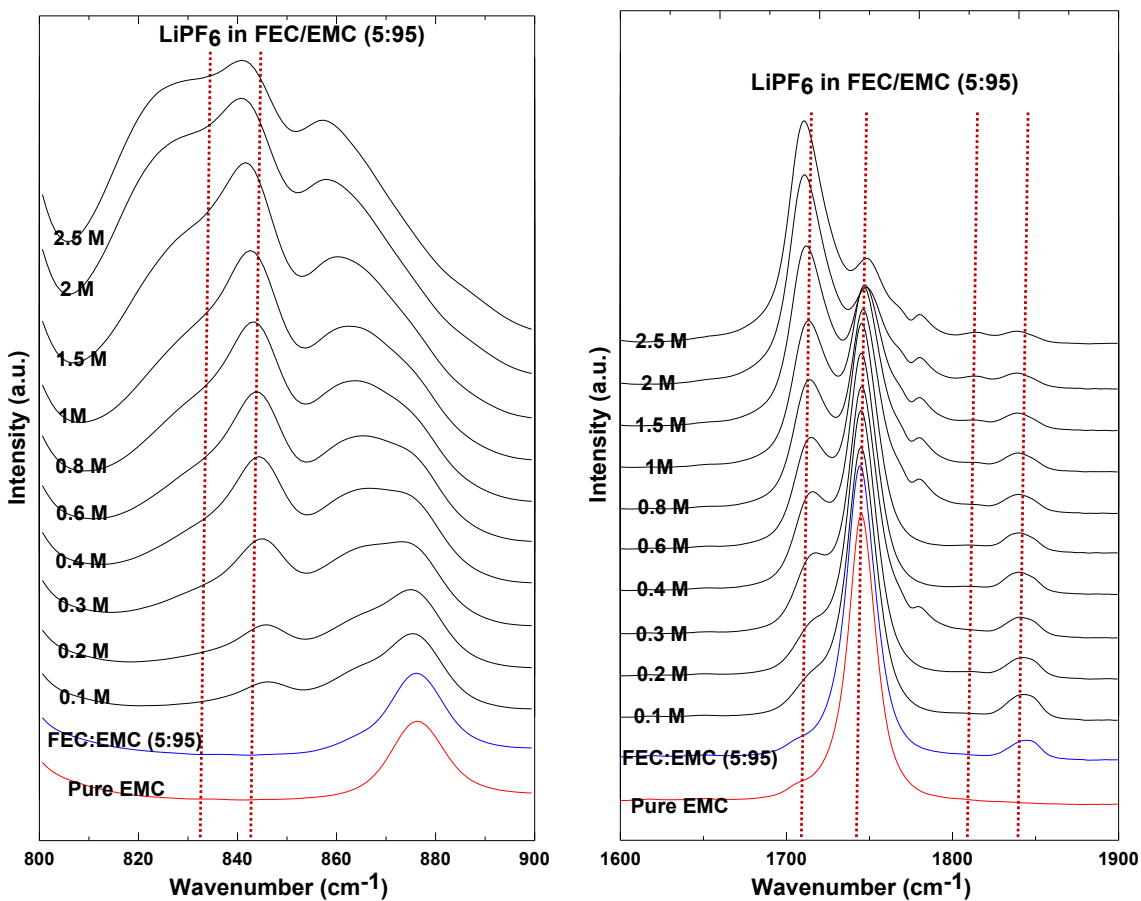
Figure F1 The FT-IR (800-900 and 1600-1900 cm-1) spectra of LiPF6: FEC:EMC (5:90) and pure EMC. Dashed lines indicating the 834, 843, 1710, 1745, 1810 and 1845 cm-1 positions have been inserted into the Figures to guide readers.